

**Optimal Design and Operation of Solid Oxide Fuel Cell Systems
for Small-scale Stationary Applications**

By

Robert J. Braun

A dissertation submitted in partial fulfillment of the requirements for the degree of

DOCTOR OF PHILOSOPHY

(Mechanical Engineering)

at the

UNIVERSITY OF WISCONSIN –MADISON

2002

© Copyright by Robert J. Braun 2002
All Rights Reserved

Abstract

The advent of maturing fuel cell technologies presents an opportunity to achieve significant improvements in energy conversion efficiencies at many scales; thereby, simultaneously extending our finite resources and reducing “harmful” energy-related emissions to levels well below that of near-future regulatory standards. However, before realization of the advantages of fuel cells can take place, systems-level design issues regarding their application must be addressed. Using modeling and simulation, the present work offers optimal system design and operation strategies for stationary solid oxide fuel cell systems applied to single-family detached dwellings.

A one-dimensional, steady-state finite-difference model of a solid oxide fuel cell (SOFC) is generated and verified against other mathematical SOFC models in the literature. Fuel cell system balance-of-plant components and costs are also modeled and used to provide an estimate of system capital and life cycle costs. The models are used to evaluate optimal cell-stack power output, the impact of cell operating and design parameters, fuel type, thermal energy recovery, system process design, and operating strategy on overall system energetic and economic performance.

Optimal cell design voltage, fuel utilization, and operating temperature parameters are found using minimization of the life cycle costs. System design evaluations reveal that hydrogen-fueled SOFC systems demonstrate lower system efficiencies than methane-fueled systems. The use of recycled cell exhaust gases in process design in the stack periphery are found to produce the highest system electric and cogeneration efficiencies while achieving the lowest capital costs.

Annual simulations reveal that efficiencies of 45% electric (LHV basis), 85% cogenerative, and simple economic paybacks of 5-8 years are feasible for 1-2 kW SOFC systems in residential-scale applications. Design guidelines that offer additional suggestions related to fuel cell-stack sizing and operating strategy (base-load or load-following and cogeneration or electric-only) are also presented.

Acknowledgements

The past five years have been among the best of my life. The work, while at times arduous and anxiety producing, was well worth the many benefits that it provided. While my name appears on the cover of this thesis, it was by no means an individual effort. I hold a deep gratitude to the many people who have contributed to this research work and my success.

First and foremost, I am most thankful to my wife, Annemarie, who never doubted me when I questioned my own capabilities and was always there with positive support. Whether it was when feeling overwhelmed, during times of frustration, or just plain exhausted, Love, you were a guiding light who always saw the best in me; you were always my best inspiration and I could not have done it without you. This Ph.D. is just as much yours as it is mine.

I am also most thankful to Professor Sandy Klein who took on a virtually ‘unknown’ student who walked into his office one day in the fall of 1997 wanting to do a Ph.D. project on fuel cell technology. Sandy humbled me on the First Law of Thermodynamics and system boundary selection and while he may not always see his own genius, he defines the meaning of horsepower –able to jump into a problem at any level, make significant contributions, and produce useful work in short periods of time. Sandy, thank you for taking the risk, for investing the enormous amount of time and energy on a project that, initially, we both knew little about, for always remaining positive and excited about the work, for your sharp wit and humor, and for your unswerving confidence in me. It was a pleasure.

I also thank Professor Doug Reindl, my co-advisor, who always kept me on track and laughing over the years. Doug never let you get by with something; he was always able to hone in on the difficult or problematic issues, as well as, keep an eye on the big picture. Doug, I thank you for your quiet support and confidence in my work and your ceaseless efforts at looking out for my best interests. Additionally, the quality of the text of this thesis would be reduced were it not for Doug’s superb ‘word-smithing.’ Without the guidance of professors Sandy Klein and Doug Reindl, very few of the ideas in this work would have come

to fruition or been appropriately explored. I am grateful to have had such an opportunity to work with both of you and to call you friends, colleagues, and as always, advisors.

A special thanks is also extended to Professor Bill Beckman, who always put the 'direct' in director, Professor Tim Shedd for our many fun conversations, Professors Greg Nellis and Dave Foster for helpful comments, and Dr. Peter Holtappels, Dr. Comas Haynes, and Joseph Hartvigsen for the many helpful conversations and e-mails on fuel cell electrochemistry, experimental data, and SOFC operation.

I began my time at UW-Madison as a teaching assistant, which is a rather archaic way to pursue a Ph.D. these days. However, I am thankful that I did because I was fortunate enough to meet Dan Olis, a fellow TA, who became an excellent friend and steadying force in my first and subsequent semesters at UW. I am thankful to Dan for helping me see where I was going when I could not, and for being the true friend and authentic person that he is.

The atmosphere of the Solar Energy Lab, my research work and education, and the numerous friends and colleagues at the University of Wisconsin have provided me with so many positive and growth producing experiences that I cannot possibly elaborate on all of them. Overall, the Solar Energy Lab was a great place to work with lots of good humor and spirit. As a Ph. D. student, many students came and went during my time. Many stand out to me, including Mohammed El-Morsi, Kyle Manske, Nate Blair, Josh Plaisted, Helge Klockow, Alex Wei, Amr Abdo, and Mark (Markus) Reichler. Without them, my time in school would have felt eternal. Other students and colleagues also deserve mention, including Rusi Debu, Dr. Claus Linnemann, Stefan Beschnitt, Myriam Lange, and Sandra Liebermann, Dr. John Collins, Dr. Manoj Neergat, and Dr. Juergen Meier at the Technical University of Munich, where I spent 5 months doing research while enjoying German beer and culture.

I am also thankful for the support of my family, without whom this work would not have so much meaning. Special thanks go to my mother, Mark, Ray and Cherla, and Marie; all of whom made crucial contributions in their own way to my success.

Last but not least, I must extend my gratitude to the Energy Center of Wisconsin, the primary funder of my work. I also wish to thank the Edwin A. Link Foundation, the German Academic Exchange Service (DAAD), and ASHRAE for providing me with additional funds during my tenure at UW.

Table of Contents

Abstract	i
Acknowledgements	iii
List of Figures	xv
List of Tables	xix
Nomenclature	xxi
1.0 Chapter One Introduction	1
1.1 Motivation for Study	2
1.2 Recent Trends in the Electric Power Industry	4
1.2.1 Deregulation of the Power Industry	5
1.2.2 Distributed Generation	6
1.2.3 Emerging Distributed Generation Technologies	7
1.3 Overview of Fuel Cell Technology	8
1.3.1 Fuel Cell Systems	8
1.3.2 Advantages and Disadvantages of Fuel Cells	10
1.4 Comparison of Two Leading Types of Fuel Cells	11
1.4.1 Proton Exchange Membrane Fuel Cells (PEMFCs).....	11
1.4.2 Solid Oxide Fuel Cells (SOFCs)	11
1.5 Objectives	13
1.6 Methodology.....	14
1.7 Thesis Outline.....	16
1.8 Chapter References.....	17
2.0 Chapter Two Literature Review	19
2.1 Design and Operation Aspects of Residential-scale Systems	20
2.1.1 Process Design.....	20

2.1.2	Operating Point Selection.....	21
2.1.3	Off-design Point simulation	22
2.2	Residential Application Studies of Fuel Cell Systems	23
2.2.1	Solid Oxide Fuel Cell Studies	23
2.3	SOFC Modeling.....	23
2.3.1	Steady-state SOFC Modeling.....	24
2.3.2	Dynamic SOFC Modeling.....	27
2.4	Transient Response of SOFC Systems	28
2.4.1	Dynamics of Systems and BOP Components	29
2.5	Summary of Research Gaps in Previous Systems-level Work.....	31
2.6	Chapter References.....	33
3.0	Chapter Three Introduction to SOFC Systems	37
3.1	Simple SOFC System Descriptions.....	37
3.2	Fuel Processing.....	40
3.2.1	Desulfurization	41
3.2.2	Catalytic Steam Reforming (CSR)	42
3.2.3	Partial Oxidation (POX).....	48
3.2.4	Autothermal Reforming (ATR)	49
3.3	Fuel Cell Stack	50
3.3.1	Operational Features, Cell-stack Assemblies, and Component Materials	50
3.3.2	Fuel Cell Performance.....	55
3.4	Power Conditioning & Energy Storage.....	57
3.4.1	Basic Operation of an Inverter	58
3.4.2	Considerations for Dynamic Load Changes or Losses.....	59
3.4.3	Design Challenges of Power Conditioning	60
3.5	Advanced SOFC Systems.....	61
3.5.1	Gas Process Design	61
3.5.2	System Concepts for Residential Applications	63
3.6	System Modeling Approach.....	64

3.7	Chapter References.....	67
4.0	Chapter Four Modeling of Solid Oxide Fuel Cells.....	71
4.1	The Need for a 1-Dimensional, Cell-level Model.....	71
4.2	General Approach to SOFC Stack Modeling.....	72
4.3	Model Assumptions.....	73
4.4	Electrochemical Model.....	77
4.4.1	Charge Balance.....	79
4.5	Thermochemical Model.....	83
4.5.1	Material Balances.....	84
4.5.2	Energy Balances.....	88
4.5.3	Gas Phase Hydrodynamics.....	94
4.5.4	Boundary Conditions.....	96
4.5.5	Transport and Thermodynamic Properties.....	98
4.6	Numerical Solution Technique.....	101
4.7	Chapter References.....	106
5.0	Chapter Five Validation of Cell Model.....	109
5.1	Model Verification.....	109
5.1.1	IEA Benchmark.....	109
5.2	Model Calibration for Anode-supported SOFC Designs.....	110
5.3	Summary.....	117
5.4	Chapter References.....	121
6.0	Chapter Six System Component and Cost Modeling.....	123
6.1	General Approach.....	123
6.2	Balance-of-Plant Component Modeling.....	124
6.2.1	Cell-stack Heat Loss and System Efficiencies.....	124
6.2.2	Fuel Pre-reformer.....	125
6.2.3	Desulphurizer.....	127

6.2.4	Fuel Compressor, Air Blower, and Water Pump.....	128
6.2.5	Air and Fuel Preheaters	131
6.2.6	Jet pump/Ejector	132
6.2.7	DC/AC Inverter	134
6.2.8	Hot Water Storage Tank.....	134
6.3	Cost Model	136
6.3.1	Fuel Cell Cost-Of-Electricity	136
6.3.2	Balance-Of-Plant Costing.....	139
6.3.3	Utility Costing	143
6.4	Chapter References.....	145
7.0	Chapter Seven Effect of Cell-stack Design and Operating Variables on Steady-state Performance.....	147
7.1	Overview of Cell-stack Parameter Variation and Control	148
7.1.1	SOFC Sub-System Process Variables	148
7.1.2	Fuel Cell Steady-State Operating Control.....	150
7.1.3	Parameters Under Study	152
7.1.4	Base Case Inputs and Setup.....	153
7.2	Variation of Control Parameters.....	155
7.2.1	Influence of Control Method (1): constant cell fuel utilization and temperature.....	155
7.2.2	Influence of control method (2): constant cell voltage and temperature.....	163
7.2.3	Influence of control method (3): constant fuel and air feeds.....	164
7.2.4	Summary of control methods	167
7.3	Effect of Variation of Cell Operating Parameters	167
7.3.1	Inlet air flow	168
7.3.2	Inlet air temperature	170
7.3.3	Inlet fuel composition (extent of pre-reforming).....	171
7.4	Variation of Physical Cell-stack Design Parameters.....	173
7.4.1	Interconnect Thermal Conductivity.....	173

7.4.2	Cell Resistance (power density)	174
7.5	Summary.....	176
7.6	Chapter References.....	178
8.0	Chapter Eight System Design and Performance Considerations	179
8.1	General System Design Considerations	179
8.1.1	Residential Application Requirements	179
8.1.2	Process Design and Operation.....	182
8.2	Influence of Cell Parameters on System Performance	184
8.2.1	Design Operating Voltage	185
8.2.2	Fixed Fuel And Air Input Operation	188
8.2.3	Extent of Fuel Conversion In Pre-Reformer	190
8.2.4	Cell Power Density.....	192
8.3	Variation of System Conceptual Design	192
8.3.1	Performance Comparisons Of System Design Alternatives.....	192
8.3.2	Gas Process Design Summary.....	201
8.4	Design Strategies for Variable Thermal-to-electric Ratios	204
8.4.1	High Thermal / Low Electrical Load Condition.....	204
8.4.2	Seasonal High Electric Load (Summer).....	206
8.5	Chapter References.....	207
9.0	Chapter Nine Design and Operation for Residential Applications.....	209
9.1	SOFC System Design via Economic Optimization.....	210
9.1.1	Cell-stack design operating point selection.....	210
9.2	Annual Simulation Setup.....	216
9.2.1	Overview of Example System Design and Performance	216
9.2.2	Simulation Conditions	218
9.3	Evaluation of Operating Strategy (load-following v. base-load)	220
9.4	Economic Sizing of the SOFC stack	222
9.5	Evaluation of Electric-only vs. Cogeneration Operation	224

9.6	Emission Performance.....	225
9.7	Evaluation of Methods to Achieve Variable Thermal-to-electric Ratios.....	228
9.7.1	Net Metering (base-load).....	228
9.7.2	Hot Water Storage Tank System (cogeneration).....	228
9.7.3	“Oversizing” of BOP.....	228
9.8	Design Recommendations for Residential Cogeneration SOFC Systems	230
9.9	Chapter References.....	233
10.0	Chapter Ten Conclusions and Recommendations.....	235
10.1	Summary of Findings and Conclusions.....	235
10.1.1	Cell and System Model Development.....	236
10.1.2	Influence of Cell-Stack Parameters On Cell and System Performance	236
10.1.3	Optimal System Design Concepts.....	238
10.1.4	Optimal Cell-Stack Design Operating Point Selection	239
10.1.5	Residential Applications.....	239
10.2	Recommendations for Further Work.....	240
10.2.1	Modeling.....	240
10.2.2	System Control.....	242
10.2.3	Design.....	243
10.2.4	Other Application Studies	243
10.3	Final Remarks.....	244
10.4	Chapter References.....	247
Appendix I	249
A1.1	Evaluation of Streamwise Radiation Heat Transfer	250
A1.2	Temperature Dependence of the Ionic Conductivity of Yttria-stabilized Zirconia Electrolytes.....	252
A1.3	Evaluation of Fuel Channel Concentration Gradient on Reforming Reaction Rate	253
A1.4	Determination of Shape Factor for Gas-to-Gas Heat Transfer Across Interconnect.....	255

A1.5	EES Code for the effect of concentration gradients on reforming reaction rate	259
A1.6	Appendix I References	261
Appendix II Sample Finite Difference EES Code for SOFC Model.....		263
Appendix III Balance-of-Plant EES Model.....		269
A3.1	Pre-reformer	270
A3.2	Jet Pump/Ejector.....	272
A3.3	Hot Water Heater.....	274
Appendix IV EES Economic Cost Model.....		277

List of Figures

Figure 1.1	Generic Fuel Cell System Description.....	9
Figure 2.1	Schematic of cross-flow geometry and a unit cell for the planar SOFC.....	24
Figure 3.1	Schematic diagram of a hydrogen-fueled SOFC system	38
Figure 3.2	Schematic of a natural gas-fueled SOFC system with external reforming	39
Figure 3.3	Steps involved in fuel processing of fuels for use in fuel cells.....	41
Figure 3.4	Fuel Cell CSR Configurations	45
Figure 3.5	Equilibrium reformat composition from CSR vs. reactor temperature	47
Figure 3.6	Effect of steam-to-carbon ratio on equilibrium reformat composition	48
Figure 3.7	Schematic of a hydrogen-oxygen fuel cell (based on a PEM type).....	51
Figure 3.8	Cell-stack assembly for flat planar fuel cells	53
Figure 3.9	Internal and external manifolding configurations	53
Figure 3.10	Types of losses in fuel cells	57
Figure 3.11	Power conditioning topology for fuel cell electric power output	61
Figure 3.12	Schematic diagram of an advanced natural gas-fueled SOFC system with direct internal reforming and (1) anode and (2) cathode gas recirculation	63
Figure 3.13	Winter and Summer Residential Load Profiles.....	63
Figure 3.14	A conceptual residential sofc system with electrical and thermal storage.....	64
Figure 3.15	Model Information Flow Schematic	66
Figure 4.1	Cutaway view of planar cross-flow fuel cell stack	73
Figure 4.2	Electrochemical Processes within a solid oxide fuel cell	77
Figure 4.3	Cell geometry for co- and counter-flow configurations.....	84
Figure 4.4	Axial slice of a cell displaying the energy flows.	89
Figure 4.5	Cross-section of gas flow in fuel cell channels.....	95
Figure 4.6	Property variation of the anode fuel gas in an SOFC	100
Figure 4.7	Axial discretization of a single cell.....	102
Figure 4.8	Model solution dependence on numerical grid-spacing (IEA benchmark conditions for a direct internal reforming, electrolyte supported solid oxide fuel cell in a co-flow configuration).....	105

Figure 5.1 Schematic cross-section of a SOFC based on the FZJ/GTE design	118
Figure 5.2 Global Thermoelectric single cell voltage-current performance	120
Figure 6.1 Schematic diagram of pre-reformer	125
Figure 6.2 BOP rotating equipment efficiency performance map.....	130
Figure 6.3 Schematic diagram of recycle jet pump.....	133
Figure 6.4 Two-Tank Fuel Cell Thermal Energy Recovery Concept	134
Figure 6.5 Effect of Capacity on Balance-of-Plant Costs	141
Figure 7.1 Schematic diagram of SOFC sub-system and process variables	149
Figure 7.2 (a) Cell voltage, power density, and air stoichs vs. cell current density, (b) Cell power and efficiency vs. cell voltage.....	156
Figure 7.3 Influence of cell voltage on cell heat generation and air flow	159
Figure 7.4 (a) Fuel gas concentration distribution, and (b) temperature distributions	160
Figure 7.5 (a) Cell temperature distribution and (b) cell temperature gradient distribution as functions of operating voltage.....	161
Figure 7.6 (a) Maximum/minimum cell temperatures and temperature gradient and (b) Ratio of heat generation-to-air gas thermal capacitance with varying operating voltage	162
Figure 7.7 (a) Comparison of amount of cooling air and (b) maximum temperature gradient between different controlling variables	163
Figure 7.8 (a) Cell power and cooling air and (b) cell efficiency and fuel utilization as functions of input fuel mass flow	164
Figure 7.9 Influence of operating voltage on cell power, efficiency, fuel utilization and temperature for fixed fuel and air input.....	165
Figure 7.10 Influence of cell voltage on Nernst potential and maximum temperature gradient for fixed fuel and air input.....	166
Figure 7.11 The effect of operating voltage and input fuel mass flow on cell power and temp.	167
Figure 7.12 Effect of air flow on cell power and average cell temperature	169
Figure 7.13 Effect of operating voltage and airflow on ζ	169
Figure 7.14 Influence of inlet air temperature on cell power and temperature	170
Figure 7.15 Influence of methane conversion on cell heat and power generation and cooling air indices (800°C cell temp., 700°C inlet air, 0.5 mA/cm ² , 85% U _f , s/c=2.0) .	172

Figure 7.16 Influence of methane conversion on cell temperature and temperature gradient distributions (800°C cell temp., 700°C inlet air, 0.5 mA/cm ² , 85% U _f , s/c=2.0).....	172
Figure 7.17 Influence of interconnect thermal conductivity on cell thermal performance (0.7 volt, 85% fuel utilization, 800°C nominal temperature, 700°C inlet air).	173
Figure 7.18 Influence of cell power density on cell voltage, efficiency, and power.....	174
Figure 7.19 Influence of cell power density on temperature and temp. gradient distributions	175
Figure 7.20 Effect of power density on ζ , cooling air, and maximum temperature gradient.....	176
Figure 7.21 Effect of (a) fuel utilization and (b) cell temperature on V-I performance.....	177
Figure 8.1 Diurnal electrical energy demand of a household.....	180
Figure 8.2 Winter and summer residential load profiles	181
Figure 8.3 Residential hot water and space heating diurnal thermal-to-electric ratios	181
Figure 8.4 Decision paths in system process design	183
Figure 8.5 Methane-fueled SOFC system concept with internal reforming	184
Figure 8.6 Influence of design cell voltage on stack and air blower power, system efficiency, and system thermal to electric ratio.....	185
Figure 8.7 Effect of design cell voltage on air stoichs, air preheater UA, and gas temperatures.....	186
Figure 8.8 T-Q diagram of steam boiler and thermal energy recovery heat exchangers	188
Figure 8.9 Influence of cell voltage on power, efficiency, and TER for fixed feed conditions.....	189
Figure 8.10 System TER and combustor temperature as a function of fuel utilization	190
Figure 8.11 Influence of methane conversion on system performance (85% U _f , s/c=2.0, average current = 0.57 A/cm ²).....	191
Figure 8.12 Efficiency comparison between conceptual SOFC system designs.....	196
Figure 9.1 Schematic diagram of 3 kW SOFC system design with anode recycle (case 4a)	210
Figure 9.2 Influence of design cell voltage on cost of electricity	210
Figure 9.3 Breakdown of the COE for 3 kW SOFC system design case	212
Figure 9.4 Influence of system fuel utilization and design cell voltage on COE	213
Figure 9.5 Influence of operating cell temperature and system power rating on life cycle costs	214

Figure 9.6 2 kW SOFC cogeneration system employing AGR and internal reforming.....	217
Figure 9.7 2 kW SOFC stack and efficiency performance (73 cells, 78% fuel utilization, 800°C operation, 100% internal reforming).....	218
Figure 9.8 2 kW SOFC operating profiles.....	220
Figure 9.9 Comparison of base-load and load-following operating strategies in terms of system size.....	222
Figure 9.10 Effect of size on payback and capacity factors	223
Figure 9.11 Sensitivity of economic payback to utility prices and SOFC stack cost.....	225
Figure 9.12 SOFC CO ₂ emission performance as a function of system size	226
Figure 9.13 Specific and total CO ₂ emissions as functions of operating strategy and size...	227
Figure 9.14 Comparison of oversized BOP and base case system performance.....	229
Figure A1.1 Channel geometry for view factor determination	250
Figure A1.2 Ionic conductivity of 8 mol% YSZ as a function of temperature	253
Figure A1.3 Effect of reaction rate and wall partial pressure with Reynolds number	256
Figure A1.4 Effect of reaction rate and wall partial pressure with temperature	257
Figure A1.5 Interconnect geometry and boundary conditions for a single gas channel	258
Figure A1.6 Temperature gradient vectors for heat conduction across a single gas channel.	259

List of Tables

Table 1.1 Comparison of PEMFC and SOFC Technologies.....	13
Table 1.2 Limiting Cases of Research.....	16
Table 2.1 Summary of SOFC modeling efforts.....	25
Table 2.2 Summary of Previous Work in Systems-related Research.....	32
Table 3.1 Possible Reactions in Reforming	43
Table 3.2 Materials Used in SOFCs	54
Table 4.1 Summary of Basic Model Equations.....	97
Table 4.2 Model inputs, outputs, and parameters.....	103
Table 5.1 Benchmark 1 Test Conditions	111
Table 5.2 Benchmark 2 Test Conditions	112
Table 5.3 Comparison of SOFC Model with IEA Benchmark 1 Results.....	113
Table 5.4 Comparison of SOFC Model with IEA Benchmark 2 Results.....	114
Table 5.5 Material and thickness data of anode-supported SOFC conceptual design	119
Table 6.1 SOFC Component Pressure Drops	131
Table 6.2 5 kWe System Capital Cost Data	138
Table 6.3 Average Natural Gas Prices for Selected States from 1997-2000.....	143
Table 6.4 1998 Average Monthly Electricity Rate and Billing Information.....	144
Table 7.1 SOFC model inputs, outputs, and parameters	149
Table 7.2 Process variables in the physical SOFC sub-system.....	150
Table 7.3 Parameters and Performance Indices	153
Table 7.4 Base case model inputs and outputs	154
Table 8.1 System Design Case Pressure Drops.....	193
Table 8.2 Performance comparison of various SOFC system design concepts	194
Table 8.3 Relative cost of common heat exchanger tube materials	200
Table 9.1 Optimal SOFC stack design parameters.....	215
Table 9.2 SOFC system design point specifications	217
Table 9.3 Base case application specifications.....	219

Table 9.4 SOFC system capital cost.....219
Table 9.5 Performance comparison of 2 system design approaches on annual basis230

Nomenclature

Roman Symbols

A	Area (m^2)
A_c	Minimum free flow area in heat exchanger core, (m^2)
A_e	Electroactive cell area, (m^2)
A_x	Cross-sectional area, (m^2)
a	Fuel channel height, (m) or Tafel parameter
b	Channel width, (m) or Tafel parameter
B	Ratio of gas-to-solid heat transfer area to electrochemical cell area
c	Air channel height, (m)
C	Component unit cost ($\$/\text{kW}$)
C_F	Fuel cell system annual capacity factor
COE	Cost of electricity, (cents/kWh)
c_i	Concentration of species i , (mol/m^3)
c_p, \bar{c}_p	Specific heat or average specific heat, ($\text{kJ}/\text{kmol}\cdot\text{K}$)
D_h	Hydraulic diameter, (m)
D_{eff}	Effective diffusion coefficient, (m^2/s)
D_{i-j}	Binary diffusion coefficient between species i and j , (m^2/s)
d_p	Catalyst bed particle diameter, (m)
e^-	Electron
E_A	Activation energy, (kJ/kmol)
E_{air}	Energy contained in the air channel (cathode channel), (kJ)
E_{cell}	Energy contained in the cell structure (anode-electrolyte-cathode-interconnect), (kJ)
E_{fuel}	Energy contained in the fuel channel (anode channel), (kJ)
E_N	Nernst potential, (V)
$\Delta \dot{E}$	Change in the rate of energy in a slice element, (kJ/sec)
\dot{E}	Rate of energy flow, (kJ/sec)
F	Faraday constant, (A-sec/mol)
F_c	Fuel cost, ($\$/\text{million Btu}$)
F_{th}	Fraction of thermal energy from fuel cell system that can be utilized
f	Friction factor
f_E	Equilibrium factor for reforming reaction
ΔG	Gibbs free energy change of the overall reaction, (kJ/kmol)

ΔH	Enthalpy change of the overall reaction, (kJ/kmol)
h	Convective heat transfer coefficient, (W/m ² -K) or mass specific enthalpy (kJ/kg)
\bar{h}	Molar specific enthalpy, (kJ/kmol)
HHV	Higher heating value, (kJ/kmol)
i	Cell current, (A)
i_{cs}, i_{as}	Limiting current density at electrode (A/cm ²)
i_d	Economic discount rate
i_o	Effective electrode exchange current density (A/cm ²)
j	Cell current density, (A/cm ²)
k	Thermal conductivity, (W/m-K) or specific heat ratio
k_1, k_2	Economic conversion factors
k_o	Pre-exponential factor, (mol/s-m ² -bar)
K	Equilibrium constant
K_e, K_c	Entrance and exit pressure loss coefficients
l_c, l_a	Electrode thickness
LHV	Lower heating value, (kJ/kmol)
L_t	Reactor tube length, (m)
m	Mass, (kg) or hardware scaling exponent
\dot{m}	Mass flowrate (g/s)
M	Molecular weight
M_C	Fuel cell system maintenance cost, (cts/kWh)
n	Number of moles, (kmol) or power plant life, (years)
\dot{n}	Molar flowrate, (mol/s)
n_e	Number of electrons transferred in the electrochemical reaction
Nu	Nusselt number
\dot{n}''	Molar flux, (moles/sec-m ²)
p, p_i	Total pressure or partial pressure of species i , (bar)
P	Cell-stack power, (kW)
q''	Heat flux, (kW/m ²)
\dot{Q}_{cv}	Rate of thermal energy transferred across the control volume, (kW)
\dot{Q}_{gen}	Volumetric thermal energy generation, (kW/m ³)
\dot{r}	Reaction rate, (mol/s)
\dot{r}'''	Volumetric reaction rate, (mol/m ³ -s)
Re	Reynolds number

R_{cell}	Total cell resistance, (Ω)
R_F	Capital recovery factor
R_u	Universal gas constant, (kJ/kmol-K)
S	Shape Factor or hardware capacity
ΔS_{fc}	Change in entropy of the overall reaction, (kJ/kmol-K)
T	Temperature, (K)
t	Time, (sec)
Δt	Time increment, (sec)
U_f	Fuel utilization
u_s	Superficial mass velocity, (m/s)
U_{tot}	Overall heat transfer coefficient
V	Voltage, (V) or gas velocity in cell channels, (m/s)
\dot{V}	Volumetric gas flow, (m^3/s)
$V_{v,c}, V_{v,a}$	Electrode porosity (cathode or anode)
\dot{W}_{cv}	Rate of work transferred across the control volume, (kW)
W_{max}	Maximum work output, (kJ)
x	Axial coordinate, (m)
x_{conv}	Fractional conversion of methane
Δx	Length of slice or discretized element, (m)

Greek Symbols

α	Electrochemical transfer coefficient
α^*	Geometric ratio of channel height over channel width
δ	Cell thickness, (m)
ε	Reactor bed void fraction or heat exchanger effectiveness
ε_H	Thermal energy recovery efficiency of the fuel cell system, (LHV)
η_R	Efficiency of thermal source displaced by fuel cell system, (LHV)
η_s	Isentropic efficiency
η_{sys}	System electric efficiency
η_{cogen}	Cogenerative system efficiency
η_{act}	Activation overpotential, (V)
η_{conc}	Concentration overpotential, (V)
λ	Excess air supplied to fuel cell (stoichs)

μ	Dynamic viscosity, (kg/m-sec)
μ^o	Chemical potential of species at atmospheric pressure, (kJ/kmol)
ν	Stoichiometric reaction coefficient or specific volume of gas, (m ³ /kg)
ρ	Density, (kg/m ³)
σ	Stefan-Boltzmann constant, (W/m ² -K ⁴) or ratio of core free-flow area to frontal area
τ_c, τ_a	electrode tortuosity

Subscripts

<i>a</i>	Air gas
<i>act</i>	Actual
AP	Air preheater
blow	Blower
<i>c</i>	Cold
chk	Check
comp	Compressor
cond	Conduction
conv	Convection or conversion
<i>CH₄</i>	Methane
<i>CO</i>	Carbon monoxide
<i>CO₂</i>	Carbon dioxide
<i>E</i>	Electrochemical reaction
<i>f</i>	Fuel gas
<i>g</i>	Gas mixture
<i>h</i>	Hot
H ₂	Hydrogen
H ₂ O	Water
HR	Heat recovered
<i>i, j</i>	Species <i>i</i> or species <i>j</i>
<i>ic</i>	interconnect
<i>irrev</i>	Irreversible
O ₂	Oxygen
<i>prod</i>	Products
<i>R</i>	Reforming reaction
<i>rad</i>	Radiation

<i>react</i>	Reactants
<i>rec</i>	Recovered
<i>rev</i>	Reversible
slice	Discretized element
w	Water
<i>wgs</i>	Water-gas shift reaction
<i>s</i>	Solid or surface

Abbreviations

AC	Alternating current
AGR	Anode gas recycle
ATR	Autothermal reforming
BOP	Balance-of-plant
CGR	Cathode gas recycle
COE	Cost-of-electricity
CSR	Catalytic steam reforming
CSTR	Continuously stirred tank reactor
DC	Direct current
DG	Distributed generation
DHW	Domestic hot water
DIR	Direct internal reforming
ER	External reforming
HHV	Higher heating value
IEA	International energy agency
IR	Internal reforming
kWe	kilowatt electric
kWth	kilowatt thermal
LHV	Lower heating value
MMBtu	Million British thermal units
PEMFC	Proton exchange membrane fuel cell
POx	Partial oxidation
SOFC	Solid oxide fuel cell
TER	Thermal-to-electric ratio
UA	Product of overall heat transfer coefficient with heat exchanger surface area
V-I	Voltage-current

Chapter One

Introduction

The advent of maturing fuel cell technologies presents an opportunity to achieve significant improvements in energy conversion efficiencies at many scales; thereby, simultaneously extending our finite resources and reducing “harmful” energy-related emissions to levels well below that of near-future regulatory standards. Due to their modular nature, fuel cells have the potential to widely penetrate energy end-use market sectors. If fuel cells are applied on a large scale, substantial reductions in both national emissions and fuel consumption can be realized. Although fuel cells-themselves have been studied extensively, primarily from materials and electrochemical viewpoints, a considerable gap exists in the area of application techniques to maximize benefits of fuel cell units for both electrical energy generation and thermal energy utilization. With fuel cell commercialization fast approaching, considerable efforts, aimed at developing component level hardware, such as fuel cell stacks and fuel reformers, are being expended. Relatively little work is being performed in systems-level research. In order to realize the high-energy conversion efficiencies offered by fuel cell devices, it is crucial that methodologies for system-level optimal design be developed to achieve the maximum overall system efficiency and cost effectiveness.

The objective of this research is to develop methods for optimal design and operation of fuel cell systems in small-scale (1-10 kW) applications (with particular focus on single-family detached dwellings). In order to gain a better perspective on the importance of this research and the driving forces behind it, the motivation for the proposed study will be discussed next followed by a summary of recent trends in the stationary electric power industry. An introduction to fuel cell technology, in which the basic system operation is reviewed, and a description of two leading types of fuel cells is then given. The chapter concludes by presenting the research objectives and methodology followed by an overview of the subsequent thesis chapters.

1.1 Motivation for Study

In the U.S., the residential and commercial market sectors alone account for over 35% of the total annual energy consumed [1]. Of this fraction, over 50% is used for low-efficiency space and domestic hot water heating, air-conditioning, and refrigeration [2]. Modern residential furnaces operate at less than 15% efficiency (based on the 2nd Law), leaving substantial room for improvement. Nearly all of the energy conversion technologies in the various end-use sectors (transportation, industrial, and utility) attain higher efficiencies than that achieved in residential heating applications. Low cost of heating fuels (natural gas, propane, and fuel oil) has allowed continued use of inefficient direct-fired heating systems. However, increasing national and international pressure to reduce greenhouse gas emissions (primarily CO₂) coupled with finite energy resources will give renewed impetus to improving fuel conversion efficiencies [3, 4]. Additionally, electric utilities (and independent power producers) nationwide are studying ways to meet the ever-increasing energy demands in a competitive environment through the use of distributed generation resources.

Driving forces that include electric utility deregulation, increasingly stringent end-use power quality requirements, environmental concerns, and the performance advancements in distributed generation technologies are triggering a movement towards a decentralized electric power industry. Congruent with this, considerable attention has been focused on fuel cells as an attractive solution for 21st century power needs. A significant portion of the recent attention has been due to a perception of proton exchange membrane fuel cells (PEMFCs) as the heir apparent to the IC engine in automobile applications. This perception has been encouraged by the commitment of nearly \$1 billion by automakers into the research and development of fuel cell vehicles. Whether the investment is a vast marketing ploy, an ill-founded rationale, or scientifically based decision, the large infusion of capital into PEM fuel cell development has also heightened awareness of the potential use of fuel cells in *other* applications. In fact, due to the severe operating and cost requirements of the automotive sector, one could reasonably expect fuel cells to first be commercialized in residential and commercial stationary power markets –most likely in the 1-300 kW range. The proposed research is being focused by the imminent entry of fuel cells into the residential market. This

application presents a timely opportunity to develop design and operation methods and to gauge the effectiveness of fuel cell systems in this important energy sector.

Unfortunately, the overwhelming attention captured by the proton exchange membrane fuel cell technology has overshadowed the steady development activities of other fuel cell types, such as the solid oxide fuel cell (SOFC). The suitability of the SOFC for residential and commercial applications has been reviewed at a “high” level and found to have several advantages over PEM type fuel cells. In these applications, the ability of the fuel cell type to meet the building energy demands will depend on both its electrical and thermal performance characteristics, as well as system design. It is therefore important that the appropriate fuel cell technology for the specific application be selected. However, as will be discussed in Chapter Two, neither optimal design methods nor comparative performance assessments between PEMFCs and SOFCs have been made. Thus, more detailed study and review of *both* technologies is required to make a critical evaluation of the relative merits of PEMFCs and SOFCs in small-scale applications.

Despite the numerous advantages of fuel cells, they are not without their disadvantages. In traditional power generation systems, a load step of 20-25% of the generator rating is considered large, causing significant transients [5]. Distributed power systems, such as in residential applications, will require load steps of 50-60% of system rating without causing safety or stability problems for both the fuel cell system components and the load. Load step changes of this magnitude may take several minutes or longer for fuel cell systems due to the thermal lag of the fuel cell and fuel processing hardware. Additionally, proper steam-to-carbon ratios in the fuel reformer feedstock must be maintained during these operating point changes in order to ensure no harmful carbon deposition occurs in either reformer or fuel cell stack components. Issues of safe operation and control also exist when stepping *down* in load. During this process, excessive unreacted fuel will exit the fuel cell stack for a short period of time and enter the combustor. Depending on how the fuel cell stack is thermally integrated with the afterburner, the subsequent fuel oxidation and heat release may generate large temperature gradients in the fuel cell components and downstream heat exchangers, causing

excessive thermal stresses or exceeding the temperature limits of the hardware. To date, the dynamic response of a SOFC has only been superficially examined.

It has often been stated that the characteristically low thermal-to-electric ratio of the SOFC makes them attractive for providing the thermal requirements of various end-use applications. The high-grade waste heat produced in a solid oxide fuel cell can be utilized for space heating, process steam, and/or domestic hot water demands. The type of heat recovery depends on the application requirements and the resulting cogenerative efficiency will depend on the design. A significant issue surrounding the use of highly efficient fuel cells in residential applications, is their ability to meet the highly non-coincident electric and thermal loads in either grid-connected or stand alone configurations. That is, in either base load operation or electric load-following conditions, electricity and/or heat may be available when it is not needed or vice-versa. Additionally, either higher or lower fuel efficiency and different proportions of electric and thermal output is derived from the fuel cell system depending on where the fuel cell stack is operated on its voltage-current characteristic. As a result, both the *system* design point and off-design point operating characteristics are dependent on (i) selection of optimal *fuel cell* design and operating point, (ii) heat recovery design, (iii) electric and thermal load management, and (iv) the performance characteristics of auxiliary hardware, such as inverters, pumps, compressors, controls, and external reformers (if any). These and other operating aspects require detailed study to elucidate and resolve implementation issues before commercialization of the technology; thereby, enabling an accelerated realization of the inherently high efficiencies of fuel cell systems.

1.2 Recent Trends in the Electric Power Industry

The combination of market forces, environmental concerns, and recent trends in the development of energy-efficient electric generation equipment, such as fuel cells, will change the manner in which energy is generated, utilized, and supplied in all end-use sectors within the next twenty-five years. A significant market force driving stationary electric power generation is deregulation of the electric utility industry. Deregulation has proceeded in several states already, such as California and Rhode Island, and most other states have

legislation in place with established deadlines for the introduction of competition. In the state of California, the recent wholesale electricity price spikes have clouded the future of deregulation there, however, deregulation will likely continue throughout the U.S. as lessons in implementation are learned. In addition to deregulation, trends in both technology advancements of smaller power generation devices and end-user requirements are also contributing to a changing landscape of the electric power infrastructure.

1.2.1 Deregulation of the Power Industry

Deregulation is designed to separate power production from distribution with the promise of lowering electricity prices through competition. The breakup of the current power utility monopolies into separate, unregulated business segments is a necessary step towards that end. In a deregulated environment, the organizational structure will likely be comprised of power producers, billing and metering companies, and power marketers who act as middlemen between producers and consumers (the transmission and distribution system will remain a regulated entity). Increased grid-electricity prices will accelerate the introduction of fuel cell technology. On the other hand, lower electricity prices could slow the penetration of new generation technologies into the market. Accomplishing the goal of lowering electricity prices for businesses and consumers is uncertain and complicated by the available installed capacity (and power demand), grid conditions (from moment to moment), real-time pricing, and demand side management practices [6]. All of these factors can substantially affect electricity price volatility and the real cost of supplying power and thereby, cloud the future success of fuel cells.

Independent of deregulation, several driving forces are creating interest in a paradigm shift from centralized to decentralized power generation. The demand for high power quality to operate increasingly sophisticated end-use equipment is one such driver. The monetary importance of power quality was quantified by one study that estimated power fluctuations cause annual losses of \$12 to \$26 billion nationwide [7]. For a precision machining plant, it has been estimated that a voltage sag with a 0.1 second duration can cause losses of \$250,000 in lost product and labor costs to reconfigure the facility [8]. Another driver promoting the

use of distributed generation resources is avoided costs associated with upgrading transmission and distribution (T&D) systems to meet growing capacity requirements. This effect will intensify as the expanding energy market continues to outdistance the addition of new generation facilities. On average, the U.S. demand for power increases at a rate of about 2% annually and the present world energy demand exceeds the *planned* addition of 1200 GW of electricity by 2005 [9]. A final motivating force is the technology advancements in distributed power generation which have made high efficiency, low cost devices that can be sited close to the demand thereby improving power quality and avoiding the cost of expanding T&D infrastructure possible.

1.2.2 Distributed Generation

The Electric Power Research Institute (EPRI) defines distributed generation as,

“the integrated or stand-alone use of small modular resources by utilities, utility customers, and third parties in applications that benefit the electric system, specific customers, or both” [10].

In a stand-alone scenario, distributed generation is synonymous with on-site generation and cogeneration. Recent trends in the number of generator orders and installations show that distributed generation technology has become an attractive alternative to the traditional method of constructing large central power plants. Presently, over 35% of the total U.S. industrial electric power demand is met by on-site generation and a recent study by EPRI indicates that 25% of new generation will be distributed by 2010 [5].

The use of distributed generation (DG) offers many advantages and non-traditional benefits that central utilities cannot match, and depending on market penetration, DG may eventually compete with utility-scale cost-of-electricity. Some of the often-stated advantages of distributed generation from both utility and consumer perspectives include:

- 1) Economy power or “peak-shaving” which allows the customer to take advantage of time-of-day pricing, effectively leveraging fuel costs against electricity prices. Demand charges can also be reduced.
- 2) Cogeneration and trigeneration for on-site customer needs are possible and large overall system efficiency augmentation is possible.
- 3) Premium power—uninterrupted power supply and high power quality.

- 4) Little or no transmission and distribution (T&D) expansion costs.
- 5) Utilities can meet energy demand in smaller increments with a lower cost, lower risk investment and capital layout enabling a “just-in-time” philosophy.
- 6) Issues surrounding new plant siting and “right-of-way” permitting for new T&D power lines are reduced.
- 7) Plant siting closer to the demand eliminates the average 7-8% busbar power loss in the T&D system and increases overall system efficiency [11].
- 8) Niche markets, such as emerging countries or remote locations where there is little or no existing T&D infrastructure and limited fuel options, can be better served.

The implementation of distributed fuel cell power generation technologies has the potential to assist in reducing “harmful” emissions and, in some cases, the annual output of greenhouse gases by virtue of their high energy conversion efficiencies. Fuel cell technologies at both large and small scales will compete against new natural gas-fueled combined cycle (NGCC) power plants that have registered 55-60% (LHV) efficiencies. (Small-scale fuel cell systems will compete with grid-based electricity, and therefore, to some extent, NGCC technology.) NGCC systems have proven to be cost competitive and efficient, but they have difficulty in siting and permitting and make use of the inefficient T&D system. Without considering the T&D inefficiencies, siting, or permitting, a recent study indicates that on a total life cycle basis solid oxide fuel cell systems, for instance, are expected to have lower global warming potential and acidification emissions than all types of power plants, including natural gas-fueled combined cycle plants [12]. In most cases, the removal of the T&D inefficiency through distributed generation represents an effective increase in overall fuel-to-electricity efficiency when compared with the traditional central power plant. Thus, increasing concern over global climate change and adverse health effects from “harmful” emissions represent additional pressures stimulating movement towards distributed generation.

1.2.3 Emerging Distributed Generation Technologies

In addition to fuel cells, there are numerous available or developing distributed generation technologies. However, at 1-10 kW scales of interest in this research, only photovoltaic (PV) technology is seen as a direct competitor –a competitor which also has high first costs. Additionally, it is quite likely that PV and fuel cell technology will be integrated in the future

to provide a completely renewable power source (cf. 13). Engine-driven generators are used primarily in remote applications or as grid-backup and microturbine technology is targeted towards small- and medium-sized commercial applications (25-250 kW). Thus, competition for fuel cells in residential-scale applications, will be with the current grid-prices and amongst other fuel cell types (i.e. between solid oxide and proton exchange membrane technologies).

1.3 Overview of Fuel Cell Technology

Electrochemical fuel cells may convert fuel directly to electricity (with heat as a byproduct) at efficiencies greater than any single conventional energy conversion technology. Their modular nature, coupled with their ability to generate electricity cleanly and efficiently, make them attractive for a wide variety of applications and markets. There are six different types of fuel cells that have received varying degrees of development attention:

- Alkaline fuel cell (AFC)
- Proton exchange membrane fuel cell (PEMFC)
- Direct methanol fuel cell (DMFC)
- Phosphoric acid fuel cell (PAFC)
- Molten carbonate fuel cell (MCFC)
- Solid oxide fuel cell (SOFC)

Presently, the 80°C proton exchange membrane fuel cell (PEMFC) and the 700-1000°C solid oxide fuel cell (SOFC) have been identified as the likely fuel cell technologies that will capture the most significant market share [14, 15]. Since both PEMFCs and SOFCs are targeted for early commercialization in the residential (1-10 kW) end-use market, system studies in these areas are of particular interest. A detailed description of these two types and an overview of fuel cell operation is presented next.

1.3.1 Fuel Cell Systems

The basic components of a fuel cell power plant consist of a fuel processor, fuel cell power module, power conditioning equipment for dc-to-ac inversion, and process gas heat exchangers. Depending on the operating temperature, fuel cells produce varying grades of

waste heat that can be recovered for process heating, gas compression requirements, or exported for cogeneration (or trigeneration) purposes. The utilization of this waste heat may significantly impact system efficiency, economics (given sufficient process loads), and environmental emissions.

Figure 1.1 exhibits a schematic diagram of a generic fuel cell system. Most fuel cell types require hydrogen for operation. Fuel entering the plant is delivered to the fuel processing sub-system where it is desulfurized, preheated, and reformed. Removal of sulfur from the fuel can take place at low or high temperature depending on the desulfurization process. Reforming the natural gas, that is, converting the hydrocarbons to carbon dioxide and hydrogen through reforming and shift reactions, requires steam. Therefore, prior to reforming, steam is injected into the natural gas supply (often at an approximate molar steam-to-carbon ratio of 2-3:1).

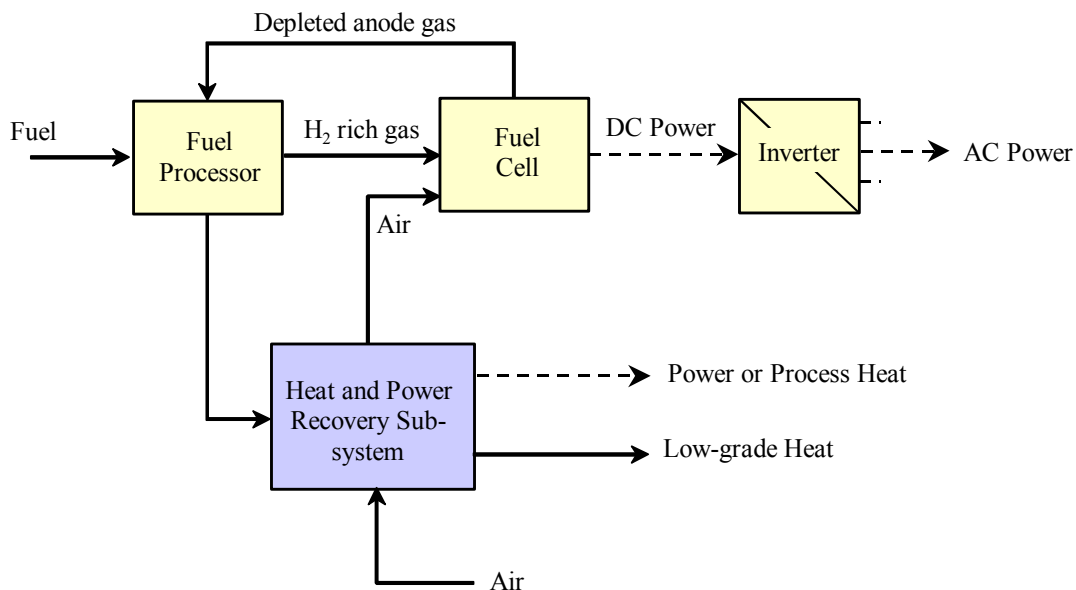


Figure 1.1 Generic Fuel Cell System Description

After fuel preparation, the gas is delivered to the fuel cell where surface reactions electrochemically oxidize the fuel. The rate of fuel oxidation varies along the surface of the cell and the rate is directly proportional to the current. Cell-stack electric efficiencies range from 30 – 60% (HHV) depending on the type of fuel cell and the system configuration. Fuel cells produce DC power which is converted to AC through power conditioning at efficiencies

as high as 98%. Using conventional heat recovery equipment, overall first law system efficiencies of 75-85% (HHV) can be realized. A more thorough introduction to fuel cells and solid oxide fuel cell systems is presented in Chapter 3.

1.3.2 Advantages and Disadvantages of Fuel Cells

The perceived advantages of fuel cells over conventional power generating equipment include high electric efficiency, low chemical, acoustic, and thermal emissions, siting flexibility, reliability, low maintenance, excellent part-load performance, modularity, and fuel flexibility. Due to higher efficiencies (for some types) and lower fuel oxidation temperatures, fuel cells output lower carbon dioxide and nitrogen oxides per kilowatt of power generated than conventional prime movers like the gas turbine and internal combustion engine. Any measurable nitrogen oxides produced in a fuel cell system are typically attributable to the fuel processor. It should also be noted that fuel cell efficiency increases at part-load conditions. This is an opposite characteristic of rotating equipment, such as gas and steam turbines, fans, compressors, etc. While in some fuel cell systems, the part-load performance of the fuel cell processor decreases, the combination of fuel processor and fuel cell produce a level efficiency curve over a range of load conditions [16]. As most fuel cell types operate on hydrogen, hydrocarbon fuel processing in general represents a significant challenge to the commercialization of fuel cells; this is particularly true for PEMFCs due to their susceptibility to poisoning from low-level CO and due to system integration issues of matching high temperature fuel reforming with low temperature cell operation.

Some additional issues of stationary fuel cell systems include short operating life (~40,000 hours), which heavily influences plant economics, high first costs, lack of substantial operating experience in the field, and unproven durability while operating on hydrocarbon-based fuels and when subjected to thermal cycling. For many fuel cell types, end-of-life cell-stacks have good salvage value that can ease the cost burden of replacing an entire stack in the system every five years. While the phosphoric acid fuel cell demonstration program has registered over 1 million hours of real life operating experience, sustained operation of PEMFCs and SOFCs on hydrocarbon-based fuels has yet to be proven.

1.4 Comparison of Two Leading Types of Fuel Cells

1.4.1 Proton Exchange Membrane Fuel Cells (PEMFCs)

The PEMFC's electrolyte is a solid polymeric membrane fitted between two platinum-catalyzed porous electrodes. PEMFCs typically operate at about 80–85°C, a temperature determined by both the thermal stability and the ionic conductivity characteristics of the polymeric membrane [17]. The proton-conducting polymer electrolyte requires liquid water to have sufficient ionic conductivity. The use of liquid water limits operating temperatures to less than 100°C. The low-operating temperature allows the PEMFC to be brought up to steady-state operation rapidly.

Reformed natural gas often contains other gas species such as carbon monoxide (CO), which are detrimental to fuel cell operation. In PEMFCs, carbon monoxide levels of 50 ppm or greater result in tenacious adsorption of CO at electrocatalytic sites, causing severe degradation in cell performance. Operating on pure hydrogen, PEMFCs can obtain an electrical efficiency of nearly 50 percent. However, because the temperature of the waste heat from the fuel cell is too low to be used in the fuel reforming process, overall system efficiency has been limited to 42 percent [18].

Historically, PEMFC development has lagged other fuel cell types. However, in the late 1980s, significant technological advancements in power density were achieved and they have developed rapidly since the early 1990s. Much of the recent development attention has been focused on PEMFCs for automotive applications due to their rapid transient capabilities, high power density, lightweight, and simple cell design. PEMFCs are expected to commercialize in the stationary power market in the 2003/4 timeframe and if cost targets can be realized, eventually in automotive markets, perhaps as early as 2010.

1.4.2 Solid Oxide Fuel Cells (SOFCs)

SOFCs employ a solid-state electrolyte and operate at the highest temperature (700-1000°C) of all fuel cell types. The SOFC uses a solid yttria-stabilized zirconia ceramic material as the electrolyte layer. During operation, oxidant (usually air) enters the cathode compartment and after the electrode reaction, oxygen ions migrate through the electrolyte layer to the anode

where hydrogen is oxidized. The operating temperature of SOFCs is sufficiently high to provide the necessary heat to support the endothermic reforming of methane. SOFCs are therefore more tolerant of fuel impurities and can operate using hydrogen and carbon monoxide fuels directly at the anode. They do not require costly external reformers or catalysts to produce hydrogen, and the use of internal reforming actually increases overall system efficiency. The relative insensitivity of SOFCs to gas contaminants normally considered “poisons” to lower temperature fuel cells makes them especially attractive for unconventional fuels, such as biomass or coal-gas.

SOFCs also have the potential for high system efficiencies. When integrated with a gas turbine, SOFC systems are expected to achieve 70–75% (LHV) electric efficiencies, representing a significant leap in efficiency over other energy conversion technologies. Additionally, developers expect commercial SOFCs to have lifetimes of 10 to 20 years, two to four times longer than other fuel cells.

The disadvantage of the SOFCs high operating temperature is the stringent materials requirement for the critical cell components. Exotic ceramics, metal-ceramic composites, and high temperature alloys drive up the cost of SOFCs, as do the manufacturing techniques demanded by these materials (electrochemical vapor deposition, sintering and plasma spraying). Because of the stringent materials requirement and demanding manufacturing techniques, developers are exploring ways to reduce the operating temperature of SOFCs to the 700–900°C range. Table 1.1 summarizes some of the relative issues of PEMFC- and SOFC-based systems.

The previous sections illustrate both the motivating factors and the timeliness of this research project. PEMFC and SOFC technologies are poised to enter into the stationary power market; however, several issues need to be addressed before successful commercialization of the technology. The lack of knowledge about the transient response of residential-scale fuel cell and fuel processing equipment coupled with the lack of established methods for optimal, cost effective design and operation of these systems, are issues that must be resolved to enable an accelerated market acceptance and concomitant realization of high system-level efficiencies.

Table 1.1 Comparison of PEMFC and SOFC Technologies [adapted from 19]

Issues	PEMFC	SOFC
Operating Temp	Cell: 80-100°C Reformer: 650-1000°C	700-1000°C
Load Following	dependent on reformer	dependent on reformer
CH ₄ Reforming	External	External or Internal
CO Management	Poison at > 10 ppm	Fuel / Water gas shift
Sulfur Management	< 5 ppm required	More tolerant (10-1000 ppm)
Water Management	Membrane sensitive to dehydration. Humidification of reactants required	No issue
Heat Quality	Low Grade (70-90°C)	High Quality (300 – 1000°C)
Cogeneration Capabilities	Moderate Water Heating (50-60°C)	Aids Reforming, Steam Gen., Water heating, & Space htg
System Electric Efficiency (LHV)	36-40%	45%

1.5 Objectives

Many cogeneration system concepts are conceivable with fuel cell systems, but the selection of one over another requires detailed study of long-term technical and economic performance. The primary objectives of the present study can be viewed as answering the following series of questions through the modeling and simulation of various SOFC energy systems:

- 1) What system design concepts may be employed and of the designs conceived, what are the optimal system configurations?
 - a. What is the optimal design operating point of the fuel cell for electric-only and cogeneration systems? That is, what should be the design operating cell voltage, fuel utilization, and temperature? What is the sensitivity of the optimum to each and what other aspects are influential to design point selection?
 - b. How well does the respective fuel cell system meet the total energy (thermal and electrical) demand of a building? What is the optimal system operating strategy (base-load or load-following)?

- 2) What are the respective environmental emissions of each system concept and what are the anticipated payback economics of mature SOFC-based residential systems?
- 3) What is the transient response of the SOFC cell-stack and how does the dynamic performance impact design and application of the technology?
- 4) In general, what advantages (if any) might the high temperature SOFC-based system possess for building cogeneration applications compared to conventional systems?
- 5) What are the guidelines for fuel cell system design and operation?

Beyond answering such questions as listed above, the broader goals of the research include:

- 1) Build appropriate component and system models to simulate the fuel cell and fuel cell system performance.
- 2) Gain insight into fundamental physics of fuel cell performance through cell-level modeling.
- 3) Validate the models.
- 4) Explore different strategies and plant design concepts for the optimal design and operation of solid oxide fuel cell systems.
- 5) Establish guidelines for the design and operation of solid oxide fuel cell systems.
- 6) Provide a SOFC cell-stack model that is available for public use.

1.6 Methodology

The research methodology for the present study was carried out in seven steps as listed below. In practice, some steps occurred in parallel rather than sequentially.

- 1) Development of computational models to simulate steady-state system operation.
- 2) Validation of the component models.
- 3) Dynamic fuel cell and system performance assessment.
- 4) Acquisition and/or generation of residential energy (thermal and electric) loads.
- 5) Formulation of objective functions for optimization.
- 6) Identification and evaluation, based on annual simulations, of system concepts. Evaluation will include annual operating efficiency, emissions, and costs.

- 7) Develop guidelines for selection and design of solid oxide fuel cell-based energy systems.

The goal of the modeling effort is to provide sufficiently realistic models that can meet the research objectives. To answer such questions, models were constructed that are capable of accurately predicting the fuel cell stack, reformer, and remaining balance-of-plant equipment performance. The fuel cell model demonstrates performance sensitivity to variations in cell voltage, operating temperature, reactant utilization, and reactant composition. The pre-reformer model shows sensitivity to changes in inlet fuel feedstock conditions and heat input. To meet the objectives, all components in the system have the ability to predict performance at part-load conditions. It is also apparent that different levels of modeling will be required to simulate system-level performance and to make assessments related to dynamic response. For example, the fuel cell stack model is capable of resolving spatial distributions of temperature, composition, and current (one-dimensional) while simulation of ancillary equipment employs relatively simple (zero-dimensional) steady-state thermodynamic models. Further discussion on the modeling effort is presented in Chapters Four through Six.

The optimization of system designs and fuel cell operating point selection will be carried out by examination of several different objective functions, such as minimum cost of ‘energy’, minimum CO₂ output, maximum thermal output, and maximum energetic efficiency. As fuel cell technology is still undergoing maturation, uncertainties in fuel cell capital cost and expected performance (e.g., efficiency and power density) exist. Fuel cost is also highly variable and may fluctuate by 100% over the course of a single year. Thus, the sensitivity to these parameters is examined when performing optimizations.

In order to maintain focus on the research objectives, the scope of the project was bounded by an analysis of limiting cases related to system size, extent of fuel processing, useful output, and operating strategy for grid-connected systems. Table 1.2 summarizes the case studies.

Table 1.2 Limiting Cases of Research

Focus	Range of Investigation
Scale	1 kW size ↔ 10 kW size
Fuel Processing	None (Hydrogen-fueled) ↔ Reforming (Natural gas)
Useful Output	Electric-only ↔ Cogeneration
Operating Strategy	Base-load ↔ Load-follow

1.7 Thesis Outline

In the following two chapters, a review of the previous work and an introduction to solid oxide fuel cell systems is given. Chapters 4 through 6 provide detailed information, on the cell-level modeling effort (Chap. 4), cell model validation (Chap. 5), and system balance-of-plant and cost models (Chap.6). These chapters provide in-depth presentations of the governing equations and modeling assumptions. Chapters 7 and 8 examine the effects of cell design and operating parameters on cell and system performance. Additionally, Chapter 8 discusses the merits of various conceptual SOFC system designs and offers design strategies for meeting the residential energy demands. Chapter 9 presents the optimization studies on SOFC operating point selection, annual simulation results for a particular residence, and design guidelines for SOFC system design and operation. Chapter 10 concludes the present study with a summary of findings and recommendations for further work.

1.8 Chapter References

- 1.1 Energy Information Administration, "Table 2.1 Energy Consumption by End-use Sector," Annual Energy Review (1996).
- 1.2 Energy Information Administration, "Residential and Commercial End-use Surveys," Annual Energy Review (1995).
- 1.3 M. Grubb, *Kyoto Protocol: A guide and assessment*, Energy and Environmental Programme, Royal Institute of International Affairs; Washington, DC: Distributed in North America by the Brookings Institution, (1999).
- 1.4 S. Oberthuer and H. Ott, *The Kyoto Protocol : international climate policy for the 21st century*, Springer, New York (1999).
- 1.5 R.H. Lassiter, "Control of Distributed Generation," *Bulk Power System Dynamics and Control IV: Restructuring Conference Proceedings*, Santorini, Greece, August (1998).
- 1.6 T.J. Overbye, "Reengineering the Electric Grid," *American Scientist*, **88**, May-June, pp. 220-229 (2000).
- 1.7 *Science*, October (1994).
- 1.8 R.Meyer, P. Bautista, M.Whelan, J.Hilyard, "Deregulation: What is the Role of Natural Gas?", *Proceedings: 2nd Annual Distributed Resources Conference*, Vancouver, British Columbia, EPRI TR-107585, November (1996).
- 1.9 C.D. Maloney, "Distributed Generation-Opportunity for the 21st Century," *60th American Power Conference Proceedings*, Chicago, IL (1998).
- 1.10 Electric Power Research Institute, Distrib. Generation webpage, www.EPRI.com, (1998).
- 1.11 S.R. Connors and W.W. Schenler, "Climate Change and Competition –On a Collision Course," *60th American Power Conference Proceedings*, Chicago, IL (1998).
- 1.12 M. Pehnt, "Source-to-Service-Analyses for Mobile and Stationary Fuel Cell Solutions," *4th European Solid Oxide Fuel Cell Forum Proceedings*, Lucerne, Switzerland, (2000).
- 1.13 O. Ulleberg, *Stand Alone Power Systems for the Future: Optimal design, operation, and control of solar-hydrogen energy systems*, Ph.D. Thesis, Ph.D. Thesis, Norwegian Institute of Technology (1998).
- 1.14 R.J. Braun, S.A. Klein, D.T. Reindl, "Review of State-of-the-Art Fuel Cell Technologies for Distributed Generation," Report 193-2 prepared for the Energy Center of Wisconsin, January (2000).
- 1.15 P. Schafer, "Commercial Sector Solid Oxide Fuel Cell Business Assessment," Electric Power Research Institute, TR-106645, August (1996).

-
- 1.16 A.J. Appleby, "Characteristics of Fuel Cell Systems," in *Fuel Cell Systems*, Leo J. Blomen and Michael N. Mugerwa, Editors, Plenum Press, New York (1993).
 - 1.17 S.Srinivisan, et al., "Overview of Fuel Cell Technology," in *Fuel Cell Systems*, Leo J. Blomen and Michael N. Mugerwa, Editors, Plenum Press, New York (1993).
 - 1.18 D. Rastler, D. Herman, R. Goldstein, and J.O'Sullivan, "State-of-the-Art Fuel Cell Technologies for Distributed Power," EPRI TR-106620, Palo Alto, CA (1996).
 - 1.19 K.Krist, K. Gleason, and J. Wright, "SOFC-based Residential Cogeneration Systems," *Proc. Of Sixth International Symposium on Solid Oxide Fuel Cells (SOFC-VI)*, Honolulu, HI, PV99-19, Electrochemical Society, (1999), pp. 107-115.

Chapter Two Literature Review

The design of solid oxide fuel cell (SOFC) power generation systems requires drawing on knowledge across a broad range of disciplines including reaction engineering, electrical engineering, electrochemistry, thermal sciences, material sciences, process dynamics, and plant economics. The relative infancy of the technology means conformity in cell-stack and process design has not yet been achieved. Thus, the designer must cover more ‘ground’ to conceive and evaluate the variety of plant design options aimed at meeting the requirements of an application. More specifically, an intimate knowledge of fuel cell stack design and gas processing options both in the stack periphery and in the downstream recuperative heat exchangers is necessary. The successful design of fuel cell systems also requires proper selection of cell-stack operating conditions, such as design cell voltage, fuel utilization^{*}, and operating temperature. Depending on the size and the transient response, the design of a SOFC power system may include sizing and integration of battery, thermal, or chemical storage devices and exploration of alternative plant concepts, such as the integration of heat pumps. Finally, for many applications, the SOFC distributed power generator is likely to experience significant load-steps and modulation through several operating modes during its lifetime. Thus, besides making an assessment of storage needs, knowledge of the dynamic response capability of SOFCs will be important for establishing design and process control strategies for load-following conditions. Consequently, an understanding of reactant gas processing, operating point selection, operating envelopes, energy storage methods, and cell-stack dynamic response characteristics are prerequisites for optimizing stationary fuel cell system designs for residential-scale power applications.

^{*} fuel utilization is defined as the number moles of hydrogen consumed over the moles of hydrogen supplied.

The following summary of technical literature is divided into four sections: design and operation of solid oxide fuel cell systems, residential applications, modeling of SOFCs, and process dynamics. The section concludes with a summary of gaps in the technical literature on design and operation of SOFC systems.

2.1 Design and Operation Aspects of Residential-scale Systems

The amount of system design research at the 1-10 kW scale is insignificant compared to the effort expended at 200 kW-scales. It is noteworthy that plant design options at the commercial scale (200 kW) may not be applicable at residential scales (~2 kW) due to the unavailability or performance limitations of hardware and specific application requirements. Despite these limitations, process designs at both scales necessitate similar design steps and evaluation of various plant concepts. This section will detail previous work in process design, operating point selection, and off-design simulation at these scales.

2.1.1 Process Design

The design of solid oxide fuel cell systems has been the subject of numerous papers. Many of these studies [1,2,3,4,5] have focused on methods for integrating gas turbines into large (>1 MW) solid oxide fuel cell power plants and are of limited use for the present effort. The concepts developed at large scales may theoretically be applied at smaller scales, however, in practice economics of doing so may be prohibitive. Studies by Achenbach et al., [6], Riensche et al., [7], Mozaffarian [8], and Taylor and Beishon [9] have focused on the exploration of process design concepts and operating parameters for combined heat and power solid oxide fuel cell plants at 200 kW scales. (In these studies, cogeneration is preferred over electric power augmentation via gas or steam turbine arrangements.) While these 200 kW-scale studies examine several gas processing designs, such as internal reforming or anode and cathode gas recycling, they do not offer clear conclusions about the relative merits of all the concepts nor do they address methods for optimal design to meet the needs of the end-use application. Additionally, the results of the previously mentioned studies

are based on ca. 1995 state-of-the-art SOFC power density performance ($\sim 0.2 \text{ W/cm}^2$) –which will not be commercialized.

At residential scales (1-10 kW), process design concepts have only been addressed in vague manufacturer status reports [10, 11, 12] or by statements on the scalability of larger system designs. The means for integration and optimization of energy storage (battery, thermal, or chemical) into residential systems has to date been unexplored. Thus, a synthesis of the relative merits of gas processing options, particularly in the context of evaluating the various process design schemes for residential applications, is needed. Additionally, a methodology or guideline for the design of fuel cell systems in the 1-10 kW scales is not available.

2.1.2 Operating Point Selection

The selection of the design operating conditions of the fuel cell stack is interwoven with gas process design. For a given design, the cell-stack operating point is determined by cell voltage, temperature, pressure, and fuel utilization. The choice of these performance parameters may maximize either electric power or electric efficiency. In addition to these parameters, the economy of the entire fuel cell *system* is influenced by cell-stack temperature rise, capital and fuel costs, and economic parameters, such as interest rates, plant life, depreciation, etc. Using simulations, Chen et al., [13], Riensche et al., [14], Braun et al., [15], and Khandkar, et al [16] have evaluated the selection of optimal cell-stack operating parameters via minimization of the plant cost-of-electricity for several different plant concepts ranging from 200-500 kW in size. Chen et al., [13] performed a parametric analysis on the economic tradeoffs in selecting optimal operating current density, fuel utilization, temperature, and pressure for a 500 kW SOFC system. The system was a direct internal reforming planar SOFC design. However, only limited specific design information and logical reasoning behind selection of optimal parameters (particularly that of optimal fuel utilization) were presented. Riensche et al., [14] examined the effect of fuel utilization, cell voltage, and excess air on the fuel cell cost of electricity for a 200 kW planar SOFC cogenerator, but the system was for a non-optimized design employing a partially direct internal reforming SOFC stack with steam for steam reforming raised by an external boiler.

Khandkar, et al. [16] have recently detailed system cost minimization methods for varying stack control parameters, but primarily as means for establishing a fuel cell performance map of their pre-commercial product.

While the method of cost-of-electricity minimization is well documented as an optimization tool, large uncertainties exist in both the final design and cost of fuel cell-based systems. Thus, there is a need for studies to elucidate the sensitivity of the cost-of-electricity (and cost-of-heat) to variations in technical and economic parameters when selecting both *design* and *operating* parameters of the fuel cell. In cogeneration systems, consideration of the plant thermal output is typically subordinated to electricity-based optimization. Evaluation of the cost of heat and its effect on design operating point may be of consequence for commercial applications in particular [17]. The effect of scale on the selection of optimal operating point is also of importance as no operating point studies for residential-sized systems have been found in the open literature. Finally, study of the impact of environmental measures on operating point selection would also be of use in the event of the implementation of incentives for high efficiency operation, such as the carbon tax.

2.1.3 *Off-design point simulation*

Most conventional engine-driven systems for primary power production are operated with base-load strategies. In residential systems, the end-use requirements are more likely to necessitate part-load operation of the cell-stack. Knowledge of steady-state air-fuel ratios, cell-stack heat flows, fuel reformer conversion, and both waste heat quantity and quality throughout the cell-stack operating regime are required for simulation of off-design operating point conditions. “Off-design” studies in the technical literature [e.g., 18, 19] typically denote the performance estimation when fuel cells have experienced material degradation, increased polarization, or other loss in cell-stack integrity rather than the variation of thermal performance of a fuel cell system operating as ‘designed,’ but at part-load. With the exception of transient analyses, numerical or experimental studies of fuel cell performance at part-load have been limited to the establishment of single cell and stack voltage-current curves. Neither system-level nor stack and reformer sub-system studies at part-load have

been found in the open literature. This information is essential to the optimal design and evaluation of systems in residential-scale applications.

2.2 Residential Application Studies of Fuel Cell Systems

2.2.1 Solid Oxide Fuel Cell Studies

Bos [20] examined system requirements and some design considerations for residential fuel cell-based systems. Bos stated that the fuel cell size ‘optimized’ at 2 kW. The analysis, primarily concerned with marketing and commercialization strategies, was not explicit in the fuel cell technology under study, and did not present the logical basis for system component sizing, operating strategies, or cogeneration efficiency and emission performance. Krist et al., [21] presented a discussion on design considerations and the potential effectiveness of SOFCs in residential applications. The authors in this work seemed to advocate a fuel cell in the 1 kW size range based on thermal-to-electric ratios of residential loads. Operating and design questions were presented therein but not answered. Additionally, the authors offered qualitative advantages of SOFCs over PEMFCs for residential cogeneration but did not perform any system studies or simulations to quantify these advantages. Sammes and Boersma [22] present a discussion of small-scale fuel cells for residential applications but do not offer optimal designs or make performance comparisons between SOFCs and PEMFCs. Their work centered on an investigation of the market and technical requirements of small-scale fuel cells in residential applications and a survey of the various PEMFC and SOFC manufacturers. Finally, there are no studies in the open literature that present any design, system integration, or long-term performance of fuel cell systems that include energy storage.

2.3 SOFC Modeling

Fuel cell hardware is presently in pre-commercial development resulting in the unavailability of performance maps for system design and simulation purposes. Consequently, prediction of fuel cell performance is highly dependent on models. The level of modeling sophistication required for both high-level system studies, as well as component dynamic and steady-state simulation is not well established.

2.3.1 Steady-state SOFC Modeling

There have been numerous steady-state models of single solid oxide fuel cell stacks [e.g., 23, 24, 25, 26, 27, 28, 29, 30, 31, 32].

Table 2.1 summarizes the chronological progression of planar SOFC modeling in terms of model developer, type of model, approach, and limitations. Early mathematical modeling of tubular SOFCs was performed by Dunbar [33] and Wepfer et al., [24]. Debenetti and Vayenas [23] were the first to model flat planar SOFCs. These authors developed a 2-D modeling approach still in use today, which approximates the cell stack as set of unit cells operating as continuously stirred tank reactors (CSTRs) as shown in Figure 2.1. The CSTR approximation assumes that the solid and gaseous phase temperature and compositions are uniform in the unit cell. This approach enables the representation of a unit cell in terms of only three mesh points (one for air and fuel gas phases, and one for the solid phase) in the calculation of the temperature distribution [34]. However, conduction heat transfer is not accounted for, the cell is considered to be adiabatic, and the model is limited to hydrogen-only fuel gases. Conduction heat transfer will alter the temperature distribution in the solid cell, especially for the thicker anode-supported SOFC designs. The adiabatic assumption is appropriate for a cell placed deep inside a stack and not exposed to surroundings, but the cell ends would still be subject to heat loss.

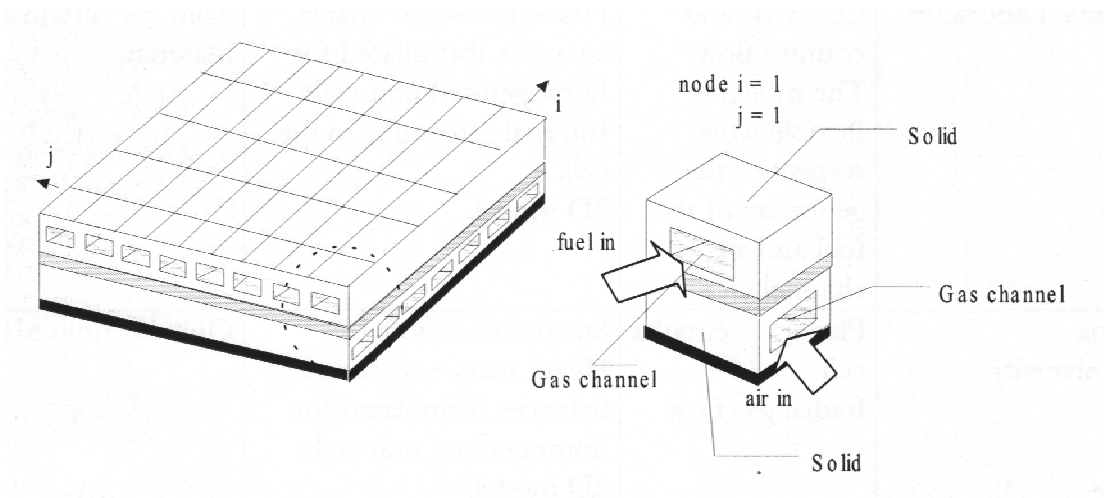


Figure 2.1 Schematic of cross-flow geometry and a unit cell for the planar SOFC [34]

Table 2.1 Summary of SOFC modeling efforts [35]

Model developer	Design type	Approach in modelling	Limitations of the models
Debendetti and Vayenas Massachusetts Institute of Technology (1983)	Monolithic co, cross and counter flow	Steady state model. Heat-, mass-and charge balances solved for unit cells of CSTR type. 2D model.	Neglected conductive heat transfer in solid parts of the cell. Adiabatic cell. Neglected activation and diffusion terms. Only H ₂ utilised as a fuel.
Ahmed , McPheters and Kumar Argone National Laboratory (1991)	Monolithic cross flow	Steady state model. Heat-, mass-and charge balances formulated for homogenised unit-cells. 2D model.	Neglected conductive heat transfer in solid parts of the cell. Adiabatic cell. Neglected activation and diffusion terms. Only H ₂ utilised as a fuel.
Karoliussen Norway Institute of Technology (1993)	Planar Co, cross and counter flow The model is flexible with respect to the geometry of the fuel and air channels.	Steady state model. Heat-, mass-and charge balances formulated for homogenised unit-cells. Internal reforming in the cell. 3D model.	Reforming kinetics is only valid for certain anode material. Diffusion losses are neglected.
Achenbach Research centre Jülich (1994)	Planar Co, cross and counter flow The model is flexible with respect to the geometry of the fuel and air channels.	Time dependent model. Heat-, mass-and charge balances formulated for homogenised unit-cells. Internal reforming in the cell. 3D model.	Reforming kinetics is only valid for certain anode material. Kinetics of hydrogen oxidation is only valid for certain anode material.
Hendriksen Risø National Laboratory (1996)	Planar Co, cross and counter flow The model is flexible with respect to the geometry of the fuel and air channels.	Steady state model Heat-, mass-and charge balances formulated for homogenised unit-cells. Internal reforming in the cell. 3D model.	Reforming kinetics is only valid for certain anode material.
Costamagna Genova University (1998)	Planar circular cell Radial gas flow	Steady state model. Heat-, mass-and charge balances formulated for homogenised unit-cells. 2D model.	Only H ₂ utilised as a fuel.

Ahmed, et al., [26] developed a 2-D model of a monolithic cell following a similar approach as the unit cell approximation described previously. The model again assumes the cell is placed deep within a stack and makes steady-state heat and mass balances on the unit cells. The limitations of the model are (i) convection is the only mode of heat transfer accounted for (conduction and radiation are neglected), (ii) pure hydrogen is used as the fuel, and (iii) only ohmic cell polarization is considered.

Hartvigsen et al., [27] developed a 3D finite element model incorporating conduction, convection, and radiation heat transfer mechanisms in a single cell channel. Cell polarizations were also rigorously calculated. The model illustrated the importance of radiation heat transfer (cross-channel and at boundaries) on the calculated cell temperature profiles.

Karoliussen [28] advanced the previous steady-state models by developing a 3-D model that accounted for internal reforming and incorporating a more complete description of all heat and mass transfer processes including interaction of the stack with its surroundings. Additionally, the work included a different method of treating activation polarization losses [34]. Reforming of methane is a kinetically controlled process and its inclusion in the model was accomplished using experimental data from the anode material. However, diffusion losses were neglected in the model and the internal reforming kinetics are only valid for the specified anode material.

The remaining models listed in Table 2.1 followed an approach similar to that of Karoliussen's, but with some modifications. Achenbach [29] added the time varying component to the 3-D spatial cell model and accounted for the effects of gas processing in the stack periphery by including anode gas recycling concepts. Hendriksen [31] eliminated the diffusion losses of Karoliussen's model and Costamagna and Honegger [32] developed a model to account for radial planar SOFC geometry.

Each of the models discussed above are believed to be constructed using Fortran code. The availability of all of these models is not definitively known by the author, but attempts to obtain the software program of more recently published models has been unsuccessful. At the

time of this thesis publication, a model called GCtool by Argonne National Laboratory is now available for a licensing fee. From the previous SOFC cell-level modeling efforts, it can be deduced that a cell-stack performance model employed for the purposes of system design and simulation must include the following considerations:

- Combined modes of heat transfer (conduction, convection, and radiation)
- Internal reforming of methane
- Cell polarizations are difficult to predict, but all three loss mechanisms should be included for anode-supported SOFC modeling. Furthermore, the inability to predict the losses can be countered by using sensitivity parameters to calibrate results to available experimental data.

2.3.2 *Dynamic SOFC Modeling*

The work of Achenbach [29, 36] examined the transient cell voltage performance of an electrode-supported, direct internal reforming planar SOFC operating at 1000°C to steps in current density using a three-dimensional, time dependent model. However, the validation of this model with experimental data has not been found in the open literature. Nevertheless, Achenbach [36] established that the cell-stack relaxation time due to perturbations in current density was most dependent on the cell temperature distribution and ranged from 120 to 220 seconds depending on the nature of the step change. The temperature distribution in the stack, in turn, is heavily dependent on the solid material properties (e.g., thermal conductivity, heat capacity, density). Dependencies on cell mass, operating conditions, and flow configuration were also shown to exist and the relaxation time of the cell-stack was shown to be independent of the magnitude of the load step. However, this study did not examine anode-supported SOFC designs with high power densities, external reforming, lower temperature fuel cell operation, or the effect of perturbations in reactant mass flow, temperature and composition on the cell voltage relaxation time. In any case, the level of detail of his model is considered beyond the scope or need of the present work.

Other modeling efforts reveal some discrepancies between the appropriateness of zero-, one-, and two-dimensional modeling. Models by Gemmen et al., [37], and Liese et al., [38] have demonstrated some success with a one-dimensional methodology and they argue that seven spatial nodes or more are necessary to resolve the non-linear temperature and current distribution effects within the cell. On the other hand, Lukas et al., [39] and Domergue et al., [40] have likewise proceeded to model dynamic fuel cell performance using zero-dimensional, single node lumped models. It is difficult to compare the relative performance of the four modeling studies above because cell designs and operating conditions are different and in all cases, the computational models have not been experimentally validated. Comte et al., [41] emphasized that zero-dimensional models cannot accurately simulate dynamic fuel cell performance, particularly those employing internal steam reforming. In fact, the authors claim that errors of 20% (relative to more complex models) are possible in predicting the fuel cell thermal and power outputs using zero-dimensional models for cross-flow configurations. Further perusal of the literature on fuel cell transient response reveals a relatively undeveloped research area that is only recently receiving attention.

2.4 Transient Response of SOFC Systems

Prediction of the transient performance of the fuel cell is important for (i) control purposes, (ii) establishing that the operating conditions inside the cell, such as solid temperature gradients, during the transient have not endangered cell integrity (or life), and (iii) determining battery storage requirements. The SOFC stack represents only a portion of the total system required for generating power. The complete system consists of fuel processors, compressors and blowers, heat exchangers, and power conditioning equipment. The dynamic response of the entire power generating system is therefore, to some extent, dependent on each of these individual components and the dynamic interactions among them. On the other hand, it is recognized that the transient capability of the fuel processor and fuel cell contain the largest uncertainties and are generally considered to be the slowest responding units of the system. For this reason, and because of the complexity in simulating the transient response of the entire power system, nearly all studies to date have focused on establishing the dynamic response of the fuel cell stack and reformer.

2.4.1 Dynamics of Systems and BOP Components

The only system-level dynamic study (known to the author) has been performed in the parallel field of molten carbonate fuel cell power systems. A numerical simulation by He [42] on an externally reforming molten carbonate fuel cell power system incorporating nine types of component models was carried out through the use of a combination of commercial software packages and custom program code. He developed the system model on a modularity approach, whereby component models were individually constructed and integrated into the larger system. It is believed that the detailed fuel cell model was experimentally validated, but not the overall system. While the conclusions of this analysis are not directly applicable to SOFC-based systems, the He modeling methodology could be employed.

Liese et al., [43] and Gemmen et al., [44] have examined the dynamic response for planar solid oxide fuel cells. These papers, however, have focused on technical development and modeling issues associated with SOFC-gas turbine systems and have presented only preliminary analyses.

The production of hydrogen from natural gas in SOFC-based systems will normally be accomplished through steam reforming of methane internal to the cell-stack. The high operating temperature of the SOFC coupled with the catalytic activity of the nickel-based anode enables *direct* internal reforming to take place at the fuel electrode without the need for external reforming equipment. In a cross-flow reactant gas manifold system (the most common), the direct internal reforming arrangement can generate unacceptably large thermal stresses via excessive cooling of the solid cell at the anode inlet. As a result of this limitation, the present SOFC technology cannot accomplish 100% direct internal reforming at the fuel electrode. However, anode-supported cell technology is expected to overcome this issue as the thicker electrode significantly reduces the in-plane temperature gradients, thereby lowering thermal stresses in the ceramic components [45]. In the near-term, approximately 50% of the methane must then be converted external to the cell-stack in a pre-reformer [29]. The pre-reformer serves two purposes: (i) to reduce the higher hydrocarbons into methane and

hydrogen, and (ii) generate enough hydrogen supply at the anode inlet so that electrical energy can be generated at the leading edge of the cell. In some cases the pre-reformer serves the additional purpose of acting as a recuperative, counter-flow heat exchanger that will raise the fuel feedstock to the prescribed cell inlet temperature. Thus, simulation of fuel processing will require development of internal reforming fuel cell stack model for advanced (ca. 2010) plant concepts and a pre-reformer model for nearer term plant designs.

The dynamic response of an external, fuel-fired steam reformer was simulated by He [46] using a lumped capacitance, two-node model. Using this model, He showed that the transition to steady-state (relaxation time) reformer temperature, process gas concentration, or flow after a perturbation of 10% in inlet gas flow and temperature, or outlet gas pressure takes on the order of 10^3 seconds with no significant overshoot. He also determined that perturbations in feed gas flow generate the largest responses and the response itself was most dependent on heat transfer phenomena. While the qualitative results are interesting, their application to the present research is questionable as external fuel-fired steam reformers are not envisioned for SOFC systems.

Liese and Gemmen [47] investigated the transient response of a steam-methane pre-reformer without external heat addition through modeling and simulation. The model presented transient results for start-up and 50% load steps that indicated transients on the order of 10^3 seconds. The paper focused on design issues, such as reactor diameter, catalyst type, and gas residence time as pre-reforming technology is still in development. No experiments were made or data collected to validate the modeling effort.

In general, nearly all SOFC systems research in the open literature is model-based, consisting of only fuel cell stack and reformer component models (no system-level simulation), both of which have yet to be experimentally validated. Additionally, due to the number of different SOFC designs (tubular, radial planar, flat planar {electrode-supported and anode-supported}) being developed, the results of one study may be limited or not applicable to all SOFC systems in use.

2.5 Summary of Research Gaps in Previous Systems-level Work

Table 2.2 summarizes the previous work in the systems-related research field according to subject focus (i.e., system process design and operation, application studies, comparative performance between SOFCs and PEMFCs, and process dynamics and control) and the size of the ‘system’ under study. All previous work representing significant contributions to the subject area (in the view of this author) are denoted in boldface. A cursory glance at the table provides an indication of where the gaps in systems-level research areas are with respect to size and therefore, application.

The need for research into residential-scale SOFC systems is clearly illustrated by Table 2.2. Process design work is limited as fuel cell manufacturers/developers have been reluctant to disclose details that would facilitate detailed assessments. Previous studies have not adequately addressed designs that would incorporate energy storage concepts (electric, thermal, fuel). Also, previous studies have not considered innovative use of space conditioning technologies such as heat pumps which would tend to close the sizable mismatch in thermal-to-electric ratios for stationary applications. Importantly, while considerable previous work in process design has been accomplished at the 200 kW scale, there has been no synthesis of the advantages and disadvantages of the various process alternatives nor has there been consideration for the utility of these schemes at smaller power scales. Operating point analyses for design of the cell-stack and subsequent balance-of-plant have only been performed at 200 kW scales. The methodology of the 200 kW studies could easily be employed for the smaller residential systems. However, due to the large uncertainties with both the performance and economics of fuel cell systems, studies of sensitivity to operating and economic parameters would be of use for both design purposes and for optimal operating point selection of an *existing* fuel cell system in which, for instance, the price of fuel has fluctuated. Lastly, to perform studies that evaluate ecological impact (e.g., CO₂ output), payback economics, and long-term fuel efficiency performance, part-load simulation is required. Thus, the advantage of part-load simulation capability (given a properly validated model) is that it enables a realistic examination of the potential benefits of various system

designs over one another and could yield a measure of the effectiveness of fuel cell systems over conventional equipment performance.

Table 2.2 Summary of Previous Work in Systems-related Research

Aspect of Research	1-10 kW Scale	200 kW Scale
Process design	Elangovan et al., (1995) Bolden et al., (1999) Pastula, et al., (2000)	Achenbach et al., (1994) Mozaffarian (1994) Taylor and Beishon (1994) Riensch et al., (1998)
Operating point analysis	None	Chen et al., (1997) Riensch et al., (1998) Braun et al., (2000) Khandkar et al., (2000)
Off-design point simulation	None	None
Residential application	Bos, (1994) A.D. Little (1995) Krist et al., (1999) Sammes and Boersma (2000)	—
Comparative assessment between SOFCs and PEMs	Reichwaldt, (1998) Kato et al., (1999)	None
System-level dynamics	None	He (1998)*
Fuel cell dynamic response	None	Achenbach (1995) Liese et al., (1999) Gemmen, et al., (2000)
Reformer dynamic response	None	He (1996)* Liese and Gemmen, (TBD)

* Papers by He are in the parallel field of molten carbonate fuel cell systems.

Application case studies have not been performed at any detailed level, in part due to the lack of *real* systems operating in the field from which to gather data and assess performance. However, methods of system integration with existing residential systems and consideration of alternative plant concepts for maximum total energy utilization (and hence, efficiency) are in need.

The field of system dynamics and control is also in need of contribution. At present, nearly all studies in SOFC systems have been numerical simulations without significant experimental validation or development of control techniques. Also, many questions regarding cell-stack and reformer dynamics remain unanswered. Finally, while some transient response work has been performed at the 200 kW scale, most of the present ongoing efforts are aimed at larger gas turbine integrated plants and not small-scale (1-10kW) combined heat and power generators.

2.6 Chapter References

- 2.1 W.R. Dunbar, N. Lior, R.A. Gaggioli, "Combining fuel cells with fuel-fired power plants for improved exergy efficiency," *Energy—The International Journal*, **16**, No. 10, (1991), pp. 1259-1274.
- 2.2 S.P. Harvey and H.J. Richter, "Improved gas turbine power plant efficiency by use of recycled exhaust gases and fuel cell technology," *Proceedings of Thermodynamics and the Design, Analysis, and Improvement of Energy Systems*, AES-Vol. 30, ASME Winter Annual Meeting, (1993), pp. 199-207.
- 2.3 W. Winkler, "SOFC-Integrated Power Plants for Natural Gas," *Proc. Of the 1st European Solid Oxide Fuel Cell Forum*, October 3-7, Lucerne, Switzerland, (1994), pp. 821-848.
- 2.4 J.Hirschenhofer, et al., *Fuel Cells –A Handbook*, 4th Ed., prepared for the U.S. Department of Energy, DOE/FETC-99/1076, November, (1998).
- 2.5 C.Haynes, "Simulation of Tubular Solid Oxide Fuel Cell Behavior for Integration Into Gas Turbine Cycles," Ph.D. Thesis, Georgia Institute of Technology, 1999.
- 2.6 E. Achenbach, E. Riensche, G. Unversagt, "Gas Processing of SOFC Plants," *Proc. Of the 1st European Solid Oxide Fuel Cell Forum*, Lucerne, Switzerland, (1994), pp. 153-162.
- 2.7 E. Riensche, J. Meusinger, U. Stimming, G. Unversagt, "Optimization of 200 kW SOFC cogeneration power plant, Part II: variation of the flowsheet," *J. Power Sources*, **71** (1998), pp.306-314.
- 2.8 M. Mozaffarian, "Solid Oxide Fuel Cells for Combined Heat and Power", *Proc. Of the 1st European Solid Oxide Fuel Cell Forum*, Lucerne, Switzerland, (1994), pp. 353-362.

-
- 2.9 M.R. Taylor and D.S. Beishon, "A study for a 200 kWe System for Power and Heat," *Proc. Of the 1st European Solid Oxide Fuel Cell Forum*, Lucerne, Switzerland, (1994), pp. 849-873.
 - 2.10 S. Elangovan, J. Hartvigsen, A. Khandkar, "Progress in the Planar CPⁿ SOFC System Design," *Proc. Of Fourth International Symposium on Solid Oxide Fuel Cells (SOFC-IV)*, PV95, The Electrochemical Society, Pennington, NJ, (1995), pp. 146-152.
 - 2.11 R. Bolden, K. Foeger, T. Pham, "Towards the development of a 25 kW planar SOFC system," *Proc. Of Sixth International Symposium on Solid Oxide Fuel Cells (SOFC-VI)*, Honolulu, HI, PV99-19, The Electrochemical Society, Pennington, NJ, (1999), pp. 80-87.
 - 2.12 M. Pastula, et al., "Development of Low Temperature SOFC Systems for Remote Power Applications," *Proc. Of the 4th European Solid Oxide Fuel Cell Forum*, Lucerne, Switzerland, (2000), pp. 123-132.
 - 2.13 T. Chen, J.D Wright, K. Krist, "SOFC Systems Analysis," *Proc. Of Fifth International Symposium on Solid Oxide Fuel Cells (SOFC-V)*, PV97-18, Germany, (1997).
 - 2.14 E. Riensche, U. Stimming, G. Unversagt, "Optimization of 200 kW SOFC cogeneration power plant, Part I: Variation of process parameters," *J. Power Sources*, **73** (1998), pp.251-256.
 - 2.15 R.J. Braun, S.A. Klein, D.T. Reindl, "Operating point analyses for solid oxide fuel cell systems," *Proc. Of the 4th European Solid Oxide Fuel Cell Forum*, Lucerne, Switzerland, (2000), pp. 459-468.
 - 2.16 A. Khandkar, J. Hartvigsen, S. Elangovan, "A Techno-Economic Model for SOFC Power Systems," to be published in *Solid State Ionics*.
 - 2.17 M. Mugerwa and L. Blomen, "Fuel Cell System Economics," in *Fuel Cell Systems*, Plenum Press, New York, (1993), pp.551-558.
 - 2.18 N. Bessette and W. Wepfer, *Energy Convers. Mgmt.*, **37**, no. 3, (1996) pp. 281-293.
 - 2.19 A. Selimovic, "On-design and Off-design Performance Prediction of a Planar SOFC," *Proc. Of the 4th European Solid Oxide Fuel Cell Forum*, Lucerne, Switzerland, (2000), pp. 375-382.
 - 2.20 P.B. Bos "Commercializing fuel cells: managing risks," *J. Power Sources*, **61**, (1996) pp. 21-31.
 - 2.21 K. Krist, K. Gleason, and J. Wright, "SOFC-based Residential Cogeneration Systems," *Proc. Of Sixth International Symposium on Solid Oxide Fuel Cells (SOFC-VI)*, Honolulu, HI, PV99-19, Electrochemical Society, (1999), pp. 107-115.
 - 2.22 N.M. Sammes, and R. Boersma, "Small-scale fuel cells for residential applications," *J. Power Sources*, **86** (1-2) (2000). pp. 98-110.

-
- 2.23 P.G. Debendetti, C.G. Vayenas, "Steady-state analysis of high temperature fuel cells," *Chemical Engineering Science*, **38**, No.11, (1983) pp.1817-1829.
- 2.24 W. J. Wepfer, M. H. Woolsey, "High Temperature Fuel Cells for Power Generation," *Energy Convers. Mgmt.*, **25**, No. 4, (1985) pp. 477-486.
- 2.25 W.R. Dunbar and R.A. Gaggioli, *J. Energy Res. Tech.*, **112**, June (1990).
- 2.26 S. Ahmed, C. McPheeters, R. Kumar, "Thermal-hydraulic model of monolithic solid oxide fuel cell," *J. Electrochem. Soc.*, **138**, No. 9, September (1991).
- 2.27 J. Hartvigsen, S. Elangovan, A. Khandkar, "Modeling, design, and performance of solid oxide fuel cells," *Proc. Of Zirconia V* (1992).
- 2.28 H. Karoliussen, "Matematisk modellering av fastoxid braenslecelle," *Ph.D. thesis*, Department of Technical Electrochemistry, Norway Institute of Technology, Trondheim (1993).
- 2.29 E. Achenbach, "Three-dimensional and time dependent simulation of a planar solid oxide fuel cell stack," *J. Power Sources*, **49** (1994), pp. 333-348.
- 2.30 N.F. Bessette, W.J. Wepfer, J. Winnick, *J. Electrochem. Soc.*, **142**, No.11, (1995).
- 2.31 P. Hendriksen, *SOFC Modelling 2: Unit cell*, Materials Department, Riso National Laboratory, Denmark (1996).
- 2.32 P. Costamagna, K. Honnegger, "Modeling of solid oxide heat exchanger integrated stacks and simulation at high fuel utilization," *J. Electrochem. Soc.*, **145**, No. 11, (1998) pp. 3995-4007.
- 2.33 W. R. Dunbar, "Computer simulation of solid electrolyte fuel cells," M.S. Thesis, Marquette University, (1983).
- 2.34 A. Selimovic, "Solid oxide fuel cell modeling for SOFC/Gas turbine combined cycle simulations," *Licentiatrapport*, Lund Institute for heat and power, Sweden, April (2000).
- 2.35 J.R. Selman, "Fuel cell modeling: Overview and status," *Proc. Of the NETL Workshop on Fuel Cell Modeling: Speeding the Porgress of Fuel Cell Development*, DOE/NETL-2000/1128, Morgantown, WV, April (2000).
- 2.36 E. Achenbach, "Response of a solid oxide fuel cell to load change," *J. Power Sources*, **57** (1995), pp. 105-109.
- 2.37 R. Gemmen, et al., "Development of Dynamic Modeling Tools for Solid Oxide and Molten Carbonate Hybrid Fuel Cell Gas Turbine Systems," *Proc. Of the International Gas Turbine Institute Meeting*, May 8-12, ASME, (2000).
- 2.38 E.A. Liese, et al., "Technical development issues and dynamic modeling of gas turbine and fuel cell hybrid systems," *Proc. Of the Internat. Gas Turbine Inst. Mtg*, (1999).

-
- 2.39 M.D. Lukas, K.Y. Lee, H. Ghezal-Ayagh, *IEEE Trans. on Energy Convers.*, **14**, No.4 December (1999).
- 2.40 J. Domergue, A.Rufer, N.Buchheit, "Dynamic model of a solid oxide fuel cell stack and power converter," *Proc. Of the 3rd European SOFC Forum*, June 2-5, Nantes, France (1998).
- 2.41 A. Comte, Ph. Mathevon, Ph. Stevens, "Simulation of a solid oxide fuel cell using a dynamic system model," *Proc. Of the 3rd European SOFC Forum*, June 2-5, Nantes, France (1998).
- 2.42 W. He, "Dynamic model for molten carbonate fuel cell power-generation systems," *Energy Convers. Mgmt.*, **39**, No.8 (1998), pp. 775-783.
- 2.43 E.A. Liese, et al., "Technical development issues and dynamic modeling of gas turbine and fuel cell hybrid systems," *Proc. Of the International Gas Turbine Institute Meeting*, ASME, (1999).
- 2.44 R.S. Gemmen et al., "Development of dynamic modeling tools for solid oxide and molten carbonate hybrid fuel cell gas turbine systems," *Proc. Of the International Gas Turbine Institute Meeting*, ASME, May 8-12, (2000).
- 2.45 D.Stolten, D. Froning, L.G. de Haart, "Modeling of Planar Anode-Supported Thin-layer SOFC Stacks," *Proc. Of the 4th European SOFC Forum*, Lucerne, Switzerland, (2000), pp. 347-354.
- 2.46 W. He, "Dynamic performance of a reformer for a molten carbonate fuel cell power-generation system," *Fuel Processing Tech.*, **53**, (1997), pp. 99-113.
- 2.47 E.A. Liese and R.S. Gemmen, "Transient Modeling Results of a Methane-Steam Prereformer," *Proc. Of the ASME Advanced Energy Systems Division*, AES-Vol. 40, International Mechanical Engineering Congress & Exposition, Orlando, FL, (2000).

Chapter Three Introduction to SOFC Systems

Chapter One gave a brief overview of fuel cell technology introducing the basic features of fuel cell systems: fuel processing, power generation in the fuel cell stack, and power conditioning. Each of these sub-systems is now discussed in greater detail emphasizing solid oxide fuel cell (SOFC) systems with the intent of providing background for the system design, modeling, and simulation efforts of subsequent chapters. In this chapter, a description of two simple SOFC systems is presented first, followed by more detailed overviews of each of the fuel cell system building blocks. Next, advanced SOFC system concepts are discussed. Finally, an overview of the modeling and simulation effort is given as segue to the detailed cell finite-difference modeling of a planar solid oxide fuel cell presented in Chapter Four.

3.1 Simple SOFC System Descriptions

Figure 3.1 depicts a conceptual hydrogen-fueled SOFC system with heat recovery. Low pressure hydrogen fuel enters the plant and is compressed to the system pressure requirements and preheated to a temperature approximately 50°C below the nominal cell-stack operating temperature of 800°C . (Depending on the method of hydrogen generation and storage, the system may not need to use a fuel-side compressor.) After fuel preheat, hydrogen is delivered to the fuel cell stack module where the fuel is distributed through a manifold to anode compartments of the individual cells. Air is filtered, pressurized and preheated to a temperature approximately 50°C below the nominal cell-stack temperature before admittance into the fuel cell stack module. In a similar fashion as the fuel delivery method, air is directed into the cathode compartments of the individual cells of the stack through the use of a manifold. The solid oxide fuel cell typically operates at temperatures near 800°C or higher. At these high temperatures, fast electrochemical reaction kinetics are achieved. After electrochemical oxidation of hydrogen and reduction of oxygen, the direct current (DC) power produced in the process is inverted to alternating current (AC) in the inverter, a portion of which is used to serve the parasitic loads for the fuel compressor and air blower (W_c and W_B , respectively). Due to the intrinsic nature of fuel cell operation, not all the hydrogen

to enter the plant and after pressurization, is stripped of its sulfur content, mixed with superheated steam, and delivered to the steam-methane reformer where the endothermic reactions are driven by the fuel cell stack exhaust gases to produce a hydrogen-rich fuel mixture suitable for the fuel cell anode. In both hydrogen- and natural gas-fueled systems, the solid oxide fuel cell temperature is maintained by air-cooling through excess air.

The addition of the fuel processing hardware adds complexity, capital cost, maintenance, and inefficiency to the system. In addition to catalytic steam reforming of methane, other fuel reforming processes are possible for SOFC power systems, including autothermal reforming and partial oxidation. The importance of the fuel reforming processes for fuel cell system design, operation, and optimization cannot be understated and for this reason they are explored in more detail in the following section.

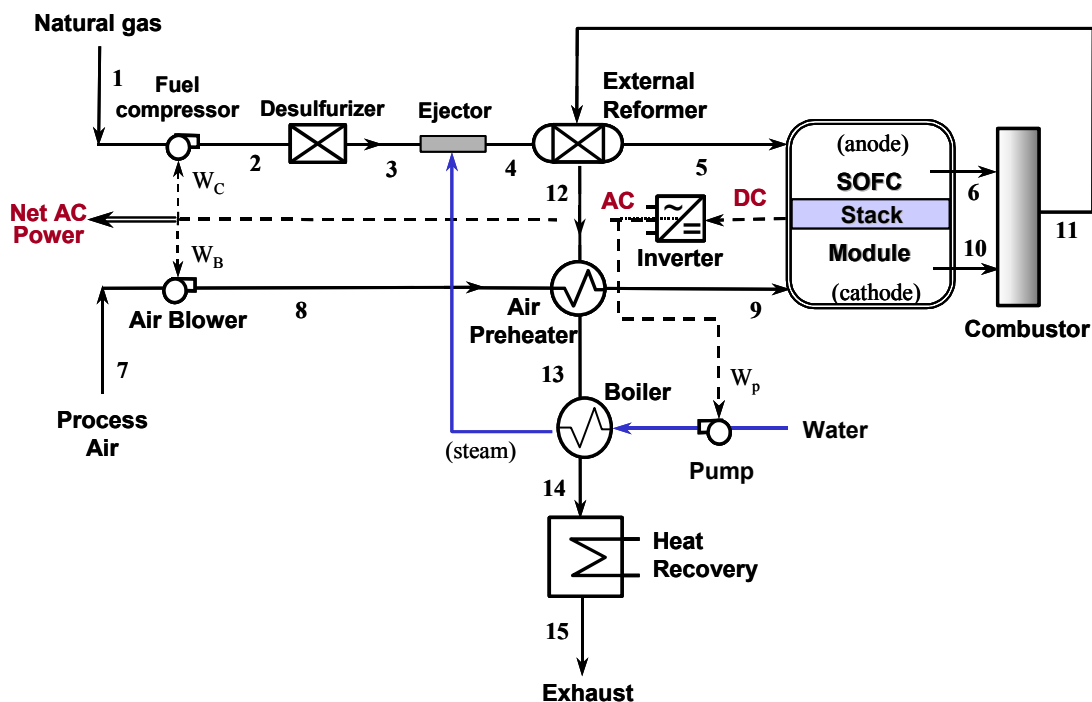


Figure 3.2 Schematic of a natural gas-fueled SOFC system with external reforming [18]

3.2 Fuel Processing

Near-term SOFC systems differ from conventional power generation systems in a single distinctive way: their operation requires a relatively pure hydrogen fuel. Because hydrogen is not readily available, fuel cell systems typically generate hydrogen from an alcohol- or hydrocarbon-based fuel source. The electrolysis of water is one of the few processes that do not rely on a fossil fuel source to produce hydrogen; however, this process is energy intensive and is envisioned primarily for fuel cell systems incorporating solar photovoltaics. Alcohols, such as methanol or ethanol, and hydrocarbons, such as natural gas, are usually reformed into a hydrogen-rich synthesis gas by several methods: catalytic steam reforming (CSR), partial oxidation (POX), or autothermal reforming (ATR) [1]. The raw fuel can be converted and reformed *external* to the fuel cell stack in a reactor (typically a packed-bed type) or *internally* in the fuel cell anode compartment. Internal reforming will be further discussed in §3.3.

Most external reformer concepts for stationary applications favor CSR for generation of hydrogen from alcohols and light hydrocarbons because it yields the highest amount of hydrogen and results in the highest system efficiencies [2]. In contrast, partial oxidation offers compactness, fast start-up, and rapid dynamic response but sacrifices fuel conversion efficiency. ATR is a combination of CSR and POX processes. In general, these reforming technologies all share approximately the same level of complexity. The major technological difference between CSR, POX, or ATR processes is the mechanism for providing the thermal energy required for the endothermic reforming reactions [21].

Fuel processing is defined in this thesis as the conversion of a commercially-available gas or liquid fuel to a fuel reformatte sufficient for serving the fuel cell anode reactions. Fuel processing encompasses the removal of harmful contaminants, such as sulfur, in the raw fuel, the generation of a hydrogen-rich gas stream, and heating (or cooling) of the reformatte to the prescribed inlet temperature of the fuel cell stack. In low-temperature fuel cells, the fuel processing may also include additional measures beyond desulfurization and reforming, such as low and high temperature shift conversion and preferential selective oxidation (see Figure 3.3). These additional processes will not be examined here since the focus of this thesis is on the high temperature solid oxide fuel cell.

The extent of fuel processing depends not only on the type of fuel cell employed, but also on the fuel type. Sulfur-bound fuels include gasoline, coal-gas, heating oils, and even natural gas. In natural gas, sulfur is not indigenous to the fuel mixture but is added by gas utilities as an odorant to detect leaks. In general, sulfur is a poison to all fuel cells and it must be stripped from the fuel feedstock before it is admitted into the cell stack as illustrated in Figure 3.2 and 3.3. An advantage of high temperature fuel cells, such as the solid oxide fuel cell, is that carbon monoxide is usable fuel and sulfur poisoning is a reversible phenomenon. Due to the fuel gas purity requirements of fuel cells (and fuel reformers), fuel preparation equipment are sacrosanct components to the power plant. Elaboration on each of the needed steps for fuel preparation in solid oxide fuel cell systems is presented next.

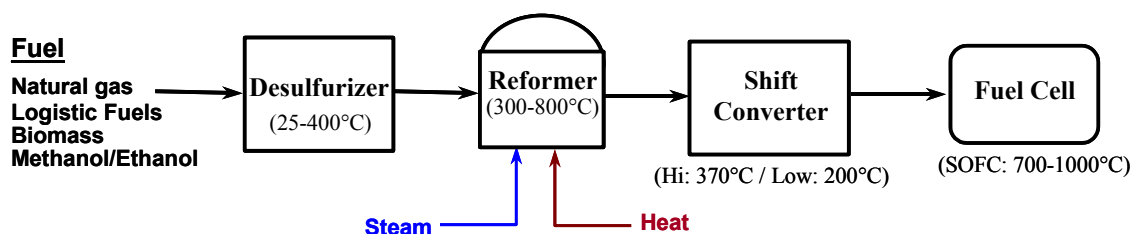


Figure 3.3 Steps involved in fuel processing of fuels for use in fuel cells

3.2.1 Desulfurization

The reforming reaction requires a catalyst which is typically elemental nickel with high surface area supported on a ceramic substrate (spinel carrier). The anode of the SOFC is also nickel based to promote rapid electrochemical reaction kinetics. The nickel catalyst in both the reformer and fuel cell is reactive with the sulfur compounds normally found in many fuels and even the normal odorant compound level in natural gas will rapidly deactivate the catalyst due to formation of nickel sulfide [3]. Thus, fuel-bound sulfur compounds are poisonous to both the reforming catalysts and the fuel cell electrocatalytic sites and they must be removed from the raw fuel feedstock. The allowable sulfur concentration for solid oxide fuel cells is limited to a range of about 1-10 ppm [4, 5], above which substantial electrode performance degradation is realized. Some fuel cell developers have claimed higher allowable sulfur concentrations in the fuel when applying sulfur tolerant electrodes [6].

Several desulfurization techniques are available; these include activated carbon, zinc oxide, and hydro-desulfurization [3]. The choice of technique is dependent on the cost effectiveness of the removal method and the type of sulfur compounds present in the fuel. For instance, the odorants employed by natural gas companies typically contain disulfides and mercaptans. Other natural gas distribution companies use odorants containing tetrahydrothiophene (THT), more commonly known as thiopane, which can require extra steps to remove [3]. The use of activated carbon enables near ambient temperature removal of sulfur but the capital and operating costs are high [3]. Zinc oxide packed bed reactors make ZnS from the reactive sulfur compounds and the adsorbent must then be periodically disposed and the reactor bed refilled. The hydrodesulfurization process makes use of a small slipstream of hydrogen from the reforming process for the purposes of hydrogenating the sulfur compounds (particularly thiopane) in the natural gas to generate a reactive H₂S compound [7]. The natural gas is then passed over zinc oxide pellets for adsorption of the H₂S compounds. Both zinc oxide and hydrodesulfurization processes require operation near 400°C and desulfurization technology, in general, is well established.

3.2.2 Catalytic Steam Reforming (CSR)

Due to the wider availability of light hydrocarbon gases (such as natural gas) in stationary applications, the focus of reforming methods presented in this section will be on steam-reforming of natural gas. Natural gas is a fuel mixture which is typically methane rich and contains low-level amounts of some higher hydrocarbons (e.g., ethane, propane, and butane) and nitrogen. While direct electrochemical oxidation of methane at the anode has been found to occur [8, 9, 10, 11], its successful use for near term commercial solid oxide cells employing zirconia-based electrolytes and nickel-based anodes is not likely. Therefore, methane is reformed to produce hydrogen according to the highly endothermic reaction,



Additional hydrogen can be produced via the mildly exothermic shift reaction,



The overall reforming reaction is endothermic,



In the case where carbon dioxide is present in the fuel feedstock, CO₂ reforming via



is also possible. As can be seen from Table 3.1, reactions (3.1), (3.3), and (3.4) are endothermic and therefore require an external heat source, such as a gas-fired burner or hot gas stream to sustain the reactions.

Steam reformers for fuel cell technology are derived from industrial reformer technology that has been in use for decades. According to Rostrup-Nielsen [12], industrial reformers typically consist of 40-400 reactor tubes situated in a large gas-fired furnace. The reactor tubes may be between 6-12 meters in length and 7-16 cm in diameter and contain catalyst, normally dispersed nickel on alumina or magnesium spinel carrier in the shape of cylinders or raschig rings. Reforming temperatures can range between 550° and 900°C and reactor pressures may operate as high as 3.0 MPa (30 atm).

Table 3.1 Possible Reactions in Reforming [adapted from 13 and 14]

Reaction	Name	ΔH_{298} (kJ/mol)	Equation
$CH_4 + H_2O \leftrightarrow CO + 3H_2$	Reforming	206.1	(3.1)
$CO + H_2O \leftrightarrow CO_2 + H_2$	Water-gas shift	-41.15	(3.2)
$CH_4 + 2H_2O \leftrightarrow CO_2 + 4H_2$	--	165.0	(3.3)
$CH_4 + CO_2 \leftrightarrow 2CO + 2H_2$	CO ₂ reforming	247.3	(3.4)
$CH_4 \leftrightarrow C_{(s)} + 2H_2$	Methane cracking	74.82	(3.5)
$2CO \leftrightarrow C_{(s)} + CO_2$	Boudouard	-173.3	(3.6)
$CO + H_2 \leftrightarrow C_{(s)} + H_2O$	CO reduction	-131.3	(3.7)

Natural gas reformers for SOFC systems require much smaller reactors, operate near atmospheric pressure and, since the cell operating temperature is sufficiently high, may be thermally integrated with the fuel cell stack such that the necessary heat for the endothermic reforming reactions is supplied by the heat release from electrochemical oxidation of hydrogen and ohmic losses associated with current generation and flow in the cell stack. Three different reforming configurations are possible: (i) external reforming (ER), (ii) indirect internal reforming (IIR), and (iii) direct internal reforming (DIR). These configurations are conceptually illustrated in Figure 3.4. External reforming requires an external heat source, such as a burner or hot waste gas and a fixed bed reactor. Internal reforming capitalizes on the heat release in the fuel oxidation process by providing a convenient and efficient setting for energy transfer between heat source and heat sink and simultaneously lowering the air cooling requirements of the SOFC. *Indirect* internal reforming physically separates the reforming process from the electrochemical process, making use of the cell-stack heat release either by radiation heat transfer (cf. [15]) or by direct physical contact between the cell hardware and the reforming unit. In *direct* internal reforming, the hydrocarbon fuel-steam mixture is admitted directly into the anode compartment and the fuel is reformed on the porous, nickel-based anode layer. In addition to the reduction of capital-intensive equipment, a major benefit of internal reforming is the higher system efficiency achieved through higher heat transfer effectiveness and reduced parasitic power associated with a decrease in cooling air requirements. Chapter 8 will show that cooling air flow reductions of greater than 50% and system electric efficiency increases of more than 8.5 points are possible with the use of internal reforming of natural gas.

Table 3.1 lists the reactions used to describe steam reforming of methane. A significant concern during reforming operation is the formation of solid carbon through undesired side reactions. These side reactions are listed in Table 3.1 as Equations (3.5) – (3.7) and are known as methane decomposition (or cracking), Boudouard coking, and CO reduction, respectively. Carbon deposition is to be avoided as it deactivates catalyst and clogs interstices within the reactor bed or porous anode microstructure. The risk for carbon formation through side reactions is reduced by increasing the steam-to-carbon ratio (SC) of the fuel feedstock

[12]. Thus, steam in an amount greater than the stoichiometric requirement of reaction (3.1) is injected into the fuel prior to high temperature heating and admittance into the reformer. However, the minimum amount of steam necessary for carbon-free operation is difficult to establish. This issue will be taken up in more depth shortly.

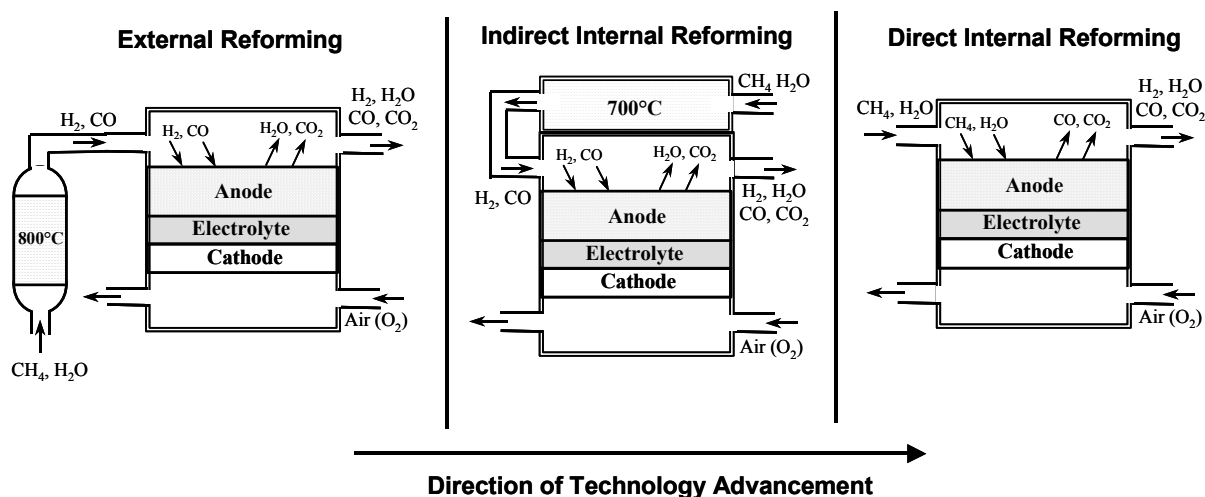


Figure 3.4 Fuel Cell CSR Configurations [adapted from 16]

Product gas leaving the reformer reactor tube(s) is normally of equilibrium composition [14]. The methane cracking reaction (3.5) is endothermic and involves an increase in number of moles and using La Chatelier's Principle, it is therefore favored by increases in temperature and reductions in pressure. Reforming for fuel cells occurs at low pressure, and high methane concentration at the reactor tube inlet is characteristic. Tube and gas temperatures therefore need to be relatively low in this region to avoid carbon deposition. At the tube outlet, the process gas temperatures reach their maximum and but nearly all the methane is consumed in this region resulting in high hydrogen concentration. In this zone, the reverse of reaction (3.5) is then favored, i.e., gasification by hydrogen [14].

Reaction equations (3.6) and (3.7) are both exothermic and involve a reduction in number of moles when the forward reaction occurs. Low temperature and high pressure favor these reactions. As with industrial reformers, CO is generally not found at the reactor tube inlet in external reforming fuel cells, and thus reactions (3.6) and (3.7) are not thermodynamically

avored. However, as methane is consumed and carbon monoxide produced, these reactions can become thermodynamically possible when the gas is cooled below 750°C [17]. But even when conditions conducive to carbon deposition are present (on either graphite or coke-based thermodynamics), the reaction kinetics may be so slow that there is no significant build up of coke over the life of the catalyst [14].

The problem of determining when or where carbon formation will occur is presently limited to evaluating thermodynamic tendencies. Accurate prediction of carbon deposition can only be achieved by experiment or analysis with the appropriate kinetic rate equations. However, according to Wagner and Froment [14], the rate equations are not available. Consequently, the tendency for carbon formation is estimated by evaluating the equilibrium constant for reactions (3.5) – (3.7) at each axial position in the reformer [17].

Control of carbon deposition is managed by balancing the thermodynamic tendency for carbon formation (and its kinetics) with the tube heat flux at each streamwise position in the reformer bed for temperature control [e.g., 15, 17]. Evaluating the tendency for carbon formation in this way is similar to what has been termed the “principle of equilibrated gas” [12]. The principle says that carbon formation is to be expected “if the gas shows affinity for carbon after the establishment of the methane reforming and shift equilibria” [12]. Estimating the minimum SC ratio based on evaluation of thermodynamic driving forces results in excessive but “safe” steam-to-carbon ratios of usually 2 or 3 to 1. Wagner and Froment [14] have used the principle of equilibrated gas to make a conservative estimate of 1.6 as the minimum steam-to-carbon ratio to prevent coking phenomenon. The validity of this method increases with increasing temperature. In fuel cell systems, the steam-to-carbon (SC) ratios are usually greater than 2 because the smaller reformer tube temperatures established using fuel cell off gases are often lower than their industrial counterparts [17].

The temperature dependence of hydrogen yield in a reformer was calculated by Gibbs energy minimization and is shown in Figure 3.5 for a steam-to-methane ratio of 2:1. As the temperature is increased, the inception of H₂ production occurs at about 150°C and increases in a nearly linear fashion from 300° to 700° C, and reaches a maximum hydrogen yield near

800°C. Thus, Figure 3.5 gives some insight into the motivation behind the selection of optimal reformer operating temperature.

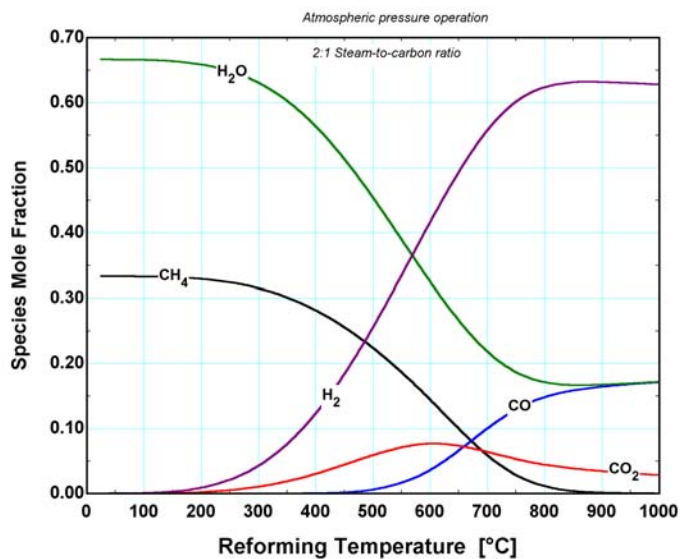


Figure 3.5 Equilibrium reformat composition from CSR vs. reactor temperature

In addition to suppression of coking, the SC ratio also affects the equilibrium yield of hydrogen. The effect of steam-to-carbon ratios on the equilibrium amount of hydrogen generated is shown in Figure 3.6. As the SC ratio is increased, the hydrogen yield decreases. Increasing the SC ratio also negatively affects the overall system energy efficiency by (i) requiring additional primary steam generation or recycle of anode effluent for reforming, and (ii) by increasing the mole fraction of water vapor in the exhaust gas, the sensible heat available in the exhaust gas for heat recovery is reduced [18]. These considerations clearly illustrate the incentive to minimize the steam requirements for fuel processing.

In general, there are two advantages to steam reforming over partial oxidation and autothermal reforming processes: (1) it produces a high concentration of hydrogen with no dilution of the product stream by nitrogen, (2) it operates with high fuel conversion efficiency (85-95%) [19]. For SOFC systems, the additional benefits of cost and parasitic power reductions are derived by the tight thermal integration between internal reforming and electrochemical fuel oxidation. The use of DIR still requires a small “pre-reformer” external

to the fuel cell which reforms the higher hydrocarbons present in the fuel feedstock and perhaps 30% of the methane present to eliminate coking phenomena and the large solid cell temperature gradients generated by the strong cooling effect from the endothermic reforming reaction that occurs on the anode surface. In external reformers, the use of CSR translates into rather slow dynamic response capability and larger-size fuel processors. However, faster load response is anticipated for DIR-SOFC systems [20] due to the close proximity of reaction processes and the reduced mass of the fuel processing system.

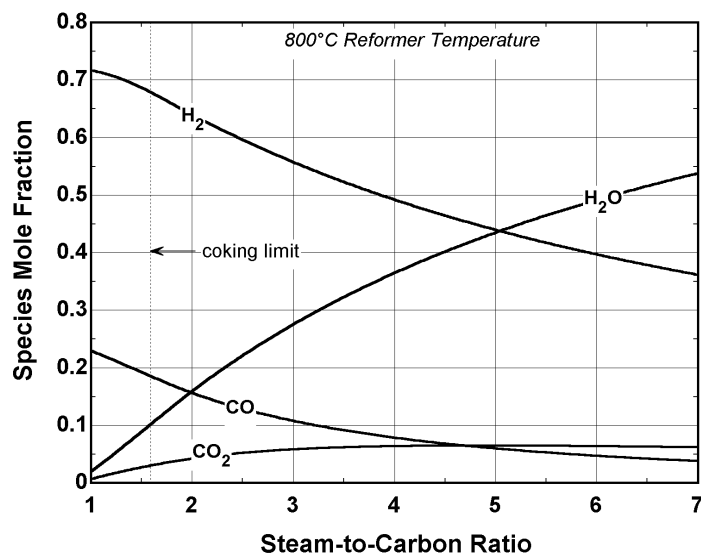


Figure 3.6 Effect of steam-to-carbon ratio on equilibrium reformat composition

3.2.3 Partial Oxidation (POX)

Hydrogen can also be liberated from methane and other hydrocarbons through partial oxidation which may be catalyzed, non-catalyzed, or a combination of both [2]. The partial oxidation process is typically used to reform heavy hydrocarbon and oil fuels in industrial processes where the required heats of reaction are provided *in-situ* by oxidizing a fraction of the feedstock [17, 21]. The use of combustion provides for a direct heat exchange where no heat transfer surface area is required. Oxygen is supplied to the POX reactor at sub-

stoichiometric levels (i.e., fuel-rich) and produces both carbon monoxide and carbon dioxide through the following reactions^{*},



The oxygen is usually supplied by air which will result in a dilution of the hydrogen product by nitrogen. Dilution of hydrogen means a lower fuel cell voltage and hence reduced efficiency. Reactions (3.8) and (3.9) may take place as low as 850°C for methane POX over Ni/Al₂O₃ heterogeneous selective catalysts. Without the benefit of catalysts, the operating temperature of the reforming process must be increased (1100-1500°C) [21]. Because this process yields a lower amount of hydrogen per mole of hydrocarbon input than CSR processes, as well as consuming a portion of its heating value to supply the heat for the endothermic reforming reaction, it results in lower system efficiencies (~1-5% below systems using CSR). Despite this inefficiency, POX reformers are likely to see use in SOFCs for remote power applications where such inefficiencies are acceptable in light of other advantages, such as cost and weight [22]. However, many developers of fuel cells and reformers have turned to autothermal reforming as a more effective alternative to the inefficient POX process [23, 24, 25].

3.2.4 Autothermal Reforming (ATR) [21]

Autothermal reforming is a hybrid technology that combines the catalytic aspect of steam reforming methods with the *in-situ* oxidation feature of partial oxidation technology. Using oxidation catalysts, a portion of the hydrocarbon feed is oxidized with a controlled addition of oxygen. The oxygen is controlled because it is critical to limiting the amount of heat release and any subsequent sintering of the catalyst. (Platinum and nickel are common reforming catalysts for ATR technology.) Thus, the heat of partial oxidation provides the necessary thermal energy to drive the endothermic reforming reaction, transforming the gaseous fuel to hydrogen and carbon monoxide. In general, the operating temperature of ATR process

^{*} If the oxygen is supplied with air, the process can also produce trace amounts of ammonia [21].

(~850°C) is lower than POX processes (1100-1500°C) and higher than CSR (~800°C). Because ATR offers many of the same advantages of POX reforming but with higher efficiency, many developers are pursuing the use of autothermal reforming in automotive and residential PEMFC systems [24, 26, 27, 28].

3.3 Fuel Cell Stack

3.3.1 *Operational features, cell-stack assemblies, and component materials*

Unlike ordinary combustion, fuel (hydrogen-rich) and oxidant (typically air) are delivered to the fuel cell separately (see Figure 3.7). The fuel and oxidant streams are separated by an electrode-electrolyte system. In a typical fuel cell, a gaseous, hydrogen-rich fuel is fed to the anode (negative electrode) compartment and an oxidant is fed to the cathode (positive electrode) compartment. The separation of the reactant gases by the cell layer generates a voltage potential proportional to the concentration of the electrochemical species. The reactant gases flow over the electrode faces in the channels of the bipolar separator plates and diffuse through the porous electrode structure to the electrode/electrolyte interface. At the interface, electrical (current) and thermal (heat) energy is generated by the simultaneous electrochemical oxidation of fuel and reduction of oxygen. The electrochemical process is a direct conversion of the chemical energy bound in the fuel to electrical energy by the ionization of reactant species at the electrodes and subsequent charge transport through the electrolyte. The primary product of *fuel cell* reactions is water; NO_x, SO_x, or particulate matter are not allowed to form due to the separation of reactants, the low reaction temperatures, and fuel processing upstream of the fuel cell. Due to the intrinsic nature of establishing the cell electrical potential, not all the reactants can be consumed in the oxidation process. Thus, it is necessary that some hydrogen exit the fuel cell stack. Typically, about 15-25% of the hydrogen delivered to the fuel cell stack is unused and often oxidized or “burned” in ancillary equipment downstream of the fuel cell module.

The amount of fuel and oxidant utilized affects both the fuel cell and overall system efficiencies. As the reactants are consumed at the electrode surface inside the cell, the electrochemical specie concentrations will decrease with streamwise position, and thereby

lower the driving force (or theoretical voltage) for current generation. If all the fuel (hydrogen, carbon monoxide, or methane) in the anode compartment were oxidized, or all the oxygen in the cathode compartment reduced, the cell voltage would proceed to zero as no chemical driving force would be present to generate a potential. This phenomenon is also due in part to the relatively high electronic conductivity of the electrodes. Because they cannot support a (measurable) voltage gradient, the electrodes act as isopotential surfaces. Therefore, to generate a cell voltage greater than zero, positive partial pressures of electrochemical species are maintained along the length of the cell by letting unreacted fuel and oxidant exit their respective electrode compartments. It follows that higher fuel utilizations generate lower cell voltages, but they also reduce the system fuel and air flow requirements.

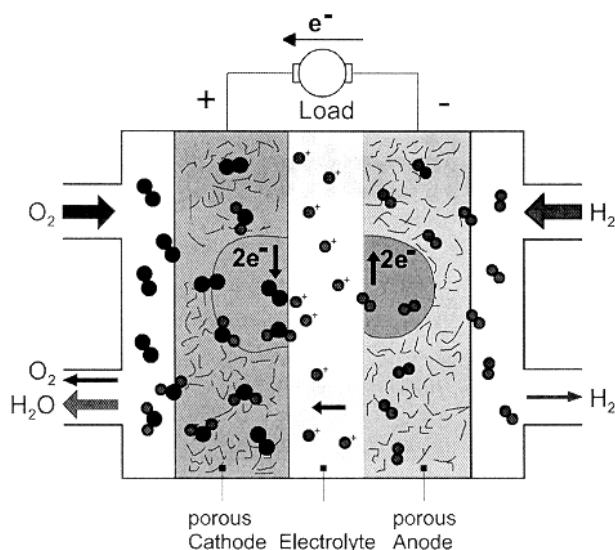


Figure 3.7 Schematic of a hydrogen-oxygen fuel cell (based on a PEM type) [2]

The amount of fuel utilized can be defined (or specified) in several ways. For hydrocarbon fuels, Bossel [29] defines the fuel utilization to be,

$$U_{f,1} = \frac{\text{moles of fuel consumed}}{\text{moles of fuel supplied}} \quad (3.10)$$

As will be seen in Chapter Four, several interpretations of Equation (3.10) are possible. For hydrogen-fueled fuel cell systems, fuel utilization is defined as,

$$U_{f,2} = \frac{\text{moles of hydrogen consumed}}{\text{moles of hydrogen supplied}} \quad (3.11)$$

Fuel utilizations for commercial SOFCs are expected to range from 75-85%. SOFCs are air-cooled by supplying air in excess of the stoichiometric requirements of the fuel feed. The amount of excess air is defined as [29],

$$\lambda_{O_2} = \frac{\text{moles of oxygen supplied with air}}{\text{moles of oxygen needed for stoichiometry}} \quad (3.12)$$

The amount of excess air needed to provide air-cooling in SOFCs can be large ($\lambda_{O_2}=7$) as the allowable temperature rise of the solid cell is limited by the thermal stress induced in the ceramic cell components. The typical air temperature rise in SOFCs is approximately 100°C. This relatively low allowable temperature rise translates into high blower parasitic power requirements and large blower equipment. Investigations of the tradeoffs in selection of fuel utilization and strategies for air-cooling of SOFCs will be examined in Chapters 8 and 9.

In practice, a single cell will produce less than one volt of electrical potential; therefore, fuel cells are stacked on top of each other and connected in electrical series to produce higher voltage levels. The number of cells stacked depends on the desired power (or voltage) output and individual cell performance; cells are usually stacked from a dozen or so (producing ~1 kW at moderate current) to several hundred (producing 250+ kW at moderate current). As illustrated in Figure 3.8, cell stacks consist of repeating fuel cell units; each comprised of an anode, cathode, electrolyte, and a bipolar separator plate between cells. In the bipolar arrangement, the bipolar separator plate connects the two electrodes with opposite polarities, thereby implementing the serial addition in the stack. The current flows perpendicular to the electrode surface and current collection is performed over the whole area of the electrodes [2]. A disadvantage of this stacking method is that a single-cell failure leads to a shutdown of the entire stack.

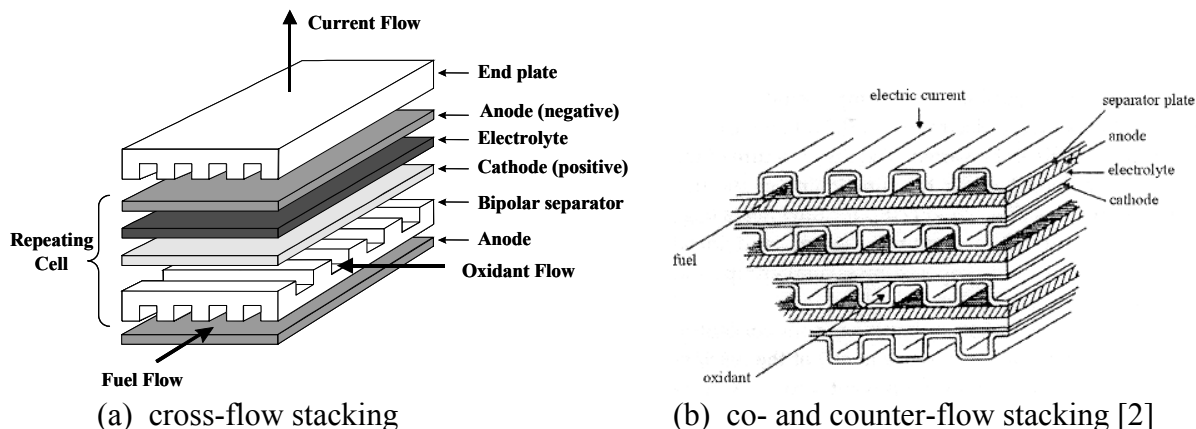


Figure 3.8 Cell-stack assembly for flat planar fuel cells

Stack manifolding dictates the way in which the reactants are supplied to a multi-cell stack. Internal manifolding (Figure 3.9) implies that the reactants are delivered to the cells through vertical leads in the stack. This delivery method results in a flow path perpendicular to the stack layering. In external manifolding, the distribution of reactants and collection of products is achieved through inlet/outlet ports where the flow path is parallel to the stacking arrangement [2].

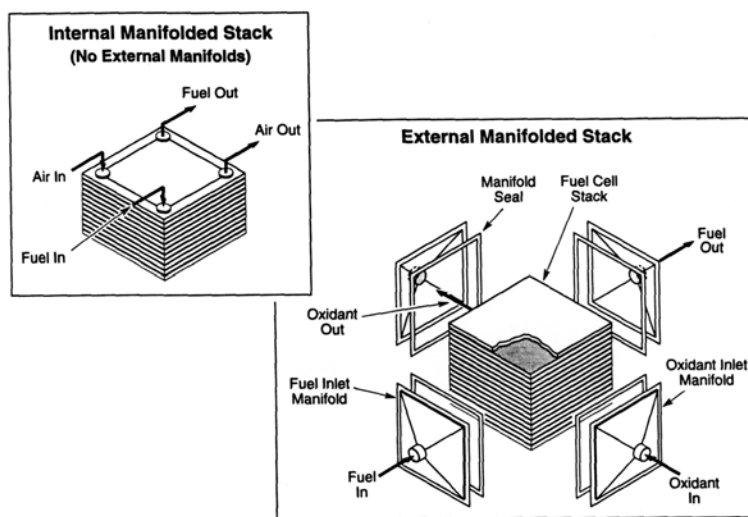


Figure 3.9 Internal and external manifolding configurations [30]

Solid oxide fuel cell component materials and thicknesses are listed in Table 3.2. The choice of material and component thickness depends on the design philosophy and the material

capabilities, but the eventual material selection must meet the basic component criteria. There are two primary functions of the **electrolyte**: (i) it must act as a transport medium for the migration of ionic charge (thus completing the electric circuit), and (ii) serve to separate gaseous fuel and oxidant streams without any gas crossover. Therefore, the electrolyte must exhibit high ionic conductivity and low electronic conductivity; that is, it must act as an insulator to the electric current, thereby preventing any short-circuiting of the cell. The **electrode** functions are to (i) conduct electrons to and from the electrochemical reaction sites, (ii) to provide porous pathways for the diffusion of gaseous species to reaction sites, and (iii) have sufficient chemical activity to promote the electrode reactions. **Separator plates** are utilized to (i) act as current collectors, providing electrical connection between cells, and (ii) to separate the fuel and oxidant gas streams in adjacent cells.

Table 3.2 Materials Used in SOFCs

Component	Thickness	Material
Anode	50 μm – 1.5 mm	Nickel-doped zirconia (Ni/ZrO ₂)
Electrolyte	5 μm – 150 μm	Yttria-doped zirconia (Y ₂ O ₃ -ZrO ₂)
Cathode	50 μm – 150 μm	Strontium-doped Lanthanum Manganite (Sr-LaMn)
Interconnect	0.8 mm – 1.5 mm	Stainless – Chromium alloy

Due to the functionality requirements of fuel cells, materials play a crucial role in their success. Critical aspects to the sustained performance of all components include corrosion, porosity, mechanical strength, conductivity, chemical and dimensional stability with both mating components and gaseous species at the cell operating temperatures / pressures, and manufacturability characteristics [1]. The high operating temperature of solid oxide fuel cells, in particular, places stringent material demands on development. Thus, the development, performance, and viability of fuel cells have been heavily dependent upon advancements from materials research, mechanical design, and manufacturing techniques.

3.3.2 Fuel cell performance

As Chapter One noted, the excitement surrounding fuel cells is largely derived from their expected high fuel conversion efficiency. In some cases, their efficiencies can nearly double the efficiency of conventional power generating equipment. To understand the reasons behind such performance advantage, the electrochemical operating process requires more careful examination. Stated once again, the fuel cell is an electrochemical device which converts the chemical energy of the fuel directly into electrical energy, requiring no intermediate conversions of the fuel to thermal and mechanical energy forms. Instead of being released entirely as heat, much of the chemical energy of the fuel is released in the form of an electron stream which, in turn, flows out of the cell through a load and is returned to the electrode [31]. The rate at which fuel is oxidized is controlled (or limited) by the load. The primary thermodynamic advantage of fuel cells over conventional engines (such as spark-ignition and diesel) lies in the oxidation of the fuel, which is generally the largest source of inefficiency in combustion processes.

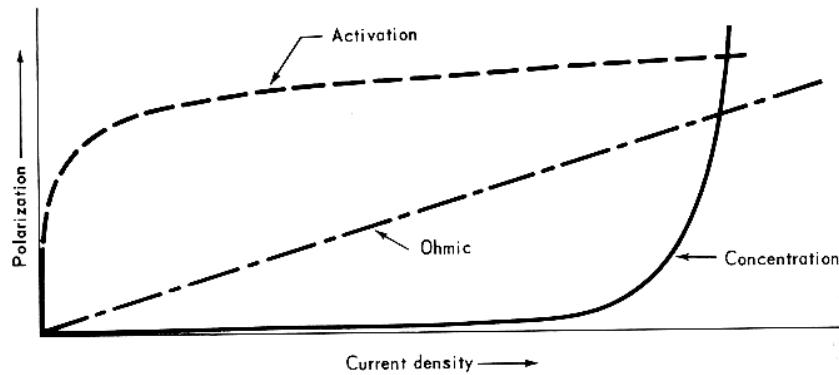
In conventional combustion, a fuel is directly mixed with oxygen and reacts to form products of combustion. The gas phase reactions in combustion are characterized by random collisions between molecules in which electrons are exchanged. From a thermodynamic standpoint, the driving force for the oxidation of the fuel is the difference between the chemical potentials of the reactants and products, that is, the chemical affinity of the reaction. The Second Law of thermodynamics indicates that the larger the driving force (e.g., temperature, concentration, or pressure difference) for a given process is, the larger the process irreversibility will be. A large fraction of the potential of the fuel to do useful work is irreversibly destroyed in the highly entropy producing combustion process. Dunbar and Lior [31] state that there are two ways to reduce entropy production (and thereby increase the fuel conversion efficiency) in the fuel oxidation process: (i) increase the temperature at which combustion occurs, and (ii) reduce the chemical affinity (or driving force) of the reaction. The fuel cell accomplishes the latter by first passing the reactant ions (O^{2-} ions in SOFCs) through an electrolyte. This allows a less violent (in comparison to conventional combustion) chemical reaction to take place inasmuch as the force driving the reaction is lower [32]. Both the high temperature feed

of reactants to the fuel cell and the “controlled” oxidation process contribute to higher electric efficiencies than experienced by conventional oxidation equipment (e.g., internal combustion engines).

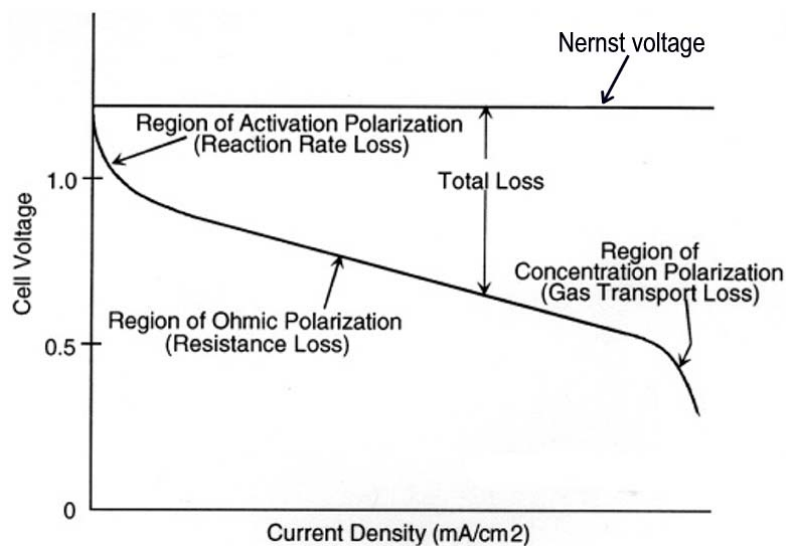
Fuel cells do, however, experience losses in efficiency due to other effects. Temperature, pressure, gas composition, and fuel and reactant utilization influence their performance. These operating variables affect the magnitude of the irreversible voltage losses and hence, the cell potential. The losses, when expressed in terms of voltages, are called polarizations. There are three main types of polarizations -- ohmic, activation, and concentration. These polarizations may arise in any of the reaction steps of a real fuel cell involving mass transport, adsorption, chemical reaction, or charge transfer [33]. Activation losses occur at all current densities but are dominant at low current density and are associated with sluggish electrode reaction kinetics at the three-phase interface (i.e., they can be viewed as a resistance to initiating the electrode reactions). Ohmic losses arise from resistances to charge conduction through the various cell components and demonstrate a linear dependence with current. Lastly, concentration polarization is a resistance to diffusional transport of reactants to and from the electrochemical reaction sites. Like activation losses, concentration losses occur over the entire operating range of the cell but the contribution to the total loss is most significant at high current density operating points. When operating the fuel cell in this regime, the cell is essentially “starved” of reactants as they cannot be supplied at the high rate at which the electrode reactions demand. The relative magnitude of each of these polarizations as a function of current is depicted in Figure 3.10(a). The cumulative effect of these inefficiencies is shown in Figure 3.10(b).

In general, a decrease in the operating cell voltage (due to an increase in current) results in a lower fuel cell efficiency. A voltage drop is also realized when the fuel utilization is increased due to dilution of hydrogen in the fuel gas stream in the anode. The dilution of reactants has the overall effect of reducing the theoretical cell voltage. An increase in cell temperature will also decrease the theoretical cell voltage; however, the numerous kinetically constrained transport processes are improved with increasing cell operating temperature and a net gain may be realized. The relationship between the relevant parameters (e.g., temperature,

pressure, reactant utilization, and gas composition) and the various polarizations is quite complex and will be discussed in more depth in Chapter 4.



(a) Types and relative magnitudes of polarizations in a fuel cell [33]



(b) Overall effect of polarization on cell voltage performance [1]

Figure 3.10 Types of losses in fuel cells

3.4 Power Conditioning & Energy Storage

The purpose of the inverter is to convert dc-power to ac-power. In most residential applications, 120 volt, single-phase ac power is required. Residential fuel cell systems may be employed in stand-alone or grid-connected configurations. In stand-alone systems, batteries or other energy storage devices are required to meet dynamic and peak loads. In a

grid-connected configuration, the cost effective use of batteries (or other energy storage methods) is uncertain and can depend on the utility net metering plan, grid-connection charges, as well as, the dynamic capability of the fuel cell. In either grid-connected or stand-alone scenarios, inverters will be required*.

3.4.1 Basic operation of an inverter

Fuel cell devices are characterized as low voltage / high current power sources with slow transient response characteristics. Over the load range (20-100% of rating), the fuel cell output voltage for a 2 kW stack may vary, for example, from 36 – 72V_{DC}. The objective for the inverter is to convert the high current, low DC output voltage from the fuel cell to a 60Hz, single-phase split 120V/240V output suitable for domestic stationary applications at high efficiency (>90%) and with low total harmonic distortion (<5% on a standard test). The basic steps in conditioning the fuel cell dc output to an acceptable sinusoidal (ac) power form are:

- (1) filtering DC output from fuel cell
- (2) generation of square wave form by chopping the DC signal with high frequency switching
- (3) boost of the DC voltage by the use of a DC/DC converter (transformer)
- (4) rectification of the wave form (full- or ½ bridge)
- (5) inversion of the wave form
- (6) filtering of the inverted signal

One of the most costly and inefficient steps above is the boosting of the DC voltage [34]. If the fuel cell output voltage was higher, step (3) could be removed for substantial reduction of cost and increase in efficiency. In general, with today's fuel cell inverters, power inversion efficiency ranges between 87-96% depending on the output voltage of the fuel cell. The maximum efficiency is typically reached at relatively small power outputs (10% of max) and is maintained over the remainder of the power range [35].

* The end-use power requirements for auxiliary or remote power applications will not require single or three phase ac power from the fuel cell system eliminating the need for an inverter, and thereby reducing the cost and simplifying the system.

3.4.2 Considerations for dynamic load changes or losses

The fuel cell may set its operating point based on a control signal from the inverter. The time constant of an SOFC can be 30 seconds or more [36]. This behavior translates into an approximate time of 140 seconds for the operating point of the fuel cell to increase or decrease from the old value to the new value set by the control signal*. During this transient, if the power demanded by the inverter is not matched by the power output from the fuel cell, there will be a power deficiency or an excess. In the case of a call for more power, the current is increased resulting in a decrease in cell voltage; simultaneously, an excess production of oxygen anions (O^{2-}) occurs at the cathode. Changes in current demand (or power) can occur on millisecond timescales. The fuel supply to the anode compartment is not likely to follow such dynamic perturbations. Thus, the oxygen anions that migrate across the solid electrolyte are likely to arrive at the anode where no fuel is available for oxidation. When such a loss of fuel supply occurs, these highly reactive anions can then oxidize the nickel in the anode cermet, effectively destroying the cell. Therefore, to avoid damage to the fuel cell, current demand should never exceed the available current.

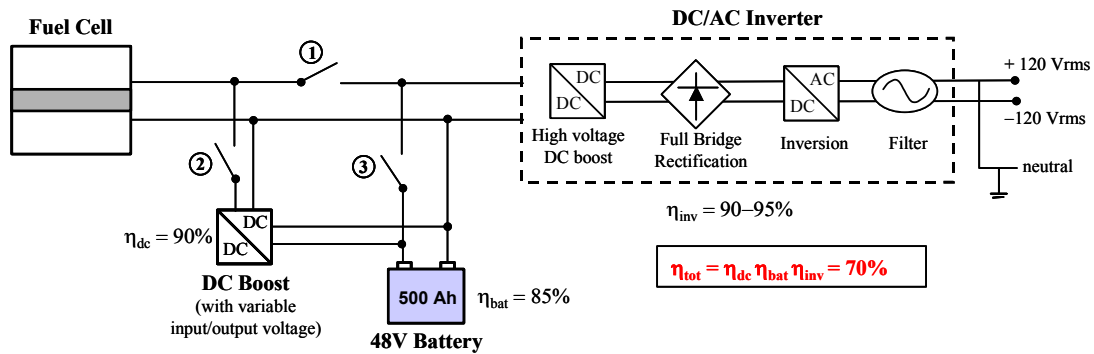
In the case of a decrease in power demand, that is, when the current demand is less than the available current, unoxidized fuel will exit the cell and reduce the system efficiency. There are additional concerns for loss in electric load beyond the concomitant inefficiency. For system designs where a catalytic combustor is positioned downstream of the fuel cell stack to burn-off the unused fuel with the air in the cathode exhaust, a fuel excess may cause large heat release in the unit generating large temperature gradients, possibly damaging combustion catalysts via sintering, or even causing an explosion. The level of safety concern for such loss in load is proportional to both the magnitude and duration of the load excursion from the previous steady-state operating point. Unless such issues can be resolved with control measures, load buffering (or energy storage) with a battery or other method will be needed.

* The time to steady-state may be even longer during load changes as control is complicated by the change in fuel cell efficiency with changes in load.

3.4.3 Design challenges of power conditioning

Cost effective and efficient power conditioning schemes depend on such design factors as selection of fuel cell stack voltage, energy storage method and integration, and power conditioning topology. The fuel cell stack voltage will vary according to the cell power density, cell area, and the number of cells stacked in electrical series. Operating on a natural gas reformate, a 96 cell-stack with a single cell electroactive area of 100 cm^2 and a power density of 0.3 W/cm^2 may generate 2.35 kW of dc power at about 68 V_{DC} (60V nominal). To boost the output voltage to eliminate the inefficient dc/dc conversion would minimally require 4 times as many cells. This means that to meet the voltage requirements, either the fuel cell area is reduced or the fuel cell capacity is larger than required.

In addition to the choice of energy storage technology (e.g., flooded or valve-regulated lead-acid battery, ultracapacitor, or flywheel), the strategy for the integration of the electrical energy storage medium into the power conditioning topology of a stand-alone fuel cell system can significantly affect the net system efficiency. Figure 3.11 depicts a power conditioning topology that could be used for power systems employing battery storage. The battery storage in this scheme is shown on the low voltage side separated from the fuel cell by the dc boost (or charger). An SOFC may convert the raw fuel entering the plant to dc electrical energy with a conversion efficiency of about 50% on a lower heating value basis. If the fuel cell power is sent directly to the inverter, usually only 10% of the dc power is lost in the inversion process (net system efficiency of 45%). However, routing the power to the battery via the dc boost before inversion can incur a 30% loss for a net efficiency of 35%. Such a scenario could occur if the topology was designed for the fuel cell to always charge the battery and in turn, the battery always discharge to the load (i.e., fuel cell-converter-battery-inverter are in series). Alternatively, one could use a higher voltage battery after the dc/dc converter in the inverter section, thereby eliminating one boost stage during battery discharge and a source of inefficiency. Such considerations are necessary for optimal design and application of *stand-alone* fuel cell systems. Investigation of stand-alone power systems and battery sizing adds another dimension of complexity and are not covered further in the present study.



- Cases:**
1. Fuel cell power to house load only (switch 1 closed, switches 2 & 3 open)
 2. Battery power to house load only, fuel cell in standby (switch 3 closed, switches 1 & 2 open)
 3. Fuel cell power to both house load and battery (switches 1 and 2 closed, switch 3 open)
 4. Fuel cell charging battery --no house load (switch 2 closed, switches 1 and 3 open)

Figure 3.11 Power conditioning topology for fuel cell electric power output

3.5 Advanced SOFC Systems

3.5.1 Gas process design

Second generation SOFC systems are likely to be more efficient and cost effective by the use of direct internal reforming at the anode, as well as incorporating advanced gas processing concepts, such as anode gas recirculation, cathode gas recycle, and integrated fuel processing. Integrated fuel processing can include combining fuel preheating and fuel cell exhaust gas afterburning steps or fuel pre-reforming and fuel cell exhaust gas afterburning together in a single component. Advanced SOFC cell-stacks are also likely to exhibit high power density performance, which can increase the challenge of providing cost-effective cell-stack air-cooling.

Figure 3.12 depicts the gas process design of an advanced SOFC system that includes (1) anode gas recycle (AGR) and (2) cathode gas recycle (CGR) and a pre-reformer to reduce the fuel-bound higher hydrocarbons to CH_4 and to convert a fraction of the methane to hydrogen. Note that instead of generating steam for the reforming reaction externally as in Figure 3.2, H_2O produced in the electrochemical reactions at the anode can be used by recycling a portion of the depleted anode exhaust back to the pre-reformer inlet. Riensche et al., [37] report that the main advantages of AGR are (i) no external steam production, (ii) a reduced number of cells in stack (and therefore cost) due to lower in-cell fuel utilization, and (iii) a lower steam

concentration in the exhaust gas improving the overall system efficiency by virtue of a reduction in the unusable heat content exiting the system. An additional advantage can be the reduction of fuel preheating heat transfer area by direct contact mixing of the fuel feed and the anode exhaust gas. Recirculation of fuel cell exhaust gases can be achieved by blowers, hot gas fans, or jet pump like ejectors [37]. The most cost-effective is the use of an ejector [38]. However, higher compression energy for the natural gas driven jet pump type ejector is necessary to accomplish the recycle and is the primary disadvantage of the concept [37].

Cathode gas recycle is also depicted in Figure 3.12. The main objective of a cathode gas recycle loop is to preheat the incoming air by direct contact mixing with the hot cathode exhaust gas. This method of heat exchange reduces the size of the air preheater and can also reduce the size of the air blower. The primary disadvantage is the dilution of oxygen at the cathode inlet which then results in an increase in required number of cells to produce the same power.

Heat recovery from the fuel cell exhaust gases also requires some optimization. The temperature of the useful waste heat product depends on where the heat is extracted in the system. In Figure 3.12, heat extraction immediately downstream of the combustor produces the highest grade of heat, where on the other hand, heat recuperation after the air preheater will produce the lowest grade of heat. In addition to the application requirements, another consideration for heat extraction design is that high temperature heat recuperation can lower temperature differences in the downstream heat exchangers, thereby increasing their size and the associated capital cost [37]. Numerous other processing configurations are possible including keeping the cathode and anode exhaust gases separated while performing process preheating and heat recovery. An evaluation of all possible configurations is not feasible, but further discussion of gas process design and flowsheet optimization is made in Chapter 8.

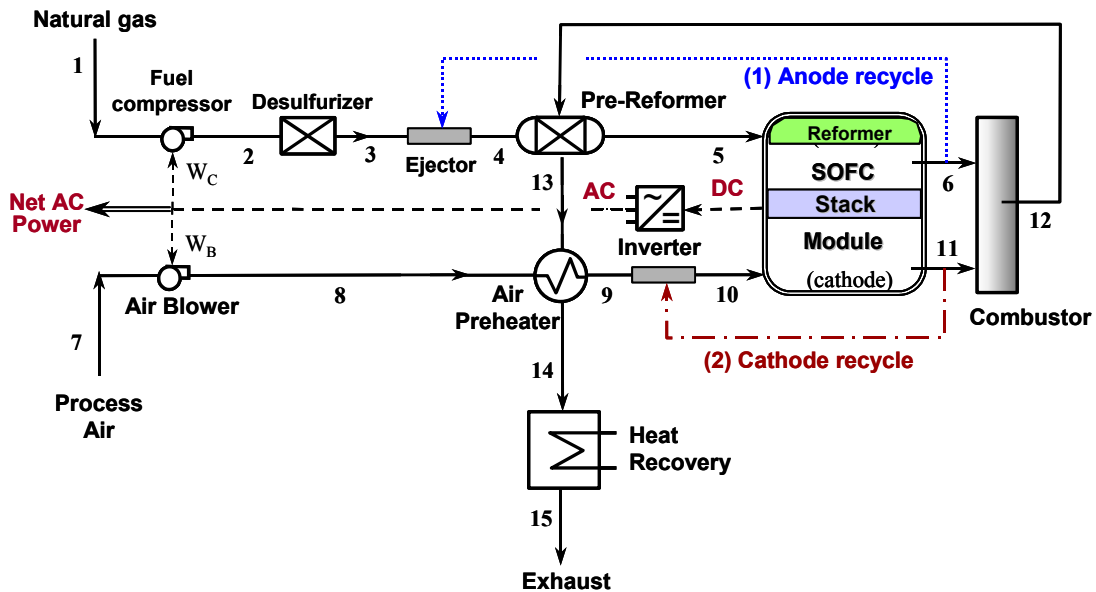


Figure 3.12 Schematic diagram of an advanced natural gas-fueled SOFC system with direct internal reforming and (1) anode and (2) cathode gas recirculation

3.5.2 System concepts for residential applications

The generic residential load profiles shown in Figure 3.13 reveal both the magnitude and the coincidence of the electrical and thermal loads that can exist in small applications. The thermal-to-electric ratio can exceed 15:1 in the winter and 2:1 in the summer with air-conditioning. The challenge is to optimally design a fuel cell system to accommodate the load variances and mismatches.

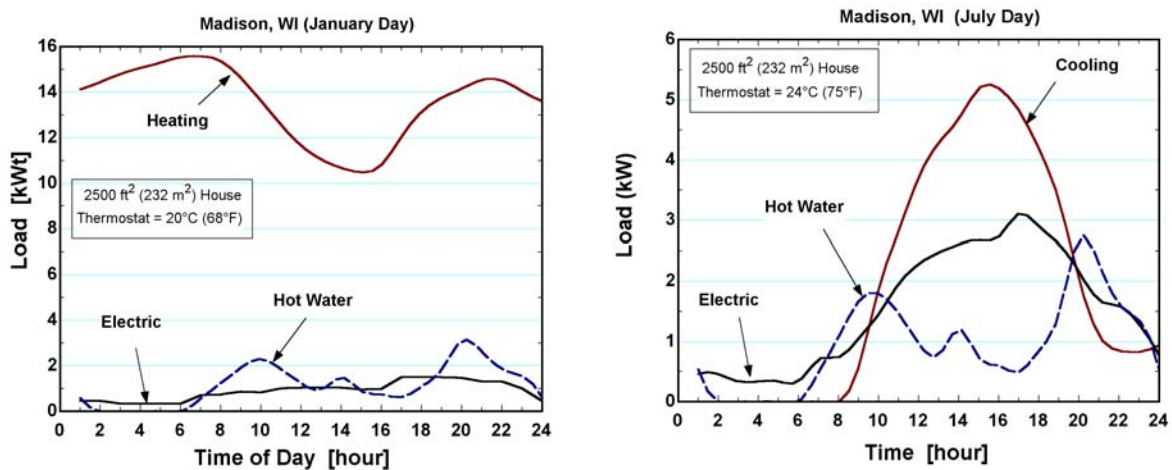


Figure 3.13 Winter and Summer Residential Load Profiles

Various system concepts can be envisioned for fuel cell distributed power systems. One system concept is illustrated in Figure 3.14. The system is designed for thermal and electrical storage and is integrated with an air-source heat pump to improve the system thermal-to-electric ratio. Also, the fuel cell sub-system can be designed to vary its thermal-to-electric ratio to better fit the requirements of the application. Determining how the above can be accomplished both technically and cost effectively is evaluated further in Chapters 8 and 9.

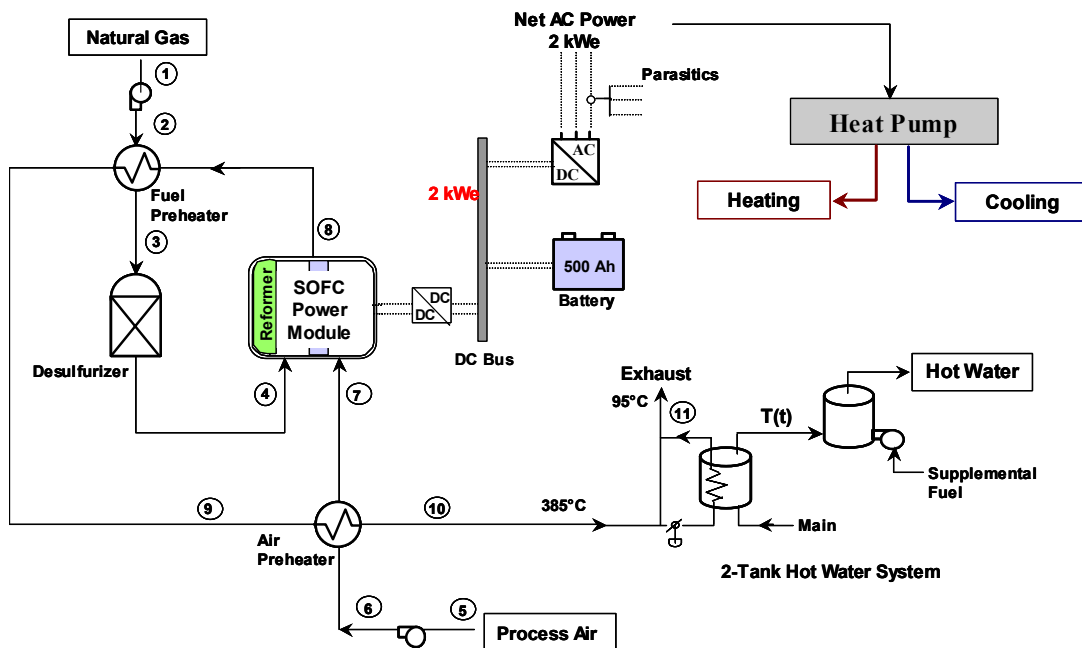


Figure 3.14 A conceptual residential sofc system with electrical and thermal storage

3.6 System Modeling Approach

The primary goal of modeling a solid oxide fuel cell (SOFC) is to provide sufficiently realistic thermal, energy conversion, and emission characteristics such that system-level models can be constructed to meet the research objectives with adequate precision. However, fulfilling the aims of the research discussed in Chapter 1 requires the development of different models, each with a different degree of sophistication and detail. For example, to answer questions related to the dynamic response of the fuel cell stack requires, transient one-dimensional finite difference models with detailed mechanistic relations for chemical reaction and heat transfer phenomena. On the other hand, for the ancillary system components relatively simple (zero-

dimensional) steady-state thermodynamic models with minimal mechanistic information can be employed to determine how well a particular fuel cell system meets the total energy demand of a building application requires. Establishing the optimal fuel cell operating point, system process design, and part-load performance necessitates a combination of elements from both detailed and simple models. Thus, the approach here is to develop two different levels of modeling, one that has a one-dimensional character for the critical fuel cell stack component and one that has steady-state, non-spatially dependent thermodynamic features for the balance-of-plant components.

Figure 3.15 shows an information flow structure from models developed and uses during this project. Experimental, weather, utility, and cost data are all utilized for model development. Experimental and design data, such as cell polarization characteristics and geometry, are input into the fuel cell model, which is one component of a larger thermodynamic system model. Similarly, manufacturing cost data for fuel cell stack, compressors, inverters, etc. are input into the cost model whose output, together with that of the thermodynamic system model, is used for the purposes of establishing a system design and parameterization of the power system performance over a range of load conditions. Weather data and building characteristics, such as a construction materials, are input to TRNSYS which computes building hourly heating and cooling demands. The generated building loads are then employed in the annual simulation. In addition to gas and electric utility rate data, operating strategies (e.g., electric and thermal load-following vs. base-load) are provided. The annual simulator computes hourly and yearly fuel cell system efficiency, economic, and environmental performance from the various inputs. Feedback between the fuel cell system design, operating strategy, and simulation results is necessary to assess “optimal” application designs.

Although some hydrogen configurations will be examined, the primary fuel for small applications (residential) studies will be based on natural gas, thus necessitating a model for equipment that provides fuel reforming. A cost model that incorporates production-scale capital cost estimates for solid oxide fuel cells was developed and will be presented in Chapter 6. The cost model makes use of component and utility costs (grid electricity and

natural gas), interest rates, and expected return-on-investment and calculates the system capital and operating costs. From this, a fuel cell cost-of-electricity (COE) can be computed and used as an optimization parameter for system design. With COE information and the thermodynamic flowsheet model, a SOFC system is designed.

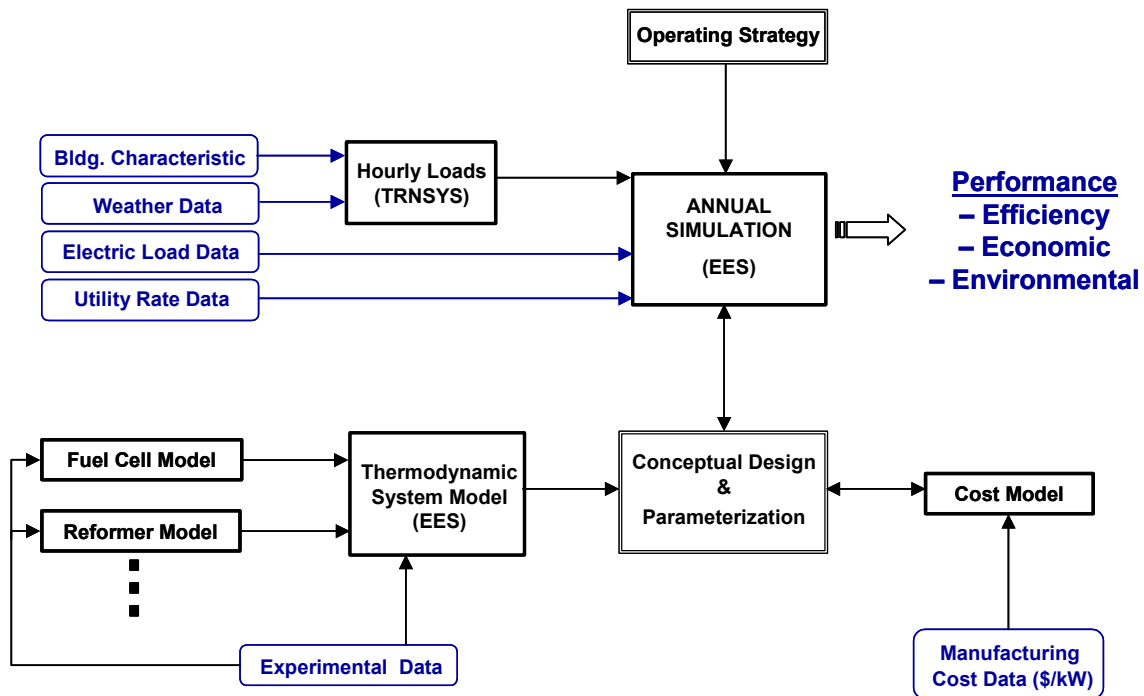


Figure 3.15 Model Information Flow Schematic

Finally, with a system design and system part-load performance characterized, the detailed model is parameterized for use in annual simulations. Annual system calculations are made for each hour in a year. The usefulness of parameterization is that it saves computational time with minimal loss in precision.

3.7 Chapter References

- 3.1 J.H. Hirschenhofer, D.B. Stauffer, and R.R. Engleman, "Fuel Cells, A Handbook," 4th Edition, prepared for the U.S. Department of Energy, November (1998).
- 3.2 L. Carrette, K. Friedrich, and U. Stimming, "Fuel Cells –Fundamentals and Applications," *Fuel Cells 2001*, **1**, (1) (2001), pp. 5-39.
- 3.3 W.L. Lundberg, "Solid Oxide Fuel Cell Cogeneration System Conceptual Design," Final Report, GRI-89/0162, Gas Research Institute, Chicago, IL, July (1989).
- 3.4 N. Maskalick, "Contaminant Effects in Solid Oxide Fuel Cells," *Proc. Of the Fourth Annual Fuel Cells Contractor's Review Meeting*, U.S. DOE/METC, July (1992).
- 3.5 N. Minh, et al., "High Performance Reduced-Temperature Solid Oxide Fuel Cell Technology," *1998 Fuel Cell Seminar Abstracts*, Palm Springs, CA (1998) p. 263.
- 3.6 M. Petrik, C. Milliken, R. Ruhl, and B.Lee, "Status of TMI Solid Oxide Fuel Cell Technology," *1998 Fuel Cell Abstracts*, Palm Springs, CA (1998) p. 125.
- 3.7 EPRI TR-102931, "Applications of Carbonate Fuel Cells to Electric Power Systems," Final Report, prepared by Fluor-Daniel for the Electric Power Research Institute, (1993).
- 3.8 S. Hamakawa et al., *J. Electrochem. Soc.*, **147** (2000) 839.
- 3.9 M. Ihara et al., *J. Electrochem. Soc.*, **146** (1999) 2481.
- 3.10 S. Park, J.M. Vohs, and R.J. Gorte, *Nature*, **404** (2000) 265.
- 3.11 U. Birnbaum, E. Riensche, and U. Stimming, *Proc. Of the 5th International Symp. On Solid Oxide Fuel Cells (SOFC-V)*, PV97-18, Germany, The Electrochemical Society, (1997) p.112.
- 3.12 J.R. Rostrup-Nielsen, "Catalytic Steam Reforming," *Catalysis Science and Technology*, Vol. 5, J.R. Anderson and M. Boudart, editors, Springer-Verlag, New York, NY (1984).
- 3.13 J. Xu, and G.F. Froment, *AIChE J.* **35**, 1 (1989) p. 90.
- 3.14 E.S. Wagner, and G.F. Froment, "Steam Reforming Analyzed," *Hydrocarbon Processing*, July (1992) p.70.
- 3.15 J.J. Hartvigsen, and A.C. Khandkar, "Thermally Integrated Reformer for Solid Oxide Fuel Cells," U.S. Patent Number 5,366,819, U.S. Patent Office, Washington, D.C., November (1994).
- 3.16 J.R. Selman, "Research, Development, and Demonstration of Molten Carbonate Fuel Cell Systems," in *Fuel Cell Systems*, Edited by L.J. M. Blomen, M.N. Mugerwa, Plenum Press, New York, NY (1993) p. 419.
- 3.17 P. Pietrogrande and M. Biezzeccheri, "Fuel Processing," in *Fuel Cell Systems*, L.J. Blomen and M.N. Mugerwa, Editors, Plenum Press, New York (1993).

-
- 3.18 E. Riensche, J. Meusinger, U. Stimming, and G. Unversagt, *J. Power Sources*, **71** (1998) pp. 306-314.
 - 3.19 D. P. Bloomfield, "Hydrocarbon fuel processing for fuel cell power plants," *2000 Fuel Cell Seminar Abstracts*, Portland, Oregon, Oct. 30- Nov. 2 (2000) pp. 329-333.
 - 3.20 J. Meusinger, E. Riensche, U. Stimming, "Reforming of natural gas in solid oxide fuel cell systems," *J. Power Sources*, **71** (1998) pp. 315-320.
 - 3.21 "Multi-fuel Reformers for Fuel Cells Used in Transportation," A.D. Little, Phase 1 Final Report, prepared for the U.S. Department of Energy, DOE/CE/50343-2, May (1994).
 - 3.22 D. Ghosh et al., "Development of low temperature SOFC systems for remote power and home cogen applications," *2000 Fuel Cell Seminar Abstracts*, Portland, OR (2000) pp. 511-514.
 - 3.23 R. Kumar, S. Ahmed, M. Krumpelt, K.M. Myles, "Improved fuel cell system for transportation applications," U.S. Patent 5,248,566 (1993).
 - 3.24 J. Mauzey, R. Woods, S. Barge, "Automotive Fuel Processor," *2000 Fuel Cell Seminar Abstracts*, Portland, Oregon, Oct. 30- Nov. 2 (2000) pp. 534-537.
 - 3.25 A. Docter, G. Konrad, A. Lamm, "Reformer for gasoline and gasoline like fuels," *2000 Fuel Cell Seminar Abstracts*, Portland, Oregon, Oct. 30- Nov. 2 (2000) pp. 538-541.
 - 3.26 J.C. Cross et al., "PEM Fuel Cell Power System Technology," *2000 Fuel Cell Seminar Abstracts*, Portland, Oregon, Oct. 30- Nov. 2 (2000) pp. 260-262.
 - 3.27 J. Ferrall et al., "System design of a combined heat and power PEM plant for building applications," *2000 Fuel Cell Seminar Abstracts*, Portland, Oregon, Oct. 30- Nov. 2 (2000) pp. 401-404.
 - 3.28 G.J. Doell, D.P. Bloomfield, T.N. Tangredi, "Status of fuel cell residential power generator program at Dais –Analytic Corporation," *2000 Fuel Cell Seminar Abstracts*, Portland, Oregon, Oct. 30- Nov. 2 (2000) pp. 487-490.
 - 3.29 U.G. Bossel, *Facts and Figures*, Final report on SOFC data, IEA Programme on Advanced Fuel Cells, Annex II, Swiss Federal Energy Office of Energy, Berne, (1992).
 - 3.30 D.T. Hooie and M.C. Williams, "Overview of Commercialization of Stationary Fuel Cell Power Plants in the United States," *Proceedings of the 30th IECEC*, paper no. EC-254, ASME (1995) p. 172.
 - 3.31 W.R. Dunbar, and N. Lior, "Sources of Combustion Irreversibility," *Comb. Sci. and Tech.*, **103** (1994) pp. 41-61.

-
- 3.32 W.R. Dunbar, N. Lior, and R.A. Gaggioli, "The Exergetic Advantages of Fuel Cell Systems," *Proc. Of the Florence World Energy Research Symp.*, S.S. Stecco and M.J. Moran, editors, Pergamon Press, New York, (1990).
 - 3.33 W.T. Grubb and L.W. Niedrach "Fuel Cells," in *Direct Energy Conversion*, Inter-University Series, G.W. Sutton, editor, McGraw-Hill, New York (1966).
 - 3.34 "Development of the University of Wisconsin's 10 kW Power Inverter for Fuel Cell Applications," Final report for the U.S. Department of Energy 2001 Future Energy Challenge, June (2001).
 - 3.35 O. Ulleberg, "Stand-alone power systems for the future," Ph.D. Thesis, Norwegian University of Science and Technology, Trondheim, Norway (1998).
 - 3.36 E. Achenbach, "Response of a solid oxide fuel cell to load change," *J. Power Sources*, **57** (1995) pp. 105-109.
 - 3.37 E. Riensche, J. Meusinger, U. Stimming, and G. Unversagt, "Optimization of a 200 kW SOFC cogeneration power plant. Part II: variation of the flowsheet," *J. Power Sources*, **71** (1998) pp. 306-314.
 - 3.38 "A system study for a 200 kWe combined heat and power package," prepared by British Gas plc, *ETSU Report FCR-008/010*, March (1994).

Chapter Four Modeling of Solid Oxide Fuel Cells

Modeling of fuel cells can proceed at numerous levels of detail ranging from molecular and electrode levels (nm- μ m scale) to stack and systems levels (cm-m scale). As this project is concerned with systems design and performance, the level of modeling detail required for most system components is limited to overall mass and energy balances and incorporation of component performance characteristics. However, the relative infancy of fuel technology requires that simulation of the fuel cell stack component be driven by a more detailed cell-level model. One-, two-, or three-dimensional cell-level models may be written depending on the requirements of the user. Two- and three-dimensional modeling is typically concerned with cell and stack design issues. Such issues are not a concern of this research effort.

In this chapter, an overview of the approach for modeling of a solid oxide fuel cell with direct internal reforming capability is presented. The associated assumptions and modeling simplifications are then discussed, followed by development of transport balances, boundary conditions, and the necessary gaseous and solid phase property relations. The chapter concludes with a discussion of the numerical solution technique and an evaluation of numerical errors and grid-mesh size. Model validation is presented in Chapter Five.

4.1 The Need for a 1-Dimensional, Cell-level Model

Prediction of both the transient and steady-state performance of the fuel cell is important for (i) control purposes, (ii) establishing that the operating conditions inside the cell, such as solid temperature gradients, during the transient have not endangered cell integrity (or life), (iii) evaluating the cell's ability to follow load transients, and (iv) determining battery storage requirements. Achieving this capability necessitates a cell-level model capable of resolving the spatial distributions during both steady and unsteady conditions (such as load changes or fuel feed flow or composition perturbations.)

In addition to dynamic considerations for a cell-level model, several steady-state justifications can be made. First, steady-state operation away from the design point of the cell (i.e., part-

load) will require maintaining acceptable solid temperatures for both cell integrity and good performance. Knowledge of the spatial temperature distributions throughout the operating range will verify that these conditions are satisfied over the cell. Secondly, one aim of the research is to recommend optimal fuel cell operating conditions. Such a recommendation must be made based on a more accurate description of the physicochemical phenomena taking place at the cell-level to ensure higher precision in cell performance predictions (e.g., in current, power, thermal output), as well as to boost the credibility of the results. Finally, integrating the more detailed physics into the model will yield some flexibility in tuning model parameters to fit different fuel cell designs and published cell current-voltage data.

4.2 General Approach to SOFC Stack Modeling

Figure 4.1 depicts the geometry for a generic planar fuel cell design in which the gases are internally manifolded in a cross-flow configuration. Recall that the two porous, gas diffusion electrodes (anode and cathode) are separated by a dense solid electrolyte layer and each cell is separated by an impermeable bipolar separator plate (or interconnect) which provides the electrical connection between cells and the flow manifolding for the fuel and air gases. Karoliussen et al., [1] summarize the requirements for a mathematical model that describes the physicochemical processes within such a fuel cell. As noted in their work, the set of equations that describes these processes includes the following:

- (1) Charge (or potential) balance for the solid including potential and current distributions.
- (2) Gas phase hydrodynamics in fuel (anode) and air (cathode) gas channels.
- (3) Mass balances for the components in the fuel and air gases.
- (4) As an integral part of the material balances, rate expressions for the chemical and electrochemical reactions occurring at the electrodes and at the electrode-electrolyte interfaces. This includes methane reforming, oxidation of hydrogen (and possibly carbon monoxide) at the anode-electrolyte interface, and reduction of oxygen at the cathode-electrolyte interface.
- (5) Energy balances for the gas and solid phases including convection, conduction, radiation, and heat production by reaction.

- (6) Boundary conditions including compositions, mass fluxes, and temperatures at inlets to stack and heat losses to an external manifold or enclosure by radiation.
- (7) Data bases for reaction kinetics, and physical and thermodynamic properties of the solid cell components as well as the constituents of the reactant and exhaust gas streams as a function of temperature.

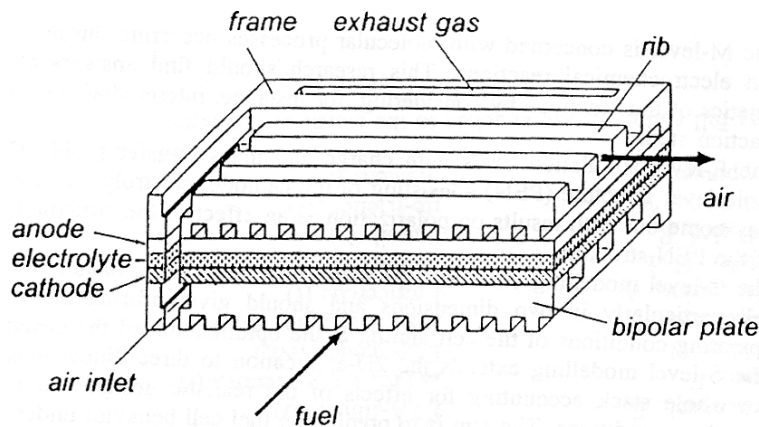


Figure 4.1 Cutaway view of planar cross-flow fuel cell stack [2]

4.3 Model Assumptions

The complexity of modeling the SOFC requires the use of fast computers to solve the finite difference representation of the coupled partial differential equations describing the various transport phenomena within. Although the processors in desktop computers have steadily increased in speed (clock speeds above 2 GHz at the time of this thesis), a rigorous approach to numerical computation of a fine, multi-dimensional finite difference grid for an SOFC stack consisting of scores of cells would be a formidable task even with the use of large main frame computers [1]. Several judicious simplifications can be made that enable a reduction of complexity in the numerical simulation and simultaneously establish a suitable level of modeling detail (and accuracy) required for this project. The assumptions are summarized as:

1. One-dimensional cell representation along the streamwise direction (co- or counter-flow). Uniform temperature and current distribution in other cell dimensions (y, z).

2. Uniform distribution of feed gases to each individual cell in the stack and among the channels in each cell.
3. Each of the gas channels in the unit cell act as continuously stirred tank reactors (CSTR) (i.e., well-mixed at each nodal location in the axial direction, x). The entire cell acts as a plug flow reactor. However, fully developed laminar flow is considered for estimation of transport coefficients.
4. Lumped temperature of the solid cell structure (anode-electrolyte-cathode). Interconnect temperature resolved (i.e., un lumped).
5. Adiabatic boundaries at the cell inlet and outlet (left and right of the computational domain). Heat is exchanged between adjacent top and bottom cells.
6. Electrodes (and current collector) act as isopotential surfaces.
7. Fuel cell operates with 100% current efficiency (i.e., no reactant gas crossover or side reactions).
8. Extrapolation of single cell performance for entire cell-stack.
9. Streamwise radiation in the gas channels is neglected.
10. Area underneath interconnect ribbing is considered 100% electroactive (see Figure 4.1).

The justifications for the above assumptions are now discussed in greater detail.

- (1) *One-dimensional cell representation along the streamwise direction.* The one-dimensional model assumes the reactant gas streams are in parallel with one another. This assumption limits the results to SOFC designs in which the reactant gas streams are in co-flow or counter-flow configurations (i.e., no cross-flow). A cross-flow configuration requires a two-dimensional modeling approach to resolve the solid cell temperature and current distributions. However, the one-dimensional approach is considered sufficient for the purposes of this project as (i) power, voltage, and outlet gas temperature predictions for cross-flow typically fall between co- and counter-flow configuration results [3], and (ii) several SOFC manufacturers are employing co- or counter-flow reactant gas configurations in their cell-stack product development. The assumption of uniform temperature and current distributions in directions perpendicular

to the gas flow in one-dimensional models has been shown to be effective for co-flow and counter-flow SOFC designs by Malandrino and Chindemi [4].

- (2) *Uniform distribution of feed gases to each individual cell in the stack and among the channels in each cell.* A uniform distribution of reactant gases has been assumed as the best case for performance. In practice, non-uniform distributions are known to exist. Achenbach and Reus [5] have shown that these non-uniformities are insignificant in predictions of cell voltage and performance, but can result in under-predictions of about 15% in solid temperature and current density gradients. For the purposes of this project, maldistribution effects will be neglected as the results of this research effort are aimed at characterizing the performance of optimized commercial cell-stack designs.
- (3) *CSTR conditions in the reactant gas channels (i.e., well-mixed at each nodal location in the axial direction, x).* Both heat and mass transfer coefficients are large in the narrow channels. Thus, small temperature and concentration gradients across the channel space result. In fact, the variation in hydrogen concentration across the channel for moderate currents was estimated at only 2% from bulk to surface value. Plug flow conditions for the entire cell can be assumed because the Peclet number for mass transport (a measure of the convective flux over the diffusive flux) in the flow direction in the bipolar SOFC plate design is greater than 50 [4, 6, 7]. However, to estimate convective heat transport coefficients and viscous pressure loss, fully developed laminar flow conditions are also considered as the numerous flow channels in a cell-stack typically result in Reynolds numbers less than 100 [4, 7] and entry lengths for small diameter channels were estimated to be less than 0.5 cm.
- (4) *Lumped temperature of the solid cell structure (anode-electrolyte-cathode).* A lumped temperature assumption for the thin cell structure is logical and is validated by the work of Ackermann et al., [8] who have shown that the cross-plane temperature difference in the heterogeneous cell structure is estimated to be less than 1°C for internally reforming SOFCs.

- (5) *Adiabatic boundaries at the cell inlet and outlet and left and right interconnect walls.* Adiabatic conditions are made at the inlet and outlet faces because the cell is very thin (<3 mm) and little information is available on gas manifold or enclosure temperatures.
- (6) *Electrodes (and current collector) act as isopotential surfaces.* The electrodes have high electronic conductivity and thus, they can be viewed as isopotential [9].
- (7) *Fuel cell operates with 100% current efficiency.* It has been assumed that all hydrogen molecules that are oxidized generate 2 electrons, that is, no side reactions or gas leakage takes place. Again, it is implicit that in an optimized commercial cell design such imperfection would be negligible.
- (8) *Extrapolation of single cell performance for an entire cell-stack.* This assumption is implicit for one- and two-dimensional simplifications of a cell-stack. In general, this linear extrapolation in performance has been carried out by many researchers with reasonable results [10, 11, 12]. The major limitation of the assumption is that a temperature gradient from top to bottom of the cell-stack can occur, which in turn, affects the performance of those cells situated near the top or bottom of the stack.
- (9) *Streamwise radiation in the gas channels is neglected.* This assumption refers to the exchange of heat between interconnect and cell tri-layer at different axial positions along the cell. The primary justification for this assumption lies in the very small radiation configuration factors between up- or downstream opposite wall elements in narrow gas channels. Configuration factors rapidly decrease from a value of 0.86 for directly opposing walls to less than 0.01 just 1 cm down or upstream from that axial position. Appendix I details this justification further. Radiation heat transfer by gas emission is assumed negligible as the gas emittance in the narrow channels for O₂, CO₂, and H₂O components is on the order of 0.01.
- (10) *Area underneath interconnect ribbing is considered 100% electroactive.* It is generally accepted that current generation is reduced in the area beneath the interconnect ribbing. However, the severity of curtailed current production in this region is not known and most modeling efforts neglect any adverse performance due to this effect (e.g., see [3]).

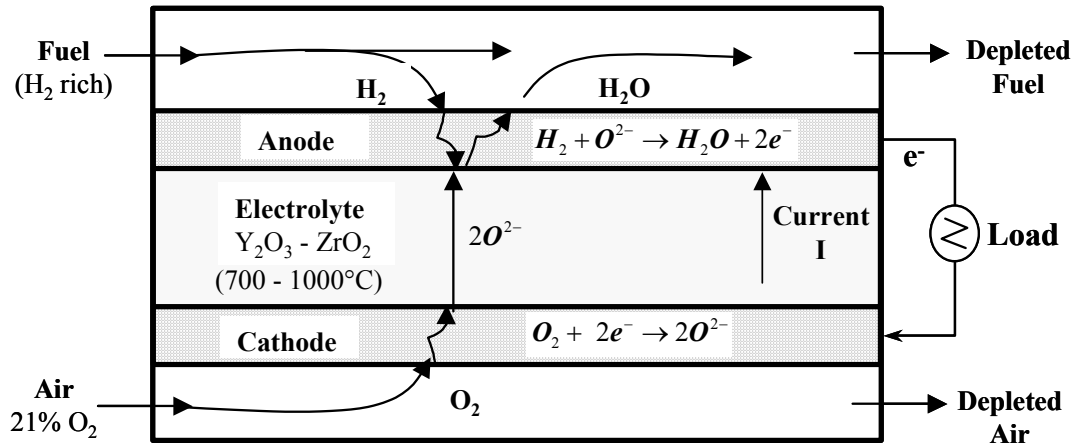


Figure 4.2 Electrochemical Processes within a solid oxide fuel cell

4.4 Electrochemical Model

To begin building an electrochemical model, it is useful to recall the electrochemical processes taking place in the solid oxide fuel cell as illustrated in Figure 4.2. As shown, fuel and air are admitted to the cell separately. Due to the chemical affinity hydrogen and oxygen have for one another, they are drawn towards the electrodes, diffuse through the porous electrode structure to the electrode/electrolyte interface and are adsorbed. At the cathode/electrolyte interface, the oxygen is reduced by incoming electrons to produce oxygen anions which are conducted through the solid electrolyte to the anode/electrolyte interface where they electrochemically combine with adsorbed hydrogen to form water vapor and release the electron charge to the external circuit. Because the potential of the electrons released at the anode is greater than that of the electrons taken up by the oxygen at the cathode, the cell delivers net power as electricity [13]. The electrochemical reactions for the anode and cathode are:



The electrochemical oxidation of carbon monoxide at the anode is also possible via the reaction,



However, this reaction is neglected as carbon monoxide oxidation on SOFC anodes has been shown to be 2-5 times slower than that of hydrogen, making the competing and faster water gas shift reaction the dominant reaction pathway for the consumption of carbon monoxide [14, 15].

The maximum theoretical work for a steady-flow open process is given by the change in molar Gibbs free energy of the process, ΔG . The electrical work done by a fuel cell is given by the amount of charge that flows from the cell multiplied by the driving force that causes it to flow –the potential difference of the cell [16]. Mathematically, this can be expressed as,

$$W_{\max} = -\Delta G = n_e \cdot F \cdot E_N \quad (4.2)$$

where ΔG is the change in molar Gibbs free energy of the process, n_e is the number of moles of electrons transferred in the overall reaction (2 for hydrogen), F , is the Faraday constant, and E_N is the Nernst potential. The product ' $n_e F$ ' is the amount of charge transferred during the overall reaction. In order for Equation (4.2) to hold true, E_N must be the reversible cell potential. Thus, the Nernst potential represents the maximum (reversible) potential difference between the two electrodes and it is a good estimate of the open circuit voltage. The Nernst potential can be expressed as the difference between the reactant and product chemical potentials of ideal gas streams,

$$E_N = \frac{1}{n_e F} \cdot \left\{ \sum_{\text{reactants}} n_i \cdot [\mu_i^{\circ} + R_u \cdot T \cdot \ln(p_i)] - \sum_{\text{products}} n_j \cdot [\mu_j^{\circ} + R_u \cdot T \cdot \ln(p_j)] \right\} \quad (4.3)$$

where μ_i° is the chemical potential of species i at atmospheric pressure, T is the absolute temperature of the gas, p_i is the species partial pressure, R_u is the universal gas constant and n_i and n_j are the number of moles of species reactant i and product j . Introducing the standard Gibbs free energy, ΔG° , and the stoichiometric coefficients of the reaction, the following relation can be developed after some manipulation,

$$E_N = -\frac{\Delta G^o}{n_e F} - \frac{R_u T}{n_e F} \cdot \ln \prod_i \left(\frac{p_i}{p^o} \right)^{v_i} \quad (4.4)$$

where v_i are the stoichiometric coefficients of the reaction and p^o is the standard reference pressure of 1 atm. The solid oxide fuel cell reaction is based on the oxidation of hydrogen by oxygen anions and thus, Equation (4.4) can be written as,

$$E_N = -\frac{\Delta G^o}{n_e F} - \frac{R_u T}{n_e F} \cdot \ln \left[\frac{p_{H_2O}}{p_{H_2} \cdot (p_{O_2})^{\frac{1}{2}}} \right] \quad (4.5)$$

It should be noted that Equation (4.5) is a measure of the driving force for the generation of current in a cell and it is sensitive to cell temperature, hydrogen and water concentration in the fuel gas (anode), and oxygen concentration in the cathode. The effect of the logarithmic term in the partial pressures is to gauge the change in potential because of changes in reactant (or product) concentration [17]. The magnitude of this term is called the *Nernstian loss*. The Nernst potential given by Equation (4.5) is a good estimate of the open circuit voltage (OCV) of the cell. In practice, however, the measured OCV can be slightly lower than the Nernst potential due to mixed potential formation and other parasitic processes [18].

4.4.1 Charge (or Potential) Balance

In practice, when current is drawn, the fuel cell operates at voltages below that of the Nernst potential due to irreversible losses (polarizations) associated with charge transfer ('activation'), mass transfer ('concentration'), and ohmic resistance from current flow through materials with finite conductivity. Activation and concentration polarizations occur at each electrode and ohmic losses occurs due to both electronic and ionic conduction of current through cell components. The cell voltage can then be expressed by a potential balance which includes the reduction of the Nernst voltage by these losses,

$$V_{cell} = E_N - \sum \eta_{act} - \sum \eta_{conc} - i \cdot R_{cell}(T_s) \quad (4.6)$$

where η is the voltage loss associated with activation or concentration polarizations at each electrode, i is the current, and R_{cell} is the overall cell resistance which includes electronic and ionic resistances, as well as the resistance across mating component interfaces, and is evaluated at the solid cell temperature, T_s . Activation losses occur at all current densities but are dominant at low current density and are associated with sluggish electrode reaction kinetics at the three-phase interface (i.e., they can be viewed as a resistance to initiating the electrode reactions). The high operating temperature of the SOFC promotes rapid chemical kinetics on the nickel cermet anode and as a result, the activation energy loss can be small relative to other voltage losses [19].

Ohmic losses that arise from resistances to charge conduction through the various cell components demonstrate a linear dependence with current. Ohmic loss due to *electronic* conduction of current occurs in electrodes and interconnect (typically small), and across component interfaces (large). Ohmic loss also occurs due to *ionic* conduction of oxygen anions through the solid electrolyte. The majority of the ohmic losses (80% of the total) associated with charge conduction (i.e., both electronic and ionic) through cell components is determined by the ionic resistance of the yttria-stabilized zirconia (YSZ) electrolyte. The ionic conductivity of the YSZ increases exponentially with increasing cell temperature. In general, the two largest contributors of ohmic resistance in the cell are (i) the ionic resistance of the electrolyte and (ii) the electronic resistance across the electrode-interconnect interfaces. The distribution of loss between these two sources varies depending on the design of the cell.

Lastly, concentration polarization is a resistance to the diffusional transport of reactants to and from the electrochemical reaction sites. Like activation losses, concentration losses occur over the entire operating range of the cell but the contribution to the total loss is most significant at high current density operating points. When operating the fuel cell in this regime, the cell is essentially “starved” of reactants as they cannot be supplied at the rate at which the electrode reactions demand. In general, activation and concentration losses are functions of both temperature and current and are highly nonlinear. In contrast to the thinner electrolyte-supported SOFC designs, the magnitude of the concentration polarization in anode-supported SOFCs can be larger due to the increase in mass transfer resistance in the

thick anode supports. Additionally, significant concentration losses at *low* current densities may also be present in these designs [20, 21, 22].

For anode-supported SOFCs, Kim et al., [20] suggest the following form of the V-I characteristic,

$$V(i) = E_N(T, p_j) - \underbrace{i \cdot R_{cell}(T_s)}_{\text{ohmic polarization}} - \underbrace{[a + b \ln(i)]}_{\text{activation polarization}} + \underbrace{\frac{R_u T_s}{2F} \cdot \left[\frac{1}{2} \ln \left(1 - \frac{i}{i_{cs}} \right) + \ln \left(1 - \frac{i}{i_{as}} \right) - \ln \left(1 + \frac{p_{H_2}^o \cdot i}{p_{H_2O}^o \cdot i_{as}} \right) \right]}_{\text{concentration polarization}} \quad (4.7)$$

where,

$$\begin{aligned} R_{cell} &= R_a + R_{el}(T_s) + R_c + R_l + R_{ic} \\ a &\approx -\frac{RT_s}{4\alpha F} \ln(i_o) \quad \text{and} \quad b \approx \frac{RT_s}{4\alpha F} \\ i_{cs} &= \frac{2n_e F}{RT_s} \cdot \frac{p_{O_2}^o D_{eff,c}}{l_c} \quad \text{and} \quad i_{as} = \frac{n_e F}{RT_s} \cdot \frac{p_{H_2}^o D_{eff,a}}{l_a} \\ D_{eff,c} &= \frac{V_{v,c} D_{O_2-N_2}}{\tau_c} \quad \text{and} \quad D_{eff,a} = \frac{V_{v,a} D_{H_2-H_2O}}{\tau_a} \end{aligned}$$

and,

E_N = Nernst potential, $f(x)$	α = electrochemical transfer coefficient
i = cell current density, $f(x)$	$D_{H_2-H_2O}$ = Binary diffusivity of H_2-H_2O
R_{cell} = total cell resistance	$D_{O_2-N_2}$ = Binary diffusivity of O_2-N_2
a, b = Tafel parameters	τ_c, τ_a = electrode tortuosity
i_{cs}, i_{as} = limiting current density at electrode	$V_{v,c}, V_{v,a}$ = electrode porosity
i_o = effective electrode exchange current density	l_c, l_a = electrode thickness
$D_{eff,c}$ = effective O_2-N_2 diffusion coefficient at cathode	
$D_{eff,a}$ = effective H_2-H_2O diffusion coefficient at anode	
p_j^o = partial pressure of species j in the bulk gas	

The second term on the right hand side of (4.7) is the ohmic polarization. The overall cell resistance, R_{cell} , is comprised of the sum of charge resistances at the anode, electrolyte, cathode, interconnect, and the component contact resistance, R_a , R_{el} , R_c , R_l , and R_{ic} , respectively. The third term is the activation polarization as represented by the Tafel relation.

The Tafel relation is an approximate estimate of the activation polarization which is made by determining the slope of the cell voltage-current characteristic at the condition of zero current [23]. Here it is used to describe sluggish reaction kinetics in the low current region [21]. The last term in (4.7) represents the voltage loss due to concentration polarization which is a function of current, temperature, and the electrode limiting current densities, i_{cs} and i_{as} . The electrode limiting current density is dependent on microstructural characteristics of the electrode, such as porosity, tortuosity, and effective diffusivity of the reacting species, as well as operating temperature. More specifically, i_{cs} is the cathode limiting current density which results when the partial pressure of oxygen at the cathode-electrolyte interface is nearly zero. Similarly, i_{as} is the anode limiting current density which results when the partial pressure of hydrogen at the anode-electrolyte interface is nearly zero. The relative magnitude of each of the terms in Equation (4.7) depends on many factors, but will typically vary with current. Thus, at low current, the activation loss usually dominates (third term), and at intermediate currents the ohmic loss term is dominant, and finally, at high currents the concentration term is largest.

For anode-supported SOFCs, $i_c \ll i_a$ and thus, $i_{cs} \gg i_{as}$. As a result, Equation (4.7) is not very sensitive to the choice of i_{cs} . Equation (4.7) can then be rewritten as,

$$V(i) = E_N(T, p_j) - \underbrace{i \cdot R_{cell}(T_s)}_{\text{ohmic polarization}} - \underbrace{[a + b \ln(i)]}_{\text{activation polarization}} + \underbrace{\frac{R_u T_s}{2F} \cdot \left[\ln \left(1 - \frac{i}{i_{as}} \right) - \ln \left(1 + \frac{P_{H_2}^o \cdot i}{P_{H_2O}^o \cdot i_{as}} \right) \right]}_{\text{concentration polarization}} \quad (4.8)$$

To use Equation (4.8) it is necessary to fit 4 parameters to experimental data: R_{cell} , i_{as} , a , and b . The advantage of this V-I representation is that these 4 parameters are physically meaningful. However, while Equation (4.8) is adequate for H₂-H₂O fueled SOFCs, the effective diffusion coefficient, $D_{eff,a}$, in the i_{as} term must be modified for H₂-H₂O-CO-CO₂ fueled systems.

It is often convenient to neglect the last two terms in Equation (4.8) because the fuel cell is expected to operate in the linear region where ohmic losses dominate. For this case, the potential balance then simplifies to,

$$V_{cell} = E_N - i \cdot R_{cell}(T_s) \quad (4.9)$$

The temperature sensitivity of the cell resistance in Equation (4.9) is obtained through either experimental data for a specific cell design, or through ionic conductivity data for zirconia electrolytes and estimates of the contact resistance. The temperature dependence of zirconia-based electrolytes given by Bossel [24] is employed for model verification in the IEA benchmark tests discussed in §4.7 and a plot of the function can be found in Appendix 1.

The cell power can be determined by multiplying the cell voltage by the cell current to get

$$P_{cell} = V_{cell} i \quad (4.10)$$

or using the current density, j (A/cm²) the cell power may be expressed as,

$$P_{cell} = V_{cell} \cdot j \cdot A_e \quad (4.11)$$

where A_e is the electroactive cell area. Note that the power generated in each individual discretized element will vary with position and thus, the total cell power is then determined by summing the contributions from all computational elements.

4.5 Thermochemical Model

Simulation of the physicochemical processes at the cell-level generally requires a heterogeneous model as in practice the air and fuel streams in cell-stacks are not allowed to mix. Furthermore, the cell potential is dependent on the fuel composition in the anode which varies with axial position. Therefore, determination of the reactant flows, variation in gas composition, and fuel and air circuit pressure rises is accomplished by making separate balances on gaseous (fuel and air) and solid (cell and interconnect) phases in the cell.

The geometry for co-flow and counter-flow configurations of a single cell is shown in Figure 4.3. The following sub-sections develop the material, energy, and momentum balances for the one-dimensional geometry as well as present a summary of the relevant boundary conditions and property data. Discretization of the cell into computational slice elements of length Δx is used to formulate each of the balances presented in §4.5.

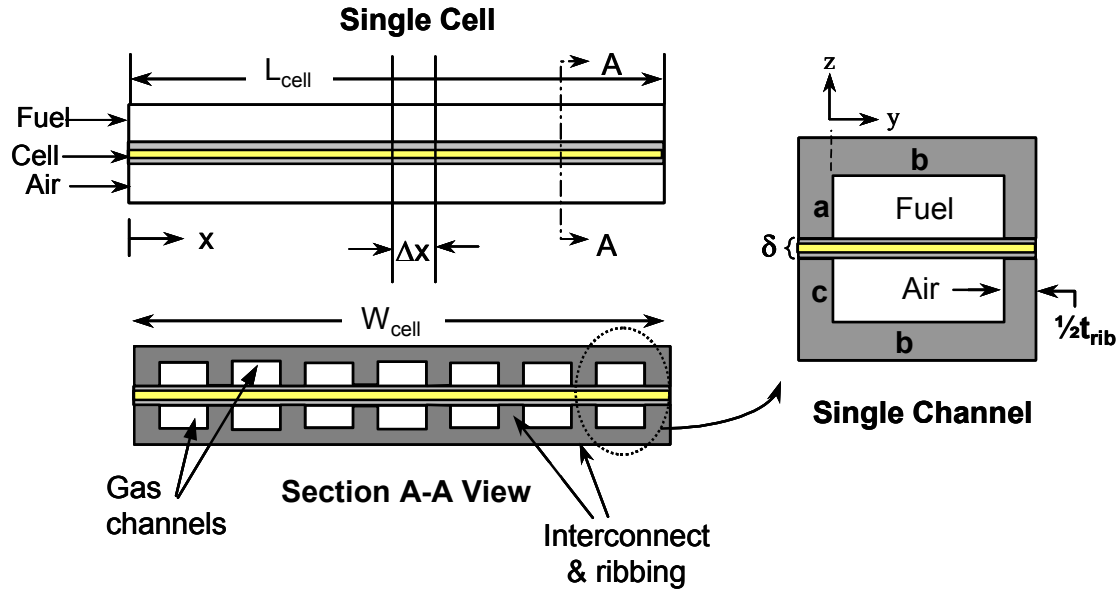


Figure 4.3 Cell geometry for co- and counter-flow configurations

4.5.1. Material Balances

The material balances for fuel and air channels take into account the flow-rate variations due to the electrochemical reactions and the mass transfer of oxygen from the cathode side of the cell to the anode side. For any slice of cell, the mass balance of species j can be written as,

$$\frac{\Delta(c_i \cdot ab\Delta x)}{\Delta t} = (\dot{n}_i''|_x - \dot{n}_i''|_{x+\Delta x}) \cdot ab + \dot{R}_i \cdot ab\Delta x \quad (4.12)$$

where c_i is the molar concentration of species i , a is the fuel channel height, b is the channel width, \dot{n}_i'' is the molar flux of species i normal to the yz -inlet plane, and $\dot{R}_i (=v_{ij}\dot{r}_j''')$ is the volumetric production of species i by chemical reaction j . Dividing by the volume element $ab\Delta x$ and taking the limit as Δx and Δt go to zero results in,

$$\frac{dc_i}{dt} = -\frac{d\dot{n}_i''}{dx} + \sum_j v_{ij}\dot{r}_j''' \quad (4.13)$$

where v_{ij} is the stoichiometric coefficient of species i for reaction j (negative for reactants, positive for products) and \dot{r}_j''' is the volumetric reaction rate of reaction j . Equation (4.13) states that the change in molar concentration of species i with time is due to the change in

convective flux of species i with x and the production/consumption of species i due to each chemical reaction j .

Hydrogen may be produced from the endothermic conversion of methane and water, and from the mildly exothermic shift of carbon monoxide. In a *direct* internal reforming solid oxide fuel cell, methane and water vapor in the fuel gas are adsorbed onto the thick nickel-based anode and combine to produce hydrogen. Additional hydrogen is produced when carbon monoxide, in the presence of water vapor, is catalytically shifted to carbon dioxide. The consumption of hydrogen is carried out by the deionization reaction at the anode/electrolyte interface. The three reactions of interest are then,

Name	Reaction	ΔH_{298} (kJ/mol)	Equation
<i>Methane reforming</i>	$CH_4 + H_2O \leftrightarrow CO + 3H_2$	206.1	(4.14)
<i>Water-gas shift</i>	$CO + H_2O \leftrightarrow CO_2 + H_2$	-41.15	(4.15)
<i>H₂ oxidation</i>	$H_2 + \frac{1}{2} O_2 \rightarrow H_2O$	-241.8	(4.16)

As Equations (4.14-4.16) show, the fuel gas composition in the anode compartment changes due to: (i) steam methane reforming, (ii) water-gas shift, and (iii) the electrochemical oxidation of hydrogen. In the cathode gas channel, the oxidant composition changes only due to the electrochemical reduction of oxygen (Equation 4.1(b)). Bookkeeping of changes in H₂, O₂, and H₂O concentration due to electrochemical reactions is performed by using the overall reaction in Equation (4.16). Due to the enhanced activity of the anode at the high cell operating temperature, rapid water-gas shift reaction kinetics are achieved along the cell length and an equilibrium assumption can be employed for reaction (4.15).

With Equations (4.14-4.16), Equation (4.13) may be re-written at steady-state as,

$$\frac{dn_i''}{dx} = \nu_{i,R} \dot{r}_R''' + \nu_{i,E} \dot{r}_E''' + \Delta \dot{n}_{i,wgs}''' \quad (4.17)$$

where $\nu_{i,R}$ is the stoichiometric coefficient of species i for the methane reforming reaction, \dot{r}_R''' is the volumetric rate of the methane reforming reaction, $\nu_{i,E}$ is the stoichiometric coefficient

of species i for the electrochemical oxidation reaction, \dot{r}_E''' is the volumetric rate of the electrochemical oxidation of hydrogen, and $\Delta\dot{n}_{i,wgs}'''$ is the volumetric change in molar flow of hydrogen due to the *equilibrium* water-gas shift reaction. The change in molar flow of a species due to the water-gas shift reaction may be either positive or negative depending on the direction of the reaction. Using Equation (4.17) one may write the species balance for hydrogen, for example, as,

$$\frac{d\dot{n}_{H_2}''}{dx} = 3\dot{r}_R''' - \dot{r}_E''' + \Delta\dot{n}_{H_2,wgs}'''$$

It should be noted that careful evaluation of the flow and reaction areas for the flux terms in Equation (4.17) is needed. However, since the channel walls are neglected for mass transfer (by virtue of assumption 10 in §4.3), any area ratio to account for axial mass convection versus mass flow normal to the electrode surface due to chemical reactions is equal to one. A general finite-difference representation of Equation (4.17) is made by multiplying the equation by the appropriate reaction and flow areas and integrating with respect to x to yield,

$$\dot{n}_i|_{x+\Delta x} = \dot{n}_i|_x + \left[v_{i,R} \dot{r}_R + v_{i,E} \dot{r}_E + \Delta\dot{n}_{i,wgs} \right]_{x+\Delta x} \quad (4.18)$$

Using (4.18) for each of the components in the fuel gas the following equations are written,

$$\text{Fuel} \quad \left\{ \begin{array}{l} \dot{n}_{H_2}|_{x+\Delta x} = \dot{n}_{H_2}|_x + \left[3\dot{r}_R - \dot{r}_E + \Delta\dot{n}_{H_2,wgs} \right]_{x+\Delta x} \\ \dot{n}_{H_2O}|_{x+\Delta x} = \dot{n}_{H_2O}|_x + \left[-\dot{r}_R + \dot{r}_E + \Delta\dot{n}_{H_2O,wgs} \right]_{x+\Delta x} \\ \dot{n}_{CO}|_{x+\Delta x} = \dot{n}_{CO}|_x + \left[\dot{r}_R + \Delta\dot{n}_{CO,wgs} \right]_{x+\Delta x} \\ \dot{n}_{CO_2}|_{x+\Delta x} = \dot{n}_{CO_2}|_x + \Delta\dot{n}_{CO_2,wgs}|_{x+\Delta x} \\ \dot{n}_{CH_4}|_{x+\Delta x} = \dot{n}_{CH_4}|_x - \dot{r}_R|_{x+\Delta x} \end{array} \right. \quad (4.19)$$

$$\text{Air} \quad \left\{ \begin{array}{l} \dot{n}_{O_2}|_{x+\Delta x} = \dot{n}_{O_2}|_x - \left[\frac{1}{2} \dot{r}_E \right]_{x+\Delta x} \\ \dot{n}_{N_2}|_{x+\Delta x} = \dot{n}_{N_2}|_x \end{array} \right.$$

The reaction rate \dot{r}_E for the electrochemical oxidation of hydrogen can be calculated on the basis of Faraday's law,

$$\dot{i}_E = \left(\frac{\nu_{i,E} \cdot j(x)}{n_e \cdot F} \right) \cdot A_{slice} \quad (4.20)$$

where $\nu_{i,E}$ is the stoichiometric factor of the electrochemical reacting component, $j(x)$ is the local current density, and A_{slice} is the electrochemical reaction area of the discretized element which is equal to $(b+t_{rib})\Delta x$ (see Figure 4.3). Thus it is apparent from Equation (4.20) that the local rate of hydrogen oxidation (and oxygen reduction) is directly proportional to the local current density. Furthermore, one can see that the rate of hydrogen oxidation in a cell-stack is then *controlled* by the load on the fuel cell. The reaction rate, \dot{i}_R , for methane reforming over nickel-cermet* anodes has been studied by several researchers [25, 26, 27, 28]. The rate expression from Achenbach and Riensche [26] is employed herein and is expressed as,

$$\dot{i}_R = k_0 p_{CH_4} f_e \exp\left(\frac{-E_A}{R_u T_s(x)}\right) \cdot A_{rx} \quad (4.21)$$

where the pre-exponential factor k_0 is 4274 mol/s-m²-bar, p_{CH_4} is the methane partial pressure in the bulk gas[†], the equilibrium factor f_e is approximated as 1, the activation energy, E_A , is estimated at 82 kJ/mol, and A_{rx} is the reforming reaction surface area of the discretized element which is equal to A_{slice} in this expression. As Equation (4.21) indicates, the rate of reaction will vary locally with the cell temperature and is first order with respect to methane partial pressure. Finally, the water-gas shift reaction is taken into account by employing the equilibrium constant at each axial position as follows,

$$K_x = \frac{\dot{n}_{H_2,x} \dot{n}_{CO,x}}{\dot{n}_{CH_4,x} \dot{n}_{H_2O,x}} \quad (4.22)$$

$$\ln(K_x) = \frac{-\Delta G_{wgs,x}^o}{R_u T_{s,x}}$$

* A *cermet* is the combination of ceramic and metallic materials.

[†] The rate expression given by Achenbach and Riensche is dependent upon a specific anode material and calls for the use of the methane partial pressure at the wall. However, investigation of the sensitivity of bulk versus wall concentration in Equation (4.21) revealed that usage of the bulk value is acceptable. The detailed analysis of the effect of bulk versus wall gas concentration on reforming reaction rate and the predicted cell performance results can be found in Appendix I.

where K_x is the equilibrium constant and $\Delta G_{\text{wgs},x}^o$ is the change in standard state Gibbs' free energy for the reaction, and $T_{s,x}$ is the solid cell temperature at location x .

Atom balances on carbon, hydrogen, and oxygen for the anode are the final step in completing mass accounting*. For each element, atom balances are made based on gas species that physically cross the anode compartment system boundary. These equations are written below. The set of equations (4.19-4.25) comprises all of the needed balances to model mass transfer in the cell.

$$C: \underbrace{\dot{n}_{CH_4}|_x + \dot{n}_{CO}|_x + \dot{n}_{CO_2}|_x}_{\text{carbon entering node}} + \underbrace{\left(\dot{n}_{CH_4,ref}|_{x+\Delta x} + \dot{n}_{CO,ref}|_{x+\Delta x} \right)}_{\text{carbon entering/exiting due to reforming}} = \underbrace{\dot{n}_{CH_4}|_{x+\Delta x} + \dot{n}_{CO}|_{x+\Delta x} + \dot{n}_{CO_2}|_{x+\Delta x}}_{\text{carbon exiting node}} \quad (4.23)$$

$$H_2: \underbrace{2\dot{n}_{CH_4}|_x + \dot{n}_{H_2}|_x + \dot{n}_{H_2O}|_x}_{\text{diatomic hydrogen entering node}} + \underbrace{\left(2\dot{n}_{CH_4,ref}|_{x+\Delta x} + \dot{n}_{H_2O,ref}|_{x+\Delta x} + \dot{n}_{H_2,ref}|_{x+\Delta x} \right)}_{\text{hydrogen entering/exiting due to reforming}} \\ + \underbrace{\left(\dot{n}_{H_2,e}|_{x+\Delta x} + \dot{n}_{H_2O,e}|_{x+\Delta x} \right)}_{\text{hydrogen entering/exiting via fuel cell reaction}} = \underbrace{2\dot{n}_{CH_4}|_{x+\Delta x} + \dot{n}_{H_2}|_{x+\Delta x} + \dot{n}_{H_2O}|_{x+\Delta x}}_{\text{hydrogen exiting node}} \quad (4.24)$$

$$O: \underbrace{\dot{n}_{CO}|_x + 2\dot{n}_{CO_2}|_x + \dot{n}_{H_2O}|_x}_{\text{oxygen entering node}} + \underbrace{\left(\dot{n}_{H_2O,ref}|_{x+\Delta x} + \dot{n}_{CO,ref}|_{x+\Delta x} \right)}_{\text{oxygen entering/exiting due to reforming}} + \underbrace{\left(\dot{n}_{H_2O,e}|_{x+\Delta x} \right)}_{\text{oxygen change due to fuel cell reaction}} \\ = \underbrace{\dot{n}_{CO}|_{x+\Delta x} + 2\dot{n}_{CO_2}|_{x+\Delta x} + \dot{n}_{H_2O}|_{x+\Delta x}}_{\text{oxygen exiting node}} \quad (4.25)$$

4.5.2. Energy Balances

Figure 4.4 depicts the energy flows in an axial slice of a single cell. The general form of the energy balance equation for a control volume is,

$$\frac{\Delta E_{cv}}{\Delta t} = \dot{Q}_{cv} - \dot{W}_{cv} + \sum_i \dot{n}_i h_i \Big|_{in} - \sum_i \dot{n}_i h_i \Big|_{out}$$

Tracking of the energy flows in the cell proceeds by making separate energy balances in the gaseous fuel channel, solid cell, air and fuel interconnects, and gaseous oxidant (air) channel.

* Alternatively, one could write $\Delta \dot{n}_{CO,wgs} = \Delta \dot{n}_{H_2O,wgs} = -\Delta \dot{n}_{H_2,wgs} = -\Delta \dot{n}_{CO_2,wgs}$ for Eqns. (4.23-4.25).

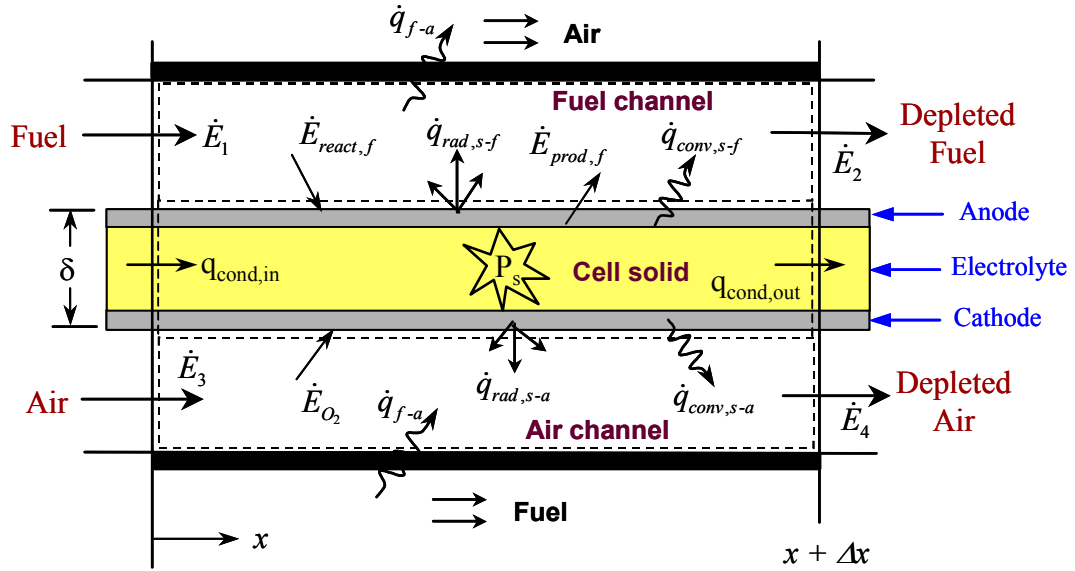


Figure 4.4 Axial slice of a cell displaying the energy flows.

4.5.2.1 Fuel gas (anode compartment) energy balance

The time varying, one-dimensional energy balance for an axial slice in the fuel channel can be written as,

$$\frac{\Delta E_{fuel}}{\Delta t} = \dot{E}_1 - \dot{E}_2 + \dot{E}_{prod,f} - \dot{E}_{react,f} + \dot{q}_{conv,s-f}'' A_{s-f} - \dot{q}_{f-a}'' A_{f-a} \quad (4.26)$$

where \dot{E}_1 and \dot{E}_2 are the rates of energy transfer accompanying the fuel mass flow into and out of the element, $\dot{E}_{prod,f}$ and $\dot{E}_{react,f}$ is the energy accompanying mass transfer of reaction products (H_2 , H_2O , CO) and reactants (CH_4 , H_2O , H_2), respectively, between bulk gases and the porous anode, $\dot{q}_{conv,s-f}''$ is the convective heat flux from the solid cell to the fuel gas in the anode channel, and \dot{q}_{f-a}'' is the heat flux across the interconnect between fuel and air gases. The time dependence (or storage) of the energy in the anode fuel channel can be neglected as the thermal capacitance of the fuel gas is small relative to that of the solid cell components.

Dropping the time-dependent term and using the component molar enthalpies, the steady-state differential equation form of Equation (4.26) can be developed by applying shell balances on the volume element $ab\Delta x$,

$$\begin{aligned}
0 = & \underbrace{ab \sum_i \dot{n}_i'' \bar{h}_i}_{\dot{E}_1} \Big|_x - \underbrace{ab \sum_i \dot{n}_i'' \bar{h}_i}_{\dot{E}_2} \Big|_{x+\Delta x} + \underbrace{b \Delta x \sum_i (\dot{n}_i'' \bar{h}_i(T_s))}_{\dot{E}_p} \Big|_{x+\Delta x} - \underbrace{b \Delta x \sum_i (\dot{n}_i'' \bar{h}_i(T_f))}_{\dot{E}_R} \Big|_{x+\Delta x} \\
& + \underbrace{h_f A_{s-f} (T_s - T_f)}_{\dot{q}_{conv,s-f}} + \underbrace{U_{tot} (T_f - T_a)}_{\dot{q}_{f-a}}
\end{aligned} \quad (4.27)$$

where the channel heat transfer area for four walls, $A_{s-f} = 2(a+b)\Delta x$, is used, $\bar{h}_i(T)$ is the molar enthalpy of component i evaluated at the temperature of interest, h_f is the convective heat transfer coefficient between solid cell and anode fuel gas, and U_{tot} is the overall heat transfer coefficient between air and fuel streams across the interconnect. U_{tot} is related by summing the heat transfer resistances,

$$U_{tot} = \frac{1}{1/h_f A_{s-f} + 1/k_s S + 1/h_a A_{s-f}}$$

where the relation for U_{tot} must include a shape factor, S , in the conduction resistance due to the 2-D interconnect geometry. The shape factor for the channel geometry is estimated by empirical means (see Appendix 1). Dividing Equation (4.27) by the gas slice volume, $ab\Delta x$, and taking the limit as $\Delta x \rightarrow 0$ it becomes,

$$\begin{aligned}
\underbrace{\sum_i \frac{d}{dx} (\dot{n}_i'' \bar{h}_i)}_{\text{change in fuel energy}} = & \frac{1}{a} \left[\underbrace{\sum_i (\dot{n}_i'' \bar{h}_i(T_s)) - \sum_i (\dot{n}_i'' \bar{h}_i(T_f))}_{\text{net energy addition by mass transfer}} \right] + \underbrace{2h_f \frac{(a+b)}{ab} (T_s - T_f)}_{\text{solid-to-gas convection}} + \underbrace{\frac{U_{tot}}{ab\Delta x} (T_a - T_f)}_{\text{convection across interconnect}}
\end{aligned} \quad (4.28)$$

where \dot{n}_i'' is the molar flux of species i , T_f is the bulk average fuel temperature, T_s is the solid cell temperature, h_f is the convective heat transfer coefficient between cell. Equation (4.28) states that the change in energy of the fuel gas is equal to the net energy added by mass transfer between the cell and bulk fuel gas plus the heat addition by convection between solid surfaces and the fuel gas, and the net heat exchange between air and fuel gases across the interconnect.

4.5.2.2 Air gas (cathode compartment) energy balance

The cathode gas energy balance can be written in a similar fashion to that of the fuel gas,

$$\frac{\Delta E_{air}}{\Delta t} = \dot{E}_3 - \dot{E}_4 - \dot{E}_{O_2} + q''_{conv,s-a} A_{s-a} + q''_{f-a} A_{f-a} \quad (4.29)$$

where \dot{E}_{O_2} is the rate of energy accompanying mass transfer of oxygen out of the bulk to the cathode solid. To generate a *steady-state* differential equation form of (4.29) a shell balance is applied to the slice,

$$0 = \left(\sum_i \dot{n}_i'' \bar{h}_i \Big|_x - \sum_i \dot{n}_i'' \bar{h}_i \Big|_{x+\Delta x} \right) \cdot bc - \left(\dot{n}_{O_2}'' \bar{h}_{O_2} \Big|_{x+\Delta x} \right) \cdot b\Delta x + h_a A_{s-a} (T_s - T_a) + U_{tot} (T_f - T_a) \quad (4.30)$$

where \bar{h}_{O_2} is the molar enthalpy of oxygen, T_a is the bulk average air temperature, c is the cathode channel height, and h_a is the convective heat transfer coefficient between solid cell and bulk cathode air flow. Dividing Equation (4.30) by the gas volume $bc\Delta x$ and taking the limit as $\Delta x \rightarrow 0$ we have,

$$\underbrace{\sum_i \frac{d}{dx} (\dot{n}_i'' \bar{h}_i)}_{\text{change in air energy}} = \underbrace{-\dot{n}_{O_2}'' \cdot \left[\frac{\bar{h}_{O_2}}{c} \right]}_{\text{net energy added by oxygen transport}} + \underbrace{\frac{2h_a(b+c)}{bc} (T_s - T_a)}_{\text{solid-to-air convection}} + \underbrace{\frac{U_{tot}}{ac\Delta x} (T_f - T_a)}_{\text{air-to-fuel convection}} \quad (4.31)$$

Equation (4.31) states that the change in energy of the cathode gas flow with spatial position is due to the energy transfer accompanying the flow of oxygen out of the bulk air to the cathode layer, the convective heat transfer from the cell solid to the air, and the net heat exchange between fuel and air streams across the interconnect.

4.5.2.3 Solid cell energy balance (anode-electrolyte-cathode layer)

The solid cell unsteady energy balance is also written for a slice element as,

$$\frac{\Delta E_{cell}}{\Delta t} = \dot{Q}_{cv} + \left[\dot{E}_{react,f} + \dot{E}_{O_2} - \dot{E}_{prod,f} \right]_{x+\Delta x} - P''_{cell} \cdot b\delta\Delta x \quad (4.32)$$

where the first term on the right hand side is the net energy transferred to the cell by heat transfer (via conduction, convection, and radiation), the second term is the net energy addition by the convective flux of reacting species to the solid cell and subsequent release of their respective reaction enthalpies, and P''_{cell} is the volumetric electrical energy generated in the

solid cell layers due to electrochemical oxidation of hydrogen. The net heat transferred to the cell can be expressed in terms of each flux mechanism,

$$\dot{Q}_{cv} = (q''_{cond,x} - q''_{cond,x+\Delta x})b\delta - (q''_{conv,f} + q''_{conv,a}) \cdot b\Delta x + (q''_{rad,s-ief} + q''_{rad,s-ica}) \cdot b\Delta x \quad (4.32a)$$

where the first term accounts for the net energy transferred into the cell element by conduction, the second term includes heat transferred to the fuel and air gases by convection, and the last term accounts for the net cross-channel radiation between cell solid and air- and fuel-side interconnect surfaces. The cross-channel radiation heat transfer at a given axial position is determined by approximating the fuel and air channels as a two-dimensional, 2 surface enclosure which contain diffuse, gray surfaces. In this case, the net radiation exchange between interconnect (fuel- or air-side) and solid cell surfaces may be expressed as,

$$q_{rad,s-ic} = \frac{\sigma(T_s^4 - T_{ic}^4)}{\frac{1 - \varepsilon_s}{\varepsilon_s A_s} + \frac{1}{A_s F_{s-ic}} + \frac{1 - \varepsilon_{ic}}{\varepsilon_{ic} A_{ic}}} \quad (4.32b)$$

where ε is the surface emissivity, T_{ic} is the interconnect temperature, A_s and A_{ic} are the heat exchange surface areas, and F_{s-ic} is the view factor between cell solid and interconnect [29].

The second term in Equation (4.32) accounts for the cell heat generation and can be expressed in terms of the rate of energy transfers due to the oxidation of hydrogen and steam reforming of methane as,

$$\begin{aligned} \dot{E}_{react,f} + \dot{E}_{O_2} - \dot{E}_{prod,f} = & \left(\dot{n}_{H_2,e} \bar{h}_{H_2}(T_f) + \dot{n}_{O_2,e} \bar{h}_{H_2}(T_a) - \dot{n}_{H_2O,e} \bar{h}_{H_2O}(T_s) \right) \\ & + \left(\dot{n}_{CH_4,ref} \bar{h}_{CH_4}(T_f) + \dot{n}_{H_2O,ref} \bar{h}_{H_2O}(T_f) - \dot{n}_{H_2,ref} \bar{h}_{H_2}(T_s) - \dot{n}_{CO,ref} \bar{h}_{CO}(T_s) \right) \end{aligned}$$

Rewriting this equation in terms of reaction rates yields,

$$\begin{aligned}
\dot{E}_{react,f} + \dot{E}_{O_2} - \dot{E}_{prod,f} &= \left(\bar{h}_{H_2}(T_f) + \frac{1}{2} \bar{h}_{O_2}(T_a) - \bar{h}_{H_2O}(T_s) \right) \cdot \dot{r}_E \\
&\quad + \left(\bar{h}_{CH_4}(T_f) + \bar{h}_{H_2O}(T_f) - 3\bar{h}_{H_2}(T_s) - \bar{h}_{CO}(T_s) \right) \cdot \dot{r}_R \quad (4.33) \\
&= \Delta H_E \cdot \dot{r}_E + \Delta H_R \cdot \dot{r}_R
\end{aligned}$$

where the ΔH 's in (4.33) are evaluated using the designated temperatures. Inserting Equation (4.33) and the appropriate rate expressions for the heat conduction, convection, and radiation terms into Equation (4.32) gives,

$$\begin{aligned}
m_s c_{ps} \frac{\Delta T_s}{\Delta t} &= k_s \frac{\Delta^2 T_s}{\Delta x^2} \Delta x \cdot b \delta - h_a B (T_s - T_a) \cdot b \Delta x - h_f B (T_s - T_f) \cdot b \Delta x + (q''_{rad,s-icf} + q''_{rad,s-ica}) \cdot b \Delta x \\
&\quad + (\Delta H_E \cdot \dot{r}_E''' + \Delta H_R \cdot \dot{r}_R''' - P''_{slice}) \cdot b \delta \Delta x \quad (4.34)
\end{aligned}$$

where m_s , c_{ps} , and k_s are the mass, specific heat, and thermal conductivity of the solid cell, respectively. B is the ratio of gas-to-solid heat transfer area to electroactive cell area. Note that k_s is considered to be constant. Dividing Equation (4.34) by the elemental volume, letting $q''_{rad,tot} = q''_{rad,s-ica} + q''_{rad,s-icf}$, and taking the limit as $\Delta x \rightarrow 0$ and $\Delta t \rightarrow 0$ we have,

$$\underbrace{\rho_s c_{ps} \frac{\partial T_s}{\partial t}}_{\text{energy storage}} = \underbrace{k_s \frac{\partial^2 T_s}{\partial x^2}}_{\text{solid heat conduction}} - \underbrace{\frac{h_a B}{\delta} (T_s - T_a)}_{\text{air convection}} - \underbrace{\frac{h_f B}{\delta} (T_s - T_f)}_{\text{fuel convection}} + \underbrace{\frac{q''_{rad,tot}}{\delta}}_{\text{radiation}} - \underbrace{(\Delta H_E \cdot \dot{r}_E''' + \Delta H_R \cdot \dot{r}_R''' - P''_{slice})}_{\text{heat generation}} \quad (4.35)$$

Equation (4.35) states that on a cell volume basis, the rate of change in energy of the solid cell over any time interval is due to the net energy transfer accompanying heat conduction, convective heat transfer from solid cell to anode and cathode gases, radiation heat exchange between cell trilayer and fuel- and air-side interconnects, and the net heat generation. Note that the heat generation term in (4.35) was derived without explicit reference to ohmic dissipation or reversible heat generation; that is, these terms are implicitly included by tracking the energy flows.

4.5.2.4 Cell interconnect energy balances

Cell modeling in the literature typically avoids resolving the cell interconnect in favor of lumping it with the cell trilayer. However, to account for cross-channel radiation heat transfer the interconnect temperatures must be resolved. An energy balance on the air-side interconnect includes conduction, convection, and radiation terms,

$$m_{ic} c_{pic} \frac{\Delta T_{ic,a}}{\Delta t} = k_{ic} \frac{\Delta^2 T_{ic,a}}{\Delta x^2} \Delta x \cdot b \delta - h_a (T_{ic,a} - T_a) \cdot b \Delta x + (q''_{rad,ica-s}) \cdot b \Delta x \quad (4.36)$$

where m_{ic} , c_{pic} , and k_{ic} are the mass, specific heat, and thermal conductivity of the interconnect, respectively. $T_{ic,a}$ is the air-side solid interconnect temperature. Dividing Equation (4.36) by the elemental volume and taking the limit as $\Delta x \rightarrow 0$ and $\Delta t \rightarrow 0$ we have,

$$\underbrace{\rho_{ic} c_{pic} \frac{\partial T_{ic,a}}{\partial t}}_{\text{energy storage}} = \underbrace{k_{ic} \frac{\partial^2 T_{ic,a}}{\partial x^2}}_{\text{solid heat conduction}} - \underbrace{\frac{h_a}{\delta} (T_{ic,a} - T_a)}_{\text{air convection}} + \underbrace{\frac{q''_{rad,ica}}{\delta}}_{\text{radiation}} \quad (4.37)$$

In a similar manner, the fuel-side interconnect energy balance is obtained,

$$\underbrace{\rho_{ic} c_{pic} \frac{\partial T_{ic,f}}{\partial t}}_{\text{energy storage}} = \underbrace{k_{ic} \frac{\partial^2 T_{ic,f}}{\partial x^2}}_{\text{solid heat conduction}} - \underbrace{\frac{h_f}{\delta} (T_{ic,f} - T_a)}_{\text{fuel convection}} + \underbrace{\frac{q''_{rad,icf}}{\delta}}_{\text{radiation}} \quad (4.38)$$

The radiation terms in Eqs. (4.37) and (4.38) are obtained using equation (4.32b).

4.5.3. Gas Phase Hydrodynamics

Gas flow through the small cell channels is laminar ($Re \approx 5$ to 100) and develops quickly. Usage of the fully developed laminar flow solutions of the Navier-Stokes equations is generally adequate for the gas flow hydrodynamics. However, the flow is neither isothermal nor steady due to thermal gradients and cathode-to-anode mass transfer, respectively, making the situation slightly more complex. When considering estimation of the pressure loss in a cell-stack, conceptualization of the cell-stack as a heat exchanger core is useful (Figure 4.5).

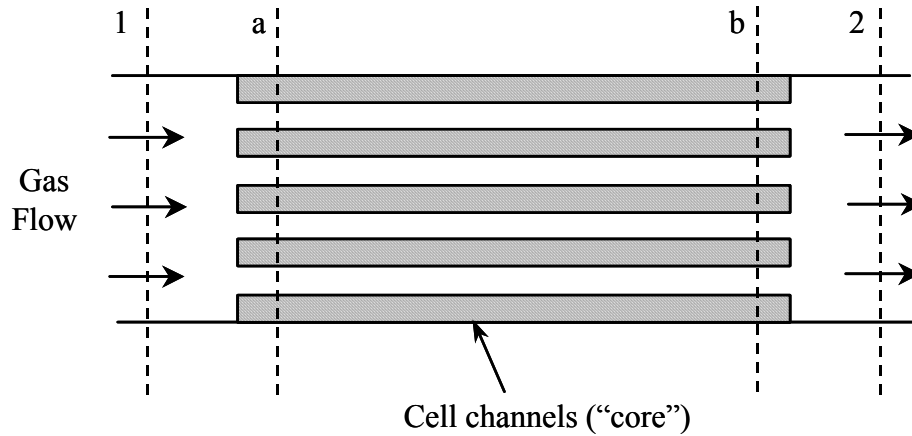


Figure 4.5 Cross-section of gas flow in fuel cell channels

Kays and London [30] write the pressure loss from station 1 to station 2 as,

$$\Delta p_{1-2} = \frac{\rho_1 \cdot V_1^2}{2} \left[\underbrace{(K_c + 1 - \sigma^2)}_{\text{entrance effect}} + \underbrace{2 \left(\frac{v_2}{v_1} - 1 \right)}_{\text{flow acceleration}} + \underbrace{f \frac{A}{A_c} \frac{v_m}{v_1}}_{\text{core friction}} - \underbrace{(1 - \sigma^2 - K_e)}_{\text{exit effect}} \cdot \frac{v_2}{v_1} \right] \quad (4.39)$$

where,

v = specific volume of gas

σ = ratio of core free-flow to frontal-area

A_c = exchanger minimum free flow area

A = total heat transfer area on one side

K_c = entrance (contraction) loss coefficient

f = friction factor $\propto Re$

K_e = exit (expansion) loss coefficient

\bar{V} = average gas velocity in core

\bar{v} = average specific volume of gas in core

Equation (4.39) states that the pressure loss in a cell channel will be due to entrance flow effects at the gas manifold/cell inlet interface, gas flow acceleration due to gaseous temperature rise, viscous forces in the interconnect flow field and exit flow effects at the gas manifold/cell outlet interface. Flow acceleration or deceleration due to mass addition or loss by oxygen transport from cathode to anode chambers must also be accounted for. As a first approximation, mass transfer can be accounted for by computing the average fluid velocities and gas mixture properties in the core. Then Equation (4.39) becomes,

$$\Delta p_{1-2} = \underbrace{\frac{\rho_1 \cdot V_1^2}{2} \cdot (K_c + 1 - \sigma^2)}_{\text{entrance effect}} + \underbrace{\left(\frac{\rho_1 \cdot V_1^2 - \rho_2 \cdot V_2^2}{2} \right)}_{\text{flow acceleration}} + \underbrace{\left(f \frac{A}{A_c} \frac{\bar{\rho}_{\text{core}} \cdot \bar{V}_{\text{core}}^2}{2} \right)}_{\text{core friction}} - \underbrace{\frac{\rho_2 \cdot V_2^2}{2} (1 - \sigma^2 - K_e)}_{\text{exit effect}} \quad (4.40)$$

where recall that for laminar flow in a duct, $f = 16/Re_D$. As with mass and energy balances, the momentum balance of (4.40) may also be employed on fuel and air discretized elements in the core to determine the incremental pressure drop through each flow channel. In this case, the first and last terms in Equation (4.40) are dropped for interior nodes. As it turns out, the second term in (4.40) can also be dropped as the pressure loss from acceleration/deceleration of the reactant gas streams due to oxygen transport and temperature rise is insignificant compared to the viscous losses.

Because the fuel and air gases are chemically reacting flows, their gas compositions vary along the length of the cell. Hence, transport and thermodynamic properties will also vary. In particular, the dynamic viscosity can change substantially from cell inlet to cell outlet. Property evaluation is discussed in greater detail in §4.5.5. For the cell-stack assembly, pressure losses in the gas manifolds (upstream or downstream of the core) can also be included using the equations developed by Costamagna et al., [31]. A summary of the relevant fuel cell modeling equations can be found in Table 4.1.

4.5.4. Boundary conditions

The top and bottom of the cell domain are considered adiabatic surfaces, that is, each cell is thermally isolated from its neighbor. Also, due to the use of highly insulating end plates, the cell-stack itself is insulated from heat transfer to the surroundings in the vertical z-direction. In real cell-stacks, the inlet and outlet sides of the cell are subject to convective heat transfer from both fresh reactants and depleted products as well as, radiative heat transfer between cell-stack and enclosure. However, as the cell is thin relative to its length ($L/\delta \gg 1$), the convection at the tip is negligible and it can thus be viewed like a fin with an adiabatic tip at both inlet and outlet. (Depending on the cell-stack design, radiation heat transfer between the tip and stack enclosure may be important and is explored in Chapter Five.) Consequently, the only boundary conditions are the inlet fuel and air temperatures as summarized in Table 4.1.

Table 4.1 Summary of Basic Model Equations

Charge Balance		Either Equation (4.7) or $V_{cell} = E_N - i \cdot R_{cell}(T_s)$ where $E_N = -\frac{\Delta G}{n_e F} - \frac{R_u T_s}{n_e F} \cdot \ln \left[p_{H_2O} \cdot p_{H_2}^{-1} \cdot (p_{O_2})^{-\frac{1}{2}} \right]$
Mass Balances	Gas	$\frac{d\dot{n}_i''}{dx} = v_{i,R} \dot{i}_R''' + v_{i,E} \dot{i}_E''' + \Delta \dot{n}_{i,wgs}'''$
Energy Balances	Fuel	$\sum_i \frac{d}{dx} (\dot{n}_i'' \bar{h}_i(T_f)) = \frac{1}{a} \left[\sum_i (\dot{n}_i'' \bar{h}_i(T_s)) - \sum_i (\dot{n}_i'' \bar{h}_i(T_f)) \right] + 2h_f \frac{(a+b)}{ab} (T_s - T_f) + \frac{U_{tot}}{ab\Delta x} (T_a - T_f)$
	Air	$\sum_i \frac{d}{dx} (\dot{n}_i'' \bar{h}_i) = -\dot{n}_{O_2}'' \cdot \left[\frac{\bar{h}_{O_2}}{c} \right] + \frac{2h_a(b+c)}{bc} (T_s - T_a) + \frac{U_{tot}}{ac\Delta x} (T_f - T_a)$
	Solid	$\rho_s c_{p_s} \frac{\partial T_s}{\partial t} = k_s \frac{\partial^2 T_s}{\partial x^2} - \frac{h_a B}{\delta} (T_s - T_a) - \frac{h_f B}{\delta} (T_s - T_f) + \frac{q_{rad,tot}''}{\delta} - (\Delta H_E \cdot \dot{i}_E''' + \Delta H_R \cdot \dot{i}_R''' - P_{slice}''')$
	Fuel IC	$\rho_{ic} c_{p_{ic}} \frac{\partial T_{ic,a}}{\partial t} = k_{ic} \frac{\partial^2 T_{ic,a}}{\partial x^2} - \frac{h_a}{\delta} (T_{ic,a} - T_a) + \frac{q_{rad,ica}''}{\delta}$
	Air IC	$\rho_{ic} c_{p_{ic}} \frac{\partial T_{ic,f}}{\partial t} = k_{ic} \frac{\partial^2 T_{ic,f}}{\partial x^2} - \frac{h_f}{\delta} (T_{ic,f} - T_a) + \frac{q_{rad,icf}''}{\delta}$
Momentum Balance	Gas	$\Delta p_{channel} = \frac{\rho_1 \cdot V_1^2}{2} \cdot (K_c + 1 - \sigma^2) + \left(\frac{\rho_1 \cdot V_1^2 - \rho_2 \cdot V_2^2}{2} \right) + \left(f \frac{A}{A_c} \frac{\bar{\rho}_{core}}{2} \frac{\bar{V}_{core}^2}{2} \right) - \frac{\rho_2 \cdot V_2^2}{2} (1 - \sigma^2 - K_c)$
Boundary Condition	Gas	$T_f(x=0) = T_f _{inlet}$ and $T_a(x=0) = T_a _{inlet}$
	Solid	$\dot{Q} = 0$ at cell inlet and outlet
Reaction Rate	H ₂	$\dot{i}_E = \left(\frac{v_{i,E} \cdot j(x)}{n_e \cdot F} \right) \cdot A_{slice}$ for electrochemical oxidation of hydrogen
	CH ₄	$\dot{i}_R = k_0 p_{CH_4} f_e \exp \left(\frac{-E_A}{R_u T_s(x)} \right) \cdot A_{rx}$ for methane reforming

4.5.5. Transport and Thermodynamic Properties

The convective heat transfer coefficients in Equations (4.28), (4.31), and (4.35), can be found using the relation,

$$h = \frac{Nu \cdot k_g}{D_h} \quad (4.41)$$

where D_h is the hydraulic diameter of the rectangular gas channel, Nu is the Nusselt number, and k_g is the thermal conductivity of the gas mixture. Many correlations for the Nusselt number can be found in the literature (e.g., 33, 34, 35, 36, 37). However, the Nusselt relation given by Shah and London [38] for the case of fully developed laminar flow with uniform temperature distribution at four walls in a rectangular duct is selected to be consistent with the lumped cell temperature assumption and the isothermal condition for each computational cell slice. The fitted Nusselt relation by Shah and London is expressed as,

$$Nu_T = 7.541(1 - 2.61\alpha^* + 4.97\alpha^{*2} - 5.119\alpha^{*3} + 2.702\alpha^{*4} + 0.548\alpha^{*5}) \quad (4.42)$$

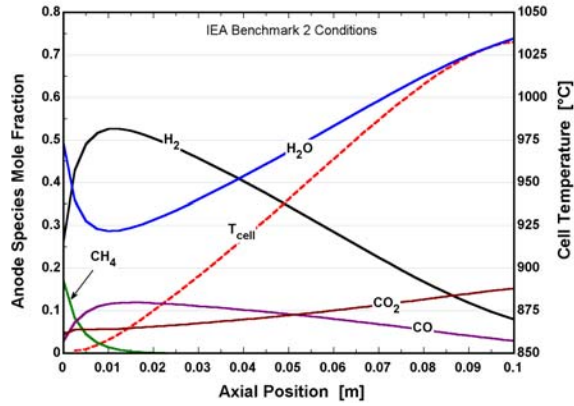
where α^* is the geometric ratio of channel height over width ($\alpha^*=a/b$). Since both fuel and air gas flows in the cell are firmly in the laminar region, Equation (4.42) may be used for both reactant gases. Also note that based on this relation, the heat transfer coefficient is independent of the fluid velocity in the channel. However, the heat transfer coefficient will vary with axial cell position due to the changing gas composition, which in turn affects the thermal conductivity of the gas mixture. Evaluation of both the thermal conductivity and viscosity transport properties of low-pressure multicomponent gas mixtures requires application of the kinetic theory of gases. Various methods exist to estimate these properties and most are complex functions of gas composition [39]. The method of Wilke [40] is employed herein to determine gas mixture viscosity and is summarized with the following two equations,

$$\mu_m = \frac{\sum_{i=1}^n y_i \mu_i}{\sum_{j=1}^n y_j \phi_{ij}} \quad \text{where } \phi_{ij} = \frac{\left[1 + (\mu_i / \mu_j)^{1/2} \cdot (M_j / M_i)^{1/4} \right]^2}{\left[8(1 + M_i / M_j) \right]^{1/2}} \quad (4.43)$$

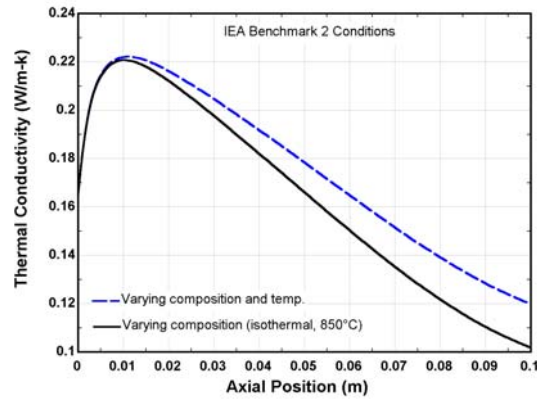
where μ_m is the viscosity of the mixture, μ_i is the viscosity of the pure species i , y_i is the mole fraction of species i , and M_i is the molecular weight of species i . The method of Wassilijewa [41] with the Mason and Saxena modification [42] is used to evaluate the thermal conductivity of the gas mixtures and is nearly identical to Equation (4.43),

$$k_m = \sum_{i=1}^n \frac{y_i k_i}{\sum_{j=1}^n k_j A_{ij}} \quad \text{where } A_{ij} = \frac{\varepsilon \cdot \left[1 + (k_i / k_j)^{1/2} \cdot (M_j / M_i)^{1/4} \right]^2}{\left[8(1 + M_i / M_j) \right]^{1/2}} \quad (4.44)$$

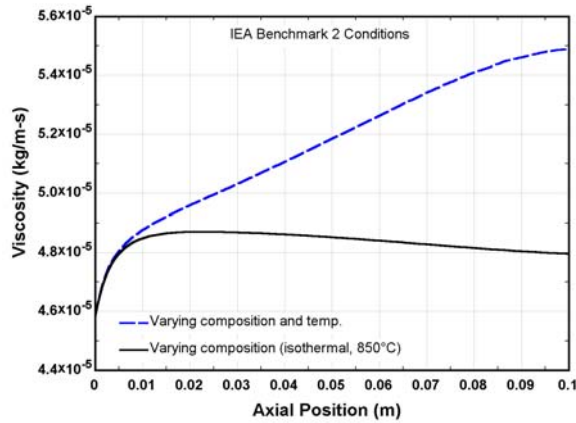
where ε is a numerical constant near unity [39], k_m is the conductivity of the mixture, k_i is the conductivity of the pure species i , y_i is the mole fraction of species i , and M_i is the molecular weight of species i . Equations (4.43) and (4.44) are linearly increasing functions of temperature. To see how these relations are affected by changes in composition, the compositional variation of the anode fuel gas along the streamwise direction of the fuel cell for a specific set of operating conditions is depicted in Figure 4.6(a). The axial cell temperature distribution is also depicted. Of the fuel gas constituents, the change in H₂ and H₂O composition from cell inlet to outlet is the most significant (and demonstrates non-linearity in the reforming region). The cell temperature rise over the length of the cell is also significant, but is relatively linear. Comparing Figure 4.6(a) and (b), at 850°C the behavior of the conductivity of the anode fuel gas is strongly linked to the fraction of hydrogen in the gas and changes by as much as 50% from cell inlet to outlet. As the heat transfer coefficient is directly proportional to the gas thermal conductivity, the resistance to convective heat transfer from the cell solid to the anode fuel gas will nearly double from cell inlet to outlet. The large change in heat transfer coefficient of the fuel gas has only a minor effect on the cell temperature as the cell cooling is driven by the cathode airflow. When the effect of temperature is included (see dashed line in the figure), the shape of the distribution is relatively unchanged; although the two curves gradually diverge from one another because the thermal conductivity increases with axial position.



(a) Streamwise variation of anode fuel gas composition



(b) Streamwise variation of the anode fuel gas thermal conductivity



(c) Streamwise variation of the anode fuel gas viscosity

Figure 4.6 Property variation of the anode fuel gas in an SOFC

Interestingly, at first glance the viscosity of the fuel gas mixture appears to be driven by CO concentration as a comparison between Figure 4.6(a) and (c) shows. However, the magnitude of viscosity for the pure H₂O, CO, and CO₂ components is very similar at 850°C. Thus, as H₂O concentration increases (the sum of CO and CO₂ concentrations are relatively constant with axial cell position), the mixture viscosity becomes more anchored to the pure viscosity values of these species. The linear dependence of viscosity on temperature is also apparent from the figure, causing a 20% increase in viscosity over the length of the cell. From Equation (4.40), a proportional change in cell pressure drop is also then expected. While the change in transport properties along the cell is significant, the effect of these changes on cell temperature distribution, power, and voltage predictions is relatively small. All relevant cell component property data can be found in Bossel, [24] and is summarized in Table 5.1. Engineering Equation Solver (EES) software [43] supplies all thermodynamic property data.

4.6 Numerical Solution Technique

The governing equations of charge, mass, energy, and momentum are written in the Eulerian domain for a single cell taken as the control volume. The governing equations are solved numerically using an explicit finite difference method, where the domain of interest is divided into a finite number of computational cells (or slices) as shown in Figure 4.7. Each computational slice has its own equilibrium potential, constituent partial pressure, and gaseous or solid phase temperature. The magnitude of the equilibrium potential as described by Equation (4.6) will depend on the constituent partial pressures and cell temperature at the slice location. As the operating voltage is the same for each computational slice (see assumption 6 in §4.3), it serves as a common parameter among the different slices enabling the slice current to be iteratively solved for [44].

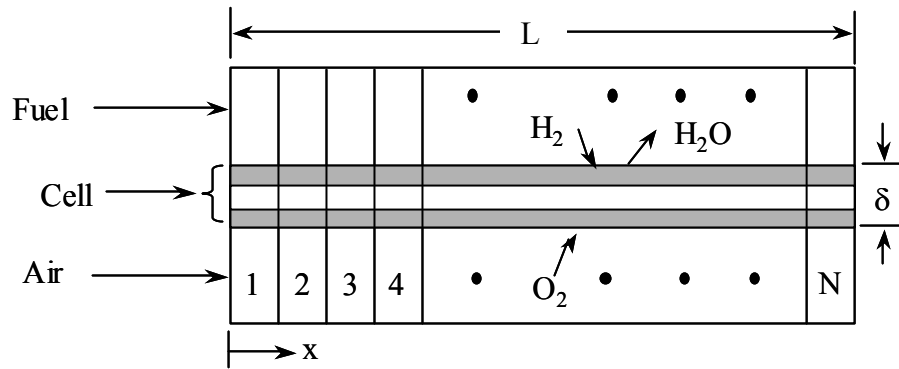


Figure 4.7 Axial discretization of a single cell

Each governing equation provides a variable of interest. The charge balance provides the cell current; the mass balances provide the specie partial pressures; the energy balances provide the gaseous and solid phase temperatures; and the momentum equation provides the gaseous static pressure. The conservation equations of charge, mass, energy, and momentum are functions of composition and temperature and hence, are coupled. For example, in the mass balance equations of §4.5.1, the change in species concentration is dependent on the rates of both electrochemical hydrogen oxidation and methane reforming reactions (and water-gas shift equilibrium chemistry). In turn, these reaction rates are functions of the local concentration of the relevant reacting species and the solid temperature. The coupled nature of the governing equations typically requires an iterative numerical solution algorithm. In the model developed for this study, the four conservation balances on each axial slice are solved simultaneously using an EES code (see Appendix II).

The inputs to the cell model are average current density (or cell voltage), mass flow of fuel, air-to-fuel ratio, inlet fuel and air temperatures and composition. The outputs of the model are cell voltage, power, efficiency, solid cell and gaseous reactant temperature distributions, current density distribution, fuel utilization, excess air amount, and outlet temperature of the fuel and air streams. The cell geometric dimensions (width, height, channel dimensions, and component thicknesses), cell V-I performance characteristic, reforming reaction rate, flow configuration (co-flow or counter-flow), and computational grid-size are parameters which

can be varied in the cell model. These are summarized in Table 4.2. The cell voltage-current (V-I) characteristic is parameterized as described in Equation (4.8).

Table 4.2 Model inputs, outputs, and parameters

Inputs	Outputs
Fuel flow* (kg/h)	Cell voltage* (V)
Excess air ratio, S (stoichs)	Cell power (W)
Avg. current density* (A/cm ²)	Cell efficiency (% LHV)
Inlet fuel temperature (°C)	Cell temperature distribution, $T(x)$
Inlet fuel composition (-)	Cell temperature gradient, $dT/dx(x)$
Inlet air temperature (°C)	Fuel and air temperatures, $T_f(x)$, $T_a(x)$
Inlet air composition (-)	Current density distribution, $j(x)$
	Fuel utilization and air flow*, U_f , S
Model Parameters	
Cell width, W_{cell}	Cell material properties (e.g., k_s , $c_{p,s}$)
Cell length, L_{cell}	V-I characteristic (R_{cell} , i_{as} , a , b)
Channel height, h_{ch}	Reforming reaction rate, \dot{r}_R
Channel width, w_{ch}	Flow configuration (co- or counter)
Cell thickness, δ	

*can be either an input or output.

Overall mass and energy balances were made on the fuel cell to serve as a calculation check on the validity of the individual slice balances. The overall mass balance was written as,

$$\dot{m}_{fuel,in} + \dot{m}_{air,in} = \dot{m}_{fuel,out} + \dot{m}_{air,out} + \Delta\dot{m} \quad (4.45)$$

where $\Delta\dot{m}$ is the difference between inlet and outlet mass flows. The percent error was then defined as,

$$\varepsilon_{mass} = \left(\frac{\Delta\dot{m}}{\dot{m}_{fuel,in} + \dot{m}_{air,in}} \right) \cdot 100 \quad (4.46)$$

The overall energy balance was written similarly as,

$$\sum_j \dot{n}_j \bar{h}_j \Big|_{fuel,in} + \dot{n}_{air,in} \bar{h}_{air,in} = \sum_j \dot{n}_j \bar{h}_j \Big|_{fuel,out} + \dot{n}_{air,out} \bar{h}_{air,out} + \dot{P}_{chk} \quad (4.47)$$

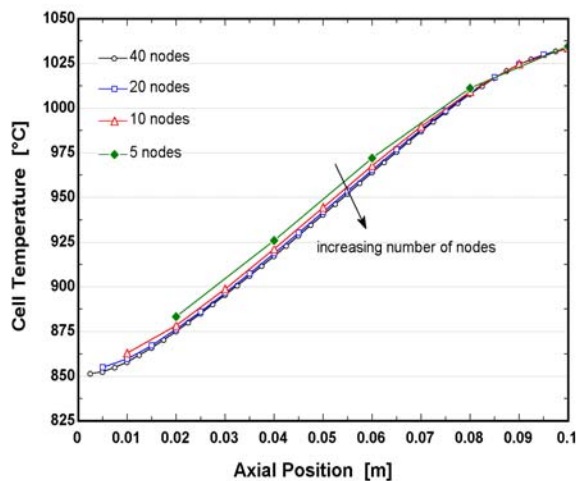
where \dot{n}_j is the molar flow of species j , \bar{h}_j is the molar enthalpy, and \dot{P}_{chk} is the calculated power from the cell based on the overall difference between cell inlet and outlet energy flow. The energy balance error was defined as the difference between the calculated cell power from the overall cell energy balance and the sum of the power generated in all the cell slices,

$$\mathcal{E}_{energy} = \left(\frac{\sum \dot{P}_{slice} - \dot{P}_{chk}}{\sum \dot{P}_{slice}} \right) \cdot 100 \quad (4.48)$$

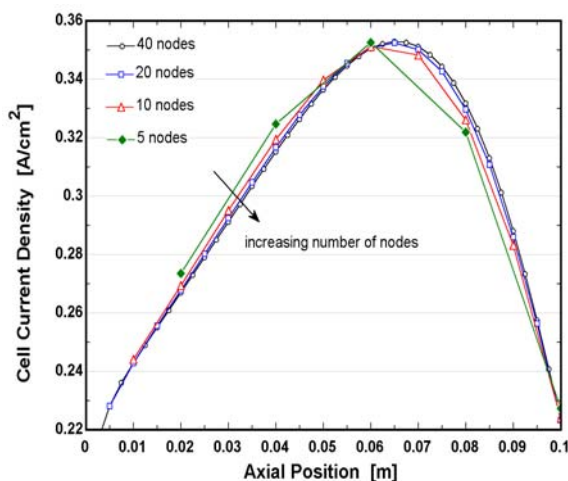
where $\sum \dot{P}_{slice}$ is the sum of the power generated in each slice. The resulting percent error was found to be on the order of 10^{-5} and 10^{-13} for the mass and energy balances, respectively. The change in mass and energy balance errors due to changes in grid-mesh size was negligible.

In addition to mass and energy balance checks, the effect of grid-mesh size was also evaluated to optimize computational and economic efficiency. In general, a point exists where the extent of discretization is limited by the increase in processing requirements and a needless increase in solution accuracy [44]. A single planar solid oxide fuel cell is typically 10 cm long by 10 cm wide. When the computational domain is discretized into 5 nodes, each slice element, Δx , is 2cm in length. The resolution of the solution is, typically, increased with decreasing Δx , however, the computational time also increases. To estimate the minimum number of nodes, the sensitivity of the solution to grid spacing was checked. Figure 4.8 (a-d) depicts the model solution dependence with increasing number of computational nodes for (a) the cell temperature distribution, (b) current density distribution, (c) hydrogen and methane composition, and (d) the solid temperature gradient distribution. Computational time is doubled when moving from 20 to 40 node domains ($\Delta x=0.5 \rightarrow 0.25$ cm) and, as each of the plots in Figure 4.8 show, little improvement in accuracy is gained. Below 20 nodes, the

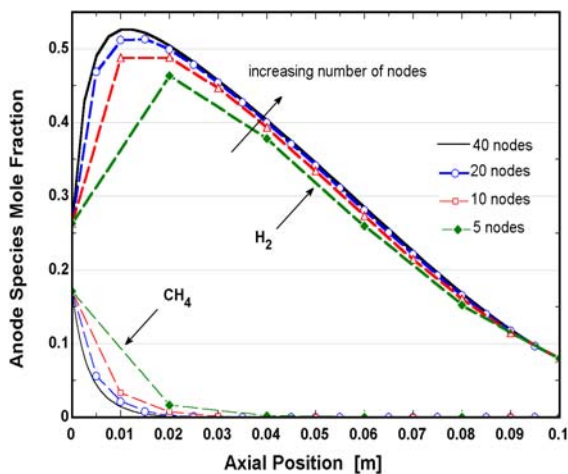
solution resolution of both the magnitude and location of extrema in current density, gas concentration, and temperature gradient becomes noticeably poorer for larger grid-spacing conditions.



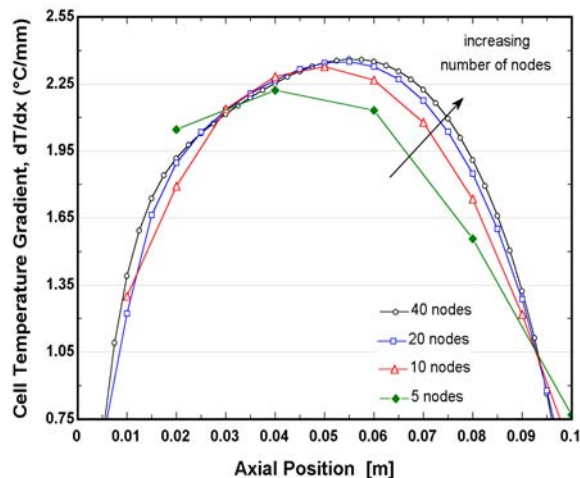
(a) cell temperature distribution



(b) current density distribution



(c) hydrogen and methane compositions



(d) solid temperature gradient

Figure 4.8 Model solution dependence on numerical grid-spacing (IEA benchmark conditions for a direct internal reforming, electrolyte supported solid oxide fuel cell in a co-flow configuration)

While distributions such as temperature and current density were significantly affected by grid spacing, changes of less than 1% in calculated cell voltage and cell power were observed

when the grid spacing was reduced from 2 cm to 0.25 cm. Based on these results, 20 nodes or a grid-spacing of 0.5 cm was deemed satisfactory to resolve spatial distributions while providing reasonably fast computational times.

4.7 Chapter References

- 4.1 H. Karoliussen, K. Nisancioglu, and A. Solheim, *J. Appl. Electrochem.*, **28** (1998) 283-288.
- 4.2 E. Achenbach, *J. Power Sources*, **52**, (1995) 105-109.
- 4.3 E. Achenbach, "SOFC Stack Modelling," Final Report of Activity A2, Annex II: Modelling and Evaluation of Advanced Solid Oxide Fuel Cells, International Energy Agency Programme on R, D&D on Advanced Fuel Cells, Juelich, Germany, March, (1996).
- 4.4 A. Malandrino and M. Chindemi, "Effect of cell configuration and fuel on SOFC modeling," *Proc. Of the Third Internat. Symp. On SOFCs*, (SOFC-III), PV93-4, The Electrochemical Society (1993).
- 4.5 E. Achenbach and U. Reus, "The effect of mass flow distribution on the characteristics of a solid oxide fuel cell system," *Proc. Of the Sixth International Symp. On SOFCs*, (SOFC-VI), PV99-19, The Electrochemical Society (1999).
- 4.6 J. Ferguson, "Heat and Mass Transfer Aspects of SOFC Assemblies and Systems," *Proc. Of the IEA Workshop on Mathematical Modeling of Natural Gas Fueled Solid Oxide Fuel Cells and Systems*, July, Charmey, CH, Swiss Federal Office of Energy (1989).
- 4.7 K. Nisancioglu, "Theoretical Problems in the Mathematical Simulation of SOFC Performance," *Proc. Of the 5th IEA Workshop on SOFC Materials, Process Engineering, and Electrochemistry*, Forschungszentrum Juelich, Germany, March (1993).
- 4.8 T. Ackermann, L.G.J. de Haart, W. Lehnert, F. Thom, "Modelling of Mass and Heat Transport in Thick-Substrate Thin-Electrolyte Layer SOFCs," *Proc. Of the 4th European SOFC Forum*, July, Luzerne, Switzerland (2000).
- 4.9 A.J. Appleby, "Characteristics of Fuel Cell Systems," in *Fuel Cell Systems*, edited by L.J. Blomen and M. Mugerwa, Plenum Press, New York (1993).
- 4.10 S. Ahmed, C.McPheeters, R. Kumar, *J. Electrochem. Soc.*, **138**, No. 9, September (1991).
- 4.11 O. Melhus and S.K. Ratkje, *Denki Kagaku*, **6**, 662 (1996).
- 4.12 N.F. Bessette, W.J. Wepfer, J. Winnick, *J. Electrochem. Soc.*, **142**, No.11, (1995).
- 4.13 W.R. Dunbar and R.A. Gaggioli, *J. Energy Res. Tech.*, **112**, June (1990).

-
- 4.14 P. Holtappels, L.G.J. DeHaart, U. Stimming, I.C. Vinke, and M. Mogensen, "Reaction of CO/CO₂ gas mixtures on Ni±YSZ cermet electrodes," *J. Appl. Electrochem.*, **29**, 561-568 (1999).
- 4.15 Y. Matsuzaki and I. Yasuda, *J. Electrochem. Soc.*, **147** (5) 1630-1635 (2000).
- 4.16 S.W. Angrist, *Direct Energy Conversion*, 4th Ed., Allyn and Bacon, New York (1982).
- 4.17 J. Winnick, *Chemical Engineering Thermodynamics*, John Wiley & Sons, New York, (1997).
- 4.18 L. Carrette, K. Friedrich, and U. Stimming, *Fuel Cells* **1** (1) (2001) pp. 5-39.
- 4.19 N.Q. Minh and T. Takahashi, *Science and Technology of Ceramic Fuel Cells*, Elsevier Science, New York (1995).
- 4.20 J.W. Kim, A.V. Virkar, K.Z Fung, K. Mehta, and S.C. Singhal, *J. Electrochem. Soc.*, **146** (1) 69-78 (1999).
- 4.21 J.W. Kim and A.V. Virkar, "The Effect of Anode Thickness on the Performance of Anode-supported Solid Oxide Fuel Cells," *Proc. Of the Sixth Int. Symp. On SOFCs*, (SOFC-VI), PV99-19, The Electrochemical Society, pp.830-839 (1999).
- 4.22 H. Yakabe et al., *J. Power Sources*, **86**, (2000), pp. 423-431.
- 4.23 A.J. Baird and L.R. Faulkner, *Electrochemical Methods: Fundamentals and Applications*, 2nd Ed., Wiley Interscience, New York, (2001).
- 4.24 U.G. Bossel, *Facts and Figures*, Final report on SOFC data, IEA Programme on Advanced Fuel Cells, Annex II, Swiss Federal Energy Office of Energy, Berne, (1992).
- 4.25 A.L. Lee and R.F. Zebransky, *Ind. Eng. Chem. Res.*, **29**, No. 5, (1990), pp.766-773.
- 4.26 E. Achenbach and E. Riensche, "Methane-steam reforming kinetics for solid oxide fuel cells," *J. Power Sources*, **52** (1994), pp. 283-288.
- 4.27 R. Odegard, E. Johnsen, H. Karoliussen, "Methane Reforming on Ni/Zirconia SOFC Anodes, *Proc. Of the Fourth Internat. Symp. On SOFCs* (SOFC-IV), The Electrochemical Society, Pennington, NJ (1995), pp. 810-819.
- 4.28 R.Peters, I.Drescher, and J.Meusinger, "Kinetics of Methane Steam Reforming," *2000 Fuel Cell Seminar Abstracts*, Oct. 30-Nov.2, Portland, Oregon (2000), pp.305-308.
- 4.29 F.P. Incropera and D.P. DeWitt, *Fundamentals of Heat and Mass Transfer*, 3rd Ed., John Wiley & Sons, New York, NY (1990).
- 4.30 W. Kays and A. London, *Compact Heat Exchangers*, 3rd Ed., McGraw-Hill, New York, (1984).
- 4.31 P.Costamagna, E.Arato, E.Achenbach, U.Reus, *J.Power Sources*, **52**, (1994), 243-249.
- 4.32 R.H. Perry and D.H. Green, *Perry's Chemical Engineer's Handbook*, 6th Ed., McGraw-Hill, New York, Chapter 5, (1984).

-
- 4.33 L.F. Carter, W.N. Gill, "Asymptotic solution for combined free and forced convection in vertical and horizontal conduits with uniform suction and blowing," *AIChE Journal*, **10**, No.3, (1964) pp.330-339.
- 4.34 R.M. Terrill, "Heat transfer in laminar flow between parallel porous plates," *Int. J. Heat Mass Transfer*, **8**, (1965), pp.1491-1497.
- 4.35 W.M. Rohsenow, J.P. Hartnett, Y.I. Cho, *Handbook of Heat Transfer*, 3rd Ed., McGraw-Hill, New York, (1998).
- 4.36 W.M. Kays and Crawford, *Convective Heat and Mass Transfer*, 3rd Ed., McGraw-Hill, New York, (1990).
- 4.37 A. Selimovic et al., "Analysis and Effects of Heat Transfer and Friction Factor on SOFC Performance Characteristics," *Proc. Of the 4th European SOFC Forum*, July 10-14, Lucerne, Switzerland (2000).
- 4.38 R.K. Shah, and A.L. London, "Laminar Flow Forced Convection in Ducts," *Supplement 1 to Advances in Heat Transfer*, eds. T.F. Irvine, and J.P. Hartnett, Academic Press, New York, (1978). Nusselt relation also found in *Handbook of Heat Transfer*, 3rd Ed., McGraw-Hill, (1998), p. 5.68.
- 4.39 R.C. Reid, J.M.Prausnitz, and B.E. Poling, *The Properties of Gases and Liquids*, 4th Ed., McGraw-Hill, New York (1987).
- 4.40 C.R. Wilke, *J. Chem. Phys.*, **18**: 517 (1950).
- 4.41 A. Wassiljewa, *Physik. Z.*, **5** 737 (1904).
- 4.42 E.A. Mason, and S.C. Saxena, *Phys. Fluids*, **1**: 361 (1958).
- 4.43 *Engineering Equation Solver (EES)*, F-Chart Software, Middleton, WI (2000).
- 4.44 C. Haynes, Ph.D. Thesis, Georgia Tech University, Atlanta, GA (1998).

Chapter Five Validation of Cell Model

The generation of a useful fuel cell model requires some form of validation. Typically, model validation is accomplished with experimental data and cell design information. The fuel cell power module is the key component of these power systems and due to its relative technological infancy, there is limited access to manufacturer experimental and design data to validate computational models. Some data exists for hydrogen operation in the technical literature, but performance data on SOFCs fueled with natural gas reformat are scarce. In both cases, experimental and design data are not sufficiently comprehensive to validate the model.

To assist in model validation, the International Energy Agency (IEA) sponsored a steady-state modeling benchmark test for fuel cell research which enables the performance results of the developed model to be compared with the results of other “certified” models developed by several international research organizations. Given the atmosphere of tightly guarded experimental and cell-stack design data by manufacturers, the approach was to gauge the computational effectiveness of the steady-state SOFC model developed herein by using the IEA benchmark. Once the model integrity was verified, it could be calibrated to other SOFC designs and operating conditions with the available experimental data in the technical literature. The approach is discussed in more detail in the following sub-sections.

5.1 Model Verification

To validate the fuel cell model, the following comparisons are made: (i) cell voltage, (ii) cell power, (iii) solid cell temperature distribution in the streamwise direction, (iv) current density distribution, and (v) outlet product gas temperatures. While Chapter 4 presented a dynamic solid oxide fuel cell model, a transient capable model was not employed here due to the unavailability of sufficient data (modeling or experimental) to validate the effort. While others have presented some simulation results for the dynamic response of SOFCs [1, 2, 3], there is insufficient consensus on the thermal response rate. At this time, all that can be stated

is that the electrochemical response of the SOFC is on the order of 10^{-3} seconds and the thermal response is on the order of $10^2 - 10^3$ seconds.

5.1.1. *IEA Benchmark*

In 1995, the International Energy Agency conducted a fuel cell stack modeling exercise that involved seven European countries and Japan. The aim of the effort was to “bring the SOFC stack modelers together on an international level to form a community engaged in mutual exchange of problems, knowledge, and results” [4]. Employing a common database, two cases of SOFC stack operation were simulated: (1) one-cell stack operation with humidified hydrogen fuel and ambient air feed, and (2) one-cell stack operation with direct internal steam reforming of methane and air. These cases are designated ‘Benchmark 1’ and ‘Benchmark 2,’ respectively, and the test conditions for each are specified in Table 5.1 and 4.4, respectively. To the author’s knowledge, no benchmark is available for cell transient response.

The Benchmark 1 test conditions listed in Table 5.1 describe the simple case of a single adiabatic square, electrolyte-supported SOFC operated with air as oxidant and coolant, and humidified hydrogen as fuel. “To avoid discrepancies caused by different treatment of the electrochemical kinetics, the anodic and cathodic overpotentials are regarded as being of the same amount as the ohmic loss of the electrolyte” [4], where the ohmic loss can be characterized by the component conductivity relations in the table. The benchmark states that the mechanisms for internal heat transfer are forced convection, conduction through gaseous and solid phase, and radiation. However, whether or not benchmark modeling participants included the radiation heat transfer mechanism is unknown. Since the cell is considered to be adiabatic, boundary conditions that might result from a stack in an enclosure or other surroundings are not considered. It is also noteworthy that the explicit definitions for fuel utilization and excess air are not provided in the published results for the IEA SOFC Benchmark. The definitions used for model verification are based on those given by Bossel [5] and are discussed shortly.

Table 5.1 Benchmark 1 Test Conditions

Cell Geometry	
Electroactive area	10 x 10 cm ²
Anode thickness	0.05 mm
Cathode thickness	0.05 mm
Electrolyte thickness	0.150 mm
<u>Bipolar plate</u> thickness	2.5 mm
-Number of rect. channels	18
-Channel width	3 mm
-Channel height	1 mm (both air and fuel)
-Rib width	2.42 mm
Thermal Properties (ceramic)	
Thermal conductivity	2 W/m-K
Heat capacity	400 J/kg-K
Density	6600 kg/m ³
Electrical Properties	
Anode conductivity	$\frac{95 \times 10^6}{T_s} \exp\left(\frac{-1150}{T_s}\right) [\Omega \cdot m]^{-1}$
Cathode conductivity	$\frac{42 \times 10^6}{T_s} \exp\left(\frac{-1200}{T_s}\right) [\Omega \cdot m]^{-1}$
Electrolyte ionic conductivity	$3.34 \times 10^4 \cdot \exp\left(\frac{-10300}{T_s}\right) [\Omega \cdot m]^{-1}$
Bipolar plate conductivity	$\frac{9.3 \times 10^6}{T_s} \exp\left(\frac{-1100}{T_s}\right) [\Omega \cdot m]^{-1}$
Operating Conditions	
System pressure	1 bar
Temperature (air and fuel inlet)	900 °C
Excess air ratio (O ₂ basis)	7 (stoichs)
Fuel utilization	85%
Mean current density	3000 A/m ²
Inlet gas composition	Fuel: 90% H ₂ ; 10% H ₂ O Air: 21% O ₂ ; 79% N ₂

Table 5.2 Benchmark 2 Test Conditions

Cell Geometry	Same as Table 5.1
Thermal Properties (ceramic)	Same as Table 5.1
Electrical Properties	Same as Table 5.1
Operating Conditions	
System pressure	1 bar
Temperature (air and fuel inlet)	900 °C
Excess air ratio (O ₂ basis)	7 (stoichs)
Fuel utilization	85%
Mean current density	3000 A/m ²
Inlet gas composition	Fuel*: CH ₄ = 17.1% H ₂ = 26.26% H ₂ O = 49.34% CO = 2.94% CO ₂ = 4.36% Air: O ₂ = 21% N ₂ = 79%
Reactions	
Methane reforming	$\dot{i}_R = 4274 \cdot p_{CH_4} \cdot \exp\left(\frac{-8.2 \times 10^4}{R_u T_s}\right) \cdot A_{rx}$
Water-gas shift	at equilibrium

*fuel composition is based on 30% pre-reformed fuel gas at CO-shift equilibrium

Benchmark 2 test conditions differ from Benchmark 1 in that the fuel feed is now carbonaceous and partially reformed at a steam-to-methane ratio of 2.5:1. Additionally, it is assumed that the nickel cermet material of the anode will provide the catalytic activity for the endothermic reforming reaction. The corresponding kinetics for this reaction are found in Table 5.2. The purpose of this benchmark is to describe the steep temperature, current, and gas composition gradients induced by the highly endothermic reforming reaction [4].

IEA benchmark 1 has published modeling results from eight participating research organizations for co-, counter-, and cross-flow configurations for an SOFC operating near

1000°C at a single voltage-current point. The results from the benchmark participants for counter- and co-flow configurations are displayed in Table 5.3 and Table 5.4. “High” and “low” in the tables refer to the highest and lowest values reported by the participants. The tables also show the results generated by the SOFC model developed in the present investigation.

Table 5.3 Comparison of SOFC Model with IEA Benchmark 1 Results

Parameter	Counter-flow Configuration		Co-flow Configuration	
	Benchmark	SOFC Model	Benchmark	SOFC Model
Voltage (V)				
High	0.730	0.716	0.722	0.709
Low	0.709		0.702	
Power (W)				
High	21.89	21.47	21.67	21.27
Low	21.26		21.06	
Efficiency* (%)	High / Low		High / Low	
η_1	46.9 / 49.0	48.5	48.0 / 46.4	48.1
η_2	55.2 / 57.0	57.1	56.3 / 54.6	56.6
Current Density (A/m ²)	High / Low		High / Low	
Max	8970 / 7107	7393	3957 / 3725	3799
Min	1235 / 1080	1152	1366 / 1020	1211
location of max [†]	– NR –	0.25 cm	– NR –	0.25 cm
Temperature (°C)	High / Low		High / Low	
Max	1084 / 1062	1073	1098 / 1048	1059
Min	913 / 904	910	930 / 909	924
location of max [†]	– NR –	0.25 cm	– NR –	10 cm
Outlet Gas Temp.[‡] (°C)	High / Low		High / Low	
air	1082 / 1064	1068	1067 / 1048	1058
fuel	914 / 906	910	1068 / 1048	1059

* η_1 = dc cell power/rate of inlet fuel energy (LHV); η_2 = η_1 /fuel utilization, respectively

[†] distance from fuel inlet; NR = not reported

[‡] inlet gas temperature = 900°C

A comparison of the modeling results with the IEA benchmark values in Table 5.3, show that the performance parameters fall nicely within the high/low range of the benchmark values, indicating excellent agreement. The calculated efficiency values are at the high end of the benchmark envelope and may reflect a slightly different evaluation of the fuel heating value.

Table 5.4 Comparison of SOFC Model with IEA Benchmark 2 Results

Parameter	Counter-flow Configuration		Co-flow Configuration	
	Benchmark	SOFC Model	Benchmark	SOFC Model
Voltage (V)				
Hi	0.692	0.693	0.649	0.650
Low	0.680		0.633	
Power (W)				
Hi	20.76	20.78	18.99	19.49
Low	20.40		19.47	
Efficiency* (%)	– NR –		– NR –	
η_1		53.1		49.8
η_2		62.5		58.6
Current Density (A/m ²)	Hi / Low		Hi / Low	
Max	6554 / 5330	5395	3665 / 3040	3457
Min	1332 / 994	1260	2508 / 1748	2149
location of max [†]	– NR –	1.25 cm	– NR –	6.25 cm
Temperature (°C)	Hi / Low		Hi / Low	
Max	1089 / 1062	1058	1034 / 1021	1020
Min	915 / 906	912	862 / 847	845
location of max [†]	– NR –	2.0 cm	– NR –	9.75 cm
Outlet Gas Temp.[‡] (°C)	Hi / Low		Hi / Low	
air	1028 / 1018	1014	1026 / 1016	1014
fuel	915 / 906	914	1026 / 1021	1019

* η_1 = dc cell power/rate of inlet fuel energy (LHV); η_2 = η_1 /fuel utilization

[†] distance from fuel inlet; NR = not reported

[‡] inlet gas temperature = 900°C

Five research organizations participated in the IEA Benchmark 2 test. Table 5.4 shows a comparison of the direct internal reforming (DIR) results for the IEA Benchmark 2 and the

SOFC model. The table indicates good agreement between DIR models. The SOFC DIR model in Benchmark 2 slightly overshoots the benchmark cell voltage and power, and undershoots the gas and solid phase temperatures.

Four possible sources of discrepancy between the SOFC model and the IEA Benchmark results were investigated. The first possible source of error is the treatment of radiation heat transfer in the cell. Many models do not resolve the interconnect temperature, preferring instead to lump it with the solid cell tri-layer using equivalent resistances or some other method (e.g., Selimovic [6]). In such cases inclusion of cross-channel radiation heat exchange between interconnect and cell layer is not possible with a 1- or 2-D cell model and will affect the temperature distribution calculation. Use of radiation heat transfer is then limited to boundary conditions. Hartvigsen et al., [7] have shown the importance of radiation heat transfer in temperature distribution and Nisancioglu [8] also asserts that it should not be neglected. Inclusion of radiation heat transfer tends to lower the average cell temperature and provides a more uniform temperature distribution. How radiation heat transfer is treated by IEA benchmark participants is not known. The present SOFC model accounts for cross-channel radiation heat transfer by resolving the interconnect temperature. The inclusion of radiation heat transfer in the present SOFC model would contribute to lower gas and solid temperatures when compared with IEA benchmark results.

Another likely discrepancy source is due to variations in implementing the numerical scheme. That is, IEA benchmark participants based the calculation of the reversible cell voltage on the average of the nodal inlet and outlet gas compositions at each computational grid-point. In the present model, the calculated reversible cell voltage is based on the upstream values which would tend to result in higher predicted current generations (and heat) than the IEA method. However, this trend is not observed in the model results comparison. Given a sufficiently high number of grid points in both the present model and IEA models, this difference should be insignificant. The number of grid points used by IEA participants is unknown. It is possible that the inclusion of radiation heat transfer in the present model (and the resulting lower temperatures) offsets the effects of having a higher reversible cell voltage.

A third possible source of difference is the method of estimating the gas mixture properties. The present SOFC Model estimates the gas mixture thermal conductivity and viscosity at each axial location using high accuracy correlations and rather complicated mixture rules. It is doubtful that many of the research organizations in the IEA benchmark performed such property estimations. In the course of investigating the sensitivity to property variations, it was determined that the relative effect of varying transport properties due to changing gas composition on model output was minimal. However, the IEA participants did employ average specific heat values in their computations, while in the present model, the gas enthalpies were computed at each grid-point. Thus, although average property values appear to provide sufficient accuracy for transport coefficients and are not likely to be a significant source of error, use of average specific heats could account for some result differences.

The last possible source of error investigated lies with the definition of fuel utilization and excess air. There are several ways to define reactant utilizations and the lack of such definitions in the IEA SOFC Benchmark leaves substantial room for interpretation. Based on the good agreement achieved in Benchmark 1, the fuel utilization and excess air definitions for this case are believed to be correct. However, for the hydrocarbon fuel feedstock in Benchmark 2, interpretation of these definitions can be uncertain. Without explicit definitions, such a source of error cannot be eliminated. For example, from Chapter 3 the definition of fuel utilization was given as,

$$U_{f,1} = \frac{\text{moles of fuel consumed}}{\text{moles of fuel supplied}} = \frac{(\dot{n}_{CH_4} + \dot{n}_{H_2} + \dot{n}_{CO})_{in} - (\dot{n}_{CH_4} + \dot{n}_{H_2} + \dot{n}_{CO})_{out}}{(\dot{n}_{CH_4} + \dot{n}_{H_2} + \dot{n}_{CO})_{in}} \quad (5.1)$$

where the first quotient of (5.1) is the definition given in Chapter 3 and the second quotient is the mathematical *interpretation* of that definition. “Moles of fuel supplied” could technically include inert and reforming and shift reaction product species, such as CO₂, N₂, and H₂O. The inclusion of these molar flows would lower the fuel utilization substantially and making it improbable that true utilizations greater than 70% could even be obtained. The species selected as “fuels” in Equation (5.1) are based on the fact that each of them could conceivably

produce hydrogen via reforming or shift reactions. Alternatively, since the model tracks the actual number of moles of hydrogen consumed electrochemically,

$$U_{f,2} = \frac{\text{moles of hydrogen consumed}}{\text{moles of hydrogen supplied}} = \frac{(\dot{n}_{H_2,cons})}{(4\dot{n}_{CH_4} + \dot{n}_{H_2} + \dot{n}_{CO})_{anode\ inlet}} \quad (5.2)$$

where the denominator of (5.2) represents the maximum amount of hydrogen that could be supplied with 100% conversion of the reforming and shift reactions. Equations (5.1) and (5.2) are not equivalent and will produce different results. Equation (5.2) is considered the most logical choice and the values shown in Table 5.4 are based on this definition. The amount of excess air on an oxygen basis, λ_{O_2} , is specified in Table 5.1 and Table 5.2 to be 7 “stoichs.” The definition given by Bossel [5] and its interpretation are expressed below as,

$$\lambda_{O_2} = \frac{\text{moles of oxygen supplied with air}}{\text{moles of oxygen needed for stoichiometry}} = \frac{(\dot{n}_{O_2})_{cathode\ inlet}}{2(\dot{n}_{CH_4})_{anode\ inlet} + \frac{1}{2}(\dot{n}_{H_2} + \dot{n}_{CO})_{anode\ inlet}} \quad (5.3)$$

The definitions in Equations (5.2) and (5.3) are appropriate for cell modeling, but are dependent on the fuel type, as well as whether there is any recycle of fuel cell gases back to the electrode compartment inlet. Fuel utilization definitions for the case of recycled gases will be revisited in Chapter 8. In the situation where the SOFC is fueled with pure hydrogen, the CH_4 and CO molar flows are dropped from the denominator of Equation (5.3).

5.2 Model Calibration for Anode-supported SOFC Designs

The IEA benchmark conditions were for electrolyte-supported SOFC designs. Anode-supported SOFC designs are being developed for lower temperature operation to reduce capital costs and are likely to be more widely prevalent once SOFC technology is commercialized. While the IEA benchmarks provided sufficient information to verify the SOFC Model capabilities, the model must be employed for anode-supported design types and operating conditions.

Forschungszentrum Juelich (FZJ) of Germany has been a leading developer of the anode-supported SOFC and has licensed their technology for commercial development to Global Thermoelectric (GTE) Corporation of Calgary, Canada. In general, the detailed design and performance of any given SOFC is proprietary, but some limited information is available in the published literature from the above organizations. Figure 5.1 depicts a cross-sectional view of the FZJ anode-supported cell design showing both edge sealing and electrode contact layers. The standard materials used for the cell components and their approximate dimensions are listed in Table 5.5. The edge seal prevents escape and crossover of reactant gases. The nickel wire mesh and cathode contact layer (i.e., a paste that is applied to the interconnect ribs) ensure good contact area exists between interconnect and electrodes.

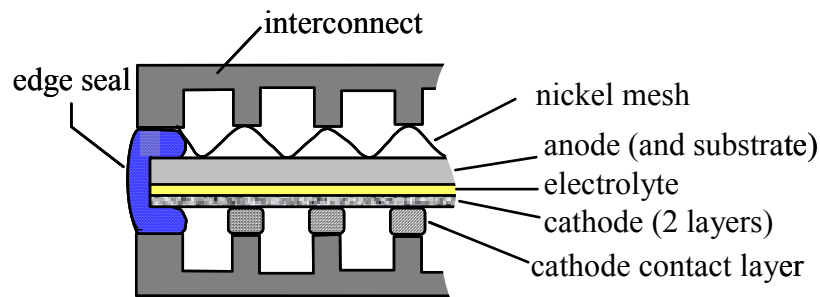


Figure 5.1 Schematic cross-section of a SOFC based on the FZJ/GTE design [9, 10] (dimensions of the layers are not to scale)

The detailed design information depicted in Figure 5.1 show a more complex cell design than previous illustrations (e.g., Figures 4.1 and 4.3). The electrode contact layers increase the difficulty in estimating parameters that affect cell performance, such as gas flow and cell current resistances. When modeling real cell designs, it is not surprising that a significant source of error in numeric computations typically occurs in estimating the cell overpotential (or polarization). Thus, the SOFC Model developed herein is calibrated for anode-supported SOFC designs by employing Global Thermoelectric's polarization (and geometric) characteristics shown in Figure 5.2. The voltage-current data for a 5 cm x 5 cm SOFC operating on humidified hydrogen at different temperatures are depicted by symbols. Using the 4-parameter relation of Equation (4.8), curve fits to the experimental data were made at each temperature. The temperature dependent parameters a , b , R_i , and i_{as} of Equation (4.8)

were individually fitted to the data, and the resulting V-I relations are shown by the solid lines in Figure 5.2.

The temperature dependence of the GTE cell-stack voltage-current characteristic for operation on reformat fuels or with direct internal reforming is not available. However, as a first approach, one could employ the experimental parameters determined for the H₂-H₂O V-I characteristic and modify the diffusion coefficients in Equation 4.8 for hydrocarbon or reformat fuels. Additionally, the dilution of hydrogen by other species in the feed gas would also be taken into account by the calculated Nernst voltage. These two effects would correctly capture the decreased voltage-current performance *trend* (relative to a pure hydrogen feed) of a hydrocarbon-fueled cell-stack. Accurate calibration would require experimental data for operation on reformat fuels.

Table 5.5 Material and thickness data of anode-supported SOFC conceptual design

Component	Material	Thickness (μm)
Interconnect with gas channels	Stainless steel (X10CrAl18)	2000
Anode contact layer	Nickel mesh	~250
Anode substrate	NiO + 8 mol% YSZ*	1500
Anode functional layer	NiO + 8 mol% YSZ*	5
Electrolyte	8 mol% YSZ*	15
Cathode intermediate layer	La _{0.65} Sr _{0.3} MnO ₃ + 8mol% YSZ*	10
Cathode	La _{0.65} Sr _{0.3} MnO ₃	40
Cathode contact layer	LaCoO ₃	~75

* YSZ = yttria-stabilized zirconia

The temperature-dependent parameter curve fits derived from Figure 5.2 data and employed in the subsequent modeling and simulation are:

$$\begin{aligned}
 R_{cell} &= 23.487 - 0.0844467 T_{cell} + 0.0001022 T_{cell}^2 - 4.13333E-08 T_{cell}^3 \\
 a &= 0.343333 - 0.000275 T_{cell} \\
 b &= 0.0153693467 + 0.0000259170854 T_{cell} - 1.08040201E-08 T_{cell}^2 \\
 i_{as} &= 169.8 - 0.707666667 T_{cell} + 0.000975 T_{cell}^2 - 4.33333333E-07 T_{cell}^3
 \end{aligned}$$

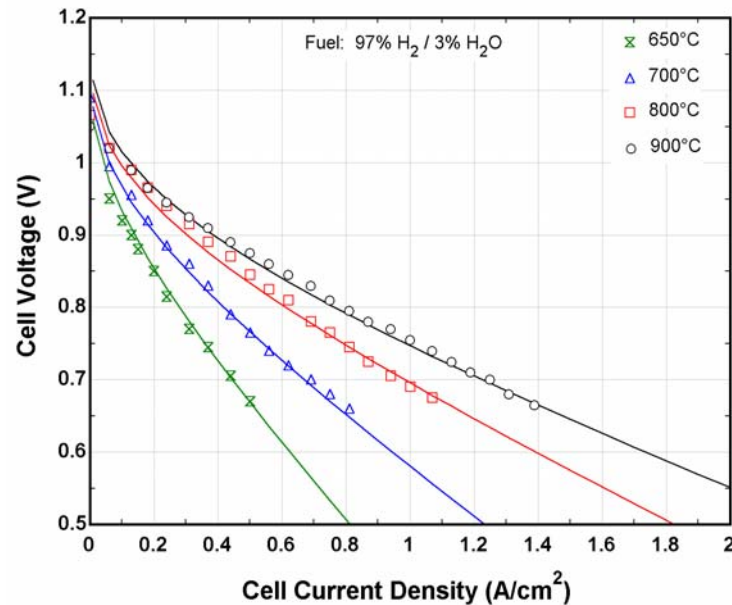


Figure 5.2 Global Thermoelectric single cell voltage-current performance [9]

The model partially incorporated cell polarizations associated with mass transport resistance by the usage of a temperature and current dependent V-I characteristic that allows the input of physically meaningful parameters (see Equation 4.8). The physical parameters that were fit from Figure 5.2 data are based on a 5 cm x 5 cm cell, which will tend to underestimate the concentration polarization loss at high currents. That is, a real 10 cm x 10 cm cell will exhibit sharper voltage losses at much lower current densities than the model predicted performance. Despite this, the present model is believed to be accurate for current densities up to 1.5 A/cm². In actuality, none of the annual simulation results presented in Chapter 8 and 9 exceeded current density operation of 1.3 A/cm².

5.3 Summary

The one-dimensional SOFC cell model developed in Chapter 4 has been shown to be in excellent agreement with the models developed by the participants in the IEA Benchmarks. The good agreement indicates that no simple errors were made and that the model appears to be sound. Unfortunately, the IEA Benchmark does not include performance predictions for an entire voltage-current characteristic. However, the strength of the model lies in its ability

to be either calibrated to a given voltage-current performance characteristic or to generate its own voltage-current performance given sufficient material and electrode performance parameter information. Chapter 6 will continue with modeling of ancillary hardware, including the natural gas pre-reformer, jet pumps, blowers, compressors, and heat exchangers. The chapter also includes a description of the system cost model for the economic system design optimization efforts presented later in Chapter 9.

5.4 Chapter References

- 5.1 E. Achenbach, *J. Power Sources*, **52**, (1995) 105-109.
- 5.2 C. Haynes, Ph.D. Thesis, Georgia Tech University, Atlanta, GA (1998).
- 5.3 E.A. Liese, et al., "Technical development issues and dynamic modeling of gas turbine and fuel cell hybrid systems," *Proc. Of the Internat. Gas Turbine Inst. Mtg*, (1999).
- 5.4 E. Achenbach, "SOFC Stack Modelling," Final Report of Activity A2, Annex II: Modelling and Evaluation of Advanced Solid Oxide Fuel Cells, International Energy Agency Programme on R, D&D on Advanced Fuel Cells, Juelich, Germany, March, (1996).
- 5.5 U.G. Bossel, *Facts and Figures*, Final report on SOFC data, IEA Programme on Advanced Fuel Cells, Annex II, Swiss Federal Energy Office of Energy, Berne, (1992).
- 5.6 A. Selimovic, "SOFC Modelling for SOFC/Gas Turbine Combined Cycle Simulations," Ph.D. thesis, Lund Institute, Dept. of Heat and Power, Sweden, April (2000).
- 5.7 J. Hartvigsen, S. Elangovan, A. Khandkar, "Modeling, design, and performance of solid oxide fuel cells," *Proc. Of Zirconia V* (1992).
- 5.8 K. Nisancioglu, "Theoretical Problems in the Mathematical Simulation of SOFC Performance," *Proc. Of the 5th IEA Workshop on SOFC Materials, Process Engineering, and Electrochemistry*, Forschungszentrum Juelich, Germany, March (1993).
- 5.9 D. Ghosh et al., "Performance of Anode Supported Planar SOFC Cells," *Proc. Of the 6th Int. Symp. on SOFCs (SOFC-VI)*, PV99-19, The Electrochemical Society, (1999) p.822.
- 5.10 D. Stover et al., "Recent developments in anode supported thin film SOFC at Research Center Juelich," *Proc. Of the 6th Int. Symp. on SOFCs (SOFC-VI)*, PV99-19, The Electrochemical Society, (1999) p.812.

Chapter Six System Component and Cost Modeling

The fuel cell stack only represents one part of the solid oxide fuel cell system necessary to produce useful heat and power. To assess the performance of a fuel cell system, other system components, such as fuel pre-reformers, inverters, gas-to-gas heat exchangers, compressors, and blowers have to be modeled. In addition, optimal system design must consider the economics associated with operating and component capital costs.

This chapter first presents the modeling approach for each of the system balance-of-plant (BOP) components. Part-load performance estimation methods are also included to support annual system simulations in Chapter 9. Next, cost models are presented. It is important to recognize that solid oxide fuel cell and sub-system component capital cost data are presently uncertain. Nevertheless, the best available published information is presented as a function of component rating to estimate the system capital costs and economy of scale, which are pertinent for optimization of system design concepts and operating strategies. The chapter concludes with a short discussion on utility electricity and natural gas rates in the Midwestern United States.

6.1 General Approach

The system components required for the solid oxide fuel cell system analyses are:

- Fuel pre-reformer
- Desulfurizer
- Blower, compressor, pump
- Heat exchangers, boiler
- Recycle jet pump/ejector
- DC-to-AC inverter
- Hot water storage tank

The steady-state modeling of each system component employs a basic thermodynamic approach using a single-node (i.e., zero dimensional) model. Each model is made up of a system of governing equations, the formulation of which is derived from: (1) boundary conditions, (2) conservation laws, (3) property relations, and (4) performance characteristics

of the component. With this approach, a program was written using EES [1], a general-purpose equation solver, to determine all the state point variables in the thermodynamic flowsheets. Mass and energy balances are written for each component in the system. Performance characteristics, such as blower and compressor efficiencies, and heat exchanger effectiveness or UA are included in the analyses. Thermodynamic properties are computed using correlations provided by EES and the resultant system of nonlinear equations is then solved in the same program.

6.2 Balance-of-Plant Component Modeling

Fuel cell balance-of-plant components are dictated by the specific requirements of each individual application. The performance characteristics for power conditioning and other SOFC system components such as blower and compressors were established based on information available in the open literature and manufacturer's information. Unless noted otherwise, component efficiencies are assumed to be constant (i.e., irrespective of load). The following highlights the ancillary hardware modeling.

6.2.1 Cell-stack heat loss and system efficiencies

Small high temperature fuel cell stacks require high performance insulation to minimize radiation heat transfer losses. Lundberg [2] has shown tubular SOFC stack heat loss as a function of capacity to range from 1.0 to 3.5% of the fuel lower heating value. These fuel cell stacks are larger than their planar counterparts, but planar stack heat loss data are not accessible in the open literature. Therefore, unless stated otherwise, the planar SOFC stacks simulated in the present study (i.e., in Chapters 7-9) are considered to be *adiabatic*.

SOFC cell-stack efficiency, net system electric efficiency, and system cogeneration efficiency used throughout the present work are defined as,

$$\text{Cell-stack efficiency} \quad \eta_{stk} = \frac{P_{DC}}{\left(\dot{n}_{fuel,in} \cdot LHV_{fuel}\right)_{system\ feed}} \quad (6.1)$$

$$\text{Net system electric efficiency} \quad \eta_{\text{sys},e} = \frac{P_{\text{net},AC}}{\left(\dot{n}_{\text{fuel},in} \cdot LHV_{\text{fuel}}\right)_{\text{system}_{\text{feed}}}} \quad (6.2)$$

$$\text{System cogeneration efficiency} \quad \eta_{\text{cogen}} = \frac{P_{\text{net},AC} + \dot{Q}_{\text{rec}}}{\left(\dot{n}_{\text{fuel},in} \cdot LHV_{\text{fuel}}\right)_{\text{system}_{\text{feed}}}} \quad (6.3)$$

where P_{DC} is the stack dc power developed, $P_{\text{net},AC}$ is the net system AC power, \dot{Q}_{rec} is the amount of thermal energy recuperated, $\dot{n}_{\text{fuel},in}$ is the molar system fuel flowrate, and LHV_{fuel} is the fuel heating value. A 2nd Law (or exergetic) efficiency for cogeneration systems is preferable to Equation (6.3) because of the non-equivalency of thermal and electrical energy, however, Equation (6.3) has been selected as a measure of system performance because of industry convention.

6.2.2. Fuel pre-reformer

The fuel pre-reformer is a small packed bed reactor that integrates fuel preheating and pre-reforming processes. The pre-reformer converts higher hydrocarbons to methane and a fraction of the methane to hydrogen. Thermal energy is required to drive the endothermic partial reforming of methane and decomposition of higher hydrocarbons. Figure 6.1 depicts a general schematic diagram of the hardware component.

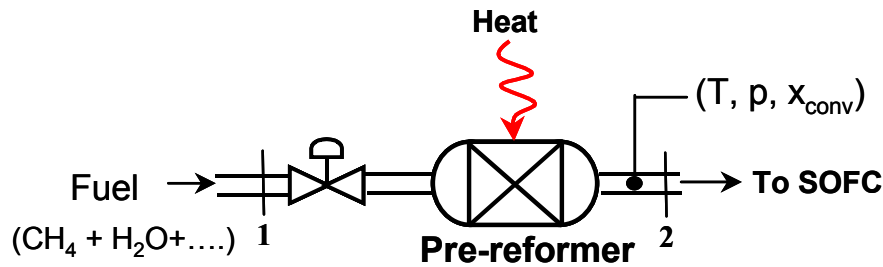
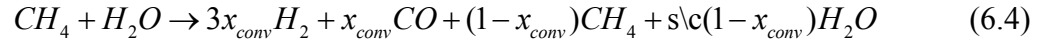


Figure 6.1 Schematic diagram of pre-reformer

Three processes are considered in the pre-reformer: (1) preheat of fuel-steam mixture to the desired pre-reformer temperature, (2) partial conversion of methane, and (3) water-gas shift

equilibration. These processes are modeled as occurring in series. Steam reforming of methane proceeds according to the reaction $CH_4 + H_2O \rightarrow 3H_2 + CO$. For partial reforming, the reforming reaction is written as,



where x is the extent of methane conversion and s/c is the molar steam-to-carbon ratio. The concentration of reactants for the subsequent water-gas shift process ($CO + H_2O \rightarrow H_2 + CO_2$) is then determined from reaction Equation (6.4). For example, $\dot{n}_{CO,i} = \dot{n}_{CO,1} + x_{conv}\dot{n}_{CH_4,1}$, where $\dot{n}_{CO,i}$ represents an intermediate species. Mass balances are then written as,

$$\begin{aligned} \text{Carbon:} \quad & \dot{n}_{CO,i} + \dot{n}_{CO_2,i} = \dot{n}_{CO,2} + \dot{n}_{CO_2,2} \\ \text{Hydrogen:} \quad & \dot{n}_{H_2,i} + \dot{n}_{H_2O,i} = \dot{n}_{H_2,2} + \dot{n}_{H_2O,2} \\ \text{Oxygen:} \quad & \dot{n}_{CO,i} + 2\dot{n}_{CO_2,i} + \dot{n}_{H_2O,i} = \dot{n}_{CO,2} + 2\dot{n}_{CO_2,2} + \dot{n}_{H_2O,2} \end{aligned} \quad (6.5)$$

Pre-reformer outlet concentration is then determined from equilibrium thermodynamics using the following relations,

$$K = \left(\frac{\dot{n}_{H_2} \cdot \dot{n}_{CO_2}}{\dot{n}_{CO} \cdot \dot{n}_{H_2O}} \right)_2 \quad (6.6)$$

$$\ln(K) = \frac{\Delta G_{wgs}}{R_u T} \quad (6.7)$$

where K is the equilibrium constant, ΔG_{wgs} is the change in Gibbs free energy of reaction, R_u is the universal gas constant, and T is the gas temperature. Since CH_4 does not participate in the water-gas shift reaction, the number of moles of methane leaving the pre-reformer is frozen, i.e., $\dot{n}_{CH_4,2} = (1-x_{conv})\dot{n}_{CH_4,1}$.

For steady-state system simulation of the pre-reformer throughout the operating range, it has been assumed that a zero-dimensional model incorporating chemical equilibrium calculations will suffice. The model requires that the extent of methane conversion be specified and the resulting reactor product gas is then determined by using water-gas shift equilibrium on the remaining gas constituents. This method of determining reactor product gas composition was compared against the method of Gibbs energy minimization for 100% methane conversion and found to be in good agreement. At present, an equilibrium routine is sufficient for steady-state simulation objectives as the reformat composition of pre-commercial reformers operating at design load is very near the equilibrium composition [3, 4]. The pre-reformer equation set is developed as an EES module and is called in the finite-difference cell model. The EES module program equations can be found in Appendix III.

6.2.3. *Desulphurizer*

The desulphurizer is a packed bed reactor in which zinc oxide is used to catalytically promote the removal of sulphur compounds that were added by natural gas utilities as odorants [2]. As the heat and mass changes across the desulfurizer unit are small relative to the bulk flow of fuel, modeling the reactor is not considered. However, a relatively large pressure drop is incurred across the reactor [2] and the magnitude of the pressure drop is estimated at design conditions from literature data [2, 6]. At off-design conditions, the pressure drop through the desulphurizer is estimated by assuming the pressure loss is proportional to the square of the volumetric flowrate. This assumption is a good one as the pressure drop in a packed bed reactor is proportional to the square of the superficial velocity as described in the relation below,

$$\Delta p = f \cdot \frac{L_t}{d_p} \cdot \rho \cdot u_s^2 \quad (6.8)$$

where L_t is the reactor tube length, d_p the catalyst particle diameter, ρ the fuel gas density, and u_s the superficial mass velocity.

6.2.4. Fuel compressor, air blower, and water pump

The work required to supply the system process gases and water is determined from the general equation,

$$\dot{W}_{input} = \frac{\dot{V} \cdot \Delta P}{\eta_s} \quad (6.9)$$

where \dot{V} is the volumetric flow of the fluid, ΔP is the pressure rise of the device, and η_s is the isentropic efficiency. The required system pressure rise is estimated from summing the individual component pressure drops. With the pressure rise specified, two outputs are desired from the fuel compressor component model, the required work input and the outlet fuel gas temperature. Using Equation (6.9) and assuming that the compressor operates adiabatically, the power input (\dot{W}_{comp}) into the compressor is determined from,

$$\dot{W}_{comp} = \frac{\dot{V}_{fuel} \cdot \Delta P_{fuel,sys}}{\eta_{s,comp}} \quad (6.10)$$

where \dot{V}_{fuel} is the volumetric flowrate of the fuel gas entering the compressor, $\Delta P_{fuel,sys}$ is the required fuel-side system pressure rise, and $\eta_{s,comp}$ is the isentropic efficiency of the compressor. The outlet state of the compressor is determined from the definition of isentropic compression efficiency, which is stated as,

$$\eta_s = \frac{(\bar{h}_{2s} - \bar{h}_1)}{(\bar{h}_2 - \bar{h}_1)} \quad (6.11)$$

where, \bar{h}_1 and \bar{h}_2 are the molar specific enthalpies of the inlet and outlet state, respectively, and \bar{h}_{2s} is the enthalpy at the outlet state for an isentropic compression process. The isentropic compressor efficiency was chosen to be 70%. To calculate \bar{h}_{2s} it is necessary to determine the isentropic temperature, T_{2s} , at the outlet state. This was accomplished using the relationship for a polytropic compression process,

$$T_{2s} = T_1 \cdot \left(\frac{P_2}{P_1} \right)^{\left(\frac{k-1}{k} \right)} \quad (6.12)$$

where T_1 is the inlet fuel gas temperature, P_1 and P_2 are the inlet and outlet gas pressure, respectively, and k is the specific heat ratio of the gas mixture. With T_{2s} calculated from Equation (6.12), \bar{h}_{2s} can then be determined from an equation of state where $h_{2s}=h(T_{2s})$.

Like the fuel compressor model, the air blower model makes use of Equation (6.9),

$$\dot{W}_{blow} = \frac{\dot{V}_{air} \cdot \Delta P_{air,sys}}{\eta_{s,blow}} \quad (6.13)$$

where \dot{V}_{air} is the volumetric air flowrate, $\Delta P_{air,sys}$ is the system air-side pressure rise required, and $\eta_{s,blow}$ is the isentropic blower efficiency. The blower outlet air temperature is also determined using Equations (6.11) and (6.12).

The pressure rise for both fuel- and air-side are determined from summing component pressure drops which were obtained from several literature references [5, 6]. The efficiency of the fuel compressor and air blower will vary with their respective loading. The part-load performance for these components is based on Department of Energy ancillary equipment target values for fuel cell vehicle technology development [7]. Figure 6.2 presents the DOE target values (data points) and a curve-fit expressing component efficiency as function of % of rated flow.

The water pump (and steam generator) is used to supply water for methane reforming in systems which do not make use of anode gas recycle. The work input required to pump the water is also determined from Equation (6.9). The efficiency of the water pump is considered to be constant with load variation.

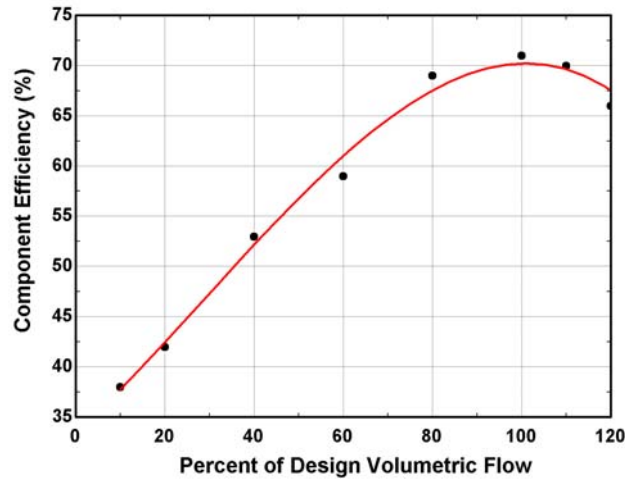


Figure 6.2 BOP rotating equipment efficiency performance map

Table 6.1 presents the component pressure drops employed throughout the present study. Once a system design is established, the system pressure drop will vary with the operating point of the cell-stack and is typically proportional to the square of the volumetric gas flow. Changes in system pressure drop due to changes in the volumetric gas flow through the plant were estimated using the relation,

$$\Delta P_{sys} = \Delta P_{design} \cdot \left(\frac{\dot{V}_{gas}}{\dot{V}_{design}} \right)^2 \quad (6.14)$$

Insertion of Equation (6.14) into (6.13) or (6.10) indicates a cubic dependence of blower and compressor power requirements on the volumetric gas flow*. The system cooling airflow is an order of magnitude greater than the system fuel flow. Thus, the system parasitic power is very sensitive to the amount of cooling air required by the fuel cell stack module. This relationship gives further insight into the advantage of internal reforming SOFCs over fuel cell systems employing external reforming. That is, because the endothermic fuel reforming reaction acts as a heat sink for the cell-stack, less cooling air and fan horsepower are required.

* After system simulation using Equation (6.14), the required blower pressure rise at off-design conditions (in particular, at greater than design flow conditions) was found to be too strong, therefore the exponent was reduced from a value of 2 to 3/2.

Component pressure drop data was adapted from that presented in Riensche et al., [5] and A.D. Little [6]. In general, component pressure drop information is approximate and strict adoption of the pressure drops presented in the aforementioned studies is not followed due to differences in specific equipment designs, ratings, and operating points. Additionally, when anode or cathode gas recycle is employed in the system design, the jet pump/ejector model described in section 6.2.6 is utilized to establish driving pressure requirements.

Table 6.1 SOFC Component Pressure Drops [5,6]

Component	Pressure drop mbar (in. H₂O)
Air Filter	10 (4")
Air preheater (hot and cold side)	100 (40")
Boiler	15 (6")
Catalytic combustor	20 (8")
Cell-stack (fuel side)	20 (8")
Cell-stack (air side)	30 (12")
Desulphurizer	100 (40")
Fuel pre-reformer (fuel-side)	50 (20")
Fuel pre-reformer (exhaust gas)	25 (8")
Hot water tank (heat recovery)	10 (4")
Piping, elbows,.. (~25eq. ft)	5 (2")

6.2.5. *Air and fuel preheaters*

The simulation of process gas heat exchangers assumed constant effectiveness versus load performance. The definition of heat exchanger effectiveness is,

$$\varepsilon = \frac{q_{act}}{q_{max}} \quad (6.15)$$

where q_{act} is the actual heat transferred in the gas-to-gas heat exchanger and q_{max} is the maximum amount of heat that could have been transferred had the hot inlet gas stream temperature been reduced to that of the cold inlet gas stream temperature. The heat transferred in the air preheater is expressed as,

$$\dot{Q}_{AP} = \varepsilon_{AP} \cdot \dot{n}_{air} \cdot c_{p,air} \cdot (T_{h,i} - T_{c,i}) \quad (6.16)$$

where \dot{n}_{air} is the molar flow of fresh air entering the system, $c_{p,air}$ is the molar specific heat of the air, $T_{h,i}$ is the hot gas entering the air preheater, and $T_{c,i}$ is the cold air supplied.

The design air preheater effectiveness is dictated by the selection of process air temperature into the fuel cell stack, outlet exhaust gas temperature coming from the fuel gas heater/pre-reformer, and the air blower outlet temperature. These process temperatures are set by the required cell-stack design operating conditions (i.e., voltage, temperature, and fuel utilization). The effectiveness of the air preheater is assumed to be constant once determined for the design point.

A similar approach is used for the preheating section of the integrated fuel preheater/pre-reformer where equations of the same form as Equations (6.15-6.16) are employed. Steam generator effectiveness is assumed to be constant with load.

6.2.6. *Jet pump/Ejector**

The use of jet pumps (or ejectors) for fuel cell exhaust gas recycling is a useful system design concept that is advantageous for increasing system efficiency while reducing capital costs (see Chapter 8). The operating concept of the jet pump is to use a high-pressure gas stream to entrain gas flow at a lower pressure by momentum transfer. Figure 6.3 depicts the jet pump concept for mixing preheated fresh air and recycled hot cathode exhaust gas.

* The literature on these devices often refers to “jet pumps” for those devices that employ liquids and “ejectors” for those which use gases. In the present study, the term “jet pump” is used interchangeably with “ejector.”

The jet pump model assumes adiabatic operation with steady, fully developed turbulent (flat) velocity profiles, negligible shear stresses on the pipe wall, no changes in potential energy, and ideal gas behavior with two inlets and one outlet as shown in Figure 6.3. The inlet planes (1a) and (1b) are chosen to be the cross-sections at which the fluids first begin to mix. The outlet plane (2) is chosen far enough downstream that complete homogeneous mixing has occurred. Simulating the jet pump operation requires that mass, momentum, and energy balances between these two locations be developed.

$$\text{Mass:} \quad \dot{m}_{1a} + \dot{m}_{1b} = \dot{m}_2 \quad (6.17)$$

$$\text{Momentum:} \quad (\dot{m}_{1a} v_{1a} + p_{1a} A_{1a}) + (\dot{m}_{1b} v_{1b} + p_{1b} A_{1b}) = \dot{m}_2 v_2 + p_2 A_2 \quad (6.18)$$

$$\text{Energy:} \quad \dot{m}_{1a} \cdot \left(h_{1a}(T_{air}) + \frac{v_{1a}^2}{2} \right) + \dot{m}_{1b} \cdot \left(h_{1b}(T_{recyc}) + \frac{v_{1b}^2}{2} \right) = \dot{m}_2 \cdot \left(h_2(T_{mix}) + \frac{v_2^2}{2} \right) \quad (6.19)$$

where \dot{m}_i is the mass flow at location i , v is the velocity of the gas, p is the static pressure, A is the cross-sectional flow area, and h_i is the gas enthalpy at location i . The set of Equations (6.17-19) are also applied for jet pump induced anode gas recycling. The jet pump equation set is developed in EES and the program equations can be found in Appendix III.

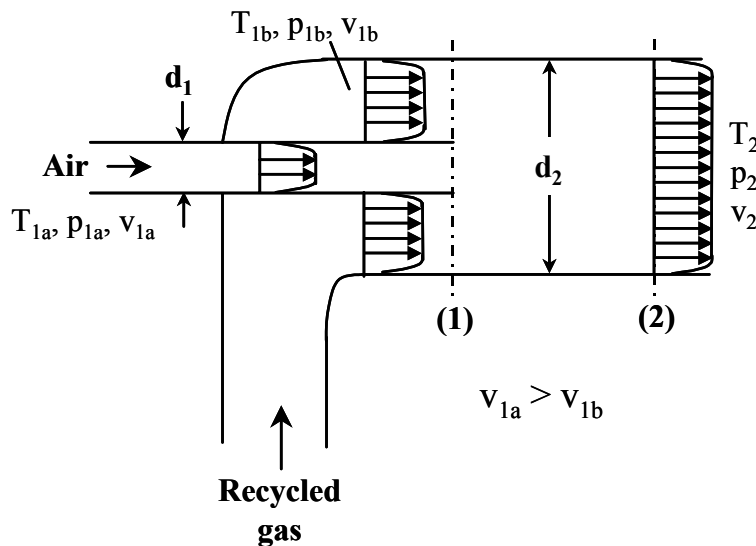


Figure 6.3 Schematic diagram of recycle jet pump [8]

6.2.7. DC/AC inverter

The present inverter model is a simple one. It uses a constant efficiency performance characteristic as a function of load and thus, a simple energy balance is the only pertinent equation. The use of constant efficiency appears reasonable as inverters generally achieve maximum efficiency at 1/3 of maximum power and the efficiency change with load over the range from 20-100% of rated power is less than 3% [9]. Ulleberg's measurements [10] on a DC/AC inverter in a demonstration renewable power plant also support this efficiency performance characteristic. The efficiency selected for residential-scale inverters is 92%. In actuality, present day inverters for small-scale applications (1-20 kW) achieve efficiencies between 87-94% depending on load and inverter type [11, 12]

6.2.8. Hot water storage tank

A two-tank fuel cell thermal energy recovery arrangement is shown in Figure 6.4. Waste heat from the solid oxide fuel cell is directed into Tank 1 where at design conditions heat recovery (sensible only) lowers the fuel cell stack gas from near 400°C to about 60°C. Depending on the temperature of Tank 1, supplementary heating may take place in Tank 2 to ensure a 60°C hot water delivery temperature to the residence. This design concept enables continuous heat recovery irrespective of the domestic hot water load.

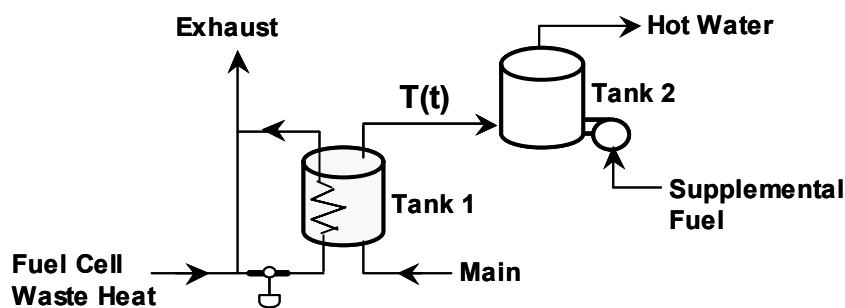


Figure 6.4 Two-Tank Fuel Cell Thermal Energy Recovery Concept

The thermal storage configuration of Figure 6.4 is time-dependent. Tank 2 was modeled without any storage (i.e., instantaneously). Tank 1 was modeled using a fully-mixed, single-node scheme. The unsteady energy balance for Tank 1 is expressed as,

$$m_w \cdot c_{p_w} \cdot \frac{dT}{dt} = \varepsilon \cdot \dot{m}_g \cdot \bar{c}_{p_g} \cdot (T_g - T) + \dot{m}_w \cdot \bar{c}_{p_w} (T_s - T) - UA_{loss} \cdot (T - T_o) \quad (6.20)$$

where,	\bar{c}_{p_w}	specific heat of the water
	\bar{c}_{p_g}	average specific heat of fuel cell exhaust gas
	\bar{c}_{p_w}	average specific heat of heated water
	ε	storage tank heat exchanger effectiveness
	\dot{m}_g	mass flowrate of fuel cell exhaust gas
	m_w	mass of water in storage tank
	\dot{m}_w	mass flowrate of hot water from Tank 1 to the load
	T_g	fuel cell exhaust gas temperature entering tank 1
	T	time-dependent temperature of Tank 1
	T_s	water mains supply temperature
	T_o	ambient temperature outside of tank
	UA_{loss}	tank UA heat loss performance characteristic

The first term on the left hand side of (6.20) expresses the rate of energy accumulation in the tank. The first term on the right hand side of Equation (6.20) represents the heat transfer rate from the fuel cell gas to the tank water. The second term represents the rate of energy removal from the tank in the form of hot water; the final term represents the heat loss from the tank to the ambient air. The tank temperature, T , can be calculated from integration of Equation (6.20) as follows,

$$T = T_i + \int_0^t \frac{dT}{dt} dt \quad (6.21)$$

where limit of integration, t , is the time of interest. The heat exchanger effectiveness, ε , in Equation (6.20), is a function of time as it depends on the amount of heat recovered at any instant divided by the maximum that could be recovered if the fuel cell exhaust gas was brought to the water main temperature. The actual and maximum amount of heat recovery are determined from,

$$\dot{Q}_{HR} = UA_{\text{tank}} \cdot \left(\frac{(T_g - T) - (T_{g,o} - T)}{\ln \left(\frac{T_g - T}{T_{g,o} - T} \right)} \right) \quad (6.22)$$

$$\dot{Q}_{HR_{\text{max}}} = C_{\text{min}} \cdot (T_g - T_s) \quad (6.23)$$

where UA_{tank} is the tank heat transfer performance characteristic, $T_{g,o}$ is the tank outlet fuel cell gas temperature, and C_{min} is the minimum heat capacity rate of the two fluids in the heat exchanger (tank). The tank UA in Equation (6.22) is largely dependent on the mass flow rate of fuel cell gas and is determined from relating it to reference values as follows,

$$UA_{\text{tank}} = UA^* \cdot \left(\frac{\dot{m}_g}{\dot{m}_g^*} \right)^{0.8} \quad (6.24)$$

where the star values in (6.24) are reference values determined from the system design point. The outlet gas temperature, $T_{g,o}$, is determined from a simple energy balance on the fuel cell gas,

$$\dot{Q}_{HR} = \dot{m}_g \cdot \bar{c}_{p_g} \cdot (T_g - T_{g,o}) \quad (6.25)$$

6.3 Cost Model

6.3.1. Fuel cell cost-of-electricity

A cost model that incorporates production cost estimates for solid oxide fuel cells was developed. The model makes use of component costs, utility costs (grid electricity and natural gas), interest rates, expected return-on-investment, system efficiency, and calculates the system capital and operating costs. From these costs, a fuel cell cost-of-electricity (COE) is computed. The fuel cell COE is then utilized as an optimization parameter for system design.

In a combined heat and power (CHP) system, the cost of electricity is dependent on the amount of thermal energy recovered. This amount is reflected as a “heat credit.” The COEs

(expressed in ¢/kWh) for electric-only and CHP systems can be determined from the contributions of capital and operating costs and are given by [13],

$$\text{Electric-only: } COE_1 = k_1 \cdot \frac{(R_F \cdot C_{sys,1} + M_C)}{C_F} + k_2 \cdot \frac{F_c}{\eta_{sys,e}} \quad (6.26)$$

$$\text{Cogeneration: } COE_2 = k_1 \cdot \underbrace{\frac{(R_F \cdot C_{sys,2} + M_C)}{C_F}}_{\text{capital and maintenance cost}} + k_2 \cdot \underbrace{\frac{F_c}{\eta_{sys,e}}}_{\text{fuel cost}} - k_2 \cdot \underbrace{\frac{F_{th} \cdot \varepsilon_H \cdot F_c}{\eta_{sys,e} \cdot \eta_R}}_{\text{thermal energy credit}} \quad (6.27)$$

where R_F is the capital recovery factor, $C_{sys,1}$ and $C_{sys,2}$ are the unit fuel cell system cost for electric-only and cogeneration systems in \$/kW, respectively, C_F is the electric capacity factor, M_C is the unit annual maintenance cost in \$/kW, F_c is the unit fuel cost in \$/MMBtu, $\eta_{sys,e}$ is the fuel cell system electric efficiency (lower heating value basis), ε_H is the heating or thermal energy recovery efficiency, F_{th} is the fraction of thermal energy from the fuel cell system that can be used, η_R is the efficiency of the thermal source that is displaced by the exported thermal energy of the fuel cell system, and k_1 and k_2 are unit conversion constants. ε_H is equivalent to $(\eta_{cogen} - \eta_{sys,e})$, where η_{cogen} is the system cogeneration efficiency. It should be noted that for on-site distributed power generation, transmission and distribution costs do not factor into the cost of electricity.

The capital recovery factor is based on the discount rate, i_d , and the life of the fuel cell plant, n , and is expressed as,

$$R_F = \frac{i_d \cdot (1 + i_d)}{(1 + i_d)^n - 1} \quad (6.28)$$

where the discount rate is the sum of the interest rate (cost of capital) and the return on investment. The cost of capital was set to 8% and a return on investment goal of 12% (before taxes) giving a discount rate of 20%, which would yield a payback of approximately five years for a capacity factor of 100%.

Table 6.2 5 kWe System Capital Cost Data¹

	Parameters				
	Reference Cost		Reference variable	Reference size	Scaling exponent
Component	Unit cost (\$/kWe)	Total cost (\$)			
Cell hardware ²		\$500/m ²			0
Inverter	250		P_{net}	5 kW	-0.22
Air Preheater		5350	UA	2.0 kW/K	0.83
Air Blower		2950	\dot{W}_{blow}	2.67 kW	0.83
Fuel Processing ³		1950	\dot{m}_{fuel}	8.7 kg/h	0.67
Catalytic combustor	20				0
Jet pump/ejector		25			0
Instrumentation & Controls ^{4,5}		300		60 gallon	0
Hot Water Tank ⁵		350			0
Miscellaneous ⁶	50				0
Fabrication/Assy ^{5,6}		250			0
System Life = 20 years					
Cell Life = 5 years					

¹ 2001 USD, ² 800°C cost shown (cell costs are a decreasing function of temperature.) ³ Includes desulfurizer and catalyst, fuel compressor, preheat/pre-reformer, and ejector. ⁴ Includes startup burner, boiler, and N₂ purge system. ⁵ Fixed cost. ⁶ Includes piping, valves, wiring, and insulation, etc.

The system capital cost is estimated from summing each of the component costs,

$$C_{sys} = C_{FC} + C_{FP} + C_{AP} + C_{Blow} + C_{CC} + C_{INV} + C_{tank} + C_{IC} + C_{Misc} + C_{Fab} \quad (6.29)$$

where C_{FC} is the fuel cell stack unit cost, and C_{FP} is the fuel processing unit cost including fuel compressor, pre-reformer, jet pump/ejector, desulphurizer, and catalyst. The desulphurizer requires the catalyst to be replaced every 4 years and this replacement cost is

also included. Finally, C_{AP} , C_{Blow} , C_{CC} , C_{INV} , and C_{tank} are the unit costs for the air preheater, air blower, catalytic combustor (afterburner), inverter, and hot water storage tank, respectively. The last three terms in Equation (6.29) represent the costs associated with instrumentation and controls (C_{IC}), piping, valves, wiring, and insulation (C_{Misc}), and fabrication and assembly (C_{Fab}). The unit costs are summarized in Table 6.2. The values shown are for a 5 kW planar solid oxide fuel cell systems. Cost differences between the two system ratings are described in more detail in §6.3.2.

The stack manufacturing costs given by Chen et al., [14] are employed in this analysis and are based on 200 MW/yr production levels. These manufacturing cost estimates were also found to be consistent with an Arthur D. Little study [6]. SOFC stacks are assumed to have an operational life of 5 years with a salvage value of 1/3 the original investment. These considerations translate into a replacement of the entire fuel cell stack three times during the life of the plant. In general, the SOFC manufacturing costs are dependent on the materials employed and the cell component thicknesses. The economy of the cell stack is based on the use of Ni/Zr cermet anode (100 μm thick), yttria-stabilized zirconia electrolyte (5 μm), strontium-doped lanthanum manganite cathode (100 μm), and either 1mm stainless steel (700-800°C), high alloy metal (900°C), or La Chromite (1000°C) for the interconnect depending on operating temperature. Physical cell area is 100 cm^2 and cell electroactive area is 80 cm^2 .

6.3.2. *Balance-of-plant costing*

There can be significant uncertainty in estimating equipment costs, especially for small capacities as required for residential-scale systems. Factors, such as component size and availability, hardware technology status, purchase volumes, supplier contracts, and competitive bidding will affect hardware cost estimates. Nevertheless, system cost estimates that take into account economies of scale and production can be made to within about $\pm 30\%$ of the actual system cost [6]. The balance-of-plant costs are adapted from Lundberg [2] and A.D. Little (ADL) estimates [6] as these two studies often represented the high and low cost figures. Cost values were updated to 2001 US\$ using published data from the Chemical Engineering Plant Cost Index [15].

The inherent nature of system design necessitates a variation of process parameters to find optimal operating points. The variation of parameters, such as airflow rate, fuel cell operating voltage, fuel utilization, etc., result in changes in the required equipment capacity. Thus, equipment cost must be scaled appropriately depending on their size. Scaling of balance-of-plant capital costs for the parametric optimization studies followed the cost scaling techniques detailed in Boehm [16], Perry et al., [17], and Peters et al., [18]. The cost scaling equation employed is based on using reference cost and size data and is expressed as,

$$C_{new} = C_{ref} \cdot \left(\frac{S_{new}}{S_{ref}} \right)^m \quad (6.30)$$

where C_{new} is the new cost, S_{new} is the new capacity, C_{ref} and S_{ref} are the reference cost and capacity, respectively, and m is the cost scaling exponent. BOP cost scaling exponents were estimated from the economic data of Lundberg [2] (see Figure 6.5) who performed cost analyses for SOFC systems ranging from 50 kW to 2000 kW. The reference costs, sizes, and scaling exponents are summarized in Table 6.2. Reference costs were chosen using unit costs (\$/kWe) for variables where the size of the unit was judged to be directly related to the electric power output of the system. Otherwise, the total component reference cost was employed. In either case, the scaling exponents were the same.

Figure 6.5(a) and (b) depict the cost sensitivity of balance-of-plant equipment to fuel cell electric capacity as reported by Lundberg [2]. The fuel cell capacity data range from 50 kW to 2000 kW. The exponential character is apparent in both figures, particularly for fabrication and assembly, and instrumentation and controls (I&C) costs. Figure 6.5 indicates that these costs can be significant at the sub-10 kW scales. Due to the uncertainties in fabrication and assembly cost estimations for planar SOFC systems, estimates were made from more recent data from A.D. Little [6]. The scaling exponent is then simply determined from the curve fit exponent value shown in Figure 6.5. Note that if the reference cost was chosen to be a *unit* cost, the scaling exponent must be negative to reflect economy of scale. If the scaling exponent was a reference cost was a total cost, then the exponent was simply $m=1+a$, where a is the exponent from the curve-fits shown in Figure 6.5.

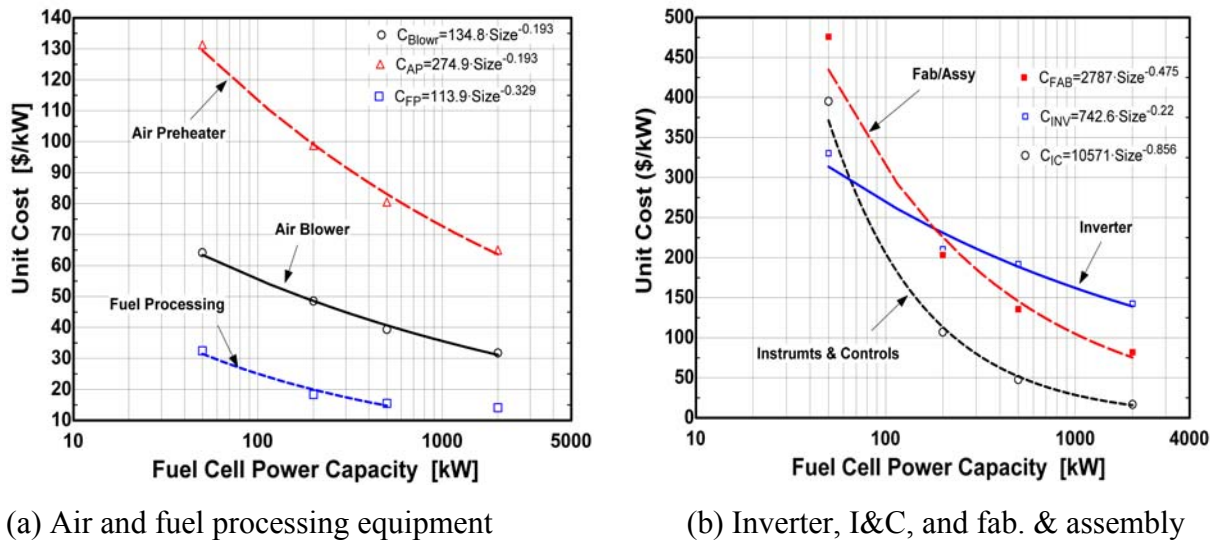


Figure 6.5 Effect of Capacity on Balance-of-Plant Costs

An example of the air blower scaling equation for a 5 kW residential system is,

$$C_{blow} = \frac{2950 \cdot \left(\frac{\dot{W}_{blow}}{\dot{W}_{blow,ref}} \right)^{0.83}}{P_{net}} \quad (6.31)$$

where C_{blow} is the unit blower cost in \$/kW of net fuel cell system power (P_{net}). For variations in system flow, the pressure drop is proportional to the square of the flow and as seen by Equation (6.13), results in a nearly cubic dependence of blower cost on system volumetric flowrate, making blower cost estimates are very sensitive to the reference volumetric flowrate chosen.

The capital costs and exponents selected are summarized in Table 6.2. However, the inverter and instrumentation and controls demonstrate extremely high unit costs at low power capacity. For residential systems of 1-5 kW in size, cost extrapolations using the correlations of Figure 6.5 result in \$520/kW and \$2,666/kW for the inverter and I&C, respectively. These correlations must be re-calibrated as the present small-scale sine wave dc-to-ac inverter (typically employed for solar photovoltaics) costs range from \$875/kW to \$1,075/kW [9,19]. Development of inverter technology for fuel cell applications is accelerating, and future

mature inverter costs have been estimated at \$150-400/kW [9]. Absolute costs associated with I&C show little sensitivity to reductions in system rating. The I&C costs are subject to detailed design and control requirements and therefore, cost estimates were adapted from the more recent ADL analysis. Fabrication and assembly costs can also be substantial and the values shown in Figure 6.5 account for significant manual labor (720 man hours/unit). In this analysis, it is assumed that robotic and other modern manufacturing techniques are employed achieving a fixed cost of \$250 for 1-10 kW sized units, a value more consistent with ADL's analysis.

Annual maintenance cost above and beyond replacement of the cell-stack and fuel preparation catalyst is estimated at 0.5 ¢/kWh. The plant life is assumed to be 20 years with an electric capacity factor of 0.8. BOP equipment depreciation is assumed to be such that at the end of life, the BOP equipment has no salvage value. Fuel cost is geographically dependent, but unless noted otherwise, is generally taken to be \$7/MMBtu. The following additional economic and performance assumptions were made in the analyses:

- SOFC stack manufacturing costs are fixed over the life of the system (i.e., no product cost reduction improvements are included)
- BOP equipment costs (e.g., catalyst cost) are fixed over the life of the unit
- Voltage degradation over the life of the stack unit is not included
- Stack performance (i.e., ASR) improvements over the system life are not considered
- BOP equipment has no salvage value at the end of plant life.
- Fuel costs are fixed, that is no fuel inflation rate is employed
- Installation, transportation (freight-on-board), fabrication and assembly, and contingency costs were not incorporated into system unit capital cost.

Cost modeling equations can be found in Appendix IV. *Despite the large uncertainties in system cost estimates, the utility of this type of analysis (as presented in Chapter 9) lies in the relative changes in capital and operating costs due to changes in system operating and conceptual design.*

6.3.3. Utility Costing

6.3.3.1 Natural Gas

From Equation (6.26), it is apparent that the price of natural gas can significantly influence the fuel cell cost-of-electricity and, as will be seen in Chapter 9, the optimal design operating point of the power generating system. Natural gas prices for residential and commercial consumers are comprised of three main components: (i) transmission costs from wellhead to consumer's local area (city gate), (ii) distribution costs from city gate to user's facility, and (iii) the cost of the gas itself [20]. Table 6.3 shows some average residential and commercial natural gas prices in \$/MMBtu for the Midwest from 1997-2000 [21]. The price variation trend is not resolved by the yearly averages shown in the table. However, residential monthly average natural gas prices for Wisconsin in 1999 show deviations ranging from \$5.47 to \$7.45/MMBtu. In Madison, the price of natural gas from Madison Gas & Electric during the April-October, 2000 time period is about \$7.40/MMBtu [22]. In Illinois, this monthly deviation is larger as prices ranged from \$5.03 to \$9.46/MMBtu in 1999. Monthly gas rates then can vary by as much as $\pm 40\%$. In some cases the higher unit prices occur in the summer months and lower prices in the winter-time. Thus both time and location will effect the price of fuel and ultimately, the payback economics of fuel cell systems.

Table 6.3 Average Natural Gas Prices for Selected States from 1997-2000 [21]

State \ Year	2000		1999		1998		1997	
	Resid.	Comm.	Resid.	Comm.	Resid.	Comm.	Resid.	Comm.
Wisconsin	6.34	5.26	6.19	4.94	6.15	4.70	6.43	5.35
Illinois	5.66	5.36	5.53	5.25	5.33	5.07	5.95	5.43
Minnesota	--	--	--	4.44	5.48	4.39	5.76	4.8
Iowa	6.24	4.33	6.11	4.8	5.96	4.67	6.17	5.18
Michigan	4.93	4.71	5.12	4.84	6.56	4.9	6.37	5.0
U.S. Average	6.68	5.35	6.62	5.27	6.82	5.48	6.94	5.79

6.3.3.2 Electricity

The price structure of the retail electricity rates resembles that of the natural gas industry as electricity bills are comprised of both transmission and distribution, and electricity charges. In the Madison, Wisconsin-area, residential electric service charges are comprised of a fixed customer charge, and distribution and electricity costs. The rates also vary depending on time of year. The electricity unit prices, not including a fixed customer charge of 20.71 ¢/day or taxes, are currently 8.31 ¢/kWh during winter months and 9.18¢/kWh during summer months [22]. Inclusion of the fixed customer charge for a monthly energy usage of 720 kWh, amounts to a further increase of about 10% in the price of electricity (~9.2 – 10.1¢/kWh). The MG&E electricity rates are relatively high when compared against the Wisconsin state average of 7.17 ¢/kWh in 1998. Average 1998 electricity price and monthly bill information for some Midwestern states can be found in Table 6.4.

Commercial electricity rate schedules are more complex including demand and time-of-day charges. Exploration of these price schedules is outside the current scope of analysis, but average commercial rate and monthly bill information can be found in Table 6.4.

Table 6.4 1998 Average Monthly Electricity Rate and Billing Information [23]

State	Residential		Commercial	
	Rate (¢/kWh)	Monthly Bill (\$)	Rate (¢/kWh)	Monthly Bill (\$)
Wisconsin	7.17	50.64	5.87	298.5
Illinois	9.85	68.55	7.77	508.4
Minnesota	7.33	53.36	6.28	246.1
Iowa	8.38	68.21	6.67	264.2
Indiana	7.01	64.85	6.08	353.4
U.S. Average	8.26	71.4	7.41	432.4

6.4 Chapter References

- 6.1 Engineering Equation Software (EES), F-Chart Software, Middleton, WI.
- 6.2 W.L. Lundberg, "Solid oxide fuel cell cogeneration system conceptual design," Final Report, GRI-89/0162, Gas Research Institute, Chicago, IL July (1989).
- 6.3 J.J. Hartvigsen and A.C. Khandkar, "Thermally Integrated Reformer for Solid Oxide Fuel Cells," U.S. Patent No. 5,366,819, Washington, D.C., November (1994).
- 6.4 J.R. Rostrup-Nielsen, *Cat. Sci. and Tech.*, **5**, Springer-Verlag, New York (1984).
- 6.5 E. Riensche, J. Muesinger, U. Stimming, and G. Unverzagt, *J. Power Sources*, **71** (1998) pp. 306-314.
- 6.6 "Conceptual Design of POX / SOFC 5 kW net System", prepared by Arthur D. Little for the Department of Energy, National Energy Technology Laboratory, Morgantown, WV, Final Report, January (2001).
- 6.7 Fuel Cells for Transportation Program, *Contractor's Annual Progress Report*, Vol. 1, U.S. Department of Energy, Office of Advanced Automotive Technologies, Washington, D.C. (1998).
- 6.8 R.B. Bird, W.E. Stewart, E.N. Lightfoot, *Transport Phenomena*, 2nd Edition, John Wiley & Sons, Inc., New York, NY (2002), Chapter 15, Figure 15.3-2, p. 420.
- 6.9 ExelTech, private communication with Ben Baker regarding MX Power Series Inverters, Ft. Worth, TX, August, (2000).
- 6.10 O. Ulleberg, "Stand-alone power systems for the future: Optimal design, operation, and control of solar-hydrogen energy systems," Ph.D. Thesis, Norwegian University of Science and Technology, Trondheim, (1998).
- 6.11 Exeltech, MX Series product brochure, Fort Worth, TX, www.exeltech.com.
- 6.12 Trace Engineering, SW Series Inverter/Charger, Rev. B, Arlington, VA, Figure 19, p. 59, Sept. (1999).
- 6.13 M.W. Ellis and M.B. Gunes, "Status of fuel cell systems for combined heat and power applications in buildings," AC-02-18-2 (RP-1058), preprint article for *ASHRAE Transactions*, vol. 108, Part 1, (2002).
- 6.14 T. Chen, J.D. Wright, and K. Krist, "SOFC Systems Analysis," *Proc. Of the 5th International Symposium on Solid Oxide Fuel Cells (SOFC-V)*, PV97-18, Germany (1997).
- 6.15 *Chemical Engineering* (Magazine), November (1988) and September (2001) issues.
- 6.16 R.F. Boehm, *Design Analysis of Thermal Systems*, John Wiley & Sons, New York, (1987).
- 6.17 *Perry's Chemical Engineer's Handbook*, 7th Ed., McGraw-Hill, New York, NY (1997).

-
- 6.18 M.S. Peters and K.D. Timmerhaus, *Plant Design and Economics for Chemical Engineers*, 3rd Edition, McGraw-Hill, Inc., New York, (1980).
- 6.19 Trace Engineering, Retail price list via Bergey Windpower Co., Norman, OK, June (2000).
- 6.20 Energy Information Administration, "Why do natural gas prices fluctuate so much?," DOE/EIA-X026, Brochure, May (1999).
- 6.21 Energy Information Administration, "Monthly Report of Natural Gas Purchases and Deliveries to Consumers," Form EIA-857, August (2000).
- 6.22 "Residential Rate Schedules," Madison Gas & Electric, Madison, WI, www.mge.com.
- 6.23 Energy Information Administration, data calculated from Tables 14, 15, and 16, "Annual Electric Utility Report," Form EIA-861, (1998).

Chapter Seven Effect of Cell-stack Design and Operating Variables on Steady-state Performance

With verification of the single cell model successfully completed, characteristic performance curves can now be generated for a variety of different design and operating parameters to illustrate the relative importance of each parameter on cell and system performance. Evaluation of the different operating methods to produce a given power output can also be made. These analyses are useful to assist in the selection of cell-stack physical design and operating conditions, as well as controlled variable selection. Additionally, these analyses can offer systems-level perspectives on the how reactant gas processing needs are met, the amount of thermal energy available for recovery, parasitic loads, and heat exchanger area requirements. This chapter focuses on the influence of physical cell design, operating, and control parameters on steady-state cell performance. The influence of these parameters on overall system performance will be taken up in Chapter 8.

The objectives of this chapter are to (i) describe and evaluate the influence of various cell-stack design and operating parameters on steady-state fuel cell and system performance and (ii) evaluate the different methods of regulating fuel cell power output. These objectives are to be met with an eye toward cell-stack and system design interactions from a thermal systems design standpoint. It should be recognized that real world considerations such as operability, control scheme implementation, and cost are also factors in practical system design.

The chapter begins with an overview of cell design and operating parameters and steady-state control methods. The effect of variation of control methods on cell performance is first explored, followed by a presentation of the influence of varying operating parameters on cell performance. Results on the variation of physical cell-stack design parameters is also presented. The relative merits of each operating scenario will provide input to design and operation of SOFCs for residential applications. A short chapter summary is also given to synthesize the results. Economic indicators of performance will be presented in Chapter 9.

7.1 Overview of Cell-stack Parameter Variation and Control

Quantities such as temperature, flowrate, composition, voltage, etc. are process variables that indicate “the state of affairs within, or in the immediate environment of,” a device [1]. To facilitate the following discussion, these variables are classified into inputs, outputs, and parameters for the numeric model. When considering a physical system, the inputs are further classified into control variables and disturbance (or uncontrolled) variables, while the outputs are designated as measured and unmeasured variables.

A *parameter* is defined herein as a model input or boundary condition that remains fixed over an entire range of input values (or individual simulation run) without regard to how such constancy was obtained. A *control variable* is taken to mean an input variable which is at our disposal to manipulate freely (i.e., a “knob”). A *disturbance variable* is a process input which we do not have active control over. A *measured variable* is a process variable whose value is made available by direct on-line measurement and can be used for active control purposes. *Unmeasured variables* are those whose values are not measured at all or frequently enough for active control [1]. Examples of each are presented in the next section.

7.1.1 SOFC sub-system process variables

The model developed in Chapter 4 is a powerful design and simulation tool that can be used to perform many permutations for optimal design and operation of a fuel cell system. Table 7.1 reviews the inputs, outputs, and parameters of the SOFC model. The flexibility of the modeling platform enables some outputs and inputs to be interchangeable with one another and they are noted as such in the table below. The model flexibility also increases the number of potential system control variables when simulating the system. To reduce the number of system control variables in the present study, consideration was given to how a physical SOFC system operates.

Figure 7.1 depicts a schematic of the fuel cell sub-system under consideration and some of the process variables that are likely to be measured when operating a real system. A methane-steam mixture is fed to a pre-reformer before delivery to the SOFC. Preheating of the fuel and air streams is accomplished by the combusted fuel cell tail gas, but is not shown in the

diagram. The process variables measured in a physical system are inlet flowrate and temperature for fuel and air streams, outlet fuel and air temperature, and cell voltage, current, and temperature. These variables as well as unmeasured variables are categorized and listed in Table 7.2. A comparison of Table 7.1 and Table 7.2 indicates that many of the model inputs cannot be actively controlled. In most cases, the steam-to-carbon ratio of the fuel is a fixed parameter and the remaining control knobs are then fuel and air flow.

Table 7.1 SOFC model inputs, outputs, and parameters

Inputs	Outputs
Avg. current density, j_{cell} (or V_{cell})	Cell voltage, V_{cell} (or j_{cell})
Inlet fuel temperature, $T_{f,i}$	Cell power, P_{cell}
Inlet air temperature, $T_{a,i}$	Cell efficiency, η
Cell temp., T_{cell} (or $m_{a,i}$ or ΔT_{air})	Cell temp. distribution, $T(x)$
Fuel utilization, U_f (or $m_{f,i}$)	Cell temp. gradient, $dT/dx(x)$
Fuel steam-to-carbon ratio, s/c	Current density distribution, $j(x)$
Methane conversion, x_{conv}	Outlet fuel and air temps. $T_{f,o}$, $T_{a,o}$
Pre-reformer temp., T_{preref}	Fuel flow, $m_{f,i}$, (or U_f)
	Air flow, $m_{a,i}$ and λ (or T_{cell} or ΔT_{air})
Model Parameters	
Cell geometry	
Cell material properties (e.g., k_s , $c_{p,s}$)	
V-I characteristic (R_{cell} , i_{as} , a , b)	
Reforming reaction rate, \dot{r}_R	
Flow configuration (co- or counter)	

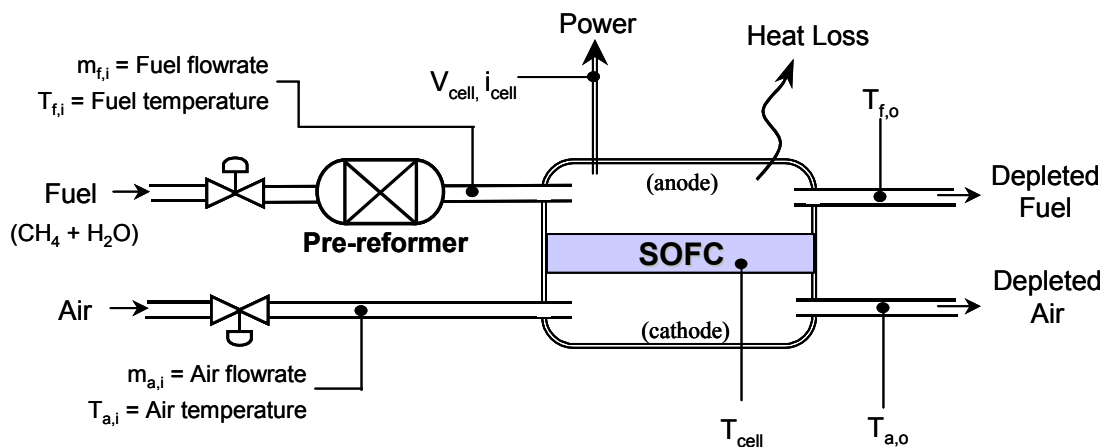


Figure 7.1 Schematic diagram of SOFC sub-system and process variables

Table 7.2 Process variables in the physical SOFC sub-system

Inputs	
Control variables	Disturbance variables
Fuel flowrate, $m_{f,i}$ Air flowrate, $m_{a,i}$ Steam-to-carbon ratio, s/c	Inlet fuel temperature, $T_{f,i}$ Inlet air temperature, $T_{a,i}$ Cell current, i_{cell} (i.e., load) Methane conversion, x_{conv} Pre-reformer temp., T_{preref}
Outputs	
Measured variables	Unmeasured variables
Outlet fuel temp., $T_{f,o}$ Outlet air temp., $T_{a,o}$ Cell temp., T_{cell} (max. or other) Cell voltage, V_{cell}	Heat loss, Q_{loss} Outlet fuel and air flows, $m_{f,o}$, $m_{a,o}$

7.1.2. Fuel cell steady-state operating control

The primary goal of the total SOFC system is to deliver net power. For the sub-system depicted in Figure 7.1, the operating (and/or control) problem could be stated as: *deliver a specified dc power to the inverter while maximizing cell efficiency and ensuring that the maximum allowable cell temperature and in-plane thermal stress are not exceeded.* The basic control variables that enable regulation of fuel cell power output are fuel and air flows (at fixed inlet temperatures). In operating a fuel cell, there are several different ways that one can regulate these flows to achieve a specific power output:

- (1) Fuel and air flow are manipulated to maintain constant fuel utilization for either a prescribed nominal cell temperature, local cell temperature, or air temperature rise ($\dot{m}_f = f(U_f)$ and $\dot{m}_a = f(T_{cell} \text{ or } \Delta T_{air})$)*.
- (2) Fuel and air flow are varied to maintain a constant cell voltage and prescribed nominal cell temperature, local cell temperature, or air temperature rise ($\dot{m}_f = f(V_{cell})$ and $\dot{m}_a = f(T_{cell} \text{ or } \Delta T_{air})$).

* U_f is equal to i/i_{max} where i is measured and i_{max} is a constant determined from knowledge of the composition of the fuel gas feed to the plant.

- (3) Fuel and air are delivered to the cell at a constant feed rate, and fuel utilization and cell temperature vary depending on the load (or current). Here $U_f = f(\dot{m}_f, j_{cell})$ and $T_{cell} = f(\dot{m}_a, j_{cell})$.

The above control methods are designated as control methods (1), (2), and (3). Each method of control must satisfy certain fuel cell design and operation constraints throughout the operating range of interest. Aside from fuel processing requirements, the solid oxide fuel cell operating conditions are primarily constrained by the thermal limitations of the ceramic and metallic cell components. Deleterious temperature-related effects on cell performance and life are associated with exceeding the maximum operating temperature of the cell and the thermal stress in the cell tri-layer.

Considerations for cell temperature limits include:

- sintering of the porous electrodes in localized hot spots
- metallic interconnect durability and chemical stability
- exposure of downstream metallic heat exchange equipment to the high temperature cell exhaust gases.
- Coking of the inlet fuel gas and carbon deposition on the anode material

Sintering of cell electrodes is less of a concern at sub-900°C operating temperatures. However, operation at 800°C is still challenging for most metals, and metallic interconnect durability in the high temperature, oxidizing environment of the gas channels has yet to be demonstrated [2, 3]. While the high temperature performance of metallic interconnects is not well established, information about maximum temperature limitations for process gas heat exchangers downstream of the cell-stack can be useful to establish estimates of the limits. It has been noted that the maximum gas temperature for recuperative process heat exchangers before high cost refractory is needed, is near 850°C [4, 5, 6].

In solid oxide fuel cells, thermal stress of the ceramic cell components is an important criterion for establishing operational limits. During operation, excessive thermal stresses may arise due to steep solid temperature gradients created by either the introduction of ‘cold’ inlet gases or the strong endothermic cooling effect from the rapid reformation of methane gas on

the anode. In either case, high thermal stress may cause cracking or delamination of the cell structure. Cell failure due to delamination is caused by the relative growth or shrinkage of individual cell layers due to their differing thermal expansion coefficients. Thus, regions of high temperature gradients are to be avoided. Presently, there is no consensus on the maximum allowable in-plane cell temperature gradient in a flat planar SOFC. Some researchers estimate thermal gradient values beneath $1^{\circ}\text{C}/\text{mm}$ to be ‘safe’ [7]; however, little experimental evidence has been reported. Thermal stress can also be generated in an individual cell layer (i.e., in the anode, electrolyte, or cathode) by the rate of change of the solid temperature gradient. The derivative (or slope) of the temperature gradient is then of considerable interest as it serves as a gauge of sub-component thermal stress. Again, no quantitative information is available on what the value of the slope should be to ensure no fracture in the cell layer.

Other permanent harmful effects on cell performance include carbon formation in the anode chamber due to cracking of hydrocarbon fuels and oxidation of the nickel-based anode by oxygen anions due to fuel feed failure or very high fuel utilization operation.

7.1.3. *Parameters under study*

The SOFC model described in Chapter 4 enables many permutations to be carried out for selection of optimal physical design, operating, and control parameters. The physical control variables and methods discussed in §7.1.1 and §7.1.2 serve as guidelines on how to carry out an analysis of the influence of certain parameters on cell (and system) performance. Table 7.3 lists the cell-stack parameters and performance indices to be studied.

The physical design parameters under investigation are reactant gas flow configuration (co-versus counter-flow), thermal conductivity of the interconnect, and cell area specific resistance. Other physical cell design parameters, such as cell geometry (rectangular vs. square), channel dimensions, component thickness, etc. can also be investigated with the existing model.

Table 7.3 Parameters and Performance Indices

Cell-stack Parameters		Performance Indices	
Physical Design	Operational	Cell-stack	System
Thermal conductivity	Cell voltage	Cell power	Combustor temperature
Cell area specific resistance	Inlet fuel and air flow	Cell efficiency	System efficiency and net power
	Inlet fuel and air temperature	Fuel utilization	Thermal energy output
	Inlet fuel gas composition*	Nernst potential	Cooling air blower hp
		Cell Distributions: -Temperature -Temp. Gradient	Heat exchanger UA requirements

*fuel gas composition is dictated by pre-reforming conditions (e.g., steam-to-carbon ratio, reactor temperature, and amount of methane conversion).

The cell-stack operating parameters under investigation are cell voltage, inlet fuel and air flow rates, inlet fuel and air temperatures, and inlet fuel gas composition (e.g., via extent of pre-reforming). The choice of operating parameters investigated is dependent on which variables can be regulated with active control measures. The manipulation of these operating parameters results in changes in performance indices, such as cell power, efficiency, temperature and temperature gradient distributions, and fuel utilization. System performance is also indicated by adjustment of the cell operating parameters. These indicators include catalytic combustor temperature, net system power and efficiency, the amount of thermal energy available for cogeneration, cooling air parasitic power, and air preheater heat transfer area. Table 6.1 summarizes the design and operating parameters, as well as cell-stack and system performance indices

7.1.4. Base case inputs and setup

A base case is defined and simulation results are examined to illustrate general fuel cell performance characteristics and to provide a basis for comparison with alternative control methods and operating parameters. The cell configuration under study is a planar design with air and fuel gas streams in a counter-flow configuration. The cell design is of the anode-supported type and employs state-of-the-art materials and the component dimensions as noted

in Table 5.5. The model simulates direct internal reforming using the reforming reaction kinetics given by Achenbach and Riensche [8]. The number of cell gas channels and the channel dimensions follow the IEA benchmark values previously described in Table 5.1. The temperature-dependent polarization characteristics reported by Ghosh et al., [9] have been employed to determine the four performance parameters for use in Equation (4.8).

Table 7.4 Base case model inputs and outputs

Model Inputs	Value
Cell type, dimension	Flat planar, 10 cm x 10 cm
Reactant gas flow configuration	Counter-flow
Interconnect material	Metallic, $k_{\text{cell}}=30$ W/m-K (weighted value)
Fuel inlet temperature	700°C
Air inlet temperature	700°C
Operating pressure	1 bar
Amount of methane conversion	30%
Steam-to-carbon ratio	2.0
Fuel utilization	85%
Nominal cell temperature	800°C
Air gas inlet composition	21%O ₂ , 79% N ₂
Cell voltage	0.35 – 0.8V
Model Outputs (control method 1)	
Fuel feed	0.365 – 4.543 mol/h
Air feed	0.127 – 5.423 mol/h
Fuel gas inlet composition*	19.44% CH ₄ , 2.6 CO, 5.7 CO ₂ , 30.7 H ₂ , 41.5 H ₂ O
Cell power, current, and heat generation	0-80 W; 0-2.3 A/cm ² ; 0-170 W
Cell efficiency	25-62% LHV
Cell temperature and temperature gradient distributions	See Figure 7.5

*based on 30% conversion of methane at water-gas shift equilibrium and with a steam-to-carbon ratio of 2

The fuel feed in the base case simulation consists of 30% pre-reformed methane at the fuel inlet temperature (700°C). The cell current, average cell temperature, fuel utilization, steam-to-carbon ratio, methane conversion, and inlet fuel and air temperatures are specified (i.e., boundary conditions). Fuel and air inputs to the cell are then computed to satisfy temperature

and utilization specifications and will necessarily vary at different operating voltages. Table 7.4 shows the base case model inputs and outputs. The model determines the pre-reformer outlet gas composition by assuming pre-reforming takes place with the water gas shift reaction in equilibrium at the fuel feed temperature of the cell.

7.2 Variation of Control Parameters

The fuel cell will behave differently depending on which variables are controlled during load variation. The three different control methods outlined in §7.1.2 will be explored next.

7.2.1. *Influence of control method (1): constant cell fuel utilization and temperature*

Figure 7.2(a) illustrates the predicted performance map as a function of average cell current density for the base case conditions listed in Table 7.4. As cell current is increased, the cell voltage is reduced due to irreversible losses. The cell power density increases with increasing current until it reaches a maximum power point. As current is increased beyond the point of maximum power, the cell power decreases in response to larger reductions in voltage for each incremental increase in current. The cell performance parameters for this design, operating temperature, and gas composition are estimated to be 0.4 W/cm² power density at 0.7 volts and an area specific resistance of 0.235 Ω-cm². Also plotted in Figure 7.2(a) is the amount of cooling air expressed in air stoichs (λ) (see Equation 3.12). As power generation is increased, larger amounts of cooling air are required to maintain the cell at an average temperature of 800°C. This cooling air flowrate is an important factor for consideration in the design of fuel cell systems because it significantly impacts heat exchanger sizes and parasitic power levels. The behavior of air stoichs with increasing cell current density is non-linear because heat is produced in greater proportions at higher currents (lower voltages) due to the increasing cell polarization and consequent lower cell efficiency.

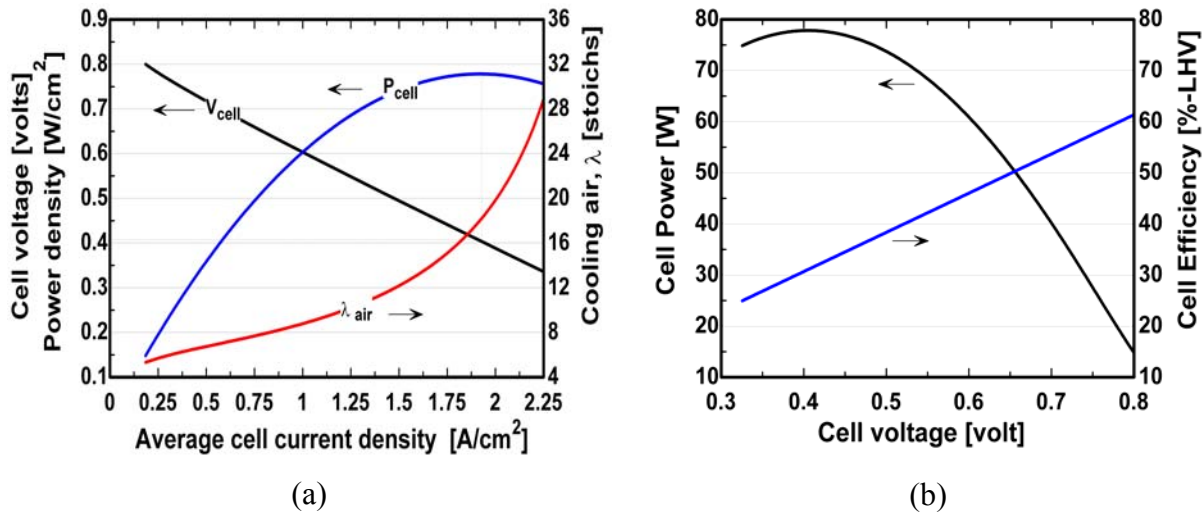


Figure 7.2 (a) Cell voltage, power density, and air stoichs vs. cell current density, (b) Cell power and efficiency vs. cell voltage

The operating voltage is a parameter of interest over cell current because it is often a controlled variable and is more easily correlated with cell efficiency. Figure 7.2(b) illustrates single cell power and efficiency results as a function of cell voltage for the base case scenario. As cell voltage is decreased from 0.8 V, the cell power increases from 15 W to a maximum of 78 W at 0.40 V. Also plotted is cell efficiency versus cell voltage. The cell efficiency is defined as the dc power produced by the cell divided by the fuel energy input to the cell based on the lower heating value of the anode feed gas. Cell efficiency is directly proportional to cell voltage and thus, efficiency increases with cell voltage in a linear fashion as shown. In the base case, the cell efficiency is only 30% at maximum cell power and increases to a value of about 61% for high voltage (0.8 V) operation. As the power is reduced, the cell efficiency increases. The trend of increased efficiency at part-load is advantageous compared to conventional power generation equipment and common among all fuel cell types.

The point of maximum power in Figure 7.2 (a) and (b) can be estimated analytically for simple voltage-current characteristics. The cell power density is expressed by,

$$P'' = V_{cell} j_{cell} \quad (7.1)$$

where j_{cell} is the local current density and V_{cell} is the operating cell voltage. In the case where activation and concentration polarizations are negligible V_{cell} can be written as,

$$V_{cell} = E_N - j_{cell} R_{tot}'' \quad (7.2)$$

where E_N is the Nernst voltage and R_{tot}'' is the total area specific resistance of the cell. Inserting (7.2) into (7.1) we have,

$$P'' = E_N j_{cell} - j_{cell}^2 R_{tot}'' \quad (7.3)$$

Differentiating the above equation with respect to j_{cell} and setting it equal to zero the location of an extremum can be found from,

$$\frac{\partial P''}{\partial j_{cell}} = E_N - 2j_{cell} R_{tot}'' = 0 \quad (7.4a)$$

$$\frac{\partial^2 P''}{\partial j_{cell}^2} = -2R_{tot}'' \quad (7.4b)$$

$$j_{cell} \Big|_{\max P} = \frac{E_N}{2R_{tot}''} \quad (7.5)$$

The second derivative of Equation (7.4a) yields a concave down behavior indicating that a local maximum exists. Solving Equation (7.4) for current, Equation (7.5) shows that the maximum occurs when the current density is equal to the Nernst voltage divided by twice the area specific resistance.

The voltage at which maximum power occurs may be found in a similar manner by solving (7.2) for j_{cell} and inserting into (7.1) to get,

$$P'' = \frac{E_N V_{cell} - V_{cell}^2}{R_{tot}''} \quad (7.6)$$

Differentiating the above equation with respect to V_{cell} and setting it equal to zero, the location of an extremum is determined from the set of following equations,

$$\frac{\partial P''}{\partial V_{cell}} = \frac{E_N - 2V_{cell}}{R_{tot}''} = 0 \quad (7.7a)$$

$$\frac{\partial^2 P''}{\partial j_{cell}^2} = \frac{-2}{R_{tot}''} \quad (7.7b)$$

$$V_{cell}|_{\max P} = \frac{E_N}{2} \quad (7.8)$$

Using the predicted outlet Nernst voltage (0.871) at a typical cell voltage of 0.7 V, and an area specific resistance of 0.235 $\Omega\text{-cm}^2$, Equation (7.5) predicts the point of maximum power to occur at an operating cell current density of 1.85 A/cm^2 . This value is 5.0% above the numerically determined value of 1.95 A/cm^2 . Equation (7.7) estimates the maximum power point at a cell voltage of 0.435 V; a value that is 8.8% above the numerical value of 0.40 V.

The analytical values deviate from the numerical prediction because of several factors. First, the numerical prediction employs a V-I characteristic where activation and polarization losses are present. In this case, Equations (7.5) and (7.7) can only provide estimates of the location of maximum power as differentiation of the V-I relation does not typically allow a closed form solution. The spatial variance in the Nernst voltage, E_N , due to its temperature- and composition-dependence introduces additional inaccuracy as there are many choices for the value in Equations (7.5) and (7.7). Logical choices include the average Nernst potential and the local minimum Nernst potential (which typically occurs at the cell outlet in counter- and co-flow fuel cells [10]). The estimation of E_N for Equations (7.5) and (7.7) is further complicated by the fact that outlet Nernst voltage will vary slightly with operating voltage.

Figure 7.3 depicts a predominately linear behavior for the amount of heat generated in the cell with changing cell voltage. This linear behavior is not surprising as the cell efficiency is also linear with cell voltage. Any non-linearity in heat generation is introduced by the i^2R loss in the cell. The plot also shows the change in air mass flow rate and the molar amount of air stoichs with cell voltage. As the cell voltage is increased, the amount of cooling air required (on both mass and volume bases) to maintain the cell at a nominal temperature of 800°C rapidly increases.

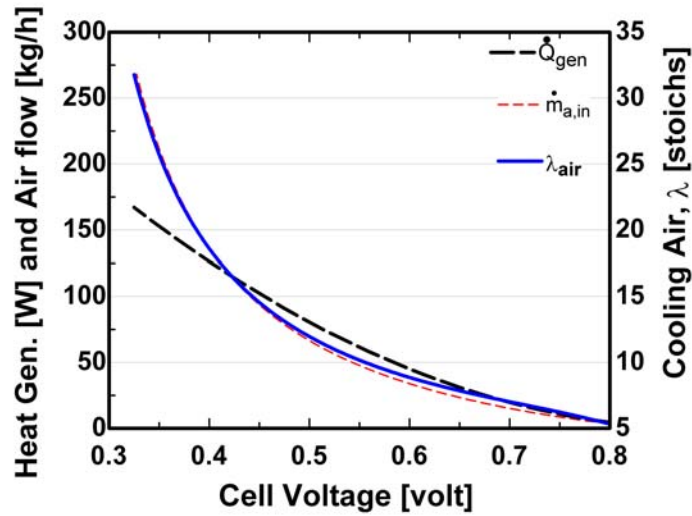


Figure 7.3 Influence of cell voltage on cell heat generation and air flow

The composition distribution of the fuel gas for the base case conditions and an operating cell voltage of 0.7 V is depicted in Figure 7.4(a). The plot clearly shows the effect of internal steam reforming of methane. At approximately 1/3 the length of the cell, the methane is completely reformed. It is interesting to note that the amount of hydrogen generated exceeds the amount that is electrochemically consumed for about first half of the reforming region in the cell. As an intermediate reaction species, the hydrogen concentration increases until reaching a maximum in the reforming region and then decreases with a linear characteristic as the fuel gas proceeds down the remainder of the cell. Carbon monoxide is also an intermediate reaction species (for reforming and water-gas shift reactions) and behaves similarly to hydrogen.

The distribution of cell-solid and gas temperatures for counter-flow of gases is shown in Figure 7.4(b). The cell solid temperature increases from the cooling air inlet (fuel outlet) location until it reaches a maximum value of about 825°C. The maximum cell temperature rise is about 80°C. The location of the peak cell temperature coincides with the region where the endothermic reforming of methane on the anode surface is completed. At the fuel inlet, the cell temperature is suppressed because of the cooling effect that the endothermic reforming reactions generate. In fact, the cooling effect is strong enough that the exiting air

temperature is actually lower than the cell temperature at the fuel inlet. Due to the low thermal capacitance and high heat transfer coefficient ($300\text{-}600\text{ W/m}^2\text{-K}$) of the fuel gas, its temperature quickly changes to that of the cell-solid. The small gas channels also produce high heat transfer coefficients ($150\text{-}250\text{ W/m}^2\text{-K}$) on the air side, but the large amount of cooling air produces a more visible temperature difference between cell-solid and air gas.

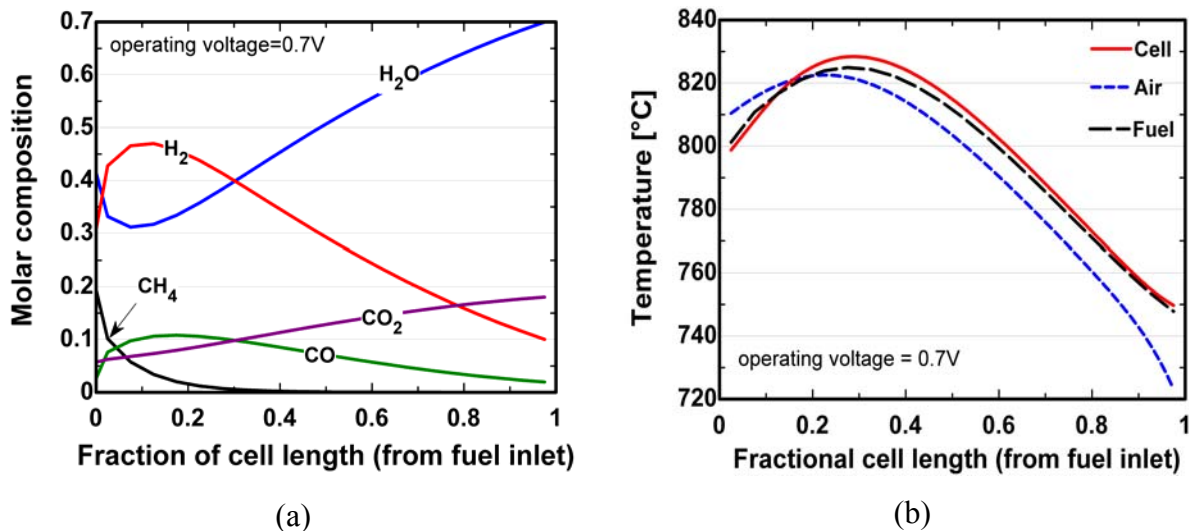


Figure 7.4 (a) Fuel gas concentration distribution, and (b) temperature distributions

The temperature distribution as a function of cell voltage is depicted in Figure 7.5(a). As one might expect the peak cell temperature increases as operating cell voltage decreases (power increase). This trend is maintained from 0.8 V to 0.6 V at which point, a maximum temperature is reached. However, as cell voltage is decreased below 0.6 V, the value of the peak cell temperature is reduced and the distribution becomes more even. This result is unexpected and will be discussed in greater detail shortly. It is also noteworthy that the location of the peak temperature varies within a spatial window of only 1 cm with operating cell voltage. Furthermore, the temperature distributions intersect at 800°C with nearly the same axial location of about 6-6.5 cm downstream of the fuel inlet. This observation is important because it implies that an average cell temperature can be achieved with only one spatially positioned temperature sensor.

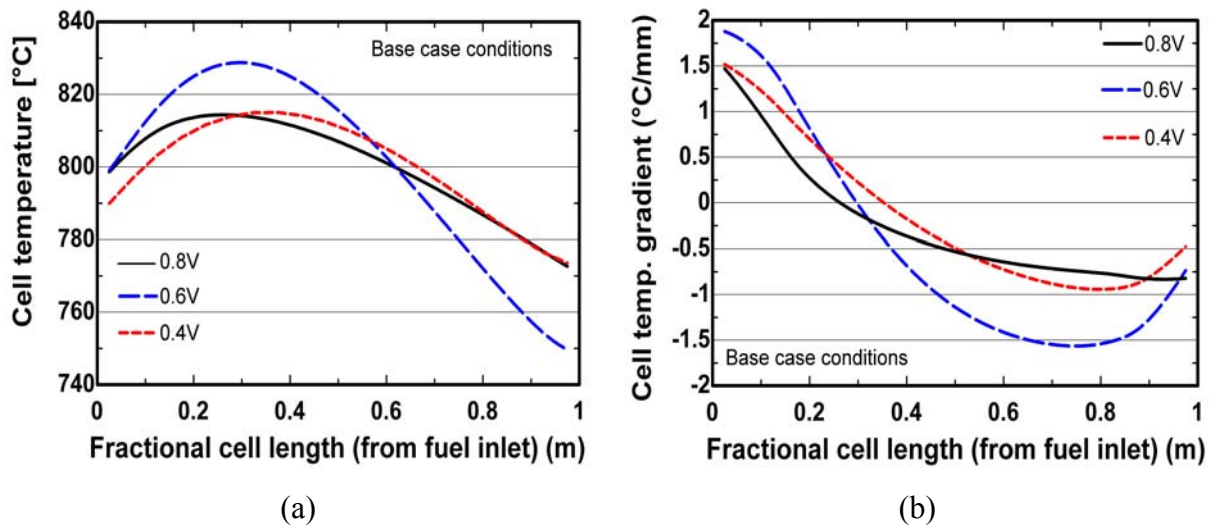


Figure 7.5 (a) Cell temperature distribution and (b) cell temperature gradient distribution as functions of operating voltage

In Figure 7.5(b), a similar trend to that shown in Figure 7.5(a) is observed for plots of temperature gradient distribution. The magnitude of the temperature gradients increases with decreasing cell voltage until a cell voltage of about 0.6 V is obtained. At 0.6 V a peak value of 1°C/mm is obtained in the region near the fuel inlet (air outlet). For the same voltage, the gradient increases to a maximum of about 1.9°C/mm at the fuel inlet (air outlet).

Figure 7.6(a) illustrates that for specification of an average cell temperature of 800°C, the model predicts a maximum cell temperature of about 830°C throughout the operating range of the cell. Figure 7.6(a) also shows the influence of cell voltage on the minimum local cell temperature. At about 0.65 V, the minimum value nearly coincides with the maximum cell temperature. The plot of maximum cell temperature gradient (at any location on the cell) shown in the same figure is explained by the maximum and minimum temperature curves. However, the behavior of decreasing peak cell temperature and peak temperature gradient from 0.6 V to 0.4 V operation is not understood until the ratio of heat generated to the amount of cooling air supplied is examined. Figure 7.6(b) plots this ratio, expressed in units of temperature, as a function of operating cell voltage. As cell voltage is decreased from 0.8 V, the proportion of heat generated to the thermal capacitance of the supplied cooling air increases until about 0.63 V. As operating cell voltage is decreased further the model predicts

that the amount of heat generated will be proportionally less than the amount of cooling air needed to maintain an average cell temperature of 800°C . This is an interesting result as it is counter-intuitive and indicates that operation near the maximum power point (0.4 V) of the cell is feasible from cell temperature and temperature gradient viewpoints.

Up to this point, operating control of the fuel cell has been dictated by maintaining a constant *average* cell temperature and constant fuel utilization. Control based on monitoring a single spatial solid temperature is more practical than the entire temperature field needed to compute an average solid temperature. The results of Figure 7.5(a) indicate that because all temperature profiles intersect at the same axial location (0.06 m downstream of the fuel inlet), it is possible to accomplish an average cell temperature control with only a single temperature sensor. While not shown, it has been computationally verified that maintaining a constant local cell temperature, in lieu of an average cell temperature, yields nearly identical cell performance throughout the operating voltage range.

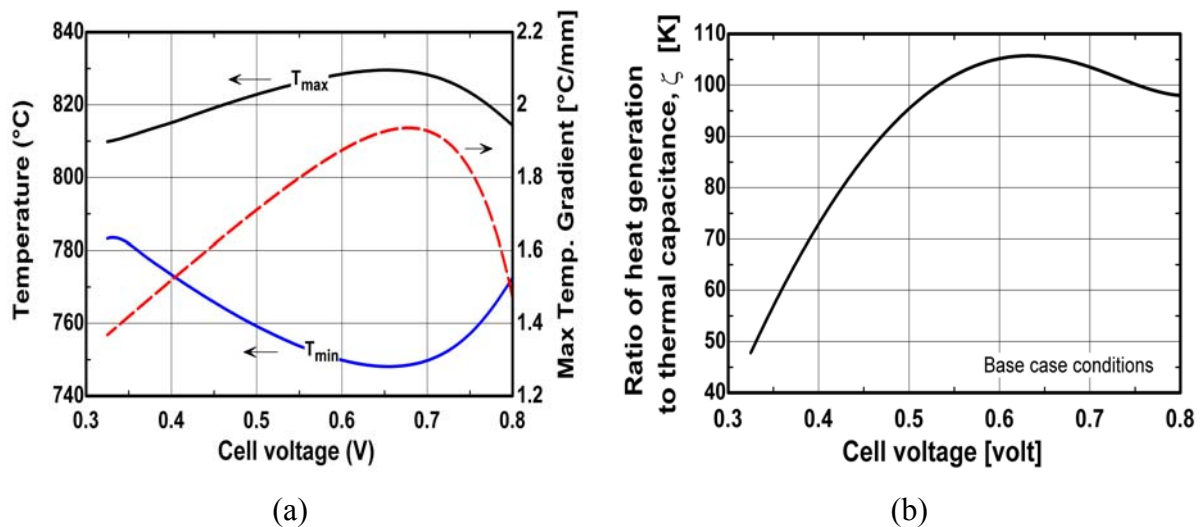


Figure 7.6 (a) Maximum/minimum cell temperatures and temperature gradient and (b) Ratio of heat generation-to-air gas thermal capacitance with varying operating voltage

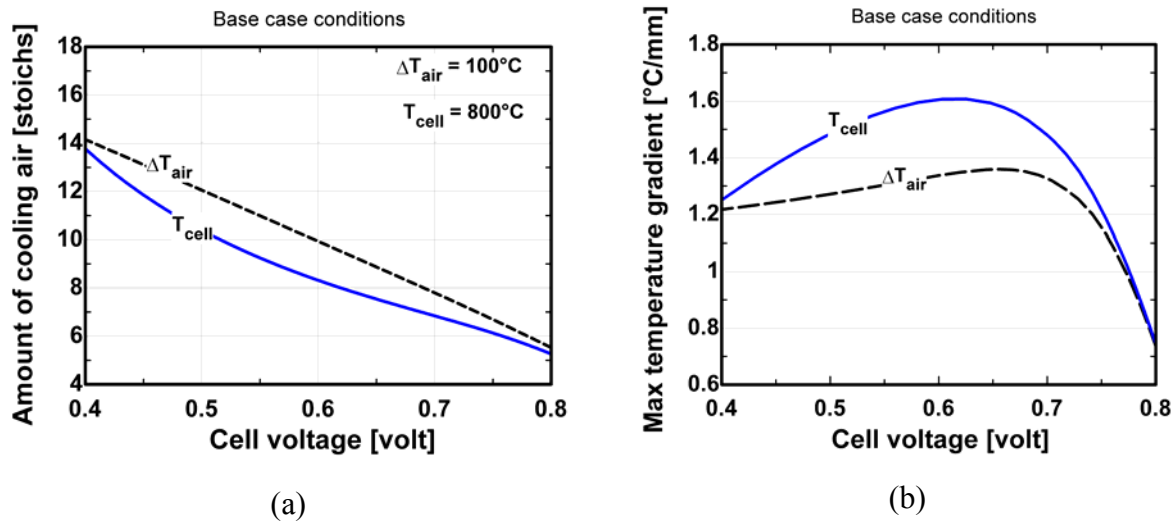


Figure 7.7 (a) Comparison of amount of cooling air and (b) maximum temperature gradient between different controlling variables

Cell temperature can also be controlled indirectly by maintaining a specified air temperature rise from cell inlet to outlet. The often cited value for air temperature rise in an SOFC stack is 100°C . Figure 7.7(a) shows a comparison of the amount of cooling air needed to maintain either a 100°C air temperature rise or a nominal cell temperature of 800°C . Regulation of an average cell-solid temperature offers the advantage of lower cooling air requirements and lower parasitic power (up to 30% lower). The main reason for this difference is that cell-solid temperature control enables a slightly higher average cell temperature and air temperature rise to be maintained. The disadvantage is that the maximum temperature gradient experienced across the operating range is generally higher for cell temperature control versus air temperature rise (Figure 7.7(b)). However, the slopes for the temperature gradient distributions at various operating voltages (an indication of in-plane thermal-induced stress) are nearly identical for the two methods. The practical control choice will depend on the allowable thermal stress but may incorporate a combination of both measured variables.

7.2.2. Influence of control method (2): constant cell voltage and temperature

Maintaining a constant cell voltage and cell temperature while varying the fuel flow to regulate cell power output is an alternative to control method (1). Figure 7.8 shows the results for this type of operation for a fixed operating cell voltage of 0.7 V and 800°C temperature.

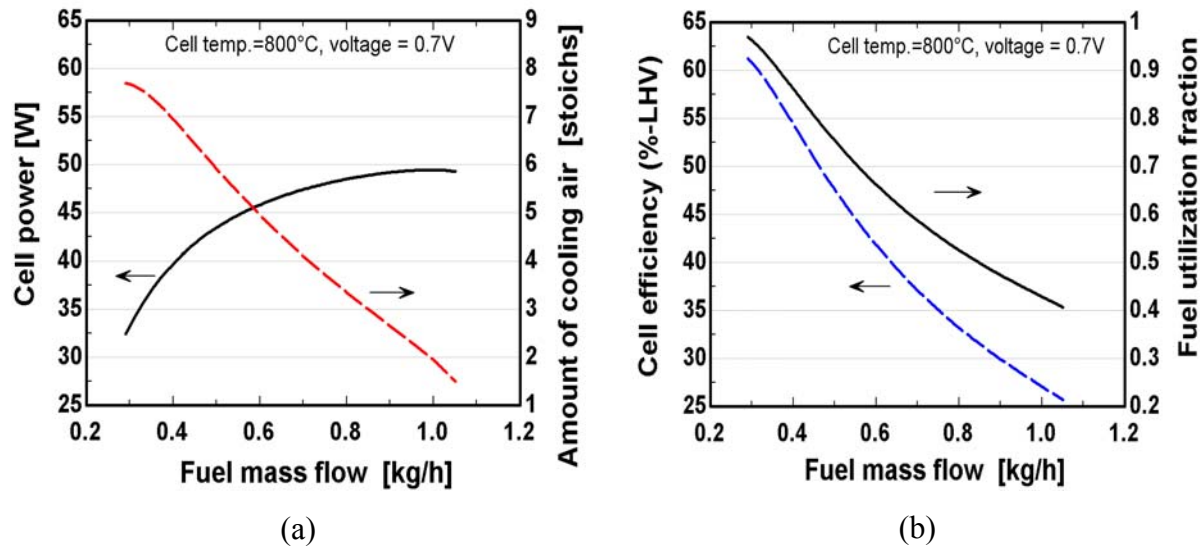


Figure 7.8 (a) Cell power and cooling air and (b) cell efficiency and fuel utilization as functions of input fuel mass flow

Note the limited power range achievable (32-50 W) and the considerable variation in air flow requirements by varying the input fuel flow. The cell efficiency plot in Figure 7.8(b) illustrates the large variation in efficiency over the relatively small change in cell power. Control method (2) is a very limited strategy, but could be appropriate for control where only small changes in power output are desired or expected (e.g., operation between 35 and 45 W). As will be shown in §7.2.3, if the constant cell temperature constraint is removed, the range of cell power output while maintaining constant voltage is increased.

7.2.3. Influence of control method (3): constant fuel and air feeds

The required flow rates of fuel and air to the cell for 0.7 volt operation and an average cell temperature of 800°C were determined and then fixed as operating voltage was varied. Fuel and air inlet temperatures and compositions were fixed throughout the analysis. Figure 7.9(a) shows the influence of operating voltage on cell power and efficiency for fixed fuel and air flow rate inputs. The maximum power (44 W) point occurs at a relatively high operating voltage of 0.66 V. (Recall from Figure 7.2 that the maximum power for constant temperature and utilization control produced nearly 80 W.) For constant fuel and air flow operating conditions, cell efficiency exhibits a maximum (59%) that coincides at the same cell voltage

as maximum power. The coincidence of maximum efficiency and power is an unusual trend and can be explained by the varying fuel utilization due to constant reactant gas feed control measures.

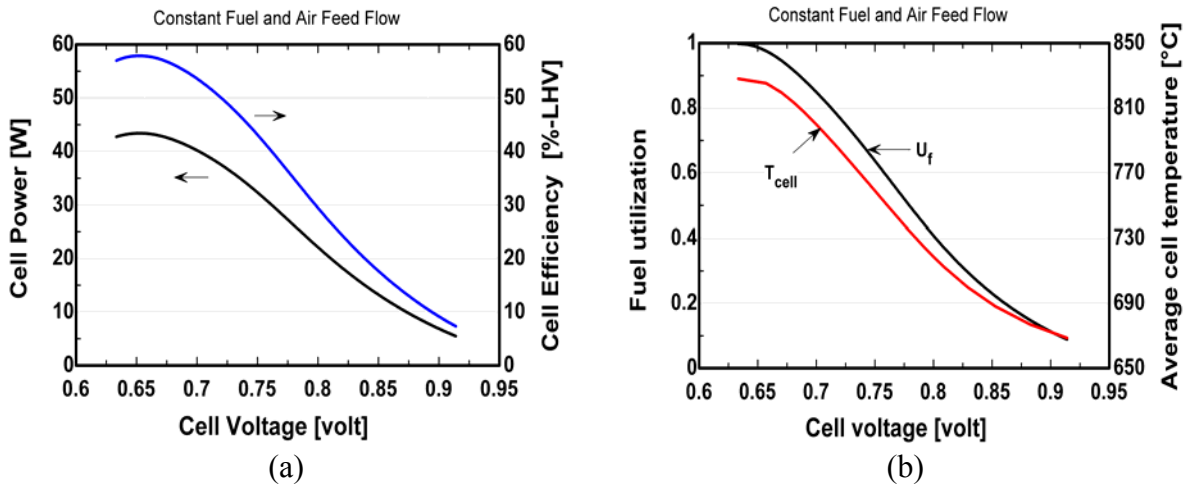


Figure 7.9 Influence of operating voltage on cell power, efficiency, fuel utilization and temperature for fixed fuel and air input.

Figure 7.9(b) shows the fuel utilization and average cell temperature plotted as functions of operating voltage. At the points of maximum power and efficiency, the fuel utilized in the cell is very near unity. In the high fuel utilization operating region, cell performance is mass transfer limited, which dramatically increases the cell polarization, resulting in a reduced maximum power. Operating at the coincidence of maximum power and efficiency is complicated by the increased risk for cell damage due to local regions of fuel starvation. In such a situation, oxygen anions may arrive at the anode with no fuel to oxidize. Instead, they tend to oxidize the nickel metal in the anode, eventually destroying the cell. The cell temperature variation with voltage indicates that a maximum is also achieved at a fuel utilization of nearly one. More importantly, the cell solid operating temperature range from 665°C to 825°C is significant and could increase the thermal cycling of the cell. Additionally, low cell temperatures can dramatically increase the risk for carbon formation on the anode.

Figure 7.10(a) plots the Nernst potential (or theoretical voltage) and fuel utilization together. As more fuel is utilized, the Nernst potential decreases indicating that the driving force for current generation is reduced as the partial pressures of the reacting species in the gas

channels are reduced. The increase in cell temperature due to increasing fuel utilization also contributes to the reduction in the Nernst potential at lower voltages. Figure 7.10(b) plots the maximum and minimum cell temperatures with operating voltage. Also plotted is the maximum temperature gradient. Interestingly, at high voltages the maximum temperature gradient is relatively constant until near the point of inflection of fuel utilization. At lower operating voltages, the cell temperature gradient increases to a value of about $2.3^{\circ}\text{C}/\text{mm}$.

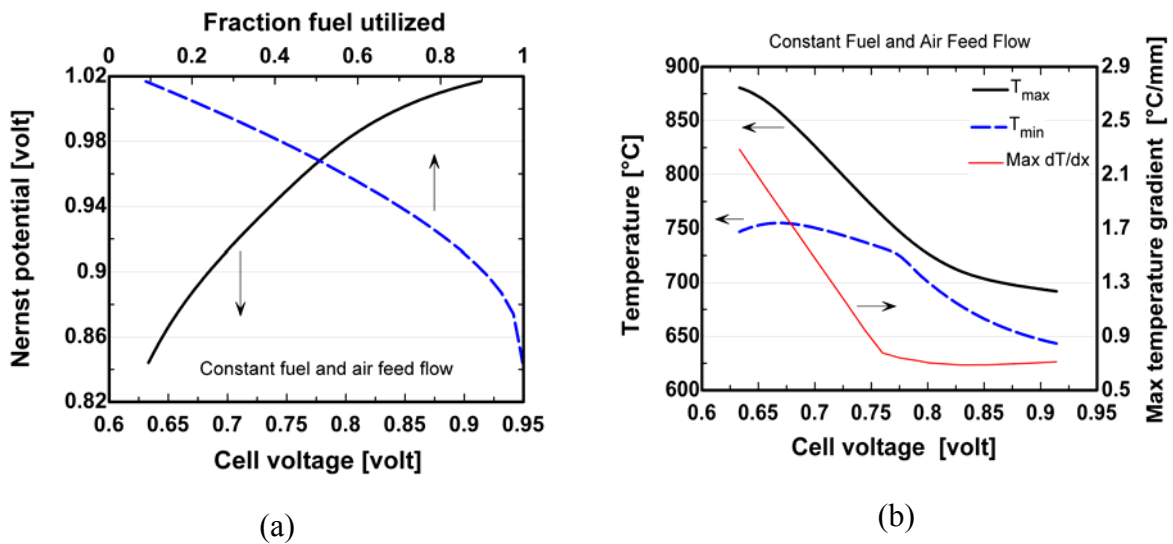


Figure 7.10 Influence of cell voltage on Nernst potential and maximum temperature gradient for fixed fuel and air input.

If the fuel flow is doubled from the value used in the figures above (air flow remains the same), then depending on the operating voltage, the cell power can in fact be *reduced*. In contrast, if the fuel flow is halved, *no change* in cell power can be observed for certain operating voltages, which in effect doubles the efficiency. Figure 7.11 illustrates these trends. One factor that induces these trends is believed to be associated with the increased cell resistance due to reduced cell temperature. For example, when the fuel flow is doubled at an operating voltage of 0.85 V, the increased amount of fuel gas flow cools the cell increasing the cell resistance and thereby reduces the power output. For a halving of the fuel flow at the same operating voltage, the cell temperature is increased thereby reducing the cell resistance, but the average partial pressure of hydrogen is also reduced and the cell power output is unchanged. This demonstrates the competing effects of operating temperature and fuel gas

composition on power output. The trends depicted in Figure 7.11 are dependent on the cell V-I performance characteristic and therefore, a change in the way the cell voltage depends on temperature and current can produce different results (cf. [11]).

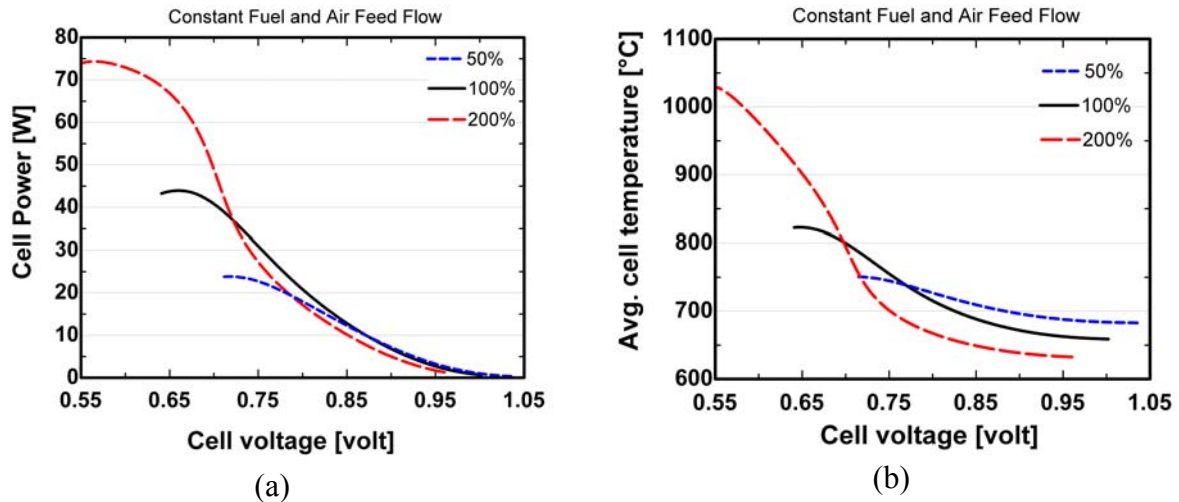


Figure 7.11 The effect of operating voltage and input fuel mass flow on cell power and temp.

7.2.4. Summary of control methods

In §7.2 we have seen that fuel cell operation with a controlled average cell temperature (or local cell temperature) and constant fuel utilization will yield a performance map that demonstrates maximum power (80 W) at a low operating voltage (0.4 V) and cell efficiency (30%). High voltage operation (0.8 V) results in more even temperature and temperature gradient distributions than lower voltages. Steeper thermal gradients are present at intermediate voltages (0.5-0.7 V) than at lower voltage operation (0.4 V) because of the amount of cell heat generation relative to the air thermal capacitance. Additionally, it was found that using the cathode air temperature rise as a parameter to control the amount of cooling air flow at constant fuel utilization could require substantially larger air flows than monitoring a single spatially positioned cell temperature.

Some limitations are apparent with each of the control methods discussed. For constant cell temperature and fuel utilization operation (CM1), it was observed that large temperature gradients and thermal stress may still be possible even when operating at 0.6 V. Control method 2 indicated that operation at constant voltage is implausible if a modest operating

range is desired. Finally, using control method 3 it was noted that poor cell efficiency and overly cool cell temperatures can result. Also, for varying fuel utilization, high voltage operation does not translate into high cell efficiency. Control method (3) is simpler than methods (1) and (2), however, thermal cycling of the cell would increase in load following situations, and there is increased risk for carbon formation due to cooler cell temperatures.

SOFC operation is likely to avoid rapid load-following situations, in favor of making relatively slow changes in power output to prevent excessive thermal cycling. In some cases, the SOFC system will be base-loaded and may only deviate from the design operating condition in a narrow bandwidth of say $\pm 10\%$ of rated power. In fact, as will be shown in Chapter 9, if the fuel cell is sized correctly load-following may not be the optimal strategy.

7.3 Effect of Variation of Cell Operating Parameters

7.3.1. Inlet air flow

To illustrate the effect of varying fuel or air input flow on cell performance, fuel utilization and cell temperature cannot be fixed. Figure 7.11 has already shown the influence of varying the input fuel flowrate on cell performance. Figure 7.12 depicts the influence of the amount of cathode airflow on cell power and temperature at varying operating voltages where 100% is base case flow condition. As cell voltage is decreased below 0.8 V, the cell power increases more rapidly for lower airflow conditions. This trend indicates that one could conceivably reduce the cell power (at constant voltage) by increasing the amount of airflow.

The temperature versus voltage and airflow plot illustrates the cooling effect of the cathode airflow for a given voltage. For instance, at 0.75 V, a doubling of volumetric airflow from 50% of the base case input to 100% changes the average cell temperature by nearly 100°C. However, a further doubling at the same operating voltage only reduces the cell temperature by about 25°C. As cell temperature is decreased, the internal cell resistance increases due to the decrease in oxygen anion conductivity of the solid electrolyte. Thus, while Figure 7.12 illustrates the coupling between cell temperature and power, the underlying reason for decreasing power with decreasing temperature is due to the temperature-dependent conductivity characteristics of the electrolyte (see Appendix I).

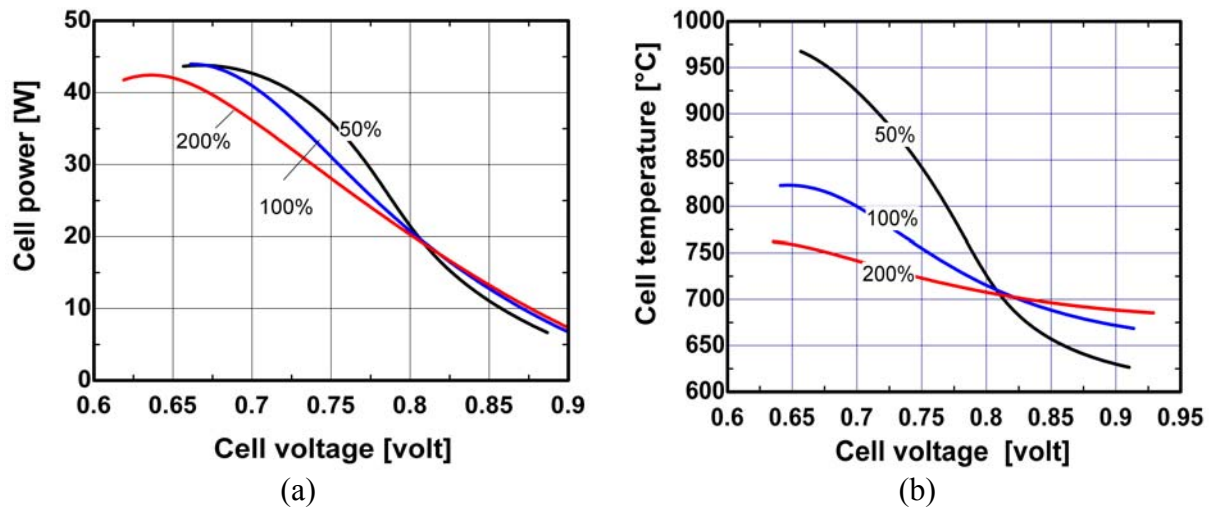


Figure 7.12 Effect of air flow on cell power and average cell temperature

The plots of cell power and temperature in Figure 7.12 intersect one another near a cell voltage 0.8 V. The reason for this cross-over is presented in Figure 7.13 where the ratio of the net heat generation in the cell to the cooling air thermal capacitance, ζ , is plotted. Above 0.8 V operation, the cell is very efficient and the net heat generation in the cell is below zero; that is, the cooling effect of the endothermic reforming reaction is greater than the heat release from the electrochemical oxidation of hydrogen and the ohmic dissipation of current flow. Thus, above 0.8 V the inlet “cooling” air actually “heats” the cell.

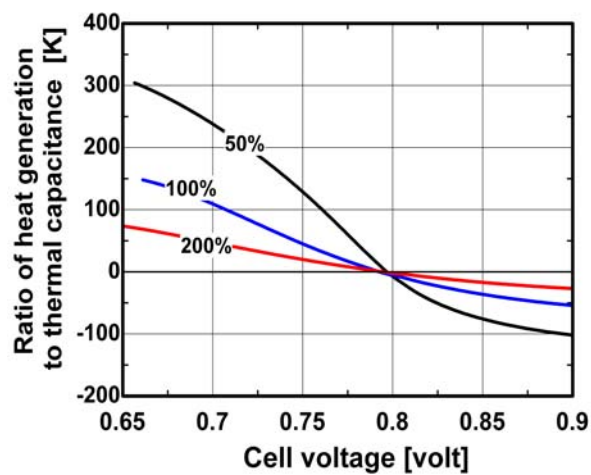


Figure 7.13 Effect of operating voltage and airflow on ζ

7.3.2. Inlet air temperature

Changes in cell operating point may induce changes in inlet gas temperature to fuel cell. To carry out any analysis on the effect of varying inlet cooling air temperature on cell performance, the amount of inlet cooling air was fixed while the inlet air temperature was varied. Figure 7.14(a) depicts the results of varying inlet air temperature on cell power. As has been shown in the previous section, decreasing cell temperature at given operating voltage will reduce the cell power output. At 0.75 V, a 100°C decrease (from the base case of 700°C air inlet) in inlet air temperature causes a 55% decrease in cell power output, whereas a 100°C increase in air temperature results in only a 17% increase in power. Figure 7.14(b) shows the change in average cell temperature when the inlet air temperature is varied. Note that a change of $\pm 100^\circ\text{C}$ in air temperature translates into a change of $\pm 125^\circ\text{C}$ in average cell temperature. Comparing the two plots it is evident that a continued increase in cell inlet air temperature will eventually produce no increase in power output. The reason for this relates to not only the effect of temperature on cell resistance but also its affect on the Nernst voltage (or driving force for current generation). Decreasing Nernst voltage with increasing temperature essentially retards the gains made in lowering the cell resistance at higher operating temperatures.

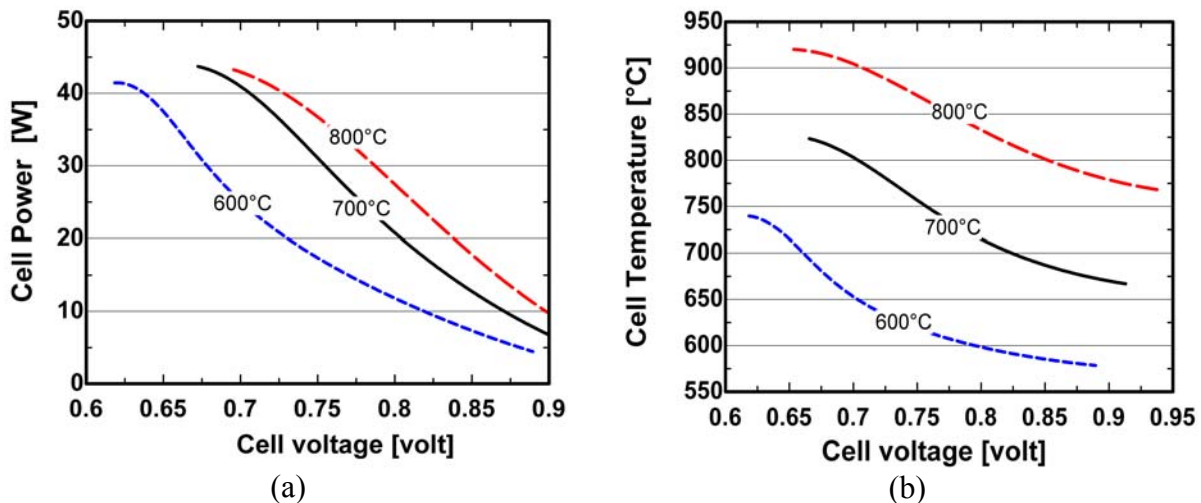


Figure 7.14 Influence of inlet air temperature on cell power and temperature

7.3.3. Inlet fuel composition (extent of pre-reforming)

Up until this point, the analyses have held the inlet fuel composition constant. Variation of the inlet fuel composition can be made by (i) changing the amount of pre-reforming of methane, (ii) adjusting the steam-to-carbon (s/c) ratio, and (iii) changing the reforming temperature. In the following analysis, the extent of pre-reforming was varied while reforming temperature and s/c were fixed. If the extent of pre-reforming, ξ , is zero (0%), then no hydrogen is produced and methane and steam are the only species entering the anode chamber. An extent of pre-reforming of 1.0 (100%) means that all of the methane is converted in the pre-reformer and a hydrogen, carbon monoxide, carbon dioxide, and water vapor mixture enters the anode chamber. For $\xi = 1.0$, the fuel gas consists of about 65% hydrogen on a molar basis. Figure 7.15(a) shows the effect of varying the amount of pre-reforming on cell heat and power generation, and efficiency for a nominal temperature of 800°C, s/c ratio of 2.0, 85% fuel utilization, and average current density of 0.5 A/cm².

Note that as the extent of pre-reforming (or conversion) is increased, the cell power remains constant, the net amount of heat generated increases, and the cell efficiency decreases. The cell power remains nearly constant because the cell voltage (and Nernst potential) increases only very slightly (<50 mV) with increasing conversion. The net heat generated in the cell increases over 250%. It is interesting that the cell efficiency decreases by over 10% in response to a greater fuel energy input for the same power output. As the conversion of methane is increased, the volumetric heating value of the fuel gas mixture at the anode inlet is reduced. A disproportionate increase in the amount of hydrogen flow (relative to the decrease in heating value) is needed to maintain the same current. Thus, an increase in fuel energy input for the same power output is realized.

Figure 7.15(b) depicts the effect on the cooling air requirements and air temperature rise as the extent of pre-reforming is varied. The number of air stoichs required to maintain a nominal cell temperature of 800°C increases by nearly 50% when going from 0 to 100% methane conversion. *If a constant air temperature rise across the cell were maintained instead of an average cell temperature, the air stoichs required would increase by over 200%.*

The use of direct internal reforming clearly reduces the amount of cooling air and the associated air temperature rise.

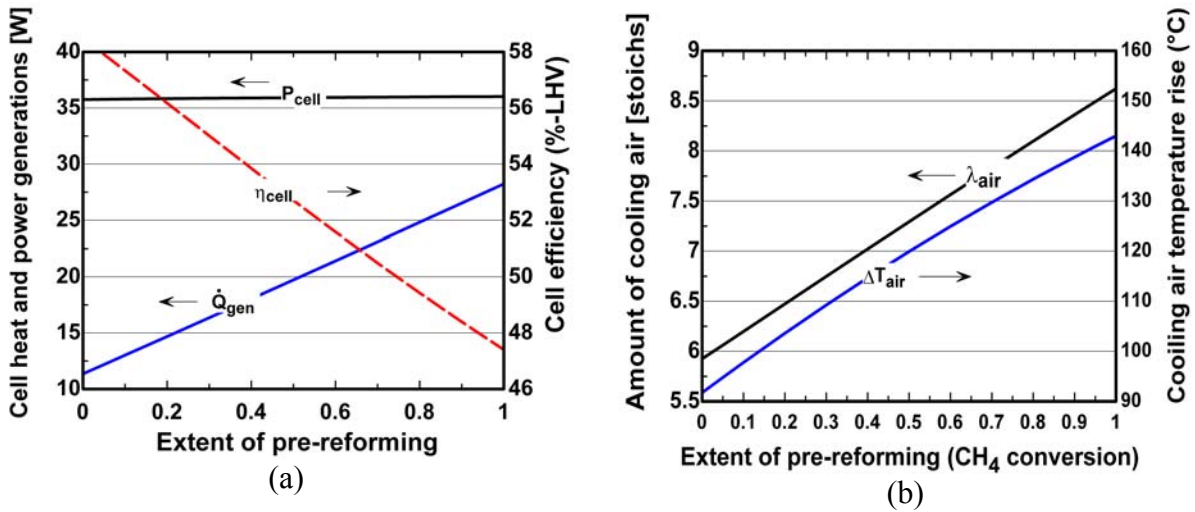


Figure 7.15 Influence of methane conversion on cell heat and power generation and cooling air indices (800 $^{\circ}C$ cell temp., 700 $^{\circ}C$ inlet air, 0.5 mA/cm 2 , 85% U_f , s/c=2.0)

Figure 7.16 depicts the temperature and temperature gradient distributions. A comparison of the two plots in the figure below indicates that while increasing the amount of pre-reforming produces higher peak temperatures, it results in a more even temperature gradient distribution and potentially lower thermal stress.

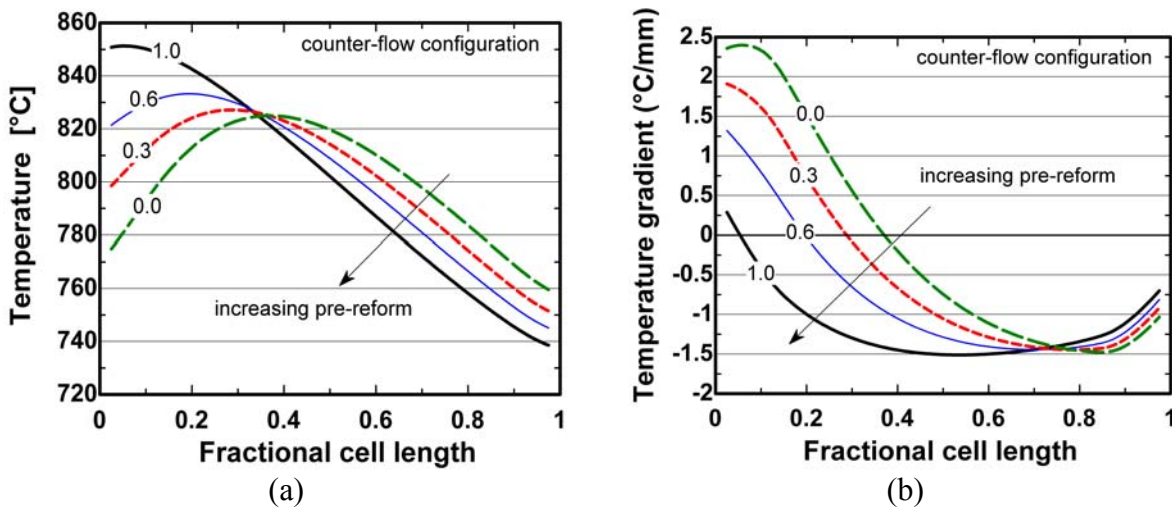


Figure 7.16 Influence of methane conversion on cell temperature and temperature gradient distributions (800 $^{\circ}C$ cell temp., 700 $^{\circ}C$ inlet air, 0.5 mA/cm 2 , 85% U_f , s/c=2.0)

7.4 Variation of Physical Cell-stack Design Parameters

7.4.1. Interconnect thermal conductivity

Planar SOFC technology development is focused on use of metallic interconnect materials to reduce manufacturing costs. Cost considerations have driven development of lower operating temperature SOFCs. However, hurdles remain before metallic interconnects are viable and in some cases, a few developers have stuck with using ceramic interconnect materials. It is most likely that metallic interconnect materials will be employed in commercial SOFC units. A comparison of the thermal performance of ceramic- ($k=3\text{W/m-K}$) and metallic- ($k=30\text{W/m-K}$) based cells is depicted in Figure 7.17(a). As one might expect, the figure shows that temperature and temperature gradient distributions flatten out with increasing thermal conductivity. A 10-fold increase in k reduces the peak temperature by 20°C . Figure 7.17(b) also depicts the distribution of the temperature gradient and the net cell heat generation. Note the strong cooling effect at the cell entrance and how it creates large temperature gradients ($2\text{--}3^\circ\text{C/mm}$). Importantly, the slope of the temperature gradient distribution is also reduced with a metallic interconnect which translates into lower thermal-induced mechanical stress. However, steep temperature gradients remain despite increases in cell thermal conductivity. No significant change in cell voltage, power, or efficiency was observed between the various interconnect materials.

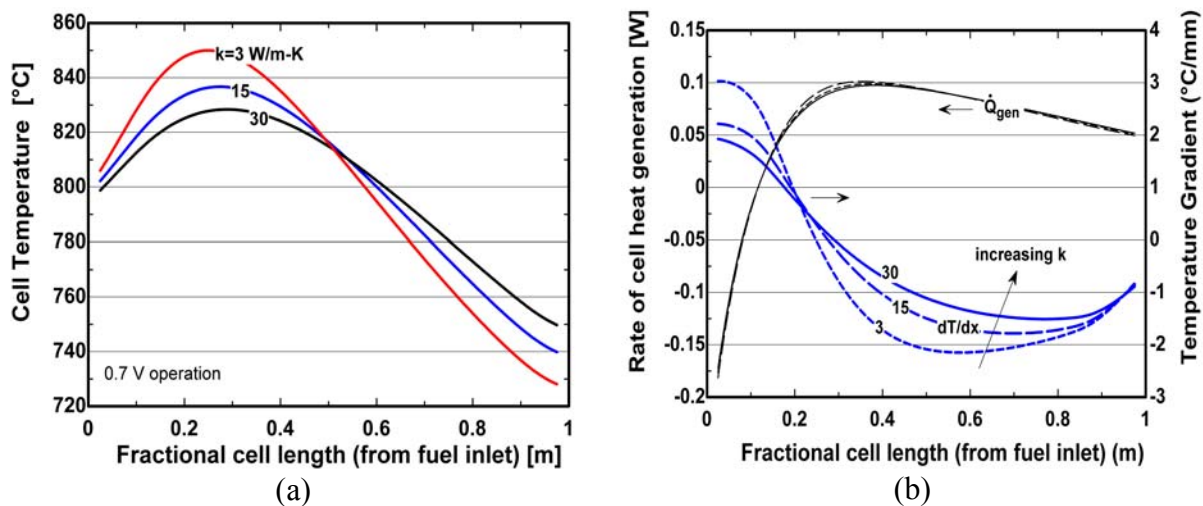


Figure 7.17 Influence of interconnect thermal conductivity on cell thermal performance (0.7 volt, 85% fuel utilization, 800°C nominal temperature, 700°C inlet air).

7.4.2. Cell resistance (power density)

Planar SOFC technology development has seen significant improvements in cell power density over the past 5 years [9, 12, 13]. One consequence of increased power density is the increased cooling air requirements due to the increase in volumetric heat generation in the cell. The sensitivity of cell performance to a variation in cell power density is evaluated next.

The calculated cell power density is dependent on the operating conditions of the cell-stack. In the following analysis, the cell power density calculation is based on employing an anode feed gas after 30% pre-reforming of methane and steam ($s/c=2$) at the fuel inlet temperature of 700°C , 0.7 V operation, 85% fuel utilization, and a nominal cell temperature of 800°C . Figure 7.18(a) illustrates the change in cell voltage, efficiency, and power for changes in cell power density. At a given current, increasing cell power density results in increased cell voltage and efficiency. Figure 7.18(b) also indicates that an increase in cell power density will increase the operating voltage at which maximum power occurs.

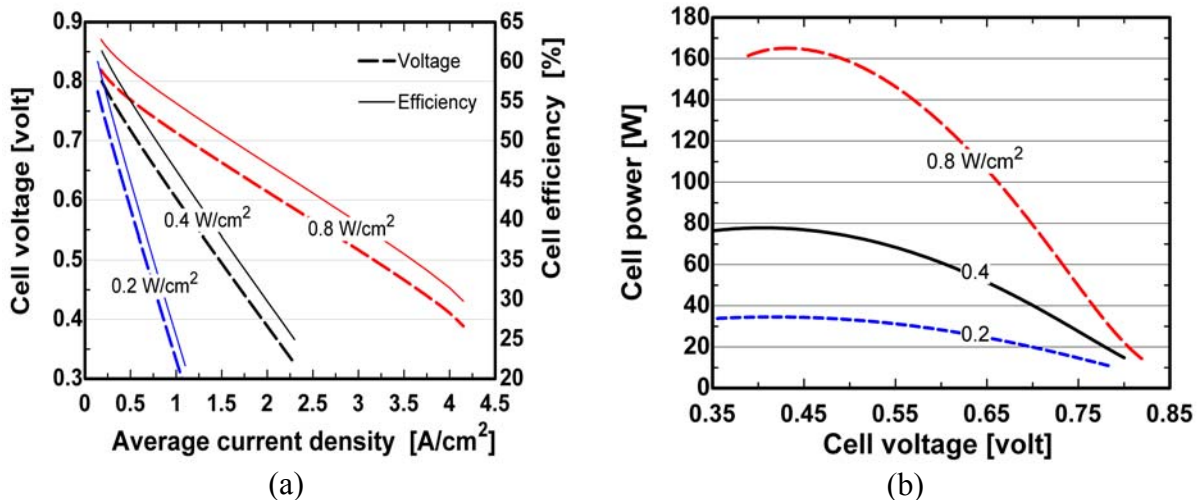


Figure 7.18 Influence of cell power density on cell voltage, efficiency, and power

For 0.7 V operation, Figure 7.19 plots the cell temperature and temperature gradient distributions for varying power density at the base case conditions summarized in Table 7.4. An increase in power density increases the peak cell temperatures and temperature gradients.

The slope of the temperature gradient profile also increases with increasing power density indicating increased thermal stress.

The cause for this trend is again found by examining the ratio of cell heat generation to the thermal capacitance of the cooling air. Figure 7.20(a) depicts this relationship, as well as, providing quantification for how the amount of air mass flow, air stoichs, and maximum cell temperature gradient changes with power density. The usefulness in plotting the ratio of cell heat generation to cooling air thermal capacitance has been previously shown in §7.2.1 and it can be used as a qualitative tool to establish trends and offer some estimate as to which operating voltage peak temperatures and temperature gradients are expected to occur at. Its utility is further validated here as it predicts that low power density cells will generate larger peak cell temperatures and steep temperature gradients than higher power density cells when operating at lower voltages ($<0.60\text{V}$). *Importantly, the simulation results presented in Figure 7.19 suggest that the channel cooling air heat transfer characteristics are sufficient to remove the heat generated in higher power density cells and that other cell cooling schemes are not necessarily required.* In other words, low heat transfer coefficients, material thermal conductivity, or geometry constraints do not exist that would fundamentally limit using air as a cooling medium. However, as shall be shown in Chapter 8, lower cooling air requirements are more desirable from system efficiency and cost considerations.

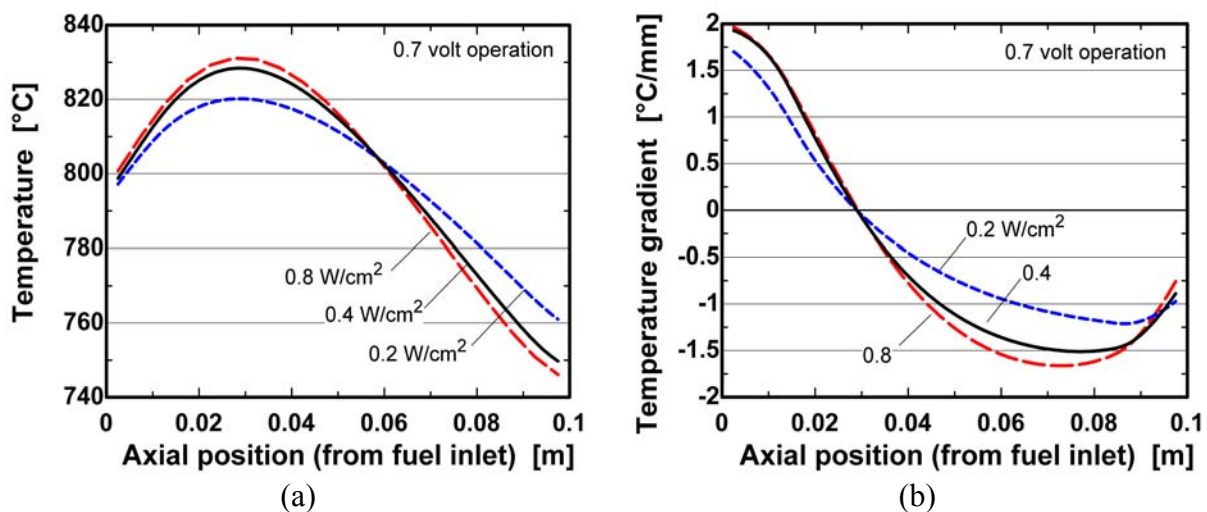


Figure 7.19 Influence of cell power density on temperature and temp. gradient distributions

Figure 7.20(b) also shows how the mass flow of air changes with increasing cell power density. Note that the air stoichs remain relatively constant as the power density is increased, indicating that air stoichs is not always a useful measure for correlating air flow requirements. A 4-fold increase in power density requires at least a 5-fold increase in cooling air mass flow but only a 15% increase in maximum temperature gradient is realized. Because of the linear relationship between laminar volumetric flow and pressure rise, it also means that the increase in required pumping power to push the air through the cell is increased by a factor of four. The implications of high power density SOFCs on system parasitic power requirements will be discussed in Chapter 8.

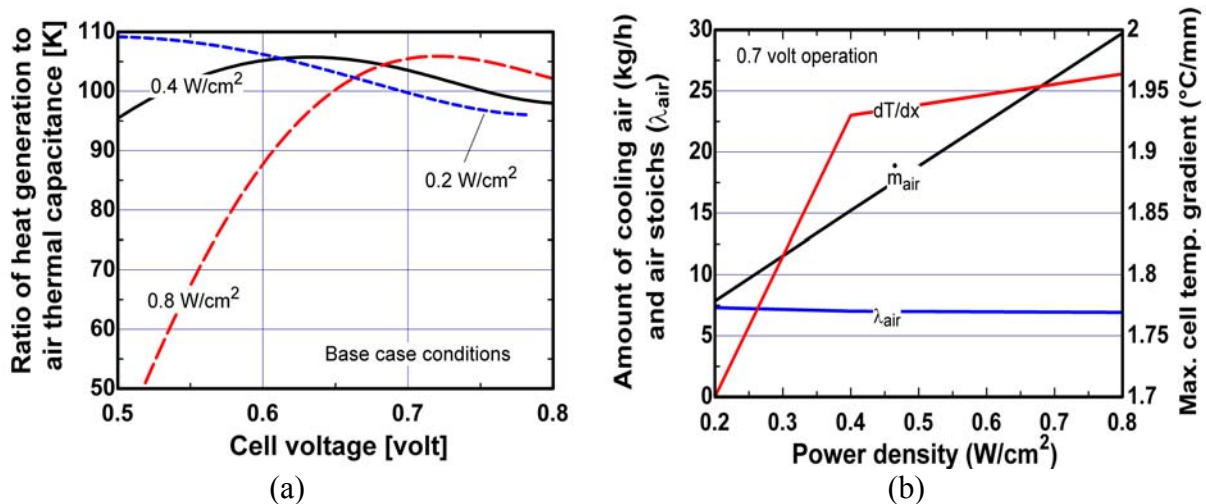


Figure 7.20 Effect of power density on ζ , cooling air, and maximum temperature gradient.

7.5 Summary

The influence of numerous variables on cell-stack performance, including control variables, and cell operating and design parameters, has been investigated in this chapter. This chapter concludes with a final analysis which will be useful in the remaining chapters. Figure 7.21(a) depicts the impact of varying fuel utilization on the cell-stack voltage-current characteristic for a 100% internally reforming, methane fueled cell operating at a nominal temperature of 800°C. An increase in the amount of fuel utilization decreases the average concentration of hydrogen (and CO) thereby reducing the theoretical voltage. The decrease in actual cell

voltage in going from 70% to 90% fuel utilization is reasonably explained by the reduction of the theoretical emf (driving force for current generation). Figure 7.21(b) presents the effect of changing the nominal cell operating temperature on V-I performance. An increase in cell temperature decreases the cell resistance significantly as shown by examining the difference in cell voltage at constant current. The net increase in voltage performance with increasing temperature is realized despite the reduction of the theoretical voltage with temperature increases. The stack power output (75 cell stack) can also be seen to increase with operating temperature as shown in Figure 7.21(b). The 2 plots illustrated in Figure 7.21 aptly summarize the impact that two important cell operating parameters (fuel utilization and operating temperature) have on the cell-stack voltage- current performance characteristics.

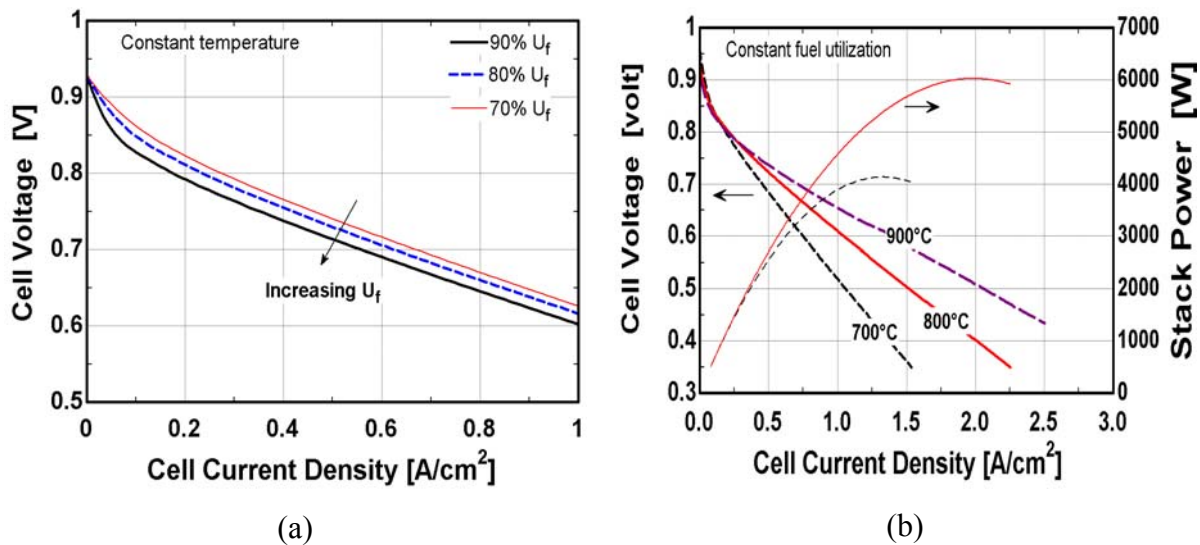


Figure 7.21 Effect of (a) fuel utilization and (b) cell temperature on V-I performance

7.7

-
- 7.1 B.A. Ogunnaike, W.H. Ray, *Process Dynamics, Modeling, and Control*, Oxford Press, New York (1994).
 - 7.2 M. Mogensen, Presentation at the DFG Workshop, Pommersfelden, Germany (2001).
 - 7.3 J.H. Hirschenhofer, D.B. Stauffer, and R.R. Engleman, "Fuel Cells, A Handbook," 5th Edition, prepared for the U.S. Department of Energy, November (2000).
 - 7.4 W.L. Lundberg, "Solid Oxide Fuel Cell Cogeneration System Conceptual Design," Final Report, GRI-89/0162, Gas Research Institute, Chicago, IL, July (1989).
 - 7.5 S. Veyo, "The Westinghouse Solid Oxide Fuel Cell Program: A Status Report," *Proc. Of IEEE*, 1996, pp.1138-43.
 - 7.6 A. Khandkar, J. Hartvigsen, S. Elangovan, "A Techno-Economic Model for SOFC Power Systems," *Proc. Of Solid State Ionics* (2000).
 - 7.7 D. Stolten, D. Frohning, L.G.J. deHaart, "Modeling of Planar Anode-supported Thin-layer SOFC Stacks," *Proc. Of the 4th European SOFC Forum*, Lucerne, Switzerland, July 10-14, (2000).
 - 7.8 E. Achenbach and E. Riensche, "Methane-steam reforming kinetics for solid oxide fuel cells," *J. Power Sources*, **52** (1994), pp. 283-288.
 - 7.9 D. Ghosh et al., "Performance of Anode Supported Planar SOFC Cells," *Proc. Of the 6th Int. Symp. on SOFCs (SOFC-VI)*, PV99-19, The Electrochemical Society, (1999) p.822.
 - 7.10 A.J. Appleby, "Characteristics of Fuel Cell Systems," in *Fuel Cell Systems*, L.J. Blomen and M. Mugerwa editors, Plenum Press, New York (1993).
 - 7.11 A. Selimovic, "SOFC Modelling for SOFC/Gas Turbine Combined Cycle Simulations," Ph.D. thesis, Lund Institute, Dept. of Heat and Power, Sweden, April (2000).
 - 7.12 M. Pastula, et al., "Development of Low Temperature SOFC Systems for Remote Power Applications," *Proc. Of the 4th European Solid Oxide Fuel Cell Forum*, Lucerne, Switzerland, (2000), pp. 123-132.
 - 7.13 J.W. Kim and A.V. Virkar, "The Effect of Anode Thickness on the Performance of Anode-supported Solid Oxide Fuel Cells," *Proc. Of the Sixth Int. Symp. On SOFCs, (SOFC-VI)*, PV99-19, The Electrochemical Society, pp.830-839 (1999).

Chapter Eight System Design and Performance Considerations

Up to this point, much of the present study has been focused on characterizing the influence of various cell parameters on cell-level performance. The cell-stack represents only a part of the system necessary in producing useful heat and power. This chapter focuses on the effect of cell operating and control parameters on overall system performance. This aspect of system design is important because of the strong interdependence between cell-stack and balance-of-plant (BOP) design, development, and performance. That is, many of the measures applied to SOFC systems to improve the balance-of-plant (BOP) influence the stack operation itself and vice-versa. The design and operation of the BOP can have a dramatic effect on the capital and operating costs of the system.

This chapter will first introduce residential application requirements to establish a context for SOFC system design. A general overview of process design decisions and an example flowsheet design will then be presented. The influence of cell-stack design and operating parameters on the net system AC power developed and BOP requirements will then be examined. Several conceptual SOFC flowsheet designs are then compared using various performance indicators including efficiency, airflow, and parasitic power consumption. Chapter 8 concludes with a discussion on fuel cell system design strategies for producing variable thermal-to-electric ratios.

8.1 General System Design Considerations

8.1.1. *Residential Application Requirements*

The electrical energy demand in residential applications varies widely over the course of a day. Figure 8.1 illustrates an example of the diurnal electrical energy usage of a household on both fifteen minute and hourly time-average bases. Fifteen-minute load data resolve the larger peak electrical demands associated with on/off switching of electrical appliances. The magnitude of these demands ranges from a 0.3 kWe base load to a 9 kWe peak load. It is

expected that short term demands (on the order of seconds) of 15 kW or more during motor starts frequently occur [1]. Figure 8.1 provides some indication of the transient load-following characteristics required by a fuel cell home power generation system. For instance, to follow the load variation in the fifteenth hour of the day would minimally require the fuel cell power system to modulate at a rate of 500 W/min. However, to truly follow the power demand associated with the cyclic operation of various appliances, the fuel cell power *system* would have to be capable of responding on millisecond timescales.

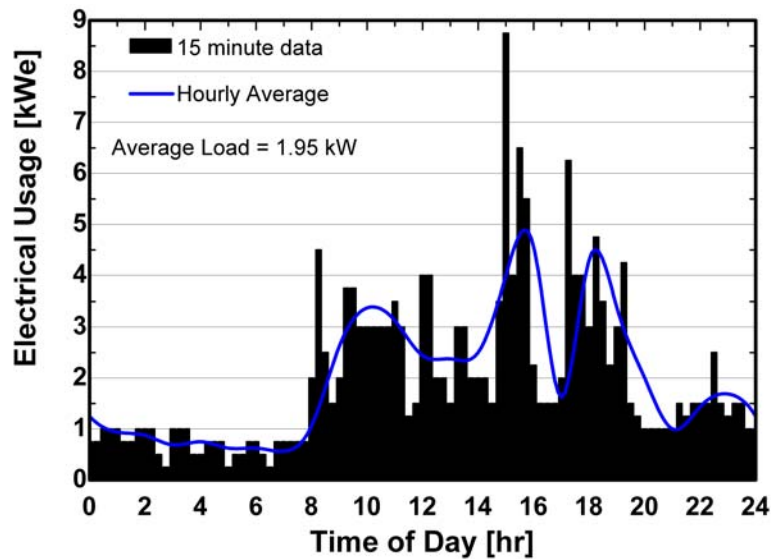


Figure 8.1 Diurnal electrical energy demand of a household [1]

Figure 8.2 depicts the hourly average residential energy demands for a home in Madison, Wisconsin during winter and summer days. Electrical load data were obtained from Krist and Wright [2], domestic hot water (DHW) demand data from Mutch [3], and space heating data were generated for a 242 m² (2,500 ft²) single family detached dwelling located in Madison, WI using a TRNSYS [4] Type56 model and typical meteorological year weather data. As the residential energy load profiles in Figure 8.2 show, both the timing and magnitude of household energy demands are widely disparate. However, over the course of an entire year, the annual average hourly electric load for the house is approximately 1.0 kWe, and the average hot water load is also about 1.0 kW_{th}.

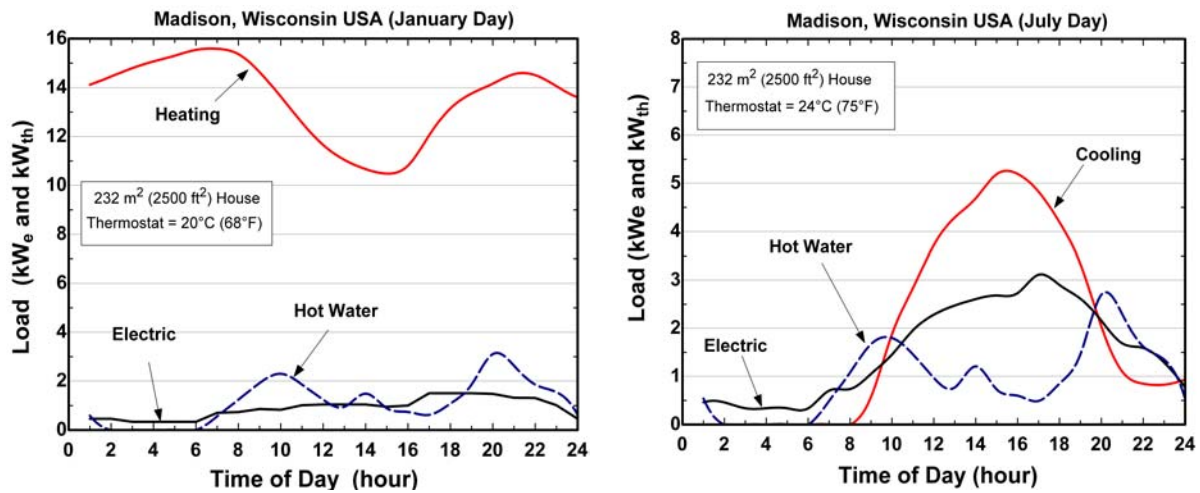


Figure 8.2 Winter and summer residential load profiles

Figure 8.3 presents the hourly average residential energy loads in terms of the thermal-to-electric ratio (TER), that is, the residential (heating or DHW) thermal energy demand over the residential electrical energy demand. Figure 8.3 shows a peak hourly domestic hot water heating demand of less than 1.5 and a base load of about 0.35 for a January day. The peak hot water TER for a July day is about 2 and the base load is near 0.2. Also, note both the magnitude and rate of change in hot water TER during the early hours of the day. The annual hourly average domestic hot water TER is about 1.0 and is typical of most households in the U.S. In contrast to domestic hot water heating, the TER data for space heating shows slower changes, a peak hourly TER demand of about 28, and a base load of 5.

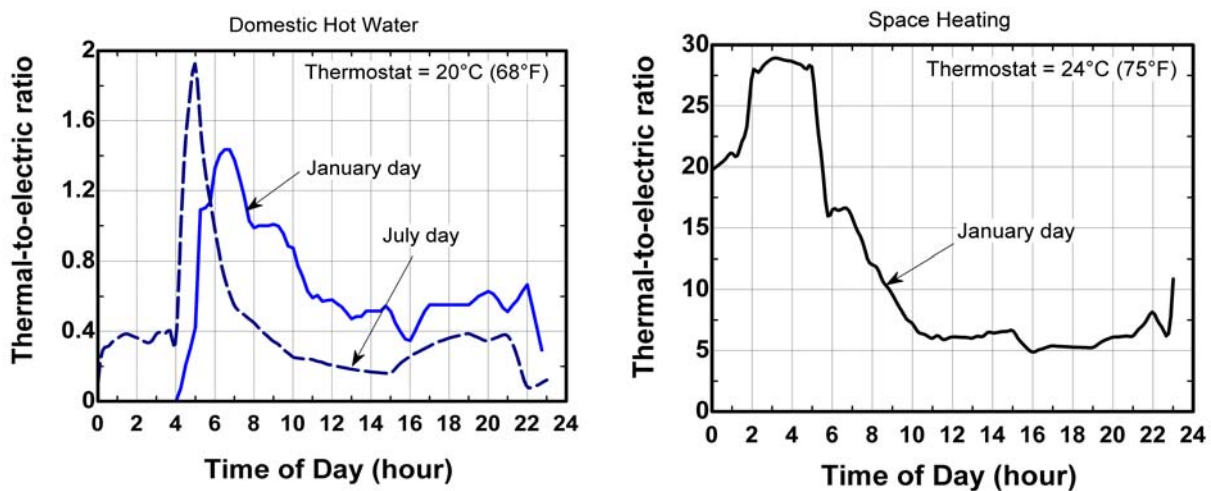


Figure 8.3 Residential hot water and space heating diurnal thermal-to-electric ratios

The following conclusions about the residential energy demands for the simulated home can be made from the brief examination given above:

- On a relative basis, large and rapid electrical energy load changes are typical for single family residential dwellings. Hourly average electric loads are near 1 kWe. Following electrical load changes requires millisecond response times.
- Large and rapid changes in domestic hot water usage (relative to electricity usage) are common. The magnitude of these demand peaks could be reduced with thermal storage, but nevertheless the annual hourly time-averaged hot water TER is near 1.0.
- Space heating loads in winter can reach large TER values (>25), especially in the early morning hours, and relatively constant TER demands (~ 5) until the late evening.
- To meet household thermal and electrical energy demands without batteries or grid-connection require a fuel cell system capable of fast electrical response with flexible TER output capability.

8.1.2. *Process Design and Operation*

In addition to the application requirements, consideration of fuel type and fuel processing are fundamental in designing any fuel cell system because they have considerable impact on system efficiency and performance. Figure 8.4 depicts process design pathways based on selection of fuel type and fuel processing. Residential solid oxide fuel cell systems will be fueled with natural gas or other hydrocarbon-based fuel type and will employ either internal or external reforming methods (see Chapter 3). Autothermal (ATR) and partial oxidation (POx) reforming methods are less efficient than catalytic steam reforming (CSR) and are more suitable for fast-start applications. These reforming methods are not considered further in the present analysis. The choice of utilizing the CSR process enables *internal* reforming of the fuel which offers higher net system efficiency than *external* reforming due to tighter thermal integration between the high temperature fuel cell and reforming processes. Water vapor for the CSR reactions is then provided by either a waste heat boiler or by recycling the depleted anode gas of the fuel cell. Four SOFC system designs are considered in the present study: (1) pure hydrogen fuel, (2) natural gas-fueled, *external* reforming with waste heat boiler, (3) natural gas-fueled, *internal* reforming with waste heat boiler, and (4) natural gas-fueled, *internal* reforming with anode gas recycle. These choices are basic considerations for any fuel cell process design. Additional process design considerations, such as cathode gas

recycle, separate air and fuel gas loops, fan and compressor selection, etc. are more pertinent to cost and product performance optimization, i.e., design trade studies.

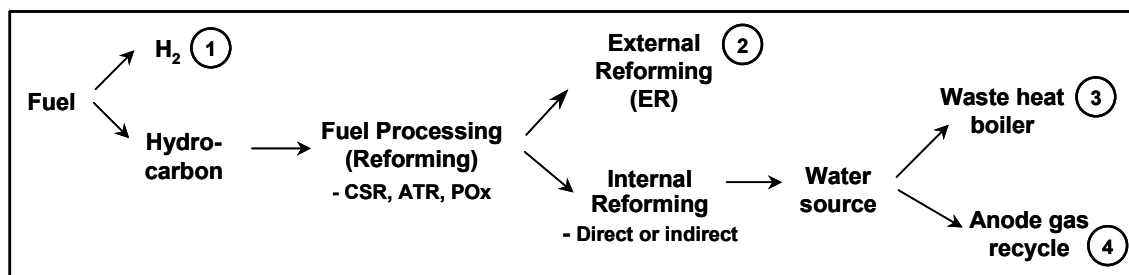


Figure 8.4 Decision paths in system process design

General overviews of hydrogen- and natural gas-fueled SOFC systems were previously given in Chapter 3 (see Figures 3.1, 3.2, and 3.12). A detailed process flowsheet for a conceptual natural gas-fueled, anode-supported SOFC system with a small pre-reformer, direct internal reforming, and externally raised steam for reforming of methane is depicted in Figure 8.5. Natural gas (station 1) is pressurized to about 1.35 bar, stripped of its sulfur content, mixed with superheated steam, and then delivered to the integrated preheater/steam-methane pre-reformer. In the pre-reformer, 25% of the methane is converted to hydrogen before delivery to the anode compartment at 700°C (station 5).

Air (740% excess) enters the plant at station 7 and is pressurized to about 1.3 bar, and after preheating is delivered to the cathode compartment of the fuel cell at 700°C. The solid oxide fuel cell temperature is maintained by both air-cooling (through excess air) and the endothermic reforming reactions. The system airflow is modulated to maintain an average cell-solid temperature of 800°C. Inside the cell-stack, the remainder of the methane is reformed directly on the anode where the endothermic reactions are driven by the heat release in the fuel cell stack. 85% of the fuel is electrochemically utilized and the depleted fuel cell product gases are catalytically combusted (station 11) and then used to serve reactant preheat, pre-reforming, and steam boiling process needs before 1008 W of thermal energy, in the form of domestic hot water, is recuperated. Steam at 5 bar is raised and superheated 5°C in the waste heat boiler for reforming. The system exhaust gases exit the system near 60°C. The 50 cell-stack in this analysis operates at an average single cell voltage of 0.7 Volt and produces

2.0 kW of DC power at a cell efficiency of 54.3% (LHV). The DC power generated is inverted to single phase AC power at an efficiency of 92%. Air blower, water pump, and fuel compressor parasitics total 0.35 kW –98% of which is for the air blower. The total net AC power delivered is about 1.48 kW, which translates into a system TER of about 0.68. System electric efficiency is 42.5% (LHV) and cogeneration efficiency is 71.3%.

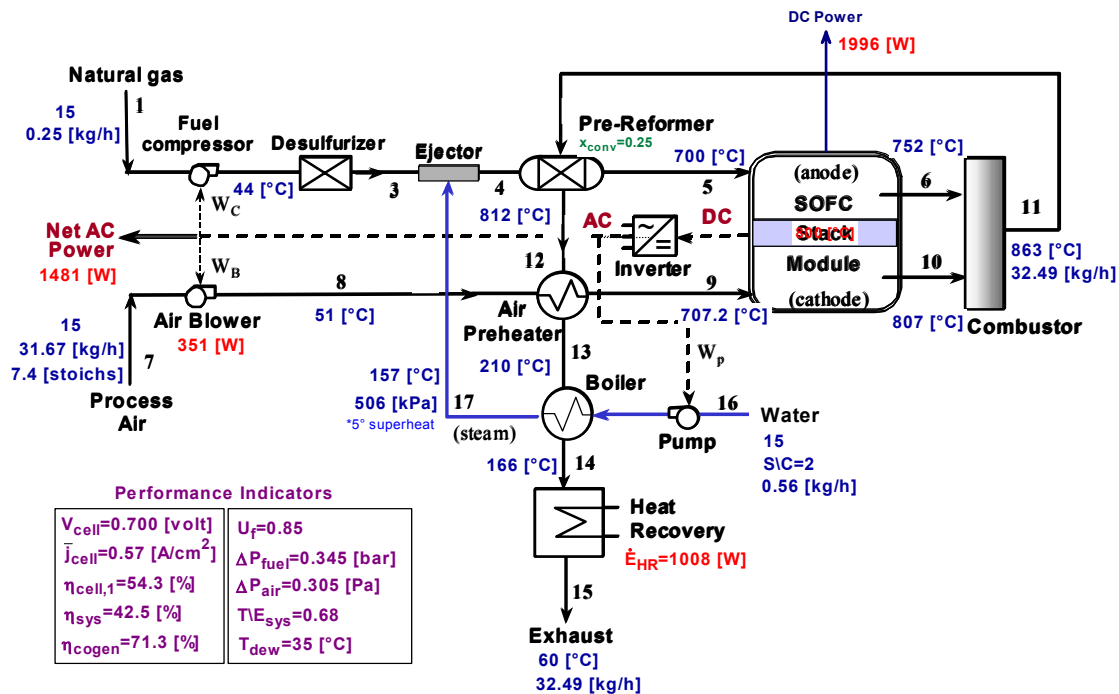


Figure 8.5 Methane-fueled SOFC system concept with internal reforming [adapted from 5]

8.2 Influence of Cell Parameters on System Performance

Changes in cell design, operating, and control parameters will produce varying TERs, as well as, impact BOP component sizing, system economics, and performance. The balance-of-plant (BOP) is defined as all system components except the SOFC cell-stack. As discussed in Chapter 7, changes in cell design parameters and operating conditions significantly alter cell performance resulting in undesirable cell-stack operating points. This section focuses on how the selection of cell parameters influence balance-of-plant and system-level performance characteristics for the flowsheet design presented in Figure 8.5. Economic considerations will be discussed in Chapter 9.

8.2.1. Design operating voltage

At 0.7 volt/cell operation, the system shown in Figure 8.5 will produce a TER about half as large as the average required for residential applications. As the fuel cell design operating voltage is changed, system process temperatures and the amount of thermal energy available for domestic hot water production will vary. Figure 8.6(a) shows the impact of *design* cell operating voltage on the gross cell-stack DC power, net system AC power, and air blower parasitic power. As *design* cell voltage is decreased, the gross stack power increases until it reaches a maximum near 0.4 V (as previously noted in Chapter 7). The net AC stack power output is reduced from the gross power primarily due to the inverter inefficiency and the ancillary equipment. Net system power reaches a maximum of 2.0 kW at 0.56 V. At maximum net AC power, air blower parasitic power requirements reach 1.0 kW, which is 34% of the AC power produced (after inversion). As cell voltage is lowered (cell current increased), the net AC power is reduced as blower power consumption exceeds the incremental increase in power developed by the stack. The inclusion of parasitic power requirements suggests a practical design operating cell voltage range between 0.56 – 0.8 V.

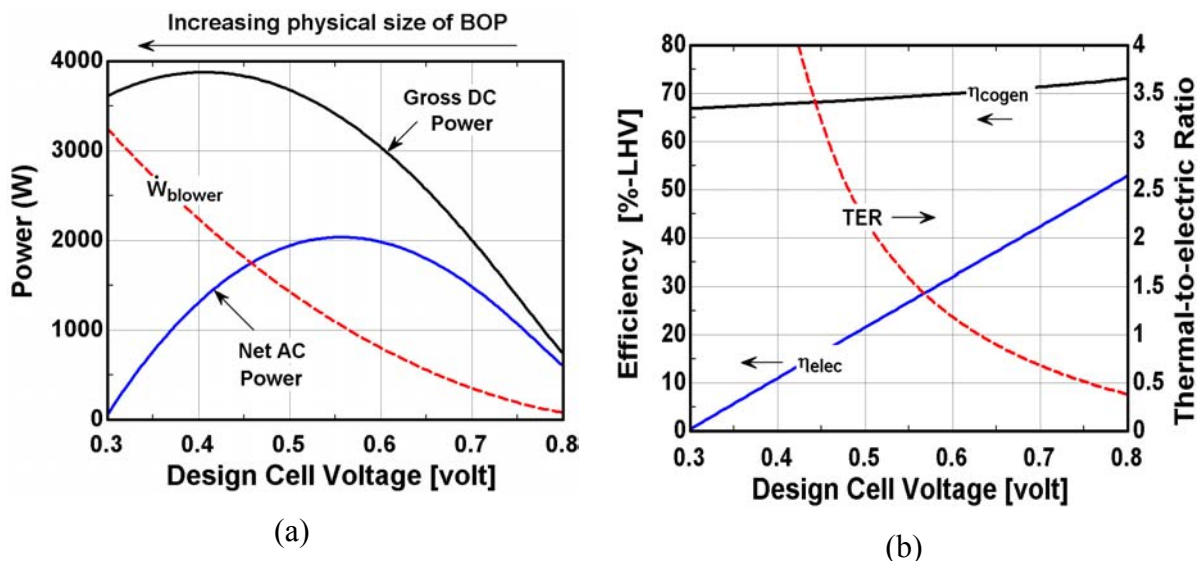


Figure 8.6 Influence of design cell voltage on stack and air blower power, system efficiency, and system thermal to electric ratio

Figure 8.6(b) depicts the effect of design cell voltage on system efficiencies and TER. As the cell voltage is increased (power reduced), the system electric efficiency increases nearly linearly as was seen previously for cell efficiency (see Figure 7.2). Interestingly, the cogeneration efficiency increases slightly with increasing cell voltage, indicating that the amount of heat output nearly offsets the loss in net electric power produced at lower cell voltages. The cogeneration efficiency changes by less than 6% over the practical design voltage range of 0.56 – 0.8 V. The system thermal-to-electric ratio increases with decreasing voltage, ranging from 0.4 to 1.5 in the suggested design voltage range. However, residential application requirements (see §8.1.1) reveal that TERs of nearly 2 may be required during certain times of the day just to satisfy DHW needs.

To match the production of domestic hot water with the demands, thermal storage is required to meet the various changes in thermal load. A supplemental burner or small hot water heater may also be required. It is interesting that the parabolic nature of the net AC power curve suggests that at least 2 different TERs are possible for a given electrical load. In order to make use of this operating characteristic, low voltage (<0.55 V) design and operating points are required. Low voltage operation is theoretically conceivable as results from Chapter 7 (see Figure 7.5) do not support concerns regarding excessive thermal gradients and stress in the cell at low voltage (high current) conditions.

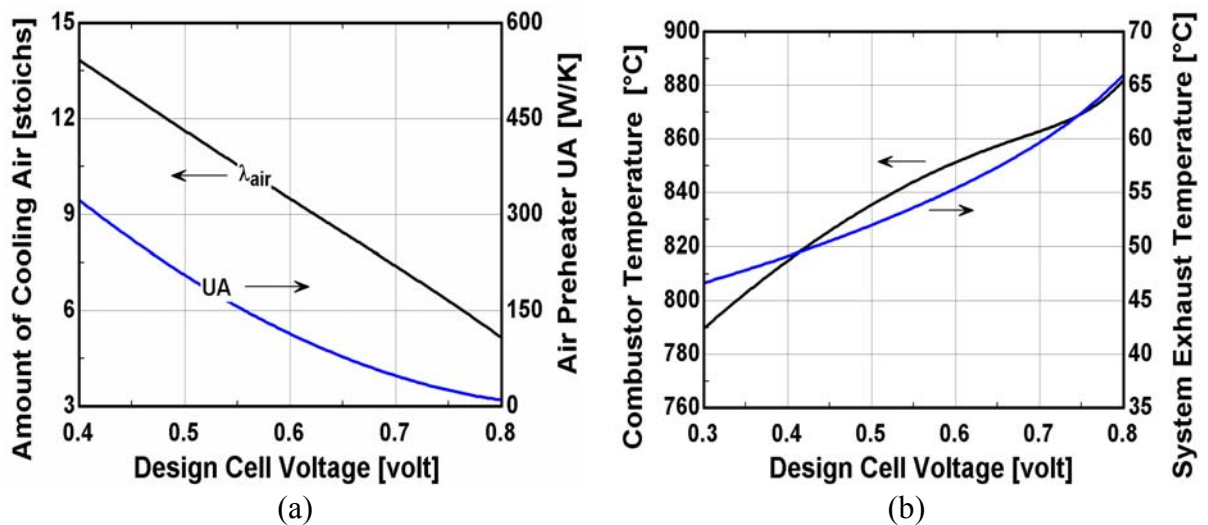


Figure 8.7 Effect of design cell voltage on air stoichs, air preheater UA, and gas temperatures

Figure 8.7(a) shows the influence of cell voltage selection on the amount of cooling air needed to maintain a nominal cell temperature of 800°C. Even at high operating cell voltages (>0.75 V) 6 or more air stoichs (% excess air) are required, which translates into high parasitic power (blower horsepower) and large air preheater surface areas. Air preheater UA as a function of cell voltage is also presented and is proportional to the airflow requirements. The air preheater UA required increases with decreasing cell voltage from about 10 W/K at 0.8 V to 150 W/K at 0.56 V; that is a 15-fold increase in UA is required for a 3.3-fold increase in net AC power produced over the same voltage range.

The impact of cell voltage on combustor outlet and system exhaust temperatures is also shown in Figure 8.7. Increasing cell voltage leads to increases in combustor outlet temperature and system exhaust temperature. Combustor outlet temperature increases with increasing cell voltage in response to lower system airflows. It is desirable to maintain the combustor temperature below 850°C to ensure that the gas is within the material temperature limits of the downstream heat exchange equipment. As the figure shows, 850°C is exceeded in this system design at cell voltages above 0.60 V. For the present study, the exhaust gas temperature was arbitrarily set to 25°C above the dew point of the gas mixture to ensure no condensation. This analysis then also reflects the changes in the moisture content of the exhaust gas. To recover the maximum amount of sensible thermal energy in the exhaust gas, the outlet gas temperature decreases from about 65°C to 55°C over the design voltage range presented in Figure 8.7(b).

Approximately 8.2 kW of heat is transferred from fuel cell product gases to the various process streams between stations 11 and 15 in Figure 8.5. Over 75% of the total heat transferred occurs in the air preheater. The total amount of heat transferred increases to over 23.4 kW when the design cell voltage is at maximum AC power (0.56 V), of which the air preheater's portion is nearly 78%. Thus, a significant fraction of the system cost and efficiency is associated with the system airflow. Aside from the air preheater, the other BOP components are comparatively small but still require careful design consideration. Figure 8.8 shows a T-Q diagram of the heat exchangers downstream of the air preheater at a nominal operating cell voltage of 0.7 V. The approach temperature (or "pinch") between fuel cell

waste gases and the boiler section is approximately 18°C. This pinch point value is sufficiently large for economic manufacture of the boiler [6]. As operating voltage is decreased the boiler pinch temperature is reduced slightly until it reaches a marginal pinch temperature of 14°C at the point of maximum net AC power.

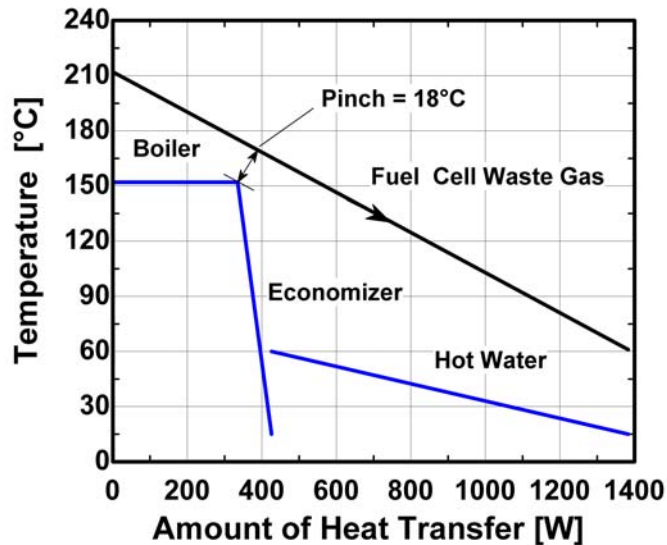


Figure 8.8 T-Q diagram of steam boiler and thermal energy recovery heat exchangers

8.2.2. Fixed fuel and air input operation

Chapter 7 discussed alternative methods of fuel cell operation based on regulating constant fuel utilization (and cell temperature), constant cell voltage (and cell temperature), or constant fuel and airflow inputs. Constant cell voltage control (CM2) was found to be only practical for small changes in load and did not offer performance advantage over constant fuel utilization (CM1). Constant fuel cell reactant flow input (CM3) is the simplest method of control, but suffers poor efficiency for low load (high voltage) conditions. However, this method of control offers the possibility of increasing the system thermal-to-electric ratio at low electrical demand conditions. Figure 8.9 illustrates the stack and system performance as a function of operating voltage for fixed fuel and air inputs. Recall that the fixed inlet flow conditions are based on a design operating voltage of 0.7 V, 85% fuel utilization, and 800°C nominal cell temperature. With decreasing cell voltage, the stack power, current, and fuel utilization are all increased. Power and system electric efficiency are maximized at about

0.65 V and 98% fuel utilization. Note that near 0.9 V (low current and fuel utilization) the net AC power is equal to zero, meaning that the only useful output of the system is the thermal energy exported (hot water in this case). Figure 8.9(b) shows that cogeneration efficiency is relatively constant with load change, but is maximized at low fuel utilization because the blower parasitic power requirement is constant.

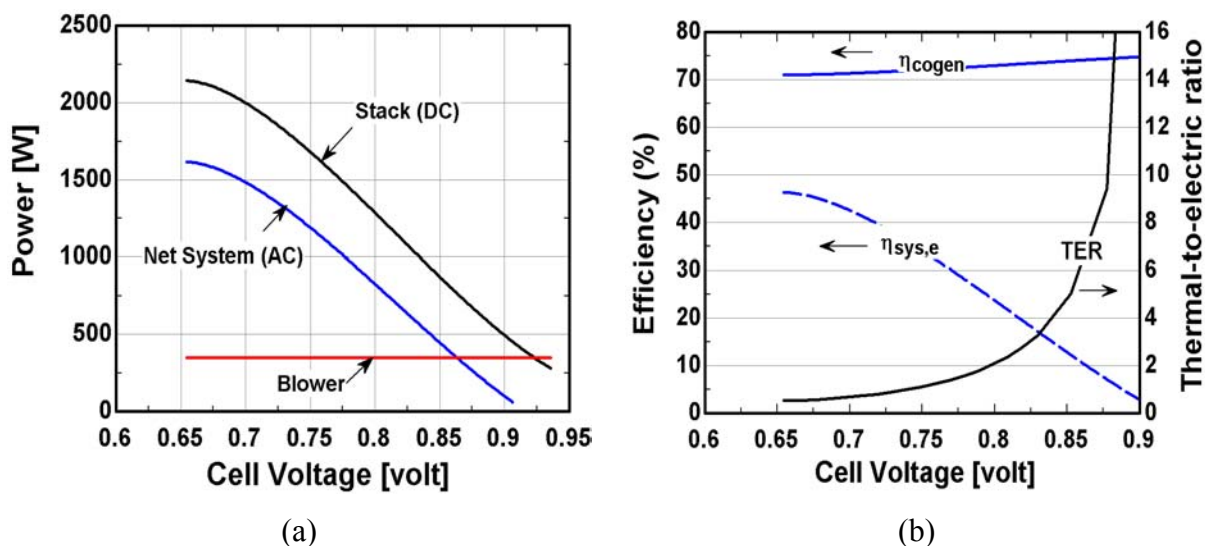


Figure 8.9 Influence of cell voltage on power, efficiency, and TER for fixed feed conditions

Figure 8.9(b) also shows that system TER increases with increasing voltage. The reason for this is better illustrated in Figure 8.10. As less fuel is electrochemically oxidized in the cell-stack, the heating value of the depleted gases delivered to the catalytic combustor increases thereby generating more thermal energy. Thus, the system TER rapidly increases to 10 or higher as the electrochemical fuel utilization falls below 20%. The catalytic combustor (or afterburner) temperature increases linearly with decreasing fuel utilization, ranging from 825 – 1125°C. These high temperatures are problematic for the downstream heat exchangers. In fact, while 850°C is considered the upper limit for use of metallic heat exchangers, they still require more expensive alloys. Taylor and Beishon [7] state that 700°C is the current temperature limit for cheap, reliable, mass-produced metallic heat exchangers. However, the high combustor temperatures could be reduced with increasing air input and/or cold air bypass from the blower outlet, thereby enabling low fuel utilization operation and a high TER. In fact, as Figure 8.9(a) shows, it is possible to operate the fuel cell system to deliver only net

thermal energy by producing just enough AC power to meet the parasitic power requirements. On the other hand, if airflow input were reduced, the combustor temperature would increase. If afterburner temperatures rise above 1300°C, thermal NO_x formation may become problematic [7] if the SOFC system is to be a “low-emission” device.

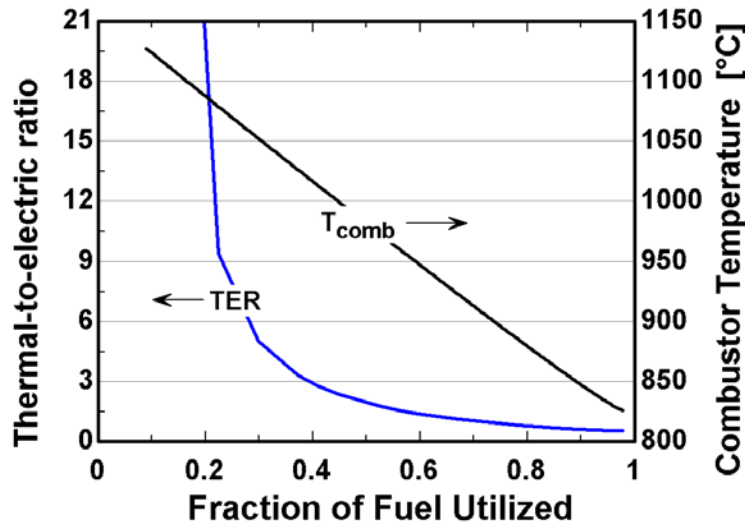


Figure 8.10 System TER and combustor temperature as a function of fuel utilization

8.2.3. Extent of fuel conversion in pre-reformer

In Chapter 7, the amount of methane reforming completed in the pre-reformer was shown to mildly affect the overall cell power and efficiency. However, the required amount of cooling air to maintain the cell temperature (see Figure 7.15) can increase by 50% when the extent of reforming changes from 0 to 1.0. This effect on system electric efficiency and power performance is shown in Figure 8.11(a). The increase in airflow required for lower extents of *internal* reforming of methane in the cell-stack decreases the net system electric efficiency by about 8.5 points. When changing ξ from 0 to 1.0, the increase in required airflow results in a 90% increase in blower power and increases the heat required for reforming by 170%. Note that the air temperature rise across the cell is fixed to 100° C in this analysis and the inlet air temperature is varied to obtain a 800°C nominal cell temperature. Once again it is important to emphasize method of operating control. If the cell-stack were controlled based on fixed inlet air temperature and variable air temperature rise across the cell-stack, then the change in

system efficiency may only decrease by 2.5 points. Thus, depending on control method, the difference between employing external and internal reforming can amount to a 2.5-8.5 point change in system electric efficiency.

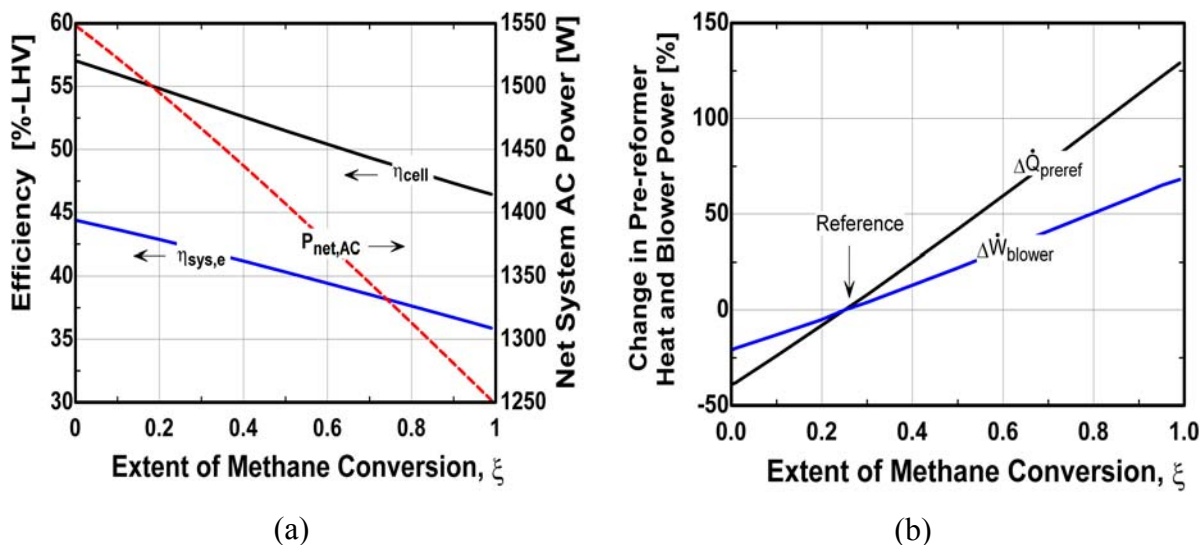


Figure 8.11 Influence of methane conversion on system performance (85% U_f , $s/c=2.0$, average current = 0.57 A/cm²)

Aside from airflow considerations, the largest effect that methane conversion has on system performance is related to meeting the process heating needs with fuel cell exhaust gases. As the heat required in the pre-reformer increases with increasing ξ , less thermal energy is available in the fuel cell product gas to serve the other system process needs. *In particular, at conversions greater than 60%, the pinch temperature in the steam boiler becomes unacceptably low and the pressure at which steam is generated must be lowered beneath 5 bar to accommodate the reforming process.* Thus, it is easy to see how difficult it is to meet both 100% external catalytic steam-reforming and process heating loads with only fuel cell product gases. To operate at conversions greater than 60% (for the operating conditions in this analysis), other process designs would have to be considered, including using autothermal or partial oxidation reforming methods.

8.2.4. *Cell power density*

Chapter 7 indicated that removal of the heat generated in high power density cells was not problematic, in terms of cell temperature maximums or temperature gradients. Figure 7.20 illustrated that the increases in the required airflow were directly proportional to the increases in power density. From a systems perspective, this result translates into linear increases in required air blower and air preheater (UA) sizes. Net system AC power also increases proportionally with increasing cell power density. These trends have been computationally verified and it appears that for the range studied ($0.2 - 0.8 \text{ W/cm}^2$), systems-level considerations do not constrain the design of higher power density fuel cell systems. In practice, engineering high power density systems may encounter problems at the cell-level, in terms of mass transfer limitations for supply of reactants to the heterogeneous reaction sites. At the systems-level, balance-of-plant component availability, performance, and sizing may restrict design optimization and overall performance.

8.3 **Variation of System Conceptual Design**

8.3.1. *Performance comparisons of system design alternatives*

The previous section illustrated how variation in cell parameters affect system-level performance. Since SOFC technology has not yet reached a mature stage of development, it is not economically competitive with conventional power generation technologies. As a result, design methodologies that lead SOFC development toward optimal economic and technical performance become crucial. An overview of how variations in the system design or arrangements affect SOFC plant performance is now given. The influence of economic factors on overall system design is discussed in Chapter 9.

Six SOFC system designs are investigated: Case (1) hydrogen-fueled (see Figure 3.1), Case (2) methane fueled with external reforming (see Figure 3.2), Case (3) methane fueled with both pre-reforming and direct internal reforming (DIR) and steam supplied by a heat recovery boiler for (3a) 50% pre-reforming/50% DIR (see Figure 8.5), and for (3b) 100% DIR, Case (4) methane fueled with 100% DIR and water supplied by anode gas recycle (see Figure 3.12), Case (5) 100% DIR with cathode gas recycle and water supplied by a heat recovery

boiler, and Case (6) employs both anode and cathode gas recycling. The analysis was carried out for a fixed SOFC stack size of 50 cells, each 10 x 10 cm, operating near 800°C with a fixed cell air temperature rise, ΔT_{air} , of 100°C, 85% system fuel utilization, and a nominal average current density* of 0.57 W/cm². System pressure drop data for each case design is presented in Table 8.1. Increases in the allowable air temperature rise across the cell-stack are also investigated in design cases 4(b) and 4(c).

Table 8.1 System Design Case Pressure Drops

Design Case	Air-side ΔP (mbar)	Fuel-side ΔP (mbar)
1	290	205
2	305	345
3(a,b)	305	345
4(a,b,c)	290	390
5	360	345
6	345	390

Table 8.2 and Figure 8.12 present performance comparisons between the system designs. From Table 8.2, it is immediately apparent how the flowsheet design and choice of fuel processing method affect the amount of stack cooling airflow (λ_{air}). The hydrogen-fueled system (Case 1) requires a significant amount of cooling air, but has a lower system pressure drop than other designs due to the absence of fuel processing equipment. It also produces the highest cell power density and the most thermal energy for domestic hot water heating.

* The average current density was selected because it produces a nominal single cell voltage of 0.7 volt for methane-fueled systems (cases (2)-(6)).

Table 8.2 Performance comparison of various SOFC system design concepts

System*	Air ratio λ_{air}	Power Density (W/cm ²)	Net AC Power (kW)	T/E (W _{th} /W _e)	\dot{W}_{blower} (kW)	Heat transfer in air preheater (kW)	Air pre- heater UA (W/K)	After- burner Temp. (°C)	Electric Efficiency (%-LHV)	Cogen. Efficiency (%-LHV)
(1) H ₂ - fueled	10.9	0.43	1.47	1.35	0.49	9.5	72.1	869	35.1	82.3
(2) External Reforming	12.4	0.40	1.25	0.86	0.59	10.8	139.4	862	35.9	66.8
(3a) 50% IR w/ boiler	9.0	0.40	1.41	0.73	0.43	7.7	72.1	863	40.3	69.7
(3b) 100% IR w/ Boiler	5.8	0.40	1.55	0.65	0.28	4.8	29.3	864	44.4	73.0
(4a) 100% IR w/ anode recycle	5.5	0.40	1.57	0.92	0.25	4.4	23.2	866	45.1	86.8
(4b) 150°C ΔT_{air}	3.7	0.40	1.65	0.87	0.17	2.7	9.9	897	47.3	88.4
(4c) 200°C ΔT_{air}	2.8	0.40	1.69	0.85	0.13	1.9	5.2	927	48.4	89.4
(5) 100% IR w/ cathode recycle	3.0	0.40	1.65	0.62	0.17	2.1	6.9	920	47.2	76.6
(6) 100% IR w/ AGR/CGR	2.9	0.40	1.66	0.88	0.15	1.9	5.4	935	47.6	89.3

*Conditions: 50 cell SOFC stack, 0.57 A/cm² current density, 85% system fuel utilization, 100°C cell air temperature rise, 700°C fuel inlet, Case (1) fuel: 97% H₂, 3% H₂O; Cases (2)-(6) fuel: 100% CH₄. Inlet air temperature to cell-stack is typically near 700°C, but was varied from case to case to obtain an 800°C ($\pm 1^\circ\text{C}$) average cell temperature. Case (1) cell voltage=0.75V. Cases (2)-(6) average cell voltage value = 0.698V ($\pm 0.004\text{V}$).

Surprisingly, the hydrogen-based system achieves the lowest electric efficiency, although it recuperates the most thermal energy (see Figure 8.12). The reason for the relatively low electric efficiency result is subtle and is associated with the system fuel energy input. All performance results in Table 8.2 are calculated for a given current density condition of 0.57 A/cm^2 . The specification of a stack current (or current density) determines the molar flowrate of hydrogen required (see Equation 4.20). From the overall methane reforming reaction, $\text{CH}_4 + 2\text{H}_2\text{O} \rightarrow 4\text{H}_2 + \text{CO}_2$, 4 moles of H_2 are produced for every mole of CH_4 (and 2 moles of water) supplied. The lower heating heating value is 242.0 kJ/mol for hydrogen and 802.9 kJ/mol for methane. The ratio of system fuel energy inputs for hydrogen and methane-fueled systems is then given as,

$$\left(\frac{\dot{E}_{H_2}}{\dot{E}_{CH_4}} \right)_{\text{system input}} = \frac{(\dot{n}_{H_2}) \cdot (LHV_{H_2})}{(\dot{n}_{CH_4}) \cdot (LHV_{CH_4})} = \frac{(4) \cdot (242.0)}{(1) \cdot (802.9)} = 1.20 \quad (8.1)$$

Equation (8.1) states that for a given current, the hydrogen system fuel energy input is 20% greater than the energy input for methane-fueled systems. This result would imply that for the same power output, hydrogen-fueled systems are 20% less efficient. A comparison of Cases (1) and (2) shows that presumption is not born out given that (i) the voltage-current performance of SOFCs operating on hydrogen is superior to operation using reformat fuels, and (ii) the system parasitic power requirements are lower in Case (1) due to lower system pressure drops and required airflow. These performance characteristics offset the larger fuel energy input of the hydrogen-fueled case, but not entirely. Additionally, the absence of the waste heat boiler in Case (1) coupled with an increase in the energy rejected from the cell-stack due to higher fuel energy input, leads to an increase in the grade of thermal energy (or exergy) available for cogeneration.

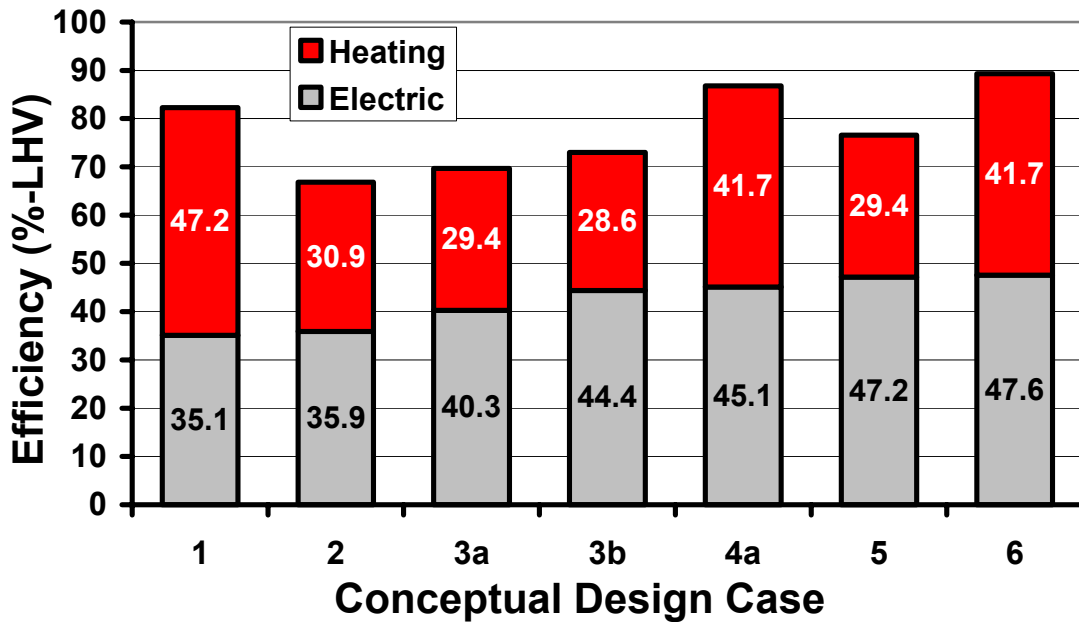


Figure 8.12 Efficiency comparison between conceptual SOFC system designs

It should be noted that for low-temperature PEM fuel cell systems, hydrogen is preferred due to the inefficiency in hydrocarbon fuel processing and the associated system complexity (due to both the number and the thermal mismatch of processes), better system dynamic response, and concerns over catalyst poisoning due to the presence of fuel contaminants in hydrocarbon fuels. These issues are not concerns for SOFC-based fuel cell systems as the tight thermal integration between hydrocarbon fuel processing and fuel cell heat generation leads to higher electric efficiencies, and in the case of anode gas recycle, higher cogeneration efficiencies.

As internal reforming is introduced into methane-fueled SOFC systems (Cases 3-6), the system parasitic power requirements are reduced and electric efficiency increases. The amount of cooling air decreases with increasing amounts of internal reforming due to the heat sink effect that the endothermic reforming reactions produce. As the extent of internal reforming increases from 0 to 100% (i.e., from Case 2 to 3), the air preheater duty is halved and the required heat exchanger surface area is reduced by more than 75% (assuming constant U value). The decrease in the required airflow leads to a decrease in the system TER as more electrical energy is generated while the thermal output remains relatively constant.

The use of anode gas recycle (AGR) in Case (4) system design is employed to reduce the external steam boiler duty or eliminate it entirely. The amount of recycle is defined as the fraction of the anode outlet molar flow that is recirculated back to the pre-reformer inlet. Thus, AGR must always be less than or equal to one at a steady-state operating condition. The amount of AGR is determined from specification of the steam-to-carbon (s\c) ratio of the fresh fuel-AGR mixture. In pure methane-fueled systems without AGR, the s\c ratio is simply the molar ratio of water to methane. In methane-fueled systems incorporating anode gas recycle, coking reactions due to CO reduction and Boudouard reactions are possible (see Equations 3.6 and 3.7) and the s\c ratio is then defined as,

$$s\c|_{AGR} = \frac{\dot{n}_{H_2O,AGR}}{\dot{n}_{CH_4,fresh} + \dot{n}_{CO,AGR} + \dot{n}_{CH_4,AGR}} \quad (8.2)$$

where $\dot{n}_{CH_4,AGR}$ is typically negligible due to the high conversion of methane in the anode compartment of the cell. The use of an anode gas recycle loop requires a distinction between *system* fuel utilization and *in-cell* fuel utilization parameters. Up to this point, such distinction between fuel utilization definitions has not been necessary as the two are equivalent in system designs without the use of AGR. That is,

$$U_{f,sys} = \frac{(\dot{n}_{H_2,consumed})}{(4\dot{n}_{CH_4})_{system\ feed}} = U_{f,cell} = \frac{(\dot{n}_{H_2,consumed})}{(4\dot{n}_{CH_4} + \dot{n}_{H_2} + \dot{n}_{CO})_{anode\ inlet}} \quad \text{without AGR} \quad (8.3)$$

The use of anode gas recycle effectively augments the anode inlet gas flow, thereby lowering the in-cell fuel utilization at a given current. To make an appropriate system performance comparison with design Cases (1)-(3), the *system* fuel utilization, $U_{f,sys}$, was held fixed in Case (4). An 85% system fuel utilization translates into a 68.6% in-cell utilization for the conditions of Table 8.2. As Figure 8.12 shows, the use of AGR has the benefit of both high electric efficiency and high heating efficiency which leads to 85+% cogeneration efficiencies without the use of a condensing stack gas heat absorber.

The amount of air excess is calculated using the following relation,

$$\lambda_{air} = \frac{\dot{n}_{O_2,sys}}{2\dot{n}_{CH_4,sys}} \quad (8.4)$$

where molar flowrates are taken at the system feed to the plant.

It is surprising that the use of anode gas recycle results in high electric efficiencies given the dilution of the anode inlet fuel gas. To achieve an s/c of 2:1 at the pre-reformer inlet, 62% of the anode outlet gas (on a molar basis) must be recirculated. As the amount of AGR increases (and the amount of steam feed from the boiler decreases), a decrease in theoretical cell voltage is expected due to greater dilution of the fresh fuel feed by CO and CO₂ gas species. Comparing Case (3b) and (4a) simulation data, the mole fraction of hydrogen at the fuel inlet can be reduced by 10% with the use of AGR. This dilution of the fuel feed leads to a reduction in the driving force for current generation and an increase in cell polarization from greater mass transport resistance. However, the in-cell fuel utilization is lower for anode gas recycle which tends to offset this effect at low to moderate current densities since the fraction of the H₂ at the cell outlet increases as the fuel utilization decreases. A comparison of the Nernst voltage between these two design cases supports this observation. The net effect is that the operating cell voltages at 0.57 A/cm² for Cases (3b) and (4a) are nearly equivalent. Further comparison between these two cases reveals that the air ratio is lowered by 0.4 stoichs (from $\lambda=5.8$ to $\lambda=5.5$ and the system electric efficiency is increased by 0.6 percentage points. The $\sim 1/2$ point increase in electric efficiency of Case (4a) is achieved by a reduction in blower parasitic power from a small lowering of system air input. The air-side pressure drop is slightly lower in Case 4 due to absence of the waste heat boiler. Interestingly, since the cell voltage (and hence, cell heat generation) is nearly identical for these two cases, the magnitude of the reduced air input is not adequately explained by a small lowering of the system pressure drop. The recycling of the anode outlet gases increases the capacitance rate of the inlet anode fuel gas (and therefore cooling capacity) and therefore also contributes to airflow reduction.

Cases 4(a-c) in Table 8.2 and Figure 8.12 also demonstrate that if the allowed air temperature rise across the cell is increased, significant reductions in airflow (at constant average cell

temperature) lead to sizeable reductions in air preheater and blower requirements, as well as marked improvements in electric efficiency. The magnitude of the increase in electric efficiency (and decrease in airflow) between Cases 4(a-c) suggests that there is an optimum air temperature rise at which further increases in ΔT_{air} do not offer sufficient cost or performance advantage. However, Table 8.2 also shows that reduced airflow elevates the afterburner temperature to over 900°C, which could be problematic with heat exchanger temperature limits if some active cooling measure (e.g., cold air bypass line) is not employed.

The heating efficiency of SOFC systems using AGR is higher than the other designs presented in Table 8.2 due to a net increase in available thermal energy of the exhaust gases as a consequence of (i) a reduction in fuel preheater duty via direct contact mixing of high temperature, recycled anode gases and low temperature fuel feed, (ii) a reduction in the air preheater duty, and (iii) an increase in the sensible thermal energy of the exhaust gas.

Cases (5) and (6) in Table 8.2 make use of cathode gas recycle (CGR). Recall from Chapter 3 (section 3.5) that purpose of cathode gas recycling is to reduce the system airflow and air preheater size by recirculating cathode outlet gases to a location upstream of the cell-stack. Prior to being readmitted to the cathode inlet, the hot recycled gases are mixed with the cooler fresh air feed from the preheater. The recycle effect can be accomplished with a blower or jet pump. The use of jet pumps are believed to offer design simplicity, lower cost, smaller physical size, and better high temperature operation than blowers or fans [7,5]. In order to produce the recycling effect, the fresh air driving pressure at the blower outlet must be increased. Table 8.2 indicates that recycling 50% of cathode outlet gases offers significant performance advantage over the other system design concepts. A comparison of Case (5) with Case (3b) reveals that the required airflow is nearly halved, the required air blower power is diminished by 39% and air preheater size is cut by an impressive 76%. The net system electric and cogeneration efficiencies are improved to 47.2% and 76.6%, respectively. However, the afterburner temperature climbs to 920°C and this design registers the lowest thermal-to-electric ratio (0.62) of all the systems.

Integration of the high thermal-to-electric ratio advantages of AGR systems with the low-air flow requirements of CGR systems can result in a high efficiency, high power output SOFC system design. Case (6) presented in Table 8.2 reveals the performance of the integrated system design. High electric and heating efficiency performance is obtained as depicted in Figure 8.12, as well as further reduction in air blower power and air preheater UA. Comparing Case (6) performance with that of the other system designs listed in Table 8.2, it clearly outperforms the other design alternatives in virtually every category.

Table 8.3 Relative cost of common heat exchanger tube materials [8]

Material	Approx. Relative Material Cost
Low-carbon steel	1.0
Copper	1.1
Aluminum	2.0
304 Stainless	2.5
316 Stainless	3.0
Nickel	5.0
Monel	5.0
Inconel	8.0
Titanium	12.0
Hastelloy	16.0

However, the benefits of reduced airflow come at the expense of higher combustor temperatures, added system complexity and control needs, and potentially higher cost. High combustor temperatures cannot be allowed due to increased material costs in the downstream heat exchangers. The importance in terms of system cost is emphasized by a comparison of heat exchanger material costs in Table 8.3. In order to prevent afterburner temperatures from rising above 850°C, an air bypass loop from the blower outlet to the combustor inlet must be incorporated into all system designs. Implementation of the air bypass scheme results in a change in operating performance of Case 6. The air stoichs are increased from 2.9 to 3.2, blower power from 0.15 to 0.17 kW, and electric efficiency is lowered from 47.6% to 47.0%.

8.3.2. Gas process design summary

As expected, the amount of cooling air is strongly coupled to the thermal integration of the stack with fuel processing and the allowable cell-stack temperature rise. The extent of direct internal reforming and the allowable stack temperature rise will ultimately depend upon the heat transfer characteristics within the cell-stack and the thermal stress constraints imposed by the materials used in cell construction. The air preheater heat exchange duty, air blower size, useful heat recovery, net system efficiency, and combustor temperature are also dependent on the amount of system airflow. Lower airflow rates result in higher combustor temperature. Thus, reductions in airflow must be balanced against combustor and metallic heat exchanger temperature limits.

There are many factors to be considered in fuel cell system design. The following sub-section summarizes the advantages and disadvantages explored in the present study and published in the technical literature.

8.3.2.1 Internal v. external reforming

Internal reforming (IR) can be accomplished both directly (DIR) and indirectly (IIR) in SOFC systems. The advantages of DIR and IIR over external reforming include:

- Capital cost savings through air blower and air preheater size reduction.
- Increase in electric efficiency due to a reduction of cooling air requirements (parasitic load). Operating fuel costs are also reduced.

The use of DIR over IIR has the following additional advantages:

- Reduction of capital cost by elimination of catalytic steam reforming equipment.
- Improvement in SOFC dynamic power response as a result of physical proximity of fuel reforming and electrochemical fuel oxidation processes [9].

The disadvantages of DIR include:

- Large cell temperature gradients in solid material due to strong cooling effect on the anode layer. Large temperature gradients can translate into large thermal stress in the ceramic material. This effect limits the degree of internal reforming. *Present capability for the degree of internal reforming in the SOFC anode compartment is estimated to be between 50-75%.*

- Increased risk for carbon formation on porous anode layer due to side reactions.

8.3.2.2 Anode gas recycle

Recycle of depleted anode gases provides an internal steam circuit, whereby a fraction of the electrochemically produced water vapor and other reaction byproducts are recirculated to the inlet of the fuel pre-reformer. As noted in Chapter 3, the use of anode gas recycle (AGR) offers the potential for reduced capital cost by elimination of the waste heat recovery steam generator. The capital cost of the boiler component has been estimated at less than 5% of the total system capital cost [5]. The use of AGR will lower the required system air input by an amount that is proportional to the desired steam-to-carbon ratio of the fuel mixture. For an s/c ratio of 2:1, the system air input is lowered by 7%. If AGR is implemented with internal reforming, significant rating (or size) reductions in numerous ancillary components, including the air blower, air preheater, and fuel preheater/pre-reformer are possible. These reductions lead to a more compact system design. Additional cell-stack capital cost reduction has been cited as possible through the higher cell power density that is achieved by virtue of the lower in-cell fuel utilization [5]. However, this performance advantage did not manifest in the results of Table 8.2. Another advantage of AGR is that it reduces the water vapor content of the exhaust gas stream, which effectively elevates the overall system efficiency due to an increase in the sensible thermal energy of the exhaust gas. Congruent with the above advantages, operating costs for SOFC systems with anode recycle are expected to be lower as a result of higher electric and cogeneration efficiencies.

The following additional advantages have been observed:

- Reduced magnitude in thermal gradients due to more uniform current density distribution. In fact simulations have revealed that a 24% reduction in the value of the maximum temperature gradient is possible at 0.7 volt operation.
- Reduced risk for carbon formation via the Boudouard reaction due to presence of CO_2 in inlet anode feed gas [10].

However, it has been noted that recycle of CO_2 contained in the anode gas can decrease the catalytic activity of the pre-reforming catalyst and increase the amount of catalyst required

[11]. It has also been observed that AGR leads to a reduction in methane conversion on the anode cermet material inside the cell-stack [11]. Whether or not the latter effect leads to a significant detriment in cell performance must be investigated further.

The use of recycle can complicate system control during load changes. Optimal jet pump/ejector design to accomplish the recycle must take into account the increased fuel compressor parasitic to achieve the necessary driving pressure for entrainment of anode gases and the pressure loss in the recycle loop (stack manifold, fuel channels, piping, etc.) [12].

8.3.2.3 Cathode gas recycle

This system design concept has been described in Chapter 3. It offers the advantage of reduced air preheater size (and investment cost) by direct contact heating of the inlet air by mixing with the high temperature cathode outlet gases. The presence of the recycle loop also reduces the fresh air feed required thereby lowering the blower capacity rating (and cost). The recycle of depleted air to the cathode inlet dilutes the oxygen concentration in the cathode compartment, lowering the cell voltage and electric efficiency. However, this trend is offset by the reduced airflow requirements [5].

The recycle effect can be accomplished with a jet pump/ejector device. As with AGR, the effectiveness of cathode recycle is negatively impacted by increases in the cell-stack and manifold pressure drops which lead to increases in the required air blower pressure rise to achieve the pumping effect.

The analysis of Section 8.3.1 has shown that CGR can be an effective design strategy to reduce the blower and air heat exchanger sizes and capital costs. *Interestingly, while hydrogen-fueled systems have been shown to be less efficient than methane-fueled systems, the use of CGR in these types of SOFC systems would enable them to obtain electric efficiencies higher than Case (1).* Additionally, this design concept would enable the efficiency performance of hydrogen-fueled SOFC systems to be more competitive with low-temperature PEMFC systems, while offering high-grade thermal energy for cogeneration.

8.4 Design Strategies for Variable Thermal-to-electric Ratios

Section 8.1 discussed the application requirements for residential fuel cell power systems. Most significant were the required transient response, magnitude of the electrical loads, and the required TER. The transient response and the magnitude of the electrical loads are not as significant for grid-connected SOFC systems where short-term load transients (and peak demands) can be met by the electric grid. Since residential applications, and power generation markets in general, require flexibility in operating modes, designing a system with variable TERs is a desirable objective.

Solid oxide fuel cell systems have difficulty in following the dynamic electrical load due to both the response time of fuel delivery system (seconds) and cell-stack thermal response (minutes). It is conceivable that the SOFC will eventually modulate up or down in power output in a relatively slowly changing manner, while the instantaneous power demand is served by the electric grid (or battery in stand-alone systems). Thus, the most difficult residential energy demand characteristic to meet with a fuel cell system is the high thermal/low electrical load condition. With this in mind, engineering design strategies have been conceived to address meeting the quasi-instantaneous thermal (hot water)-to-electric load ratios needed for the residential application as described by Figure 8.3.

8.4.1. *High thermal / low electrical load condition*

Six design strategies were conceived to either augment the thermal output of the fuel cell system or incorporate thermal storage:

1. *Net metering*

In many U.S. states it is possible to sell electricity produced from a home power generation system back to the utility through net metering. In such a case, the SOFC system could be designed to produce a fixed electric power and any excess power could be sold back to the grid. The fuel cell TER could then have flexibility in matching the residential (or other end-use) TER. However, widespread implementation of this method would significantly impact the local utility demand and needed capacity characteristics. The utility viewpoint is outside the scope of this thesis, but the merit of this design and operating strategy from the customer perspective is explored further in Chapter 9.

2. *Hot water storage tank system*

This strategy makes use of the off-peak thermal energy recuperation by storing it to serve peak demands at another time. It is the simplest of the available options to meet demand and may be integrated with a conventional hot water heater if demands cannot be met solely by waste heat recovery. An SOFC system with a 2-tank hot water system is simulated and presented in Chapter 9.

3. *Use of “excess” SOFC electrical energy generation for resistive heating of water*

The electrical demand of the application could be increased by use of a combination of resistive and thermal energy recuperative hot water heating. In this scenario, both the fuel cell electrical and thermal output would be increased, with only the resistive heating element as the additional system capital cost. However, higher SOFC load-factors should be weighed against cell-life issues.

4. *Integration with heat pump systems*

The capacity of the fuel cell can be increased to supply an electrical-driven heat pump which would serve both the heating and cooling loads of the household. In this scenario, the heat pump (when in heating mode) could be undersized as a portion of the waste heat from the fuel cell could be used to assist in serving space heating needs, in addition to hot water heating. For example, if the electrical demand of the household was 5 kW (where the heat pump provides 3kW of heat), the total “heating” system (fuel cell plus heat pump) could provide 8 kW of thermal energy. Such a scenario might be limited by the economics associated with geographic variables (utility costs and weather) and an additional waste heat recovery heat exchanger for space air heating, but deserves further investigation as the potential benefit is to meet all the energy loads of a residence with the fuel cell-heat pump system.

5. *Low fuel utilization operation and subsequent “over-fire” of the afterburner*

This strategy involves operating the SOFC system at a higher fuel flowrate than required and sending the unused fuel to the catalytic combustor (afterburner). The method would require a high temperature catalytic combustor design in which sintering or harmful temperature gradients in the catalyst were avoided. Additionally, the combustor would have to have a high turndown capability, as well as, flexibility in the fuel feed composition. In order to limit the outlet combustor temperature, water from the main could be circulated through the combustor before delivery to the hot water tank. Also, a fuel bypass line that goes directly from the desulfurizer outlet to the combustor inlet should be incorporated to avoid reforming of the “excess” fuel gas and the associated heat load for that process.

6. *Vary V-I performance characteristic*

Increases or decreases in the cell resistance would change the slope of the V-I characteristic and thereby the ratio of heat and electrical energy generated at a given current. The cell resistance could be changed by alteration of the cell temperature.

However, the response time of this control method is on the order of tens of minutes and might only be useful if the duration of the load change was known to exceed a certain time length. Cell temperature could be controlled by inlet air temperature and flow as described in Chapter 7.

Changes in the inlet fuel composition and the amount of cell fuel utilization would also alter the V-I characteristic due to changes in the thermodynamic driving force for current, as well as the mechanistic phenomena associated with activation and concentration polarizations. Fuel composition could be adjusted by controlling the extent of pre-reforming. Fuel utilization could be changed by variation of the fuel flowrate. However, this method would achieve only small changes in the V-I characteristic and would provide a larger effect on the TER by over-firing of the afterburner as discussed above.

In general, this strategy may present more problems than it solves due to the complex interactions of reactant feed conditions and cell-stack and system performance.

8.4.2. *Seasonal high electric load (summer)*

In the present study, peak electric loads will be served by the electric utility grid. However, there may be one design strategy where the hourly average household electric load can be met at any time of the year without significant increases in capital and operating costs. One strategy was conceived to meet high seasonal electrical demand:

7. *High voltage stack sizing, low voltage BOP sizing*

In this strategy, the stack size is based on a high voltage/high efficiency operating condition to meet the annual hourly average electric load. However, as we have seen throughout this study, maximum cell power occurs at lower cell voltages/efficiencies. If the lower capital cost balance-of-plant components were sized to accommodate the larger gas flows at low voltage/high power conditions, cell-stack power could be doubled depending on the original design voltage condition. Thus, hourly average electric loads could be met most of the time with high efficiency operation, but during the summer months, high power output could be achieved to serve the air-conditioning load. The disadvantage with this strategy is that system power turndowns are likely to be lowered and rotating equipment (blower, compressor, and pump) will be operating at lower efficiency, off-design conditions for most of the year.

Battery storage was considered an unattractive option for grid-connected systems due to both high first costs and significant maintenance costs. In addition to proper sizing to avoid deep discharges, system design complexity increases in terms of control and proper electrical-side design topology for maximum net system efficiency.

In any case, based on the results of section 8.3, system flowsheet design Case (6) appears to be the optimal design, however, it is a more complex system design that requires 2 recycle loops and an air bypass. Cases (4) and (6) are chosen for simulation studies of Chapter 9. Since near term (ca. 2005) commercial SOFC systems are not likely to employ AGR and CGR concepts, Case (2) design will also be simulated and compared against the results from Cases (4) and (6). Additionally, per the discussion of section 8.4 on flexible TERs, design strategies 1, 2, and 7 are considered the simplest and are investigated further in Chapter 9.

8.5 Chapter

References

8.6

-
- 8.1 P. Bos, "Commercializing fuel cells: managing risks," *J. Power Sources*, **61** (1994).
 - 8.2 K. Krist and J. Wright, "SOFC Residential Cogeneration," *Proc. of the 1999 Joint DOE/EPRI/GRI Fuel Cell Technology Review Conference*, Chicago, IL, August (1999).
 - 8.3 J. J. Mutch, "Residential water heating, fuel consumption, economics, and public policy," *RAND Report R1498*, (1974).
 - 8.4 S.A. Klein, W.A. Beckman, and J.A. Duffie, *TRNSYS –A Transient System Simulation Program*, Solar Energy Laboratory, Madison, WI, (2000).
 - 8.5 E. Riensche, J. Muesinger, U. Stimming, and G. Unverzagt, *J. Power Sources*, **71** (1998) pp. 306-314.
 - 8.6 W.L. Lundberg, "Solid Oxide Fuel Cell Cogeneration System Conceptual Design," Final Report, GRI-89/0162, Gas Research Institute, Chicago, IL, July (1989).
 - 8.7 M.R. Taylor, D.S. Beishon, "A study for a 200 kWe SOFC system for power and heat," *Proc. Of the 1st European SOFC Forum*, Lucerne, CH (1994).
 - 8.8 R.H. Dart and J. Whitbeck, "Brine Heat Exchangers," in *Sourcebook on the Production of Electricity from Geothermal Energy*, J. Kestin et al., editors, U.S. Department of Energy publication, DOE/RA/4051-1, pp. 379-413, (1980).
 - 8.9 J. Meusinger, E. Riensche, and U. Stimming, "Steam reforming of natural gas in solid oxide fuel cell systems," *J. Power Sources*, **71** (1998), pp. 315-320.
 - 8.10 M. Mozaffarian, "SOFC for Combined Heat and Power Applications," *Proc. Of the 1st European Solid Oxide Fuel Cell Forum*, Lucerne, Switzerland (1994), pp. 353-362.
 - 8.11 R. Peters, R. Dahl, U. Kluetngen, C. Palm, and D. Stolten, "Internal reforming of methane in solid oxide fuel cell systems," *J. Power Sources*, **102** (2002) pp. 238-244.
 - 8.12 E. Achenbach, E. Riensche, and G. Unversagt, "Gas Processing of SOFC Plants," *Proc. Of the 1st European Solid Oxide Fuel Cell Forum*, Lucerne, Switzerland (1994), pp. 153-162.

Chapter Nine Design and Operation for Residential Applications

Chapter 7 focused on assessing cell-stack performance capabilities and limitations while varying stack physical design and operating parameters. Chapter 8 evaluated the overall performance of alternative system-level process design concepts. Economic sizing of the SOFC system, operating strategy (base-load or load-follow), and merits of cogeneration are also important considerations in optimal system design. Supply of thermal energy to a household with a fuel cell system for space or hot water heating may not be economical. Indeed, the economics of waste heat recovery to serve residential thermal energy loads needs to be evaluated further to gauge both its potential and the conditions for when it is attractive. These aspects of fuel cell system design are explored in this chapter by performing annual simulations for system alternatives configured and operated to meet residential energy loads.

The successful design of fuel cell systems requires proper selection of cell stack design operating conditions. Studies focusing on optimal operating point selection are emerging [1, 2, 3]. The operating point of the fuel cell can be expressed in terms of performance variables, such as fuel utilization, operating voltage, cell temperature, and area specific resistance. The operating point will dictate the power density and operating efficiency of the stack module. In turn, establishment of these performance parameters enables the determination of capital, fuel, and electricity costs for a given utility requirement. The choice of relevant performance parameters may support the objective to maximize electric power or efficiency.

In addition to the design point selection for optimal operation, the fuel cell operating envelope must be capable of accommodating off-design point operation for electric load-following situations. Thus, before system simulations are performed, optimal design operating point selection through minimization of the system life cycle costs expressed as “cost-of-electricity” (COE), is first explored. The sensitivity of economic and cell performance parameters to operating point selection is also examined. The effectiveness of system sizing, cogeneration

vs. electric-only systems, base-load vs. load-following, and alternative design configurations are then explored through annual system performance simulations. The chapter concludes with a summary of design guidelines that are based on the results from the entire research effort.

9.1 SOFC System Design via Economic Optimization

9.1.1 Cell-stack design operating point selection

SOFC system design case 4(a) from Chapter 8 was selected for further study. Figure 9.1 illustrates the system design flowsheet for a SOFC system operating at 800°C with anode gas recycle and 100% internal reforming. Anode gas is recycled such that a 2:1 steam-to-carbon ratio is accomplished at the pre-refomer inlet and total system fuel utilization is 85%. The system design also incorporates a cold air bypass to ensure that the temperature of the product gases leaving the combustor do not exceed 850°C. Approximately 3 kW of AC power is delivered and 2.75 kW of thermal energy (delivered at 40°C to a second water tank) is recovered. The system achieves a thermal-to-electric ratio of 0.92 and the resulting system electric efficiency is 45% (LHV) and the cogeneration efficiency is 87% (LHV).

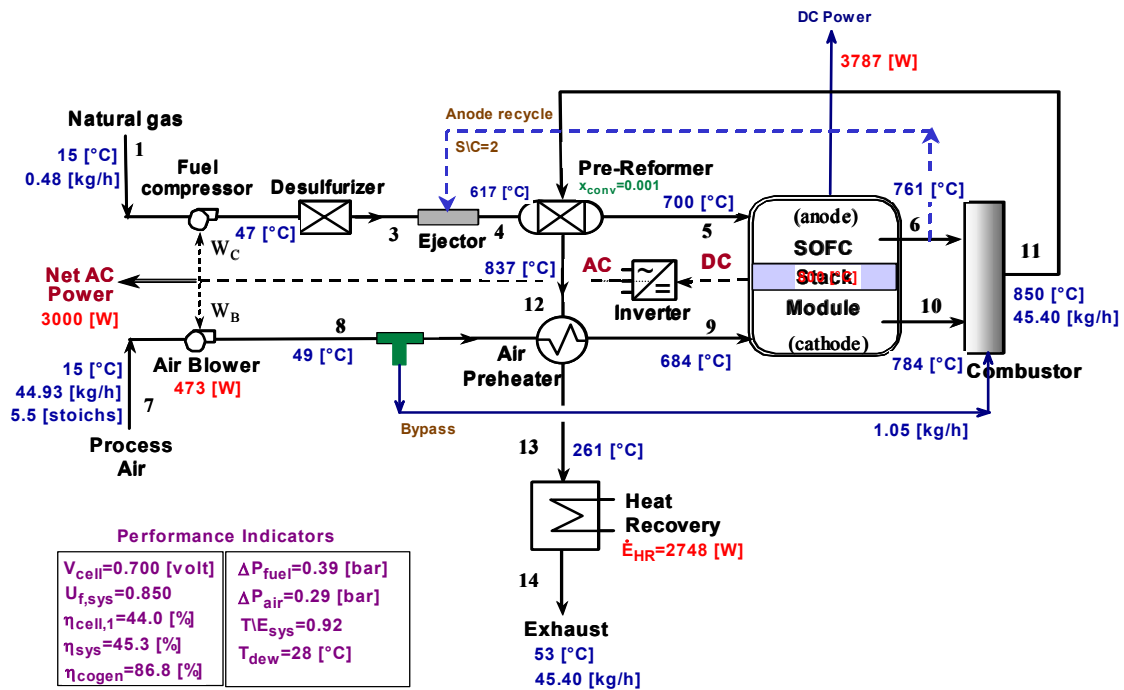


Figure 9.1 Schematic diagram of 3 kW SOFC system design with anode recycle (case 4a)

In this analysis, a fixed AC power output is specified and the variation of design cell voltage, fuel utilization, and temperature are examined. The objective is to determine the optimal design operating voltage, temperature, and fuel utilization for the system as detailed in Figure 9.1. Using the cost information presented in Chapter 6 and Equations (6.26-27), the cost-of-electricity was computed for a variety of cell design conditions[†]. Figure 9.2(a) depicts the influence of design cell voltage on the system cost-of-electricity for the case of fixed power output. As the design operating voltage is increased (increasing fuel conversion efficiency), the cell-stack costs begin to increase at a rate greater than operating costs because the lower current densities demand larger cell areas for a 3 kW output. As the fuel efficiency increases, the fuel cost savings cannot offset the increase in fuel cell capital cost; consequently, the selling price of electricity must rise to compensate. The minimum cost of electricity occurs at a design cell voltage of 0.7 V and the estimated cost of electricity (including a heat credit for exported useful thermal energy in the form of hot water) is 7.4 ¢/kWh. The unit system capital cost* associated with a 0.7 V design cell voltage is about 1500 \$/kW.

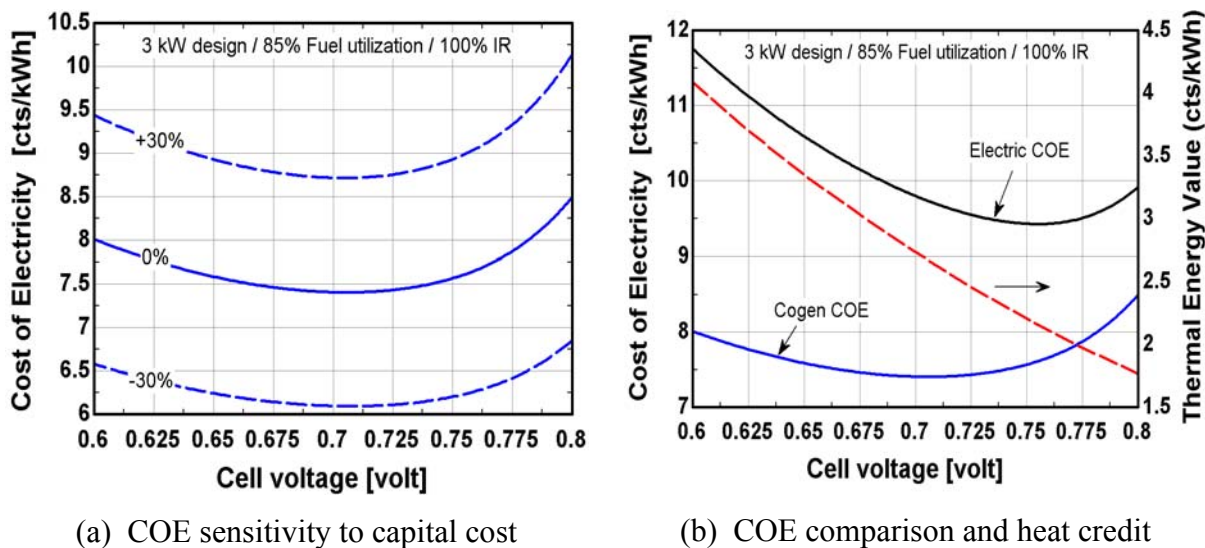


Figure 9.2 Influence of design cell voltage on cost of electricity

[†] The COE is computed using a methane (estimated from natural gas) price of \$7.0/MMBtu, a capacity factor of 0.8, 20% discount rate, 0.5¢/kWh maintenance cost, and system plant life of 20 years. See §6.3 for details.

*The unit system capital cost does not include installation, shipping, or contingency fees.

Figure 9.2(a) also shows the sensitivity of cost-of-electricity to a capital equipment cost uncertainty of $\pm 30\%$. Using the uncertainty estimate, the COE for the 3 kW SOFC system can be restated as 7.4 ± 1.3 ¢/kWh. A breakdown of the contributions to the cost-of-electricity for the 0.7 V design condition is shown in Figure 9.3. Recall that the fuel cell capital cost estimates were given for a mass production scenario (0.2 – 2.5 GW/yr) and have a 33% salvage value at the end-of-life. For this situation, fuel and balance-of-plant (BOP) costs dominate the total system life cycle costs.

In Chapter 6, methods of determining the cost-of-electricity for either electric-only or cogeneration operation were given (see Equations 6.26-27). Figure 9.2(b) presents these COE indices, as well as the value of thermal energy recovered defined in Equation (6.27), as a function of design cell voltage. Interestingly, as the design cell voltage is increased, the electric-only COE (COE_1) decreases more rapidly than the cogeneration COE (COE_2) reaching an optimal value of 0.76 V. For COE_1 , the optimum is established by the same mechanism as COE_2 – competing fuel and capital costs; however, the location of the optimum is altered as fuel savings for recuperated thermal energy from the system are not realized.

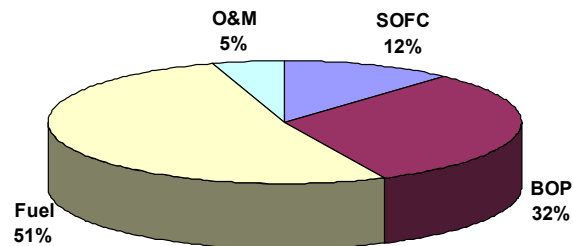


Figure 9.3 Breakdown of the COE for 3 kW SOFC system design case

As discussed in Chapters 7 and 8, system fuel utilization affects the operating cell voltage and the system thermal energy output. Figure 9.4 presents the influence of system fuel utilization and design operating cell voltage on the optimal cogenerative COE. As the system fuel utilization is increased, Figure 9.4(a) shows the COE increases due to decreases in the thermal energy recovered and thus decreases in the associated heat credit. The decrease in thermal energy output of the system shifts the optimal COE to a lower design cell voltage (i.e., lower

efficiency). An increase in the system fuel utilization also results in an increase in cell-stack capital cost due to the reduced average cell current density, which increases the number of cells required to generate the same power; however, this effect is offset by a decrease in fuel cost. The minimum COE revealed by Figure 9.4(a) occurs at 75% fuel utilization and 0.75 V. While not shown, a reduction in fuel utilization below 75% registers larger COEs. The results shown in Figure 9.4(a) demonstrate that the optimal design cell voltage and fuel utilization are not independent of one another for the case of cogeneration. For systems intended for electric-only applications, the minimum COE can be relatively insensitive to both design voltage and fuel utilization.

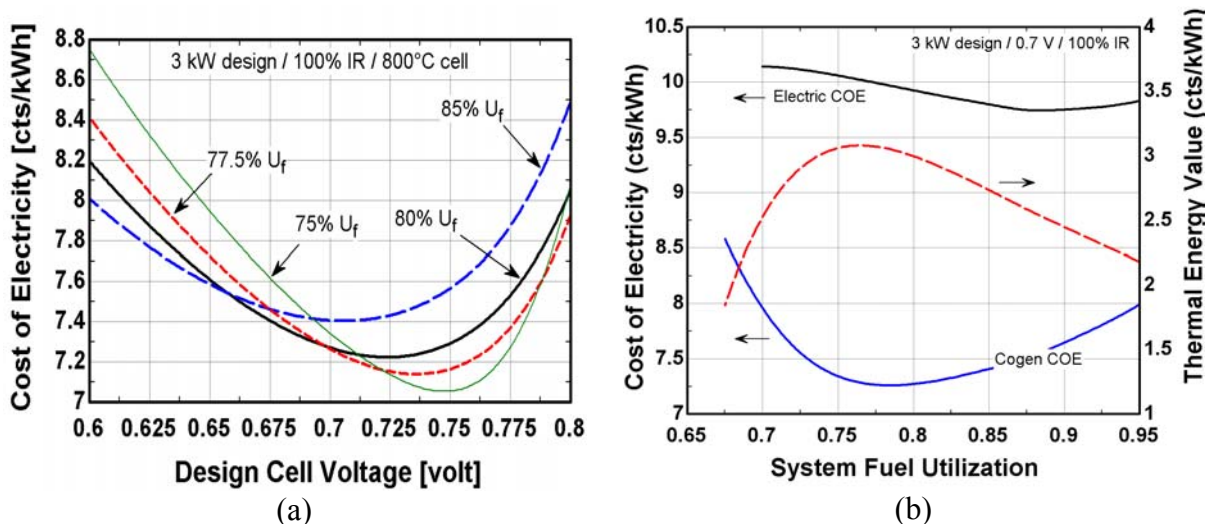


Figure 9.4 Influence of system fuel utilization and design cell voltage on COE

Figure 9.4(b) depicts the influence of system fuel utilization on the value of thermal energy and the COE for cell operating at 0.7 V. The cogenerative COE achieves a minimum at a fuel utilization of approximately 78%, whereas the electric-only COE is minimized at a fuel utilization of 88%. As with design cell voltage, Figure 9.4(b) illustrates the significant influence that thermal energy recovery has on the optimal design fuel utilization as evidenced by the near coincidence of minimum cogenerative COE with the maximum thermal energy value. (See Equation 6.28 in §6.3.1 for the valuation of thermal energy). Low fuel utilization operation requires a larger fuel input but a smaller system airflow to maintain the same system power output and cell operating temperature.

The surplus of unused fuel exiting the cell-stack increases the thermal energy available for recuperation. However, as Figure 9.4(b) shows, the amount of thermal energy recuperated at low fuel utilizations ($<0.75 U_f$) can also be reduced. This reduction is due to an increase in the water vapor concentration in the exhaust gas which results from the lower required system airflow. The reduction in thermal energy recovered for the larger fuel inputs required for low fuel utilization operation translates into lower overall system efficiencies (and lower “heating efficiency”). A maximum in the value of thermal energy is then achieved due to the tradeoff between the amount of thermal energy recoverable in the exhaust gas and the amount available after electrical energy production. The value of thermal energy is maximized at a fuel utilization of about 78%, which coincides with the maximum system thermal-to-electric ratio (not shown).

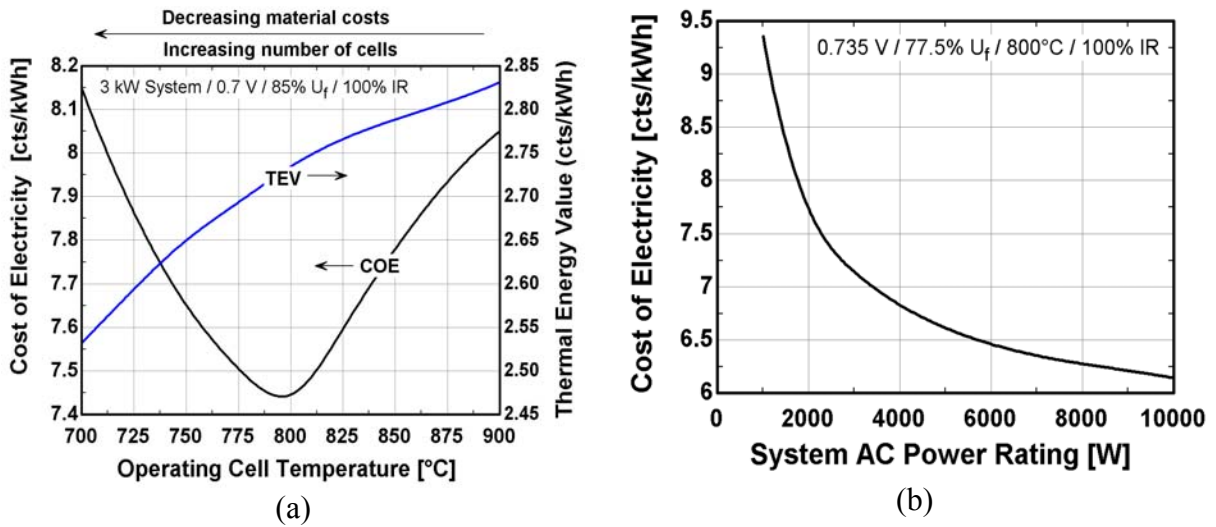


Figure 9.5 Influence of operating cell temperature and system power rating on life cycle costs

Figure 9.5(a) depicts the effect of cell operating temperature on the cogenerative cost of electricity (COE_2) and the value of the thermal energy recovered in the form of hot water. As the cell operating temperature increases, cell resistance decreases at fixed voltage which results in increases in cell-stack power density. The system cost of electricity decreases in response to decreasing cell-stack capital cost as fewer cells are needed to generate the specified power. Higher cell temperatures lead to lower cost of electricity until near an operating cell temperature of 800°C. At this point, the stack material costs rise with

increasing temperature due to the need for alloy-interconnect and eventually, all-ceramic cell component materials. Thus, above 800°C temperature operation, the stack material costs for outweigh the performance advantages of lower cell resistance. (The cell and BOP component costs and cell component thickness are assumed to be constant over the range of temperatures studied.) Also, as shown in Figure 9.5(a), the thermal energy value increases with the increasing design operating temperature due to a higher grade of thermal energy in the exhaust gas.

Figure 9.5(b) illustrates the economy of scale that can be realized when varying the system power rating for a cell-stack operating at 800°C with an average cell voltage of 0.735 V and a system fuel utilization of 77.5%. As the size of the SOFC system increases, the cost of electricity decreases from a COE of 9.4 ¢/kWh at 1 kW to 6.1 ¢/kWh at 10 kW. It should be noted that no economy of scale is present in the cost analysis of the solid oxide fuel cell stack. Thus, reductions in unit system cost arise only from the economy of scale associated with balance of plant hardware.

Table 9.1 Optimal SOFC stack design parameters

Parameter	Cogeneration Systems		Electric-only
	Load-following	Base-load	
Cell voltage	0.735 V	0.750 V	0.745 V
Fuel utilization	78 %	75%	90%
Operating temperature	800°C	800°C	800°C
Power Density	0.330 W/cm ²	0.290 W/cm ²	0.260 W/cm ²

Although cost of electricity minimization techniques are based on quantitative values of the optimal cell design parameters, these optima must be checked against other qualitative system design considerations, such as operability, control, and load turndown capability. For load-following systems, SOFC systems capable of 5:1 turndowns are desirable. Fuel cell systems with high cell voltage design points make turndown difficult as fixed air temperature rise and nominal cell temperature conditions are difficult to maintain at low-loads (high voltages). For

base-load applications, this difficulty is alleviated as the design operating point is maintained. Since waste thermal energy is not “valuable” in electric-only systems, optimum system fuel utilizations are higher. Cell operating temperatures in excess of 800°C will result in higher combustor temperatures that can exceed the metallic heat exchanger limits. With these added considerations, the optimal cell design conditions were determined as shown in Table 9.1.

The preceding analysis further reveals the following about optimal design cell-stack operating conditions:

- Optima exist for design cell voltage, and fuel utilization (and temperature); however, the optimal values for these parameters cannot be determined independently of one another for the case of SOFC cogeneration systems.
- Although not shown, the optimal design parameters are independent of cell-stack size (or rating), i.e., the same optimums are found for 1-10 kW power cell-stacks.
- As the waste heat has no economic value in electric-only systems, optimal fuel utilizations are typically 10 points or more higher than for cogeneration systems.
- Economy of scale suggests that the larger the system size, the lower the unit system cost (\$/kW). This would indicate that designing fuel cell systems for larger capacities (~10 kW) that serve multi-family dwellings or small commercial applications could be the most economical strategy.
- An optimal cell operating temperature is achieved near 800°C.

9.2 Annual Simulation Setup

9.2.1 Overview of Example System Design and Performance

Five planar SOFC systems incorporating the Case 4 design concept with anode gas recycle and a two-tank (preheat and standby) thermal storage system were designed for simulation with capacities of 1, 2, 3, 5, and 10 kW. Each system employs two water storage tanks to enable continuous heat recovery irrespective of domestic hot water loads. Table 9.2 details the system specifications.

Table 9.2 SOFC system design point specifications

Parameter	Value
Net system efficiency	45.2% (88% cogen)
Cell temperature	800°C (nom.)
Cell voltage	0.735 V
Power density	0.330 W/cm ²
Fuel utilization	78%
Turndown	5:1
T/E ratio	0.93 kW _{th} /kW _e
Air-side pressure drop	290 mbar
Fuel-side pressure drop	390 mbar
Compressor efficiency	40 – 70%
Blower efficiency	30 – 63%

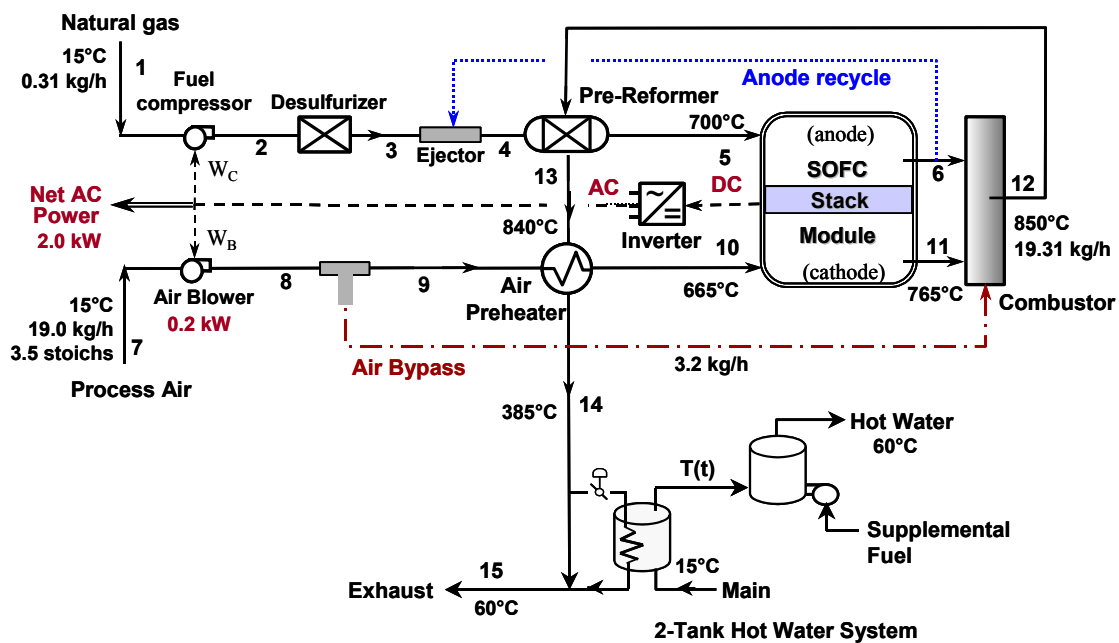


Figure 9.6 2 kW SOFC cogeneration system employing AGR and internal reforming

A 2 kW system concept complete with balance of plant equipment is shown in Figure 9.6 operating at the optimal design point conditions (0.735 V, 77.5% U_f , 800°C). Figure 9.7 shows the dramatic difference between fuel cell stack DC power and net system AC power performance. In a 2 kW cogeneration SOFC system design, the fuel cell stack can

theoretically approach 5.5 kW; however, in practice this power can never be reached due to increasing BOP (blower and compressor) parasitic loads.

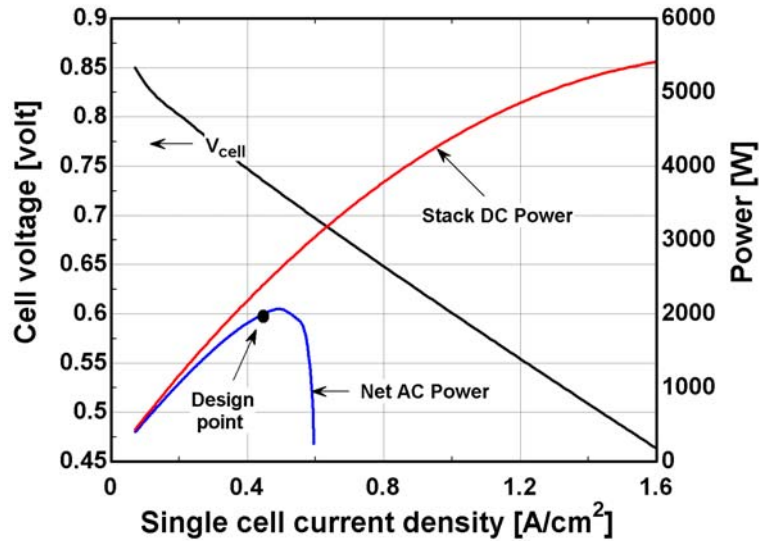


Figure 9.7 2 kW SOFC stack and efficiency performance (73 cells, 78% fuel utilization, 800°C operation, 100% internal reforming)

9.2.2 Simulation conditions

The energy demands and specifications for the residence considered are identical to those previously described in Section 8.1. To reduce the computational time for an annual simulation, only 3 days of household energy demand data in each month were used to represent a 28, 30, or 31 day month; the annual simulation is then scaled from the 36 days (864 hours) simulated. The SOFC annual system operation and maintenance cost (beyond fuel cell stack replacement) is estimated at 0.5 ¢/kWh [4]. Utility price data for natural gas and electricity were obtained from Madison Gas & Electric. In the case where net metering is employed, the rate at which a utility will buy back the electricity from the customer depends on which state the system is located in. A survey of net metering programs of 31 U.S. states indicates that most utilities will buy back any excess electricity (i.e., any electrical energy produced in excess of the net consumption over the billing cycle) at an avoided cost rate that can range from 1.5 to 2.0 ¢/kWh [5]. The simulation studies are for utility interconnect

systems in which the electric utility acts a peaking plant, providing power to the house when the instantaneous electrical demand cannot be met with the SOFC system. Grid-connection costs are dependent on the utility and can vary significantly from one utility to another. A one-time grid-connect fee of \$250/kW was chosen as a “nominal” value based on a recent study of utility interconnections [6].

Table 9.3 Base case application specs.

Parameter	Specification
Geographic location	Madison, WI
Size of home	232 m ² (2500ft ²)
Annual hourly average electric load	0.94 kW _e
Annual hourly average domestic hot water load	1.05 kW _{th}
COP of air conditioning unit	3.0
System operation and maintenance cost	\$0.005 / kWh
Utility natural gas price	\$7.0 / MMBtu (\$0.024/kWh)
Utility electricity price	\$0.088 / kWh
Avoided cost of electricity buy back (net metering)	\$0.02 / kWh
Utility interconnect	Yes
Utility grid-connection charge	\$250/kW

Table 9.4 SOFC system capital cost

System Size (kW)	Cogen. (\$/kW)	Electric-only (\$/kW)
1	2170	2030
2	1630	1645
3	1425	1490
5	1250	1355
10	1050	1225

Table 9.3 and Table 9.4 summarize the simulation parameters. The system capital cost data presented in Table 9.4 reflect both the effect of economy-of-scale and the design point selection. Thus, cogeneration system costs will differ from electric-only systems due to the lack of the hot water tank and the higher design voltage and fuel utilization. The higher the design voltage (and/or fuel utilization), the lower the cell power density and therefore the higher the cell-stack and system unit costs.

9.3 Evaluation of Operating Strategy (load-following v. base-load)

The SOFC electrochemical response is estimated to be on millisecond timescales (10^{-3} seconds). However, discussion in Chapters 2, 3, and 5, noted that the transient load-following capability of the SOFC is governed by the thermal response of the stack materials and the heat transfer characteristics within. Even in hot standby mode, the thermal lag of the cell-stack has been estimated to range from 120 – 1200 seconds. Since the system concept makes use of a small pre-reformer, the *system* thermal response will be further slowed by fuel delivery time. Nevertheless, the following analysis assumes a millisecond SOFC system power response rate in an effort to gauge whether such a system operating strategy is desirable from economic and emission performance standpoints.

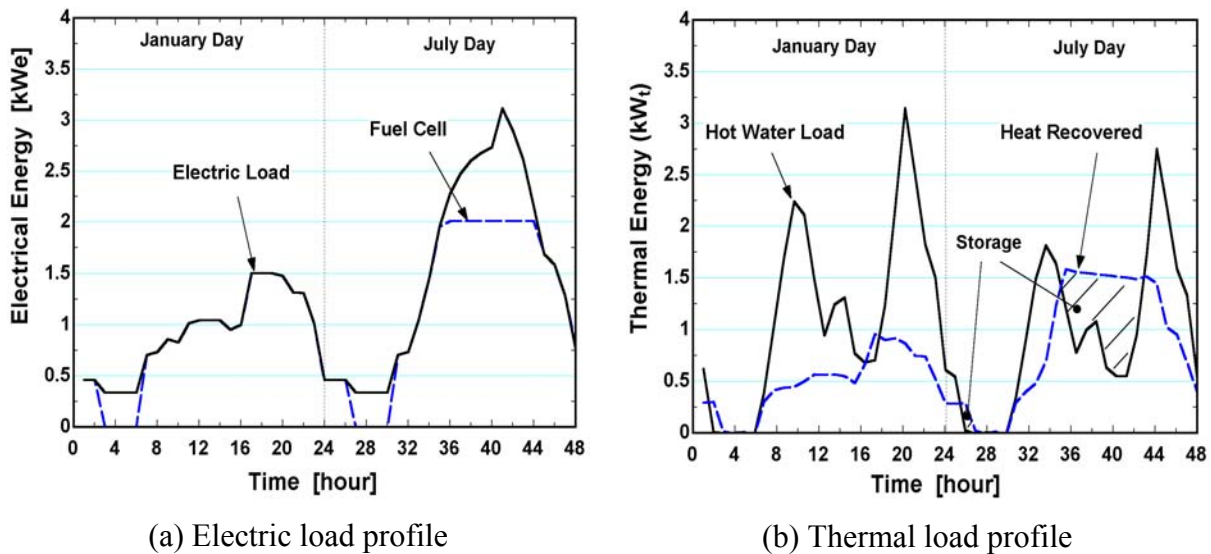


Figure 9.8 2 kW SOFC operating profiles

The fuel cell electric and thermal load-following performance for the winter and summer days are shown in Figure 9.8. The solid oxide fuel cell system was designed to handle a 5-to-1 electric turndown. Thus, for loads below 0.4 kW, the fuel cell was forced to shutdown (Figure 9.8(a)). Shutdown periods last between three and four hours, and generally occur in the early morning hours. The first hot water storage tank was sized to 60 gallons to ensure that tank water temperatures would not exceed 90°C during times when high electric demand are coincident with low water draws. Mixing cold water from the main could conceivably lower tank temperatures to accommodate a delivery temperature of 60°C. The main advantage of the 2-tank hot water configuration is that it enables continuous heat recovery irrespective of the load as evident by the thermal load profile for the July day shown in Figure 9.8(b).

The annual simulation of a 2 kW system (Figure 9.6) operating in a load-following manner reveals that an annual system electric efficiency of 53.5%, cogeneration efficiency of 90.5%, and a simple payback of 8.3 years are possible. If the operating strategy is altered to base-load with the utility buying back the excess power generated, the electric and cogeneration efficiencies are reduced to 44.3% and 81.6%, respectively, while economic payback increases to 11.8 years. In grid-connected applications, the net economic benefit of owning a fuel cell system comes from the savings realized by leveraging annual utility fuel costs against annual utility electricity costs. Therein lies the reason for the increase in economic payback when shifting to a base-load strategy; that is, for excess power generation, the price of the fuel (2.4 ¢/kWh) is larger than the selling price of the electricity (2.0 ¢/kWh).

Figure 9.9 provides a comparison of the economic effectiveness between load-following and base-load operating strategies as a function of SOFC system capacity. In the base-load scenario, the SOFC system is operating in a net metering manner. As system size is increased, fewer savings are realized for the base-load scenario resulting in an infinite payback above 3 kW-sized fuel cell systems. A 1 kW-size SOFC system operating in a base-load configuration has the lowest economic payback as the least excess power generated by the system is purchased by the utility at their retail rate. Figure 9.9 also shows that for single

family residences, the payback economics grow less attractive with increasing system size as capital costs increase at a rate greater than the annual savings. Figure 9.9 further shows that the apparent difficulty in achieving a “true” or quasi load-following solid oxide fuel cell system becomes irrelevant since the analysis indicates that when the system is sized correctly, *base-load operation is economically more favorable than load-following* for the grid-connected application. Optimal sizing of the SOFC system will be discussed in more detail in the following section.

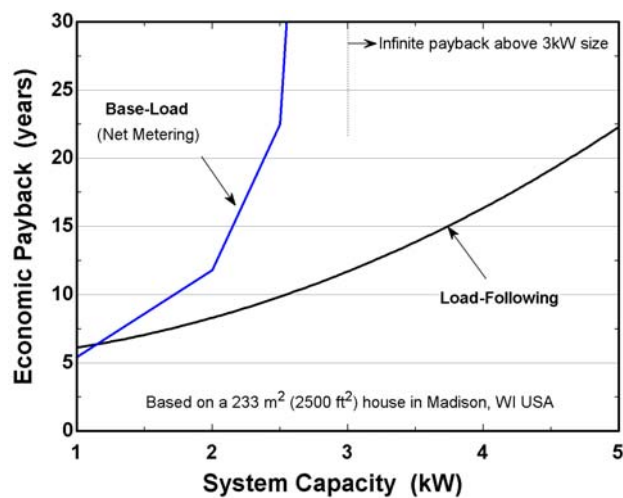


Figure 9.9 Comparison of base-load and load-following operating strategies in terms of system size

9.4 Economic Sizing of the SOFC stack

Figure 9.10(a) presents simulation results for the effect of SOFC system capacity on payback and electric capacity factors for a load-following situation. As expected, the SOFC *electric capacity factor** decreases with increasing system size. The electric capacity factor of the fuel cell system is an important performance parameter as it measures the total annual operating usage of the high capital cost system. The larger the capacity factor, the better the fuel cell payback economics appear. The electric capacity factor performance of the fuel cell indicates

*The annual fuel cell electric capacity factor is defined as the kWh supplied by the fuel cell divided by the maximum kWh it could have supplied (e.g. 2 kW * 8,760 hours.)

that a 2 kW size solid oxide fuel cell may be too large as only 43% of its annual electrical energy production capacity was utilized. Employing a smaller fuel cell system of 1 kW increases the electric capacity factor to 77%. Other methods to increase the fuel cell system electric capacity factor include using an even smaller SOFC system, base-load operation using “net metering,” employing lead acid batteries, and heat pumping.

The “house” electric capacity factor is an index that indicates the effectiveness of the fuel cell system in meeting the household electric load. That is, it is the total kWh of electricity supplied by the fuel cell system divided by the total kWh household demanded. As system capacity is increased, the house electric capacity factor passes through a maximum at 2 kW and decreases with increasing system rating due to the system turndown limitations. In other words, a 2 kW fuel cell system would have a minimum load of 400 W for a 5:1 turndown. All electrical loads below this threshold would go unmet by the fuel cell system and met by the utility grid. Thus, unless the system turndown capability can be substantially increased, a 5 kW SOFC system should not be employed in a load-following scenario for both economic and household energy effectiveness reasons.

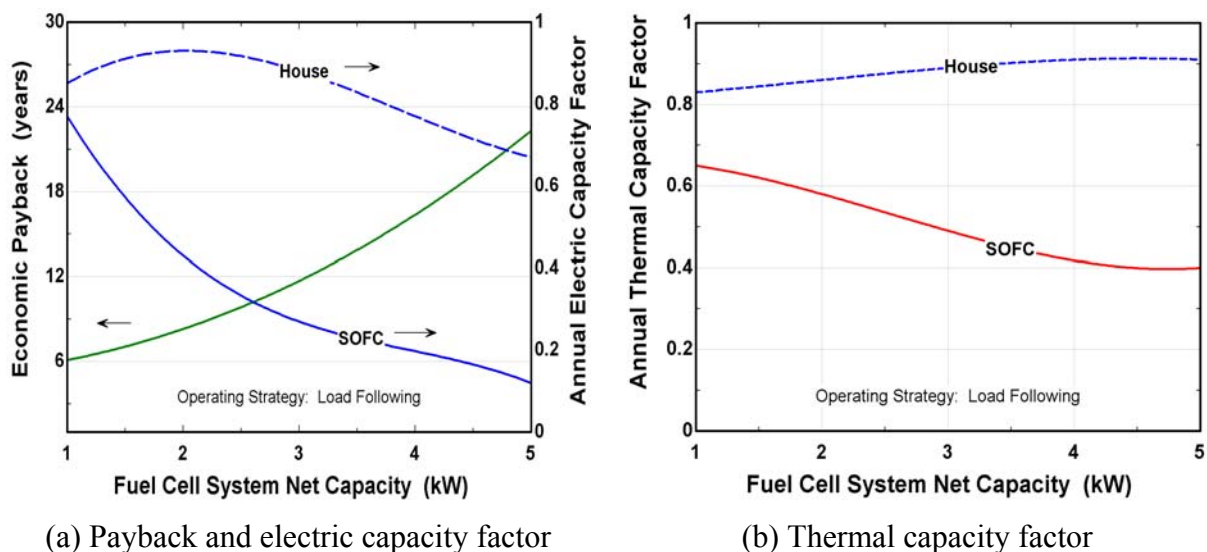


Figure 9.10 Effect of size on payback and capacity factors

The *thermal* capacity factor* of the fuel cell is also a useful measure and is depicted in Figure 9.10(b). The 1 kW SOFC system achieved an 83% fuel cell thermal capacity factor displacing 6000 kWh of thermal energy that otherwise would have been served by a conventional hot water heater. As system capacity increases, the house thermal capacity factor also increases. Unlike the household electric capacity factor, the thermal capacity factor increases continuously with increasing system size due to thermal storage for the storage size investigated. Use of electrical storage could also effectively increase fuel cell electric capacity factors; however, the added cost and maintenance from batteries (for instance) may outweigh its technical advantages.

Figure 9.9 and Figure 9.10 show that the optimal fuel cell size is one that maximizes electric and thermal capacity factors and minimizes system payback period. *The previous analysis further indicates that the optimal fuel cell system size is one based on the annual hourly averaged electric load.* It should be further noted that the absolute numeric values of economic payback are not as important as the relative changes in payback period between operating strategies and system sizes.

9.5 Evaluation of Electric-only vs. Cogeneration Operation

This section investigates the merits of thermal energy recovery for a 1 kW base-loaded SOFC system in terms of simple economic payback. Several interesting trends are apparent in Figure 9.11. First, the analysis indicates that thermal energy recuperation is more favorable than electric-only systems irrespective of the price of electricity or natural gas for the range shown. At the reference natural gas price of \$7/MMBtu (2.4 ¢/kWh) and the electricity price of 8.8 ¢/kWh, a cogeneration system payback of 5.4 years and an electric-only payback of 8.7 years are possible. As the price of the utility fluctuates, cogeneration in the form of hot water can protect the owner by offering less sensitivity to utility pricing. In particular, Figure 9.11(a) shows that the value of thermal energy recuperated increases with increasing natural

* The thermal fuel cell capacity factor is defined as the kWh recovered from the exhaust gas divided by the kWh that could have been supplied had the exhaust gases been reduced to the water main temperature.

gas price. In contrast, as electricity price increases, the economic effectiveness of cogeneration is decreased. However, if electricity prices decrease as may occur in a deregulated electric utility market, the use of cogeneration over electric-only becomes even more favorable.

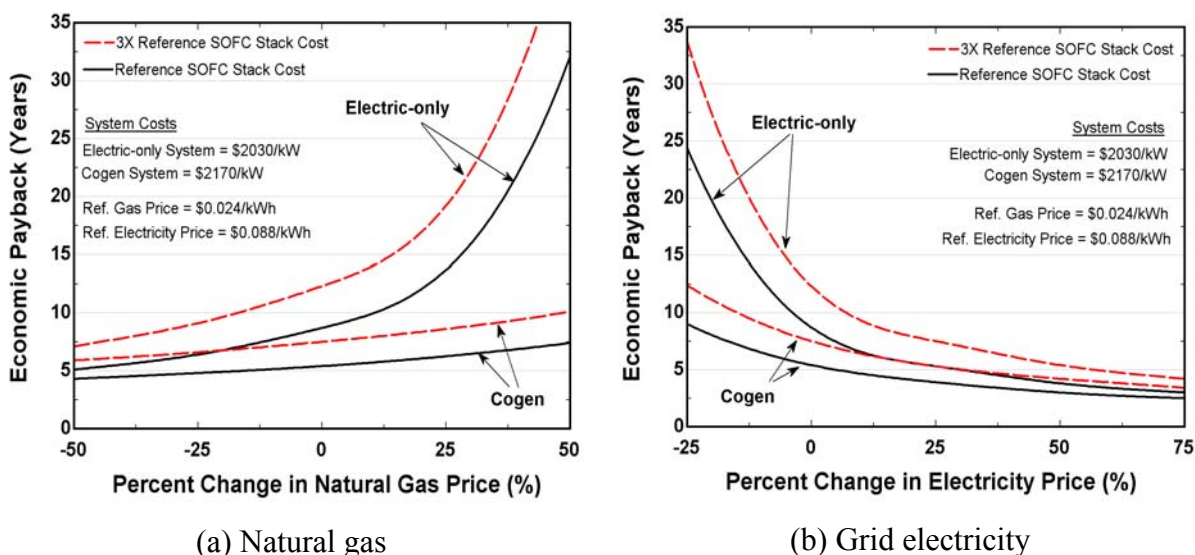


Figure 9.11 Sensitivity of economic payback to utility prices and SOFC stack cost

The preceding results have been based on a SOFC stack cost of \$450/kW, a cost only achievable in high volume manufacturing situations. A stack cost three times this value was also studied to reflect the economic sensitivity of early production units. The dashed lines in Figure 9.11 show that the payback period for both cogeneration and electric-only systems increases by about 40%, while demonstrating the same trends as the cheaper unit stack cost.

9.6 Emission Performance

The specific (kg/kWh) CO₂ emissions from supplying power to the residential application in both base-load and load-following scenarios are depicted in Figure 9.12. The ordinate includes only the CO₂ emissions from the fuel cell system to meet the electrical energy demands of the home. Thermal energy recuperated from the system and CO₂ emissions from the utility are not included. The SOFC system for base-load operation (at constant system efficiency) generates 0.44 kg of CO₂ per kWh of electrical energy provided. At 1 kW system

capacity, the total specific CO₂ emissions are lower in the load-following case than in the base-load scenario because the part-load efficiency of the cell-stack is higher than at the design point. The CO₂ emissions for the load-following strategy approach a minimum because of system turndown limitations.

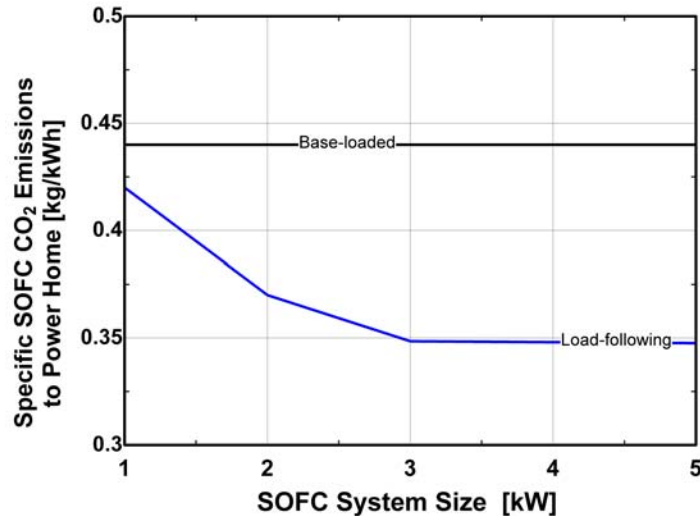
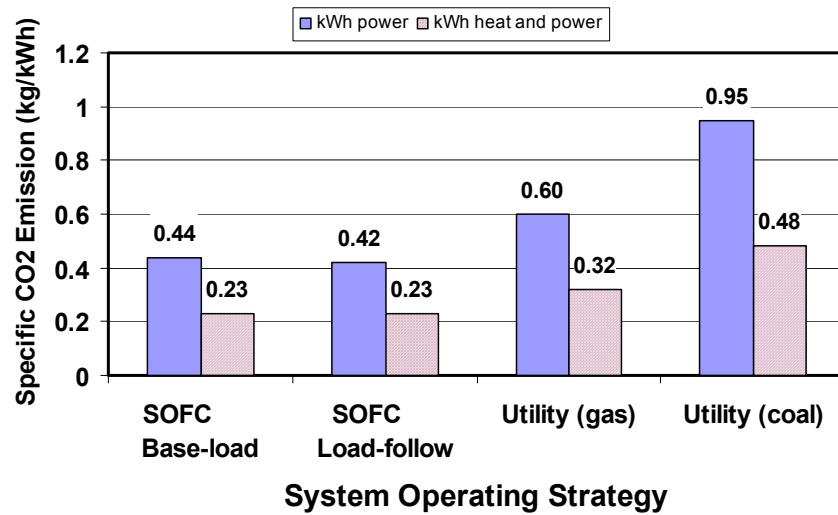


Figure 9.12 SOFC CO₂ emission performance as a function of system size

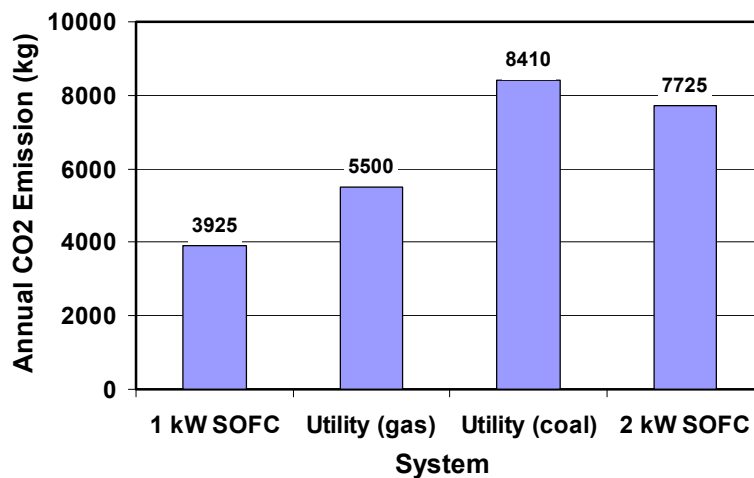
Figure 9.13(a) presents a comparison of the specific CO₂ emissions between a 1 kW SOFC system and the average (U.S.) utility when supplying electrical and thermal energy (domestic hot water, i.e., no space heat) to the residential application. The base-load SOFC system case achieves a CO₂ emission output at 0.44 kg/kWh, and the load-following case is slightly lower at 0.42 kg/kWh due to a slight efficiency advantage. Utility CO₂ emission data are based on national averages [7] and depending on fuel type (gas or coal) range between 35-115% larger than the base-loaded fuel cell system output. In a cogeneration system, the fuel utilized to provide power also supplies thermal energy to an end-user. Inclusion of the useful thermal energy supplied lowers the specific CO₂ emission by nearly 50% as Figure 9.13(a) shows.

Figure 9.13(b) presents the total annual CO₂ output of different sources to meet the domestic hot water and electric power demands of the residential application. The 1 kW SOFC CO₂ emission output is for a base-load scenario and includes approximately 85 kg CO₂ that were generated from the supplementary hot water burner in domestic hot water production. Utility

CO₂ output is shown in the figure for the case of providing energy to the residence and corresponds to about a 1 kW system. A 2 kW SOFC system could be base-load operated and produce less CO₂ emissions than a coal-fired power plant.



(a) Specific CO₂ emissions for 1 kW SOFC system on electric and cogeneration bases



(b) Comparison of total CO₂ emissions to supply residential heat and power

Figure 9.13 Specific and total CO₂ emissions as functions of operating strategy and size

9.7 Evaluation of Methods to Achieve Variable Thermal-to-electric Ratios

Chapter 8 introduced several design strategies to produce flexible thermal-to-electric ratios (TERs). The following sub-sections summarize the results presented thus far and discuss and provide additional performance information for alternative strategies.

9.7.1 *Net metering (base-load)*

Net metering has been employed for all base-load SOFC system simulations. Figure 9.9 clearly showed the economic implications of base-load operation using net metering. The relative economic merits of base-load operation are dependent on two factors: (1) the net metering program of the local utility, i.e., the price at which they will buy back excess generation, and (2) the size of the SOFC system. Based on the typical “avoided cost” buy back rate of the local utility, the fuel cell sized for the annual hourly average load is optimal and when base-load operated, registers superior economic and emission performance than load-following. It should be further noted that base-load operation is also more favorable from system control and cell-stack life viewpoints. The SOFC system has dynamic response limitations and a load-following control strategy would require additional hardware (battery), as well as increase the thermal cycling of the ceramic components thereby reducing cell life.

9.7.2 *Hot water storage tank system (cogeneration)*

The above analysis has shown that the use of cogeneration, in the form of domestic hot water with thermal storage, is more effective on both economic and emission bases than electric-only systems and is optimal when a 2-tank system arrangement is employed. Due to the large TERs necessary to provide space heat, cogeneration with or without thermal storage will not be sufficient to meet the residential space heat load without other conceptual design alternatives, such as heat pumping.

9.7.3 *“Oversizing” of BOP*

Recall from Chapter 8 (section 8.4.2) that in this strategy, the stack size is based on a high voltage/high efficiency operating condition to meet the annual hourly average electric load.

However, maximum cell power occurs at lower cell voltages/efficiencies. If the lower *unit* capital cost balance-of-plant components were sized to accommodate the larger gas flows at low voltage/high power conditions, cell-stack power could be augmented substantially depending on the original design voltage condition. Thus, hourly average electric loads could be met most of the time with high efficiency operation, but during the summer months, high power output could be achieved to serve the air-conditioning load. The disadvantages with this strategy are that higher system power turndowns are required ($\sim 8:1$) and rotating equipment (blower, compressor, and pump) will be operating at lower efficiency, off-design conditions for most of the year.

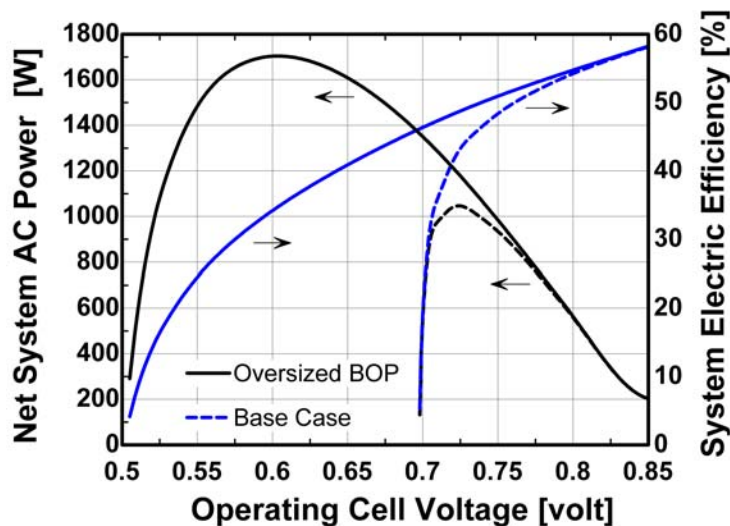


Figure 9.14 Comparison of oversized BOP and base case system performance

Figure 9.14 depicts a 1 kW system performance comparison between the base design case (high voltage cell-stack and system design, see Table 9.1) and the oversized BOP performance. Note the differences in the operating voltage and efficiency where maximum power is achieved. With the oversized BOP SOFC system design, a maximum power of 1.7 kW is achievable at an electric efficiency of 34%, whereas the base case design achieves a maximum power of 1.04 kW at 43% efficiency. However, at 1 kW power output, the oversized BOP operates at nearly 51% efficiency, a 5 point increase over the base case. The disadvantage is that the system thermal-to-electric ratio is reduced from 0.93 to 0.76.

The base design case 1 and 2 kW system unit capital costs are \$2170/kW and \$1630/kW, respectively. Thus, to provide 1.7 kW of power with a BOP sized for high voltage (low system gas flow) operation would cost nearly \$1800/kW or \$3,060. Over sizing the BOP enables nearly 0.7 kW of additional power to be produced for an incremental cost of only \$410/kW (versus \$1800/kW). A 1.7 kW system designed with an oversized BOP can achieve a total system cost of \$2,580, which translates into 16% savings and a more cost effective design approach.

Table 9.5 presents a comparison of the annual performance for “1 kW” systems with different design approaches. Base-load system power output was 1.0 kW for both cases. The SOFC system efficiency is increased at part-load, and as Table 9.5 shows, an oversized BOP design approach that capitalizes on this characteristic. The annual performance of the oversized BOP system surpasses the base case system in technical figures of merit, but is slightly inferior in terms of economic payback due to the higher overall cost. However, the economic performance of the oversized BOP system is improved when comparing the payback with the 2 kW load-following design (8.3 years vs. 6.2 yrs).

Table 9.5 Performance comparison of 2 system design approaches on annual basis

Parameter	Base case design approach		Oversized BOP approach	
	Base-load	Load-follow	Base-load	Load-follow
Electric Efficiency	44.5%	46.0%	51.2%	47.7%
Cogen. Efficiency.	84.6%	85.5%	90.3%	85.5%
Total CO ₂ emission	2554 kg	3278 kg	2248 kg	2418 kg
Payback period	5.4 yrs	6.1 yrs	6.0 yrs	6.2 yrs

9.8 Design Recommendations for Residential Cogeneration SOFC Systems

The analyses presented in this chapter have attempted to capture the salient aspects of optimal solid oxide fuel cell system design using both life cycle cost (expressed as cost of electricity)

and economic payback period minimization. The following summarizes the recommendations derived from this effort:

1) *Design SOFC systems to incorporate anode gas recycle and internal reforming.*

As Chapter 8 has shown, SOFC systems achieve improved efficiency, lower system cost, and higher thermal-to-electric ratios by the usage of anode (and cathode) gas recycle concepts. The use of internal reforming is key to thermal management of the cell-stack and helps minimize system parasitic power requirements.

2) *Select design operating point conditions based on minimum cost of electricity.*

Life cycle cost minimums exist for cell voltage and fuel utilization design parameters. The optimal design values occur at different voltage and fuel utilization values depending on whether thermal energy is recuperated or not. Cogeneration achieves lower life cycle costs than electric-only systems. Additionally, life cycle costs indicate that SOFC systems should be designed to operate at a nominal cell temperature near 800°C.

3) *Design systems for multi-family dwellings as improved economy of scale results.*

Economy of scale is realized with larger SOFC systems. Thus, the minimum COE and unit capital cost can be reduced by over 50% by manufacturing 10 kW systems versus 1 kW systems. As 10 kW systems are too large for single-family detached dwellings, larger applications should be targeted for maximum cost effectiveness and commercial market success.

4) *For single-family detached dwellings, SOFC system size should be based on the annual hourly average electric demand of the application.*

For the residential application studied herein, the annual hourly average electric load was 1.0 kW. Sizing the SOFC system at 1 kW produced the lowest payback period, the highest fuel cell electric and thermal capacity factors, and the lowest annual CO₂ emissions.

5) *Operate the system in a base-load configuration*

When sized correctly, SOFC system base-load operation offers the lowest CO₂ emissions, economic payback period, and highest fuel cell capacity factors.

6) *Cogenerate in the form of domestic hot water*

Thermal energy recuperation significantly improves the economics of SOFC systems by lowering the life cycle costs, payback period, and can protect the fuel cell system owner from natural gas price fluctuations. The value of thermal energy is estimated to range from 2.0 – 3.0 ¢/kWh.

7) *If designing for load-following, such as in a stand-alone application, the system balance-of-plant should be sized larger than suggested by the optimal (minimum COE) cell-stack design conditions.*

“Oversizing” the balance of plant equipment can increase the payback period for utility interconnected systems, but can add flexibility to operating choices. (For instance, one might consider base-loading at 1.7 kW during the months of July and August). For stand-alone applications, it is instrumental in achieving maximum cost effectiveness as the incremental unit cost for BOP equipment is significantly lower than the total SOFC system unit cost. Oversized BOP systems also achieve higher system efficiencies and lower CO₂ emissions than the high cell-stack voltage design approach.

9.10

- 9.1 T. Chen, J.D Wright, K. Krist, *Proc. Of Fifth International Symposium on Solid Oxide Fuel Cells* (SOFC-V), PV97-18, Germany (1997).
- 9.2 E. Riensche, U. Stimming, G. Unverzagt, *J. Power Sources*, **73** (2), (1998) pp. 251-256.
- 9.3 A. Khandkar, J. Hartvigsen, S. Elangovan, "A Techno-Economic Model for SOFC Power Systems," to be published in *Solid State Ionics*.
- 9.4 J. H. Hirschenhofer, D.B Stauffer, R.R. Engleman, and M.G. Klett, *Fuel Cell Handbook*, 4th Edition, U.S. Department of Energy, Office of Fossil Energy, FETC, Morgantown, WV (1998).
- 9.5 T.J. Starrs, "Summary of State Net Metering Programs," Kelso Starrs & Associates LLC, February, (2000).
- 9.6 R.B. Alderfer, M.M. Eldridge, and T.J. Starrs, "Making Connections: Case studies of interconnections and their impact on distributed power projects," NREL/SR-200-28053, National Renewable Energy Laboratory, Golden, CO, May (2000).
- 9.7 W. Barbour et al., "Carbon Dioxide Emissions from the Generation of Electric Power in the United States," The U.S. Department of Energy and Environmental Protection Agency Report, July (2000).

Chapter Ten Conclusions and Recommendations

10.1 Summary of Findings and Conclusions

Fuel cell systems are an emerging technology that offers the potential for realizing more efficient use of primary resources to deliver electricity and thermal energy in stationary end-use applications. Stationary applications can be segregated into three distinct size ranges:

- **Small** – *System Size* < 10 kW: residential, light-commercial
- **Medium** – 10 kW < *System Size* < 200 kW: medium commercial, multi-family housing
- **Large** – 200 kW < *System Size*: large commercial and industrial

The focus of this research effort has been in the small system category with end-use applications aimed at single-family detached residential dwellings. To assess the potential for fuel cell technologies to compete in the small stationary marketplace, cell-level and system-level models of solid oxide fuel cells were developed and validated. The models were exercised to evaluate strategies for optimal design and operation of fuel cell systems using a range of performance criteria as objective functions for optimization. Prior to this effort, information related to fuel cells in residential applications was scarce and inadequate for system design and for making any assessment of their effectiveness (energetic or economic) in these types of applications.

The effect of cell-stack design and operating variables on steady-state cell and system performance has been investigated. System design and operation optimization has been performed through both life cycle cost (and payback period) minimization while serving residential energy demands. *The unique contribution of this thesis is the integration and synthesis of cell- and system-level modeling with system optimal design, optimization, and annual simulation studies to provide a comprehensive assessment of high temperature fuel*

cells in residential-scale applications. The following sections summarize the findings of the aforementioned efforts.

10.1.1. Cell and system model development

Zero and one-dimensional models to characterize the performance of planar solid oxide fuel cells and the ancillary balance-of-plant equipment have been developed. Previously developed models for planar SOFCs have been investigated and found to be either inadequate or unavailable. The present SOFC model has improved upon previous modeling efforts by reducing several of the assumptions made by previous researchers (e.g., neglect of radiation heat transfer and internal reforming kinetics); thereby, increasing the accuracy of the results. Due to the emerging nature of this technology, little or no experimental data that could serve the purpose of model validation exists. As a result, the model developed herein is validated against other modeling results published in the IEA benchmark and has demonstrated effectiveness at generating its own voltage-current performance characteristic using only literature data for material geometry, properties, and reaction rate expressions and in calibrating it to SOFC developer's designs using curve-fitted temperature-dependent V-I parameters. Modeling the balance-of-plant hardware and component costing has been performed using well-established, conventional methods and capital cost information published in the open literature.

The models have been used as a tool to parametrically evaluate the impact of power control methods, cell voltage, inlet airflow and temperature, and the extent of internal reforming, on the performance of the cell and overall system. Additionally, the models have been employed to perform economic optimization studies and annual simulations of a SOFC cogeneration system in a residential application. These results are summarized in the following sections.

10.1.2. Influence of cell-stack parameters on cell and system performance

10.1.2.1 Influence of parameters on cell performance

Chapter 7 evaluated three different methods of regulating fuel cell stack power output. *Constant fuel utilization and cell (or air temperature rise) temperature control was found to*

offer the most flexibility in achieving a wide range of power output while maintaining a high electric efficiency. It was further found that intermediate to low voltage cell operation (0.5 to 0.7 V) can produce the steepest cell thermal gradients (versus 0.8 V or 0.4 V operation) because the amount of cell heat generation, relative to the air thermal capacitance in the cathode compartment, is at its highest in this operating region. Constant cell voltage and temperature control is not plausible if a modest operating range is desired and does not offer performance advantage over constant fuel utilization control. Constant reactant feed flow control could produce low cell temperatures and therefore lower cell efficiency and increased risk for carbon formation.

Constant air stoichiometric ('stoich') ratios over the load range is not possible; therefore, regulation of the cell temperature over the desired operating range must be accomplished by varying the airflow at each operating point. The fuel flowrate also must be actively controlled since any change in load will affect the fuel consumption and therefore the fuel utilization. These two factors impact system electric efficiency and operating range. As noted in Section 7.1.2, high fuel utilization is dangerous to cell integrity and life due to an increased risk for damaging the anode. The maximum safe fuel utilization is not known. The airflow should also be actively controlled to minimize parasitic power consumption while maintaining acceptably low thermal gradients (i.e., stress) in the cell.

Variation of the inlet airflow or inlet air temperature alters the operating cell temperature. Cell performance is found to be strongly correlated with cell temperature due to the temperature-dependent ionic conductivity of the solid electrolyte. Thus, variations in airflow or inlet cooling air temperature will alter the cell power output. The functional form of the variations is nonlinear due to the competing temperature-dependent effects of the reversible cell voltage and the ionic conductivity of the electrolyte (see §7.3.1 and §7.3.2). *Once again, the magnitude of the change in cell temperature due to a change in inlet airflow is directly affected by the ratio of heat generation to the thermal capacitance of the cooling stream.*

The extent of pre-reforming of methane was also investigated with the cell model. The novel finding of this analysis was that as the extent of pre-reforming increased (thereby increasing

the hydrogen content at the cell inlet), the cell efficiency decreased at the same power output due to the relative change in the heating value of the inlet fuel mixture. This trend was also found in Chapter 8. It was further noted that an increase in the extent of pre-reforming produces an increase in the internal thermal gradient of the cell, as well as an increase in the peak cell temperature.

10.1.2.2 Influence of cell parameters on system performance

Chapter 8 investigated the influence of cell design and operating parameters on system-level performance. As cell voltage is decreased a maximum power point of the cell-stack is produced. However, this maximum power can never be reached due to system parasitic power requirements. Thus a practical design cell voltage range of (0.56 – 0.8V) was judged to be appropriate. Additionally, over this voltage range, the system thermal-to-electric output can be varied by a factor of 4.

The systems-level performance viewpoint also revealed that as the extent of fuel conversion in the pre-reformer increases, the system efficiency can decrease by as much as 8.5 efficiency points due to increased parasitic power requirements. Furthermore, increases in fuel pre-reforming translate into less available thermal energy to serve process needs, such as steam generation for steam-reforming of methane. The sample system design concept presented in Chapter 8 indicated that at a fuel utilization of 85%, extent of fuel reforming conversions greater than 60% generate low boiler pinch points which result in uneconomic boiler designs.

10.1.3. *Optimal system design concepts*

Six SOFC system design concepts were evaluated for their ability to efficiently generate power and produce high thermal-to-electric ratios. A novel finding was that hydrogen-fueled SOFC systems are less efficient than all the other system concepts (despite their better V-I performance). The reason is twofold. First, hydrogen-fueled SOFC systems require higher blower parasitic power requirements. Second, the fuel energy input for hydrogen systems is some 20% larger when operating at the same current. If performance is based on comparing

fixed power output, the hydrogen SOFC system will still produce lower electric efficiencies than all the other design concepts studied *except* for the case of 100% external reforming.

Maximum efficiency and lowest cost-of-electricity system design concepts were found to be associated with those designs that included significant internal reforming (>50%) and anode and/or cathode gas recycle. The inclusion of anode gas recycling eliminated and reduced the size of ancillary system components, and increased the system thermal-to-electric ratio. It also reduced the magnitude of the cell thermal gradients due to a more uniform current density distribution across the cell. Cathode gas recycling was found to exhibit the largest reductions in the required cooling airflow; thereby, reducing the required air blower and air preheater capacities. Integration of both anode and cathode gas recycling concepts achieved the highest system electric and cogeneration efficiencies and the lowest capital cost (although changes in control and instrumentation costs from one system to the next were not evaluated). It was also observed that airflow reduction by cathode gas recycle and internal reforming must be balanced against the allowable temperature of the product gases exiting the combustor.

10.1.4. Optimal cell-stack design operating point selection

Optimal design cell voltage, fuel utilization, and temperature parameters can be selected based on minimization of the system life cycle costs. The optimal design values occur at different voltage and fuel utilization values depending on whether or not thermal energy is recuperated. Cogeneration achieves lower life cycle costs than electric-only systems. The optimal design cell parameters are independent of system rating, that is, the same optimums are found for 1-10 kW power systems.

10.1.5. Residential applications

10.1.5.1 System design recommendations

The SOFC system design recommendations are as previously summarized in Section 9.9.

10.1.5.2 Effectiveness of SOFC systems in residential applications

SOFC cogeneration systems in grid-connected single-family residential applications have the potential of offering 5-½ year paybacks in a high volume (mature cost) manufacturing market. Systems designed for internal reforming with anode gas recycle and sized for base-load operation at the annual hourly average electric load can achieve fuel cell capacity factors of 95% electric and 81% thermal, respectively. Over the course of the year, the household electric capacity factor reached 100% and the household thermal capacity factor 86% with the SOFC cogeneration system. That is, while not all the house electric peak demands were met by the fuel cell system, the net utility meter reading at year end on the home was very near 0 kWh. The total cogeneration efficiency of the system can approach 85% and the electric efficiency nearly 45%. In addition, annual CO₂ emissions to supply energy to the residence can be reduced by nearly 70% compared to coal power plants, and by over 50% compared to natural gas-fired power plants.

Installed system costs, shipping, and contingency fees have not been included in the economic analysis. The degradation of the cell performance over the course of its expected 5-year life has also not been included. The target degradation rate may make the difference in operating efficiency performance between beginning-of-life and end-of-life on the order of 3 efficiency points. When considering that SOFC stack cost estimates are also based on high volume manufacturing, a payback period of 5½ years represents an optimistic estimate. If the fuel cell stack cost is increased by three times the reference value, the payback is increased by about 40% to 7½ years.

10.2 Recommendations for Further Work

10.2.1. Modeling

A 1-dimensional, steady-state planar (rectangular) SOFC model which includes descriptions of mechanistic transport phenomena, such as conductive, convective, and radiative heat transfer, gas phase hydrodynamics in the flow channels (for pressure drop), and chemical reaction kinetics, was developed using the Engineering Equation Solver software platform.

The model partially incorporated cell polarizations associated with mass transport resistance by the usage of a temperature and current dependent V-I characteristic that allows the input of physically meaningful parameters (see Equation 4.8). However, the mass transport from bulk fluid flow in the gas channel to the electrode was not modeled in the present effort due to the continuously stirred tank reactor (CSTR) approximation. Additionally, the physical parameters that were fit for the SOFC V-I performance were based on a 5 cm x 5 cm cell, which tend to underestimate the concentration polarization loss at high currents. That is, a 10 cm x 10 cm cell will exhibit sharper voltage losses at much lower current densities than the model used in this analysis. Despite this, the present model is believed to be accurate for current densities up to 1.5 A/cm². In actuality, none of the annual simulation results presented herein exceeded current density operation of 1.3 A/cm². Nevertheless, two improvements could be made to improve the accuracy of the model (1) include a description of the actual mass transport from the bulk flow of the cell to the electrode, and (2) given sufficient experimental data on commercial size cells (i.e., ≥ 10 cm x 10 cm), refit the V-I parameters for Equation (4.8).

A third improvement to the present model would be the incorporation of radiation heat transfer in the boundary conditions. SOFC cell-stacks are housed in an enclosure that is at a cooler temperature than the stack. The incorporation of heat transfer at the cell ends would affect the cell temperature distribution and airflow required. In addition, the present model employs 2-D radiation configuration (view) factors for the cross-channel radiation. As the number of computational nodes increases, the appropriateness of the 2-D enclosure approximation is reduced.

Heat loss from the cell-stack to the surroundings can be significant from small, high temperature devices whose geometry demonstrates high volume-to-surface area ratios. Heat loss mechanisms were not accounted for in the present study. A study of cell-stack insulation and the associated heat loss to the surroundings would also improve the model.

Further improvements in model accuracy could be made by an increase in the number of spatial dimensions (2- or 3-D) used in the model. These improvements are generally for stack

design considerations and may not improve the model accuracy significantly, but given the increasing speed of personal computers, such enhancement might eventually be economical and would be beneficial to an improved understanding of stack thermal management issues, as well as dynamic response. The appropriate level of model advancement to pursue ultimately depends on the purpose of the model.

Future application studies could be improved if the cell performance degradation was also included. Present information on cell degradation rates is limited. Tubular SOFCs are eventually expected to exceed 5-year lifetimes, but planar SOFCs have not yet achieved the same level of performance.

Study of the dynamic response of the cell was an initial goal of the research effort. Preliminary results from 1- and 2-dimensional thermal models without electrochemistry (not presented herein), however, indicated that the thermal response could be on the order of 8-20 minutes even in hot standby mode. With the aim of studying utility interconnect applications, as well as, presenting limiting case results, dynamic simulation became an extraneous objective. SOFCs have been discussed for applications (e.g., stand-alone, remote, and automotive and truck auxiliary power) in which load-following operation may be necessary. In these types of applications, a thorough study of the cell-stack, fuel processing, and overall system dynamic behavior is warranted. Knowledge and elucidation of the dynamic behavior of individual SOFC stacks and the overall system would be particularly useful for design of controls. Finally, experimental validation of the cell model developed herein would advance the model accuracy.

10.2.2. System control

Fuel cell operating control is an area for further study. Control studies to evaluate methods of achieving faster thermal response of the cell-stack, as well as investigation of feed-forward and/or feed back strategies are needed and would make a valuable contribution to fuel cell technology development.

10.2.3. *Design*

The design and operation studies presented in this work have used primarily conventional parametric techniques based on life cycle cost minimization to optimize the SOFC system design. Other methods, such as the use of Pinch Technology [1, 2] and Exergy Analysis [3, 4, 5] could also be employed to offer additional perspectives on optimal system configurations. Exergy analysis could be particularly useful for cogeneration system design and optimization when used in conjunction with the growing field of thermoeconomics [5, 6, 7, 8].

Chapter 3 identified numerous considerations for SOFC system design. The need for proper attention to the electrical side of the plant in system design became obvious in preliminary analyses of battery-included fuel cell systems. The power conditioning topology for inversion of DC power to AC power can have a significant impact on overall system efficiency. Fuel cells are characterized as low voltage, high current power sources. The transformation of low voltage DC output to high voltage DC can be inefficient and costly. Thus, additional research could be expended at developing inverter technology specifically for fuel cells, as well as, optimizing the number of cells in the stack (or stack voltage) that will minimize inverter cost and maximize power conditioning efficiency.

10.2.4. *Other application studies*

Fuel cells are anticipated for many applications and therefore, numerous additional studies could be made. The following additional studies are recommended for small-scale stationary applications, some of which have been previously mentioned in Chapter 8:

- **Investigation of methods to serve the residential space heating energy demand.**
 - **Integration with heat pumps.** Can heat pumping improve the thermal-to-electric ratios for residences? To what extent does heat pumping make sense?
 - **Low fuel utilization operation** and “over-fire” of the catalytic combustor (see Chapter 8).

- **Effectiveness of SOFCs in multiple family dwellings.** How much more attractive is this option than serving single-family dwellings?
- **Electric water heating.** Does the use of excess SOFC electrical energy for resistive heating of domestic hot water make the technology more attractive for residential applications?
- **What are cost-effective and technically-attractive energy storage technologies for fuel cell technologies?**
- **Design and optimization of stand-alone fuel cell power systems.** The investigation of this topic is also appropriate for remote power applications and would involve investigation of battery technologies, system dynamic response, and optimal fuel cell/battery sizing. Preliminary investigation reveals that weekly simulation of battery state-of-charge is necessary to accurately size the component.
- **Comparison of SOFC and PEMFC technology for small-scale stationary applications.** These two types of fuel cells are considered to be the most attractive and viable options for many applications. What are the relative advantages of one over the other?

10.3 Final Remarks

This research effort has proceeded at many levels, cell-level, stack-level, and system-level modeling, design, and optimization, as well as application-level simulation. It has attempted to gain insight into the fundamental issues of fuel cell system design and development and offer possible design and operation strategies to accelerate the application of the technology. In doing so, it has managed to touch several broader development and application issues that are beyond the scope of the present work, but which the author would like to make some comment on nevertheless.

First, it is important to note that while every attempt has been made to incorporate experimental data from real fuel cell tests, the results formed from this thesis work have been

generated using mathematical models. In real life operating circumstances, important factors may arise that alter the conclusions summarized herein. In particular, cell degradation has not been accounted for and can compromise the life and economics of the fuel cell system. Additionally, other fuel processing routes may prove more economical than the catalytic steam reforming method employed in this work. One reason for this might be the added system complication and cost for proper water treatment (in systems without AGR). Whatever the case, it is recognized that modeling and simulation can optimize a system only so far. In truth, only laboratory experimentation, real field testing, (aimed at identifying the needs of the application), development of the necessary ancillary system components, verification of system operation, control, and performance, and field test experience can fully optimize a product.

The high level of optimism surrounding the “imminent” entry of fuel cell technology into many energy-use sectors is slowly being tempered by recognition of significant commercialization hurdles. The primary hurdle is system cost. In the transportation sector, fuel cell technology is competing against the internal combustion engine, a technology that already has 100 years of development history and is still gradually improving in efficiency performance and emission reduction. In stationary applications, combined cycle power plants offer 60% efficiency and small microturbines, while not efficient, are expected to be cheap (<\$500/kW).

Much research and development is underway towards cost reduction of fuel cells. It has been noted that

“cost reduction in general can be accomplished by: (1) increasing power density (enhancing the performance characteristics of fuel cell electrolyte and electrode materials), (2) lowering operating temperature (reducing the cost of materials of construction and BOP), and (3) enhancing manufacturability (eliminating or reducing the cost of manufacturing steps)”....J. Brouwer, Fuel Cell Catalyst (2002).

In addition to cost, fuel cell commercialization has been significantly impeded by fuel processing demands. The numerous steps involved to produce hydrogen add complexity and inefficiency to the system. Hydrogen has been considered by many to be the fuel of the

future. However, substantial issues in the production, storage, and distribution of hydrogen exist as barriers to achieving a hydrogen economy*. Fortunately the future of all fuel cell technologies and hydrogen are not necessarily intertwined. As previously noted, solid oxide fuel cells can theoretically operate off of methane directly (and research is underway to make this viable), are more efficient when operating off of hydrocarbons, and are more tolerant to fuel impurities than other fuel cell types.

The ultimate measure of success will be whether fuel cell technology can compete with other power generation technologies in terms of cost, total life performance, and reliability. In many instances the perceived “value” of the system is not only related to first cost, but to avoided cost, for example, where expansion of T&D infrastructure can make the alternative technology more attractive (see Chapter 1). The “value” of fuel cell technology may also be enhanced when compared to conventional generating technology in combined heat and power applications (CHP). It has been noted that widespread application of CHP systems in buildings has been limited because conventional technology tends to (1) be most efficient in large sizes and when operating near full-load, (2) to require a larger more skilled maintenance staff, and (3) be limited in new plant siting due to environmental restrictions on noise and emissions [9]. In contrast, the advanced tubular SOFC technology, developed by Siemens-Westinghouse, has demonstrated system efficiencies in excess of 58% when integrated with gas turbines. This is an impressive feat in that it is an unoptimized, first generation design at the 300 kW scale. Despite current costs, fuel cell technology is likely to find many niche markets. However, its widespread use will depend on many factors, including the regulation of greenhouse gas (e.g., CO₂) emissions. If conditions for mass commercialization of fuel cell technology are realized, the prediction of Wilhelm Ostwald may eventually come to pass,

“No smoke, no soot, no steam boiler, no steam engine, even no fire any more, because fire will only be needed for those processes which can not be accomplished in an electric manner, and their number will decrease day by day.” (Wilhelm Ostwald, 1894)[†]

* A recent paper by B. Eliason and U. Bossel discuss the issues facing development of a hydrogen economy. B. Eliasson, U. Bossel, “The Future of the Hydrogen Economy: Bright or Bleak?”, to be published in 2002.

[†] W. Ostwald: Die Wissenschaftliche Elektrochemie der Gegenwart und die Technische der Zukunft (Schluss), Z. für Elektrotechnik und Elektrochemie, 1 122-125, (1894).

10.5

-
- 10.1 B. Linnhoff and J.R. Flower, "Synthesis of Heat Exchanger Networks," *AIChE Journal*, Vol. 24, No. 4, American Institute of Chemical Engineers, New York, (1978).
 - 10.2 B. Linnhoff, *User Guide on Process Integration for the Efficient Use of Energy*, Pergamon Press, New York (1982).
 - 10.3 R. A. Gaggioli (editor), *Thermodynamics: Second Law Analysis*, ACS Symposium Series, Vol. 122, Washington D.C. (1980).
 - 10.4 M. J. Moran, *Availability Analysis: A Guide to Efficient Energy Use*, Prentice Hall, Englewood Cliffs, NJ (1982).
 - 10.5 A. Bejan, G. Tsatsaronis, M. Moran, *Thermal design and optimization*, John Wiley & Sons, Inc., New York (1996).
 - 10.6 R. A. Gaggioli (editor), *Efficiency and Costing: Second Law Analysis of Processes*, ACS Symposium Series, Vol. 235, Washington D.C. (1983).
 - 10.7 A. Valero, M. Lozano, C. Torres, "Application of the Exergetic Cost Theory to the CGAM Problem," *Energy –The International Journal*, Vol. 19, No. 3, (1994).
 - 10.8 G. Tsatsaronis and J. Pisa, "Exergoeconomic Evaluation and Optimization of Energy Systems –Application to the CGAM Problem," *Energy –The International Journal*, Vol. 19, No. 3, (1994).
 - 10.9 M.W. Ellis and M.B. Gunes, "Status of fuel cell systems for combined heat and power applications in buildings," AC-02-18-2 (RP-1058), preprint article for *ASHRAE Transactions*, vol. 108, Part 1, (2002).

Appendix I

- A1.1 Evaluation of Streamwise Radiation Heat Transfer
- A1.2 Temperature Dependence of the Ionic Resistance of Yttria-stabilized Zirconia (YSZ) Electrolyte
- A1.3 Evaluation of Fuel Channel Concentration Gradient on Reforming Reaction Rate
- A1.4 Determination of Shape Factor for Gas-to-Gas Heat Transfer Across Interconnect
- A1.5 EES Code for the effect of concentration gradients on reforming reaction rate

A1.1 Evaluation of Streamwise Radiation Heat Transfer

A1.1.1 Evaluation via configuration factors for opposing walls

This sub-section serves to justify the omission of cross-channel radiation heat transfer between channel walls and the cell tri-layer (anode-electrolyte-cathode) in the SOFC finite difference model developed in the present investigation. The neglect of cross-channel radiation heat transfer between walls at different axial positions (i.e., “streamwise” radiation heat transfer) is based upon the small view factors that result in the narrow channel space. An example of the determination of the view factors between opposing wall elements follows.

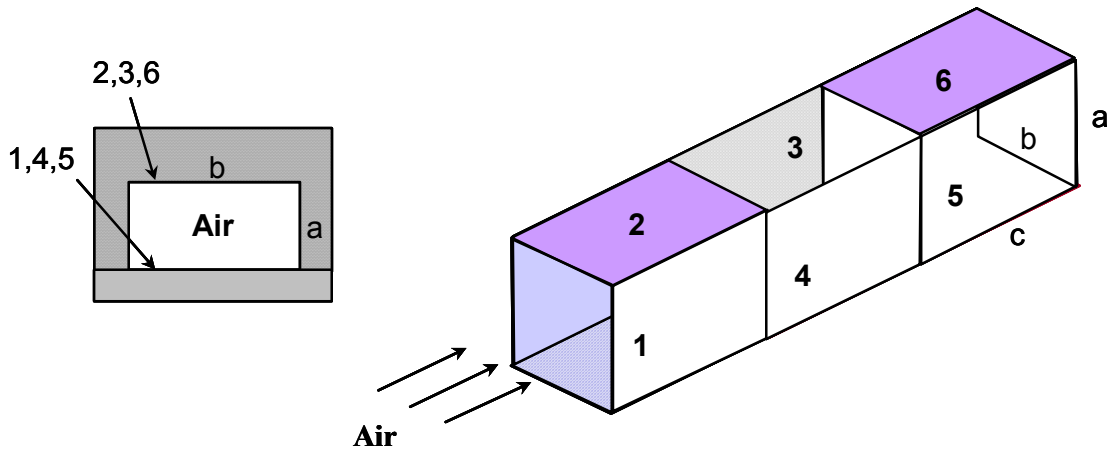


Figure A1.1 Channel geometry for view factor determination

Figure A1.1 depicts the geometry for a single air (cathode) channel in which the channel has been discretized into 3 elements along the streamwise direction. Configuration factors (or view factors) between cross-channel surfaces downstream from one another can be determined using configuration factor algebra. To determine the view factor between the bottom inlet surface (1) and the top outlet surface (6), we begin with,

$$F_{(1+4+5)-(2+3+6)} = F_{(1+4+5)-2} + F_{(1+4+5)-3} + F_{(1+4+5)-6} \quad (\text{A1.1})$$

$$(A_1 + A_4 + A_5) \cdot F_{(1+4+5)-(2+3+6)} = A_2 \cdot F_{2-(1+4+5)} + A_3 \cdot F_{3-(1+4+5)} + A_6 \cdot F_{6-(1+4+5)} \quad (\text{A1.2})$$

It is also known that $F_{x-(1+4+5)} = F_{x-1} + F_{x-4} + F_{x-5}$, where x is any of the top surfaces in Figure A1.1. Inserting this relation into Equation (A1.2) yields,

$$\begin{aligned} (A_1 + A_4 + A_5) \cdot F_{(1+4+5)-(2+3+6)} &= A_2 \cdot (F_{2-1} + F_{2-4} + F_{2-5}) + A_3 \cdot (F_{3-1} + F_{3-4} + F_{3-5}) \\ &+ A_6 \cdot (F_{6-1} + F_{6-4} + F_{6-5}) \end{aligned} \quad (\text{A1.3})$$

Using reciprocity relations from the symmetry of the geometry, as shown by Siegel and Howell [1], we have,

$$\begin{aligned} A_2 \cdot F_{2-4} &= A_3 \cdot F_{3-1} \\ A_3 \cdot F_{3-5} &= A_6 \cdot F_{6-4} \\ A_2 \cdot F_{2-5} &= A_6 \cdot F_{6-1} \end{aligned} \quad (\text{A1.4})$$

Since the areas of the top and bottom surfaces in Figure A1.1 are equal (i.e., $A_1=A_2=A_3=A_4=A_5=A_6$), Equation (A1.4) simplifies to $F_{2-4} = F_{3-1} = F_{3-5} = F_{6-4}$ and $F_{2-5} = F_{6-1}$. Also, it is clear that $F_{2-1} = F_{3-4} = F_{6-5}$. Inserting these simplifications into Equation (A1.3) and solving for F_{2-5} we have,

$$F_{2-5} = \frac{3}{2} F_{(1+4+5)-(2+3+6)} - \frac{3}{2} F_{2-1} - 2F_{2-4} \quad (\text{A1.5})$$

Configuration factors $F_{(1+4+5)-(2+3+6)}$ and F_{2-1} are obtained from Siegel and Howell [1] for identical, parallel, directly opposed rectangles. To obtain F_{2-4} in Equation (A1.5), we begin again as in Equation (A1.1), however we use only top surfaces 2 and 3, and bottom surfaces 1 and 4,

$$F_{(1+4)-(2+3)} = F_{(1+4)-2} + F_{(1+4)-3} \quad (\text{A1.6})$$

$$\begin{aligned} (A_1 + A_4) \cdot F_{(1+4)-(2+3)} &= A_2 \cdot F_{2-(1+4)} + A_3 \cdot F_{3-(1+4)} \\ (A_1 + A_4) \cdot F_{(1+4)-(2+3)} &= A_2 \cdot (F_{2-1} + F_{2-4}) + A_3 \cdot (F_{3-1} + F_{3-4}) \end{aligned} \quad (\text{A1.7})$$

Using the same simplifications as stated above and solving for F_{2-4} we obtain,

$$F_{2-4} = F_{(1+4)-(2+3)} - F_{2-1} \quad (\text{A1.8})$$

where $F_{(1+4)-(2+3)}$ is obtained again from Siegel and Howell [1] for identical, parallel, directly opposed rectangles. The finite-difference model developed in Chapter 4 employed a 20 node grid which results in wall elements that are 5 mm in length. The channel cross-section is 1 mm high by 3 mm wide. Thus, $a = 1$, $b = 3$, and $c = 5$ in Figure A1.1. Using these values the following view factor values were determined from the Siegel and Howell relation,

$$F_{(1+4+5)-(2+3+6)} = 0.6841 \quad F_{(1+4)-(2+3)} = 0.666 \quad F_{2-1} = 0.613$$

Inserting these values into Equations (A1.8) and (A1.5) we obtain respectively,

$$F_{2-4} = 0.053 \quad F_{2-5} = 0.00065$$

Thus, opposing wall elements 0.5 cm downstream from one another (i.e., walls 2 and 4, 1 and 3, and so on) only ‘see’ about 5% of each other. Opposing wall elements 1 cm away from one other ‘see’ less than 1% of each other’s area. These low view factors justify the assumption of negligible radiation heat transfer between opposing (cross-channel) wall elements at different axial positions.

A1.2 Temperature Dependence of the Ionic Conductivity of Yttria-stabilized Zirconia Electrolytes

The most common electrolyte material for the solid oxide fuel cell is yttria-stabilized zirconia (YSZ). Other electrolyte materials, such as ceria oxide, are also promising candidates. At elevated temperatures, pure zirconia is a good conductor of oxygen anions, but at high temperature ($\sim 1000^\circ\text{C}$) it also experiences phase transformation to a denser tetragonal crystalline structure which produces a catastrophic volume change and cracking [2]. The cubic crystalline structure can be maintained with high fracture toughness at elevated temperatures and during heating and cooling by doping zirconia with other materials, such as calcium oxide or yttrium oxide. Zirconia becomes fully stabilized up to 2500°C by doping it

with 8 mol% of yttria (Y_2O_3)* [3]. The ionic conductivity of 8YSZ is temperature sensitive and Bossel [4] has fitted its temperature dependence with an equation of the form,

$$\sigma_{\text{YSZ}} = A \exp\left(\frac{B}{T}\right) \quad (\text{A1.9})$$

where for 8YSZ, $A = 85000$ (S/m) and $B = 11000$ (1/K). The ionic conductivity is plotted in Figure A1.2. A planar SOFC is likely to see operating cell temperatures ranging from 1050-1150 K. Over this range, Figure A1.2 shows that the ionic conductivity nearly triples in value. This effect provides insight into one of the factors that affects the cell current density distribution.

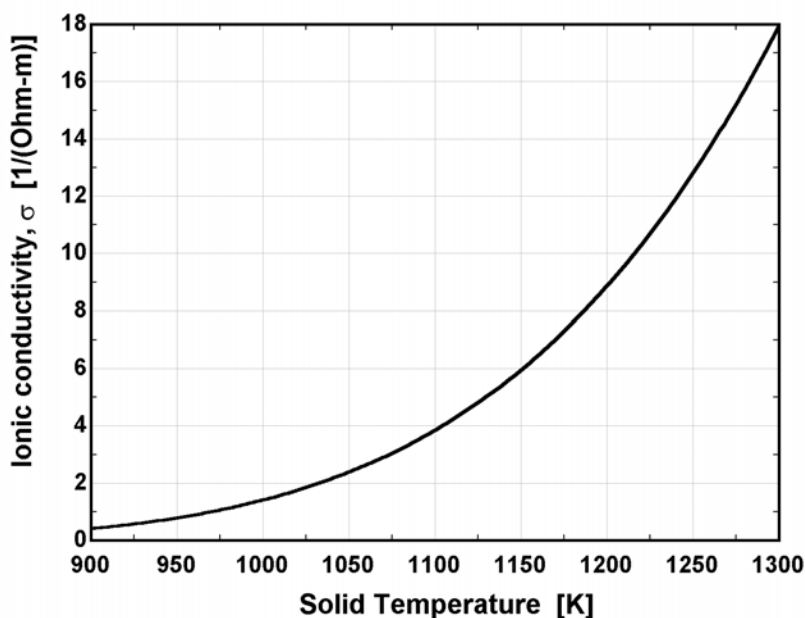


Figure A1.2 Ionic conductivity of 8 mol% YSZ as a function of temperature

A1.3 Evaluation of Fuel Channel Concentration Gradient on Reforming Reaction Rate

In real cell reactant gas flow channels, gradients in gas composition exist between the bulk and the electrode-gas interface. For the electrochemical reactions, the wall partial pressure of

* The compound is abbreviated as 8YSZ.

hydrogen must be lower than the bulk value to allow for a mass flux towards the electrode. The decrease in hydrogen concentration between bulk flow and electrode surface locations is not considered to be large (~2%) at typical cell operating conditions making the plug flow assumption in Chapter Four reasonable. While this simplification appears reasonable for the electrochemical reaction, the reforming reaction rate mechanism given by Achenbach and Riensche [5] is governed by the wall CH₄ partial pressure and its sensitivity is not known. To ensure that usage of the bulk value was legitimate, an investigation of the sensitivity of the reaction rate to Reynold's number and temperature was performed.

Recall from Chapter Four that the first order reforming reaction rate employed in the model was given by,

$$\dot{r}_R = k_0 p_{CH_4} f_e \exp\left(\frac{-E_A}{R_u T_s(x)}\right) \cdot A_{rx} \quad (A1.10)$$

where p_{CH_4} is to be taken at the wall. For a rough estimate of the convective mass flux from the bulk gas in the flow channel to the anode surface, Newton's law is assumed to be applicable and is expressed as [5],

$$\dot{n}_{CH_4}'' = \beta_{conv} \frac{(p_{CH_4}|_{bulk} - p_{CH_4}|_{wall})}{R_u T_{gas}} \quad (A1.11)$$

where \dot{n}_{CH_4}'' is the molar flux of methane (mol/m²-s) and is equal to \dot{r}_R in Equation (A1.10), β_{conv} is the convective mass transfer coefficient (m/s), p_{CH_4} is the partial pressure of methane (bar), R_u is the universal gas constant, and T_{gas} is the temperature of the gas (K). The relation for the convective mass transfer coefficient was experimentally determined by Achenbach and Riensche [5] and is given as,

$$\beta_{conv} = \frac{D_{CH_4,m}}{L_c} \cdot \frac{p_{tot}}{p_{tot} - p_{CH_4}|_{bulk}} \cdot 1.02 \sqrt{Re} \sqrt[3]{Sc} \quad (A1.12)$$

where $D_{CH_4,m}$ is the diffusion coefficient of methane in the gas mixture, L_c is the characteristic length, Re is the Reynolds number, and Sc is the Schmidt number ($=\mu/\rho D_{CH_4,m}$). As a first approximation, the diffusion coefficient of methane in the fuel gas mixture was estimated using the diffusion relation for dilute solutions [6],

$$D_{CH_4,m} = \frac{1-x_{CH_4}}{\sum_j \frac{x_j}{D_{CH_4,j}}} \quad \text{for } j \neq CH_4 \quad (\text{A1.13})$$

$D_{CH_4,j}$ is found using the Chapman-Enskog relation for binary diffusion of ideal gases [7],

$$D_{AB} = 0.0018583 \cdot \frac{\sqrt{T_g^3 \left(\frac{1}{M_A} + \frac{1}{M_B} \right)}}{p_{tot} \sigma_{AB}^2 \Omega_{AB}} \quad (\text{A1.14})$$

where σ_{AB} is the collision diameter, Ω_{AB} is the collision integral, M_A is the molecular weight of component A, and M_B is the molecular weight of component B. Values for the collision diameter and collision integral were found in Mills [8]. Given the inlet fuel gas composition of Table 5.2, the set of equations (A1.10-14) was solved in EES for varying gas temperature and Reynolds number. Figure A1.3 shows the effect of varying Reynolds number in the anode fuel gas compartment on the reforming reaction rate and the wall partial pressure at the inlet of the cell. At the inlet of the fuel cell anode, the bulk methane partial pressure is 0.171 bars. In the anode compartment, the fuel gas Reynolds number is about 3. As Figure A1.3 shows, the wall partial pressure at the cell inlet is about 0.15 bar (a Δp_{CH_4} of about 0.02 bar). As the Reynolds number is increased, the wall partial pressure increases rapidly and nonlinearly until $Re \approx 40$. Above this number, the wall methane partial pressure approaches the bulk value in an exponential fashion, reaching bulk value around $Re \approx 2000$. The reforming reaction rate follows the same trend as the methane partial pressure at the wall, decreasing by only 13% at low Reynolds numbers. That is, the reforming reaction rate is actually 13% slower than the rate given by employing a bulk value for methane concentration in Equation (A1.11). More importantly, inserting the value of the reduced reforming reaction

rate given by Figure A1.3 into the SOFC finite difference model, indicates that the predicted cell performance values are nearly unchanged. This is not a surprising result considering that at 900°C the predicted reforming reaction rate for a methane partial pressure of 0.171 bar and a cell current density of 3000 A/m² is some 42 times faster than the electrochemical reaction rate [5]. Thus, concentration gradients much larger than those calculated in Figure A1.3 would have to exist to significantly affect the predicted cell performance and resulting solid and gas temperatures.

Figure A1.4 depicts the effect of cell temperature on the methane partial pressure at the wall. For the temperature range shown in the figure, the methane concentration at the wall changes even less than it does with changes in Reynold's number. Based on the results shown in Figure A1.3 and Figure A1.4, the use of a bulk methane concentration is, therefore, considered appropriate. The full set of equations solved in EES can be found in §A1.5.

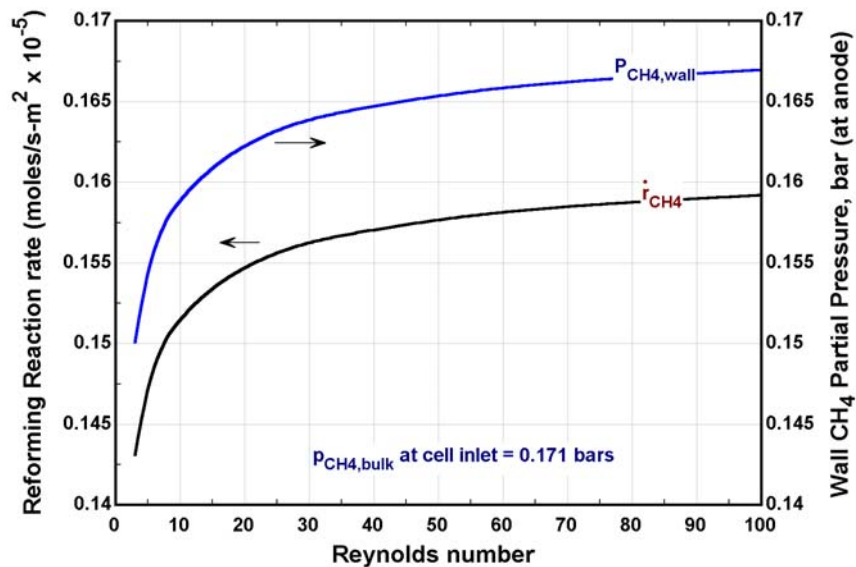


Figure A1.3 Effect of reaction rate and wall partial pressure with Reynolds number

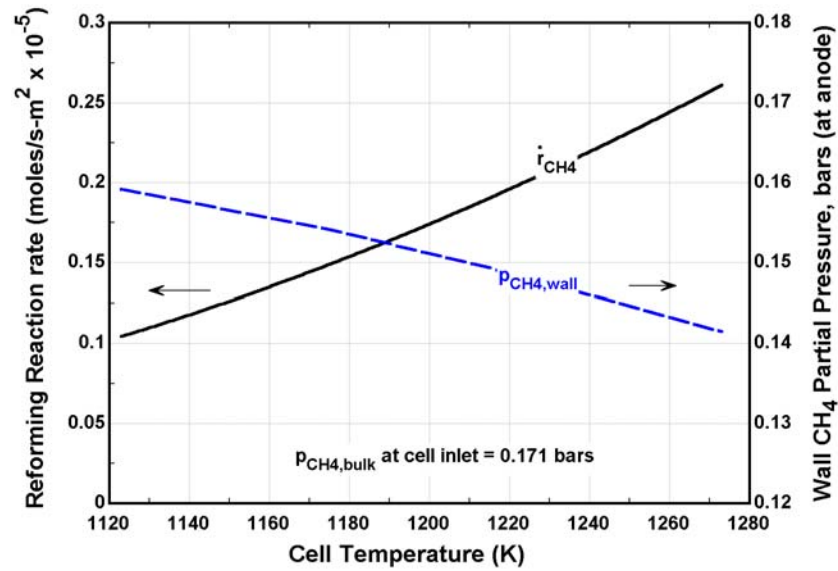


Figure A1.4 Effect of reaction rate and wall partial pressure with temperature

A1.4 Determination of Shape Factor for Gas-to-Gas Heat Transfer Across Interconnect

The determination of the amount of heat transfer between fuel and air streams across the interconnect (i.e., between adjacent cells) requires an estimate of the shape factor for the 2-D geometry. The rate of heat transfer between the two reactant streams is calculated through the expression,

$$\dot{Q}_{HX} = U_{tot} \cdot (T_f - T_a) \quad (\text{A1.15})$$

where U_{tot} is the overall heat transfer coefficient and is determined from,

$$U_{tot} = \frac{1}{1/h_f A_{s-f} + 1/k_s S_F + 1/h_a A_{s-f}} \quad (\text{A1.16})$$

The shape factor, S_F , in Equation (A1.16) is an unknown and was estimated numerically by solving the following equation,

$$\dot{Q}' = k_s S_F \frac{(T_{w,fuel} - T_{w,air})}{\Delta x} \quad (A1.17)$$

where \dot{Q}' is the heat transfer per meter of channel length, k_s is the solid thermal conductivity, Δx is the axial spacing of the finite-difference grid in the SOFC model, and $T_{w,fuel}$ and $T_{w,air}$ are the fuel and air channel wall temperatures, respectively. The shape factor has units of (m) and for the interconnect geometry of a 10 cm wide by 10 cm long SOFC with 18 fuel and air channels of equal cross-section, was calculated using Finite Element Heat Transfer (FEHT) software from F-Chart, Inc. [9]. The geometry and the finite element mesh of a single channel in the interconnect is depicted in Figure A1.5. The gas channel walls are considered to be isothermal and all other boundaries (left, right, and a portion of the top and bottom) of the computational domain are adiabatic. For the given inputs, FEHT returns \dot{Q}' and the shape factor can then be determined from Equation (A1.17). The value of the shape factor was found to be 0.019 m for the geometry shown and was checked to make sure it was constant with varying material k_s , and wall temperatures. The resulting temperature gradient vectors are also depicted in Figure A1.6.

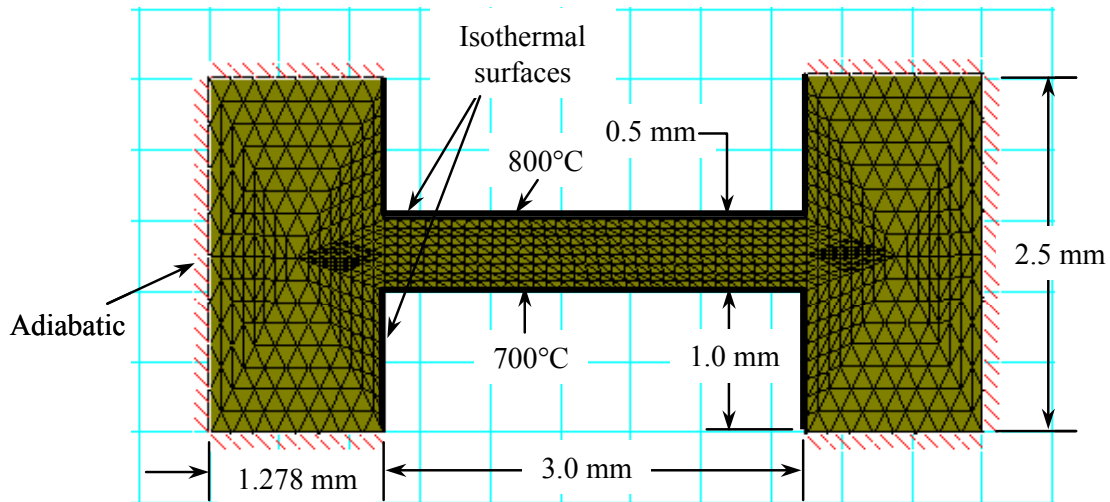


Figure A1.5 Interconnect geometry and boundary conditions for a single gas channel

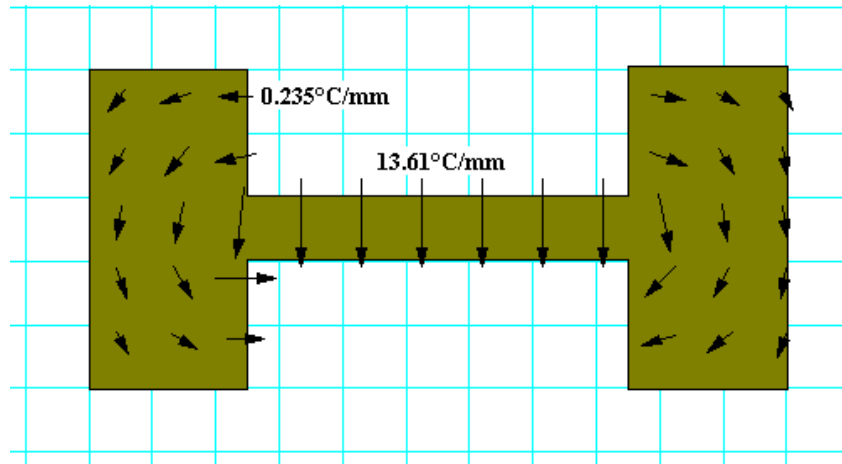


Figure A1.6 Temperature gradient vectors for heat conduction across a single gas channel

A1.5 EES Code for the effect of concentration gradients on reforming reaction rate

=====
*Examination of the effect of concentration gradients
 in the anode chamber on reforming reaction rate.*
 =====

*Mass transfer coefficients and relations taken from:
 E. Achenbach and E. Riensche, J. Power Sources, 52, (1994) 2*

Mass Transfer Relations

rate of mass transfer of CH₄

$$\dot{r} = \beta_{\text{tot}} \cdot \frac{p_{\text{CH}_4, \text{b}}}{R_u \cdot T} \cdot 100000$$

overall mass transfer coefficient

$$\beta_{\text{tot}} = \left[\frac{1}{\beta_c} + \frac{1}{\beta_{\text{ref}}} \right]^{-1}$$

reforming mass transfer coefficient

$$\beta_{\text{ref}} = 0.04274 \cdot R_u \cdot T \cdot f_e \cdot \exp \left[\frac{-E_A}{R_u \cdot T} \right]$$

convective mass transfer coefficient

$$\beta_c = \frac{D_{1,m}}{L} \cdot \left[\frac{P_{\text{tot}}}{P_{\text{tot}} - p_{\text{CH}_4, \text{b}}} \right] \cdot 1.02 \cdot \sqrt{\text{Re}} \cdot \text{Sc}^{(1/3)}$$

reforming mass transfer coefficient

$$p_{\text{CH}_4, \text{wall}} = p_{\text{CH}_4, \text{b}} - \frac{\dot{r}}{100000} \cdot \frac{R_u \cdot T}{\beta_c}$$

Schmidt number

$$Sc = \frac{\mu}{\rho \cdot D_{1,m}}$$

Inputs*Gas species designation*

[1] = CH₄, [2] = H₂, [3] = H₂O, [4] = CO, [5] = CO₂

$$x_2 = 0.2626$$

$$x_3 = 0.4934$$

$$x_4 = 0.0294$$

$$x_5 = 0.0436$$

$$\mu = 0.00004759 \quad \text{fuel viscosity}$$

$$\rho = 0.1548 \quad \text{fuel density}$$

$$f_e = 1 \quad \text{Equilibrium factor}$$

$$E_A = 82000 \quad \text{Activation energy}$$

$$P_{\text{tot}} = 101.325 \cdot \left[0.01 \cdot \frac{\text{bar}}{\text{kPa}} \right]$$

$$R_u = (8.31434 \text{ kJ/kmole-K}) \quad \text{Universal gas constant}$$

$$P_{\text{CH}_4,b} = x_1 \quad \text{partial pressure of methane in the bulk}$$

$$p = P_{\text{tot}} \cdot \left[0.986923 \cdot \frac{\text{atm}}{\text{bar}} \right]$$

Property Calculations

$$ns = 5 \quad \text{number of species}$$

$$D_{1,m} = \frac{1 - x_1}{ns \sum_{i=2} (x_i / D_{1,i})}$$

Note that Diffusion coefficients are for dilute solutions

$$D_{1,2} = 1.8583 \times 10^{-7} \cdot T^{(3/2)} \cdot \left[\frac{\sqrt{\frac{1}{M_1} + \frac{1}{M_2}}}{p \cdot \sigma_{1,2}^2 \cdot \Omega_{1,2}} \right]$$

$$D_{1,3} = 1.8583 \times 10^{-7} \cdot T^{(3/2)} \cdot \left[\frac{\sqrt{\frac{1}{M_1} + \frac{1}{M_3}}}{p \cdot \sigma_{1,3}^2 \cdot \Omega_{1,3}} \right]$$

$$D_{1,4} = 1.8583 \times 10^{-7} \cdot T^{(3/2)} \cdot \left[\frac{\sqrt{\frac{1}{M_1} + \frac{1}{M_4}}}{p \cdot \sigma_{1,4}^2 \cdot \Omega_{1,4}} \right]$$

$$D_{1,5} = 1.8583 \times 10^{-7} \cdot T^{(3/2)} \cdot \left[\frac{\sqrt{\frac{1}{M_1} + \frac{1}{M_5}}}{p \cdot \sigma_{1,5}^2 \cdot \Omega_{1,5}} \right]$$

$$M_1 = \text{MolarMass}('CH_4')$$

$$M_2 = \text{MolarMass}('H_2')$$

$$M_3 = \text{MolarMass}('H_2O')$$

$$M_4 = \text{MolarMass}('CO')$$

$$M_5 = \text{MolarMass}('CO_2')$$

$$\Omega_{1,2} = 0.7277 \quad \sigma_{1,2} = 1 / 2 \cdot (\sigma_1 + \sigma_2)$$

$$\Omega_{1,3} = 0.6933 \quad \sigma_{1,3} = 1 / 2 \cdot (\sigma_1 + \sigma_3)$$

$$\Omega_{1,4} = 0.7478 \quad \sigma_{1,4} = 1 / 2 \cdot (\sigma_1 + \sigma_4)$$

$$\Omega_{1,5} = 0.799 \quad \sigma_{1,5} = 1 / 2 \cdot (\sigma_1 + \sigma_5)$$

$$\sigma_1 = 3.758 \quad \sigma_4 = 3.69$$

$$\sigma_2 = 2.827 \quad \sigma_5 = 3.941$$

$$\sigma_3 = 3.737$$

A1.7

-
- A1. R. Siegel and J. Howell, *Thermal Radiation Heat Transfer*, 3rd Edition, Hemisphere Publishing Corporation, Washington, D.C., (1992), Appendix C, configuration factor 12, p. 1030.
- A2. J. F. Shackelford, "Ceramics, Material Properties of," in *Encyclopedia of Applied Physics*, Vol. 3, G.L. Trigg, Editor, VCH Publishers, Inc., (1992) pp. 169-187.
- A3. "Applications and Preparations of Zirconia and Stabilized Zirconia Powders," www.stanfordmaterials.com/zro2.html, Stanford Materials Company webpage, San Mateo, CA, accessed November 7, (2001).
- A4. U.G. Bossel, *Facts and Figures*, Final report on SOFC data, IEA Programme on Advanced Fuel Cells, Annex II, Swiss Federal Energy Office of Energy, Berne, (1992).
- A5. E. Achenbach and E. Riensche, "Methane-steam reforming kinetics for solid oxide fuel cells," *J. Power Sources*, **52** (1994), pp. 283-288.
- A6. R.C. Reid, J.M.Prausnitz, and B.E. Poling, *The Properties of Gases and Liquids*, 4th Ed., McGraw-Hill, New York (1987).
- A7. R.B. Bird, W.E. Stewart, and E.N. Lightfoot, *Transport Phenomena*, John Wiley, New York (1960).
- A8. A.F. Mills, *Mass Transfer*, Prentice-Hall, Inc., Upper Saddle River, New Jersey (2001).
- A9. Finite Element Heat Transfer (FEHT) by F-Chart Software, Middleton, WI.

Appendix II

Sample Counter-flow Finite-difference EES Code for Hydrogen-fueled SOFC Model*

* Only a portion of the entire code is presented here, see attached CD-ROM or contact the S.A. Klein at the University of Wisconsin-Madison, klein@engr.wisc.edu.

The EES code below shows the potential, mass, and energy balances in finite-difference form. The code below represents only a portion of the total program. Other information such as geometry inputs, property relations, etc. can be found in the attached CD-ROM, where the program is reproduced in its entirety.

----- Nodes / Steps -----

$$N_x = 20 \quad \text{number of nodes}$$

$$\Delta x = \frac{L_{\text{cell}}}{N_x}$$

$$x_0 = 0$$

$$x_1 = \frac{\Delta x}{2}$$

$$x_{21} = x_{20} + \frac{\Delta x}{2}$$

$$x_i = x_{i-1} + \Delta x \quad \text{for } i = 2 \text{ to } n_x$$

----- Air composition -----

$$X_{O_2,21} = 0.21$$

$$X_{N_2a,21} = 0.79$$

----- Finite Difference Potential Equations -----

$$V_{\text{cell}} = E_{N,i} - j_{\text{slice},i} \cdot R_i - \eta_{\text{act},i} - \eta_{\text{conc},i} + \text{SAK}_i + 0.035 \quad \text{for } i = 1 \text{ to } n_x$$

$$E_{N,i} = \frac{-\Delta G_i}{n_e \cdot F} - R_u \cdot \left[\frac{T_i + 273}{n_e \cdot F} \right] \cdot \ln \left[\frac{X_{H_2O,i}}{X_{H_2,i} \cdot \sqrt{X_{O_2,i}}} \right] \quad \text{for } i = 1 \text{ to } n_x$$

$$\Delta G_i = g('H_2O', T_i, P) - (g('H_2', T_i, P) + 1/2 \cdot g('O_2', T_i, P)) \quad \text{for } i = 1 \text{ to } n_x$$

$$\eta_{\text{act},i} = a_i + b_i \cdot \ln(j_{\text{slice},i}) \quad \text{for } i = 1 \text{ to } n_x$$

$$\eta_{\text{conc},i} = \frac{-R_u \cdot T_i}{2 \cdot F} \cdot (\ln(1 - AA_i) - \ln(1 + BB_i)) \quad \text{for } i = 1 \text{ to } n_x$$

$$AA_i = \frac{j_{\text{slice},i}}{i_{\text{as},i}} \quad \text{for } i = 1 \text{ to } n_x$$

$$BB_i = \frac{X_{H_2,i} \cdot j_{\text{slice},i}}{X_{H_2O,i} \cdot i_{\text{as},i}} \quad \text{for } i = 1 \text{ to } n_x$$

$$\eta_{\text{ohm},i} = j_{\text{slice},i} \cdot R_i \quad \text{for } i = 1 \text{ to } n_x$$

$$R_i = 23.487 - 0.0844467 \cdot T_i + 0.0001022 \cdot T_i^2 - 4.13333 \times 10^{-8} \cdot T_i^3 \quad \text{for } i = 1 \text{ to } n_x$$

$$a_i = 0.343333 - 0.000275 \cdot T_i \quad \text{for } i = 1 \text{ to } n_x$$

$$b_i = 0.01537 + 0.00002592 \cdot T_i - 1.080 \times 10^{-8} \cdot T_i^2 \quad \text{for } i = 1 \text{ to } n_x$$

$$i_{\text{as},i} = 169.8 - 0.7077 \cdot T_i + 0.000975 \cdot T_i^2 - 4.333 \times 10^{-7} \cdot T_i^3 \quad \text{for } i = 1 \text{ to } n_x$$

Fuel Gas Mass Balance

$$N_{N2f,i} = N_{N2f,i-1} \quad \text{for } i = 1 \text{ to } nx$$

$$N_{H2,i} = N_{H2,i-1} + N_{H2e,i} \quad \text{for } i = 1 \text{ to } nx$$

$$N_{H2O,i} = N_{H2O,i-1} + N_{H2Oe,i} \quad \text{for } i = 1 \text{ to } nx$$

$$N_{CO,i} = N_{CO,i-1} \quad \text{for } i = 1 \text{ to } nx$$

$$N_{CO2,i} = N_{CO2,i-1} \quad \text{for } i = 1 \text{ to } nx$$

$$N_{CH4,i} = N_{CH4,i-1} \quad \text{for } i = 1 \text{ to } nx$$

$$\dot{N}_{f,i} = N_{H2,i} + N_{H2O,i} + N_{CO,i} + N_{CO2,i} + N_{CH4,i} + N_{N2f,i} \quad \text{for } i = 1 \text{ to } nx$$

$$\dot{m}_{f,i} = \dot{N}_{f,i} \cdot MW_{f,i} \quad \text{for } i = 1 \text{ to } nx$$

Electrochemical species consumption/production via Faraday's Law

$$N_{H2e,i} = \frac{v_{H2} \cdot i_{\text{slice},i}}{n_e \cdot F} \quad \text{for } i = 1 \text{ to } nx$$

$$N_{H2Oe,i} = \frac{v_{H2O} \cdot i_{\text{slice},i}}{n_e \cdot F} \quad \text{for } i = 1 \text{ to } nx$$

Air Gas Mass Balance

$$N_{O2,i} = N_{O2,i+1} + N_{O2e,i} \quad \text{for } i = 1 \text{ to } nx$$

$$N_{O2e,i} = \frac{v_{O2} \cdot i_{\text{slice},i}}{n_e \cdot F} \quad \text{for } i = 1 \text{ to } nx$$

Stoichiometric reaction coefficients ($CH_4 + H_2O \rightarrow 3H_2 + CO$)

$$v_{CH4r} = -1$$

$$v_{H2Or} = -1$$

$$v_{H2r} = 3$$

$$v_{CO_r} = 1$$

$$E_A = 82000 \text{ J/mol}$$

$$f_e = 1 \text{ Equilibrium coefficient}$$

$$k_0 = 4274$$

Stoichiometric reaction coefficients ($H_2 + 1/2 O_2 \rightarrow H_2O$)

$$v_{H2} = -1$$

$$v_{O2} = \frac{-1}{2}$$

$$v_{H2O} = 1$$

Fuel Utilization, Cell Performance, and other parameters

$$U_f = \frac{N_{H_2, \text{cons}}}{4 \cdot N_{CH_4, 0} + N_{H_2, 0} + N_{CO, 0}}$$

$$N_{H_2, \text{cons}} = - \sum_{i=1}^{n_x} (N_{H_2e, i}) \quad \text{H}_2 \text{ consumed electrochemically}$$

$$S_{O_2} = \frac{N_{O_2, 21}}{1 / 2 \cdot (4 \cdot N_{CH_4, 0} + N_{H_2, 0} + N_{CO, 0})}$$

----- Finite Difference Energy Equations -----

Heat transfer areas

$$A_s = w_{ch} \cdot \Delta x \quad \text{h.t. area between gas and cell tri-layer}$$

$$A_{icf} = \delta_{icf, eq} \cdot (w_{ch} + 2 \cdot h_{fch}) \quad \text{x-sectional heat conduction area for fuel-side interconnect channel}$$

$$A_{ica} = \delta_{ica, eq} \cdot (w_{ch} + 2 \cdot h_{ach}) \quad \text{x-sectional heat conduction area for air-side interconnect channel}$$

$$A_{cond} = w_{eq} \cdot \delta$$

$$A_{conv, a} = (w_{ch} + 2 \cdot h_{ach}) \cdot \Delta x$$

$$A_{conv, f} = (w_{ch} + 2 \cdot h_{fch}) \cdot \Delta x$$

$$S_F = 0.019 \quad \text{m; conduction shape factor for 2-D interconnect geometry...determined by using FEHT}$$

Radiation configuration factors for 2-D, 2 wall enclosure

$$F_{1,2} = 1$$

$$F_{1,3} = F_{1,2}$$

$$F_{2,1} = \frac{w_{ch}}{w_{ch} + 2 \cdot h_{ach}} \quad \text{from reciprocity}$$

$$F_{3,1} = \frac{w_{ch}}{w_{ch} + 2 \cdot h_{fch}} \quad \text{from reciprocity}$$

--- Left Boundary ---

Solid

$$0 = \frac{k_s}{\Delta X} \cdot A_{\text{cond}} \cdot (T_2 - T_1) + ha_1 \cdot A_s \cdot (T_{a,1} - T_1) + hf_1 \cdot A_s \cdot (T_{f,1} - T_1) + \dot{Q}_{\text{gen},1} + Q_{\text{rad}12,1} + Q_{\text{rad}13,1}$$

$$Q_{\text{rad}12,1} = \frac{\sigma \cdot ((T_{\text{ica},1} + 273)^4 - (T_1 + 273)^4)}{\frac{1 - \varepsilon_s}{\varepsilon_s \cdot A_s} + \frac{1}{A_s \cdot F_{1,2}} + \frac{1 - \varepsilon_{\text{ic}}}{\varepsilon_{\text{ic}} \cdot A_{\text{conv},a}}}$$

$$Q_{\text{rad}13,1} = \frac{\sigma \cdot ((T_{\text{icf},1} + 273)^4 - (T_1 + 273)^4)}{\frac{1 - \varepsilon_s}{\varepsilon_s \cdot A_s} + \frac{1}{A_s \cdot F_{1,3}} + \frac{1 - \varepsilon_{\text{ic}}}{\varepsilon_{\text{ic}} \cdot A_{\text{conv},f}}}$$

Air-side

$$0 = \dot{N}_{a,2} \cdot h_{a,2} + ha_1 \cdot A_{\text{conv},a} \cdot (T_{\text{ica},1} - T_{a,1}) + ha_1 \cdot A_s \cdot (T_1 - T_{a,1}) + U_{\text{tot},1} \cdot (T_{f,1} - T_{a,1}) - \dot{E}_{\text{O}_2e,1} - \dot{N}_{a,1} \cdot h_{a,1}$$

Fuel-side

$$T_{f,0} = T_{\text{fuel},\text{in}}$$

$$0 = \dot{N}_{f,0} \cdot h_{f,0} + \dot{E}_{\text{H}_2\text{O}e,1} + hf_1 \cdot A_{\text{conv},f} \cdot (T_{\text{icf},1} - T_{f,1}) + hf_1 \cdot A_s \cdot (T_1 - T_{f,1}) + U_{\text{tot},1} \cdot (T_{a,1} - T_{f,1}) - \dot{N}_{f,1} \cdot h_{f,1} - \dot{E}_{\text{H}_2e,1}$$

Temperature gradient

$$\text{dtd}x_1 = \frac{-3 \cdot T_1 + 4 \cdot T_2 - T_3}{\Delta X \cdot \left[1000 \cdot \frac{mm}{m} \right]} \quad \text{left boundary...using one-sided quadratic expression}$$

Air side Interconnect

$$0 = \frac{k_{\text{ic}}}{\Delta X} \cdot A_{\text{ica}} \cdot (T_{\text{ica},2} - T_{\text{ica},1}) + ha_1 \cdot A_{\text{conv},a} \cdot (T_{a,1} - T_{\text{ica},1}) + Q_{\text{rad}21,1}$$

$$Q_{\text{rad}21,1} = \frac{\sigma \cdot ((T_1 + 273)^4 - (T_{\text{ica},1} + 273)^4)}{\frac{1 - \varepsilon_{\text{ic}}}{\varepsilon_{\text{ic}} \cdot A_{\text{conv},a}} + \frac{1}{A_{\text{conv},a} \cdot F_{2,1}} + \frac{1 - \varepsilon_s}{\varepsilon_s \cdot A_s}}$$

Fuel side Interconnect

$$0 = \frac{k_{\text{ic}}}{\Delta X} \cdot A_{\text{icf}} \cdot (T_{\text{icf},2} - T_{\text{icf},1}) + hf_1 \cdot A_{\text{conv},f} \cdot (T_{f,1} - T_{\text{icf},1}) + Q_{\text{rad}31,1}$$

$$Q_{\text{rad}31,1} = \frac{\sigma \cdot ((T_1 + 273)^4 - (T_{\text{icf},1} + 273)^4)}{\frac{1 - \varepsilon_{\text{ic}}}{\varepsilon_{\text{ic}} \cdot A_{\text{conv},f}} + \frac{1}{A_{\text{conv},f} \cdot F_{3,1}} + \frac{1 - \varepsilon_s}{\varepsilon_s \cdot A_s}}$$

--- Interior Nodes ---

Solid Energy Balance

$$0 = \frac{k_s}{\Delta X} \cdot A_{\text{cond}} \cdot (T_{j+1} - 2 \cdot T_j + T_{j-1}) + ha_j \cdot A_s \cdot (T_{a,j} - T_j) + hf_j \cdot A_s \cdot (T_{f,j} - T_j) + \dot{Q}_{\text{gen},j} + Q_{\text{rad}12,j} + Q_{\text{rad}13,j} \quad \text{for } j = 2 \text{ to } Nx-1$$

$$Q_{\text{rad}12,j} = \frac{\sigma \cdot ((T_{\text{ica},j} + 273)^4 - (T_j + 273)^4)}{\frac{1 - \varepsilon_s}{\varepsilon_s \cdot A_s} + \frac{1}{A_s \cdot F_{1,2}} + \frac{1 - \varepsilon_{\text{ic}}}{\varepsilon_{\text{ic}} \cdot A_{\text{conv},a}}} \quad \text{for } j = 2 \text{ to } Nx-1$$

$$Q_{\text{rad}13,j} = \frac{\sigma \cdot ((T_{\text{icf},j} + 273)^4 - (T_j + 273)^4)}{\frac{1 - \varepsilon_s}{\varepsilon_s \cdot A_s} + \frac{1}{A_s \cdot F_{1,3}} + \frac{1 - \varepsilon_{\text{ic}}}{\varepsilon_{\text{ic}} \cdot A_{\text{conv},f}}} \quad \text{for } j = 2 \text{ to } Nx-1$$

Air gas Energy Balance

$$0 = \dot{N}_{a,j+1} \cdot h_{a,j+1} + ha_j \cdot A_{\text{conv},a} \cdot (T_{\text{ica},j} - T_{a,j}) + ha_j \cdot A_s \cdot (T_j - T_{a,j}) + U_{\text{tot},j} \cdot (T_{f,j} - T_{a,j}) - \dot{E}_{\text{O}_2e,j} - \dot{N}_{a,j} \cdot h_{a,j} \quad \text{for } j = 2 \text{ to } Nx-1$$

Fuel gas Energy Balance

$$0 = \dot{N}_{f,j-1} \cdot h_{f,j-1} + \dot{E}_{\text{H}_2\text{O}e,j} + hf_j \cdot A_{\text{conv},f} \cdot (T_{\text{icf},j} - T_{f,j}) + hf_j \cdot A_s \cdot (T_j - T_{f,j}) + U_{\text{tot},j} \cdot (T_{a,j} - T_{f,j}) - \dot{N}_{f,j} \cdot h_{f,j} - \dot{E}_{\text{H}_2e,j} \quad \text{for } j = 2 \text{ to } Nx-1$$

Temperature gradient

$$\text{dtd}x_j = \frac{T_{j+1} - T_{j-1}}{\Delta X \cdot \left[1000 \cdot \frac{mm}{m} \right]} \quad \text{for } j = 2 \text{ to } Nx-1$$

Air side Interconnect

$$0 = \frac{k_{ic}}{\Delta X} \cdot A_{ica} \cdot (T_{ica,j+1} - 2 \cdot T_{ica,j} + T_{ica,j-1}) + h_{a,j} \cdot A_{conv,a} \cdot (T_{a,j} - T_{ica,j}) + Q_{rad21,j} \quad \text{for } j = 2 \text{ to } Nx-1$$

$$Q_{rad21,j} = \frac{\sigma \cdot ((T_j + 273)^4 - (T_{ica,j} + 273)^4)}{\frac{1 - \epsilon_{ic}}{\epsilon_{ic} \cdot A_{conv,a}} + \frac{1}{A_{conv,a} \cdot F_{2,1}} + \frac{1 - \epsilon_s}{\epsilon_s \cdot A_s}} \quad \text{for } j = 2 \text{ to } Nx-1$$

Fuel side Interconnect

$$0 = \frac{k_{ic}}{\Delta X} \cdot A_{icf} \cdot (T_{icf,j+1} - 2 \cdot T_{icf,j} + T_{icf,j-1}) + h_{f,j} \cdot A_{conv,f} \cdot (T_{f,j} - T_{icf,j}) + Q_{rad31,j} \quad \text{for } j = 2 \text{ to } Nx-1$$

$$Q_{rad31,j} = \frac{\sigma \cdot ((T_j + 273)^4 - (T_{icf,j} + 273)^4)}{\frac{1 - \epsilon_{ic}}{\epsilon_{ic} \cdot A_{conv,f}} + \frac{1}{A_{conv,f} \cdot F_{3,1}} + \frac{1 - \epsilon_s}{\epsilon_s \cdot A_s}} \quad \text{for } j = 2 \text{ to } Nx-1$$

--- Right Boundary ---

Solid

$$0 = \frac{k_s}{\Delta X} \cdot A_{cond} \cdot (T_{19} - T_{20}) + h_{a,20} \cdot A_s \cdot (T_{a,20} - T_{20}) + h_{f,20} \cdot A_s \cdot (T_{f,20} - T_{20}) + \dot{Q}_{gen,20} + Q_{rad12,20} + Q_{rad13,20}$$

$$Q_{rad12,20} = \frac{\sigma \cdot ((T_{ica,20} + 273)^4 - (T_{20} + 273)^4)}{\frac{1 - \epsilon_s}{\epsilon_s \cdot A_s} + \frac{1}{A_s \cdot F_{1,2}} + \frac{1 - \epsilon_{ic}}{\epsilon_{ic} \cdot A_{conv,a}}}$$

$$Q_{rad13,20} = \frac{\sigma \cdot ((T_{icf,20} + 273)^4 - (T_{20} + 273)^4)}{\frac{1 - \epsilon_s}{\epsilon_s \cdot A_s} + \frac{1}{A_s \cdot F_{1,3}} + \frac{1 - \epsilon_{ic}}{\epsilon_{ic} \cdot A_{conv,f}}}$$

Air gas Energy Balance

$$T_{a,21} = T_{air,in}$$

$$0 = \dot{N}_{a,21} \cdot h_{a,21} + h_{a,20} \cdot A_{conv,a} \cdot (T_{ica,20} - T_{a,20}) + h_{a,20} \cdot A_s \cdot (T_{20} - T_{a,20}) + U_{tot,20} \cdot (T_{f,20} - T_{a,20}) - \dot{E}_{O2e,20} - \dot{N}_{a,20} \cdot h_{a,20}$$

Fuel gas Energy Balance

$$0 = \dot{N}_{f,19} \cdot h_{f,19} + \dot{E}_{H2Oe,20} + h_{f,20} \cdot A_{conv,f} \cdot (T_{icf,20} - T_{f,20}) + h_{f,20} \cdot A_s \cdot (T_{20} - T_{f,20}) + U_{tot,20} \cdot (T_{a,20} - T_{f,20}) - \dot{N}_{f,20} \cdot h_{f,20} - \dot{E}_{H2e,20}$$

Temperature gradient

$$dtdx_{20} = \frac{3 \cdot T_{20} - 4 \cdot T_{19} + T_{18}}{2 \cdot \Delta X \cdot \left[1000 \cdot \frac{mm}{m} \right]} \quad \text{right boundary...using one-sided quadratic expression}$$

Air side Interconnect

$$0 = \frac{k_{ic}}{\Delta X} \cdot A_{ica} \cdot (T_{ica,19} - T_{ica,20}) + h_{a,20} \cdot A_{conv,a} \cdot (T_{a,20} - T_{ica,20}) + Q_{rad21,20}$$

$$Q_{rad21,20} = \frac{\sigma \cdot ((T_{20} + 273)^4 - (T_{ica,20} + 273)^4)}{\frac{1 - \epsilon_{ic}}{\epsilon_{ic} \cdot A_{conv,a}} + \frac{1}{A_{conv,a} \cdot F_{2,1}} + \frac{1 - \epsilon_s}{\epsilon_s \cdot A_s}}$$

Fuel side Interconnect

$$0 = \frac{k_{ic}}{\Delta X} \cdot A_{icf} \cdot (T_{icf,19} - T_{icf,20}) + h_{f,20} \cdot A_{conv,f} \cdot (T_{f,20} - T_{icf,20}) + Q_{rad31,20}$$

$$Q_{rad31,20} = \frac{\sigma \cdot ((T_{20} + 273)^4 - (T_{icf,20} + 273)^4)}{\frac{1 - \epsilon_{ic}}{\epsilon_{ic} \cdot A_{conv,f}} + \frac{1}{A_{conv,f} \cdot F_{3,1}} + \frac{1 - \epsilon_s}{\epsilon_s \cdot A_s}}$$

$$\dot{Q}_{gen,j} = \dot{E}_{H2e,j} + \dot{E}_{O2e,j} - \dot{E}_{H2Oe,j} - P_{slice,j} \quad \text{for } j = 1 \text{ to } Nx$$

$$U_{tot,j} = \frac{1}{\frac{1}{h_{a,j} \cdot A_{conv,a}} + \frac{1}{k_{ic} \cdot S_F} + \frac{1}{h_{f,j} \cdot A_{conv,f}}} \quad \text{for } j = 1 \text{ to } Nx$$

$$\dot{E}_{f,j} = \dot{N}_{f,j} \cdot h_{f,j} \quad \text{for } j = 1 \text{ to } Nx$$

$$\dot{E}_{H2e,j} = \dot{N}_{H2e,j} \cdot h('H2', T_{f,j}) \quad \text{for } j = 1 \text{ to } Nx$$

$$\dot{E}_{O2e,j} = \dot{N}_{O2e,j} \cdot h('O2', T_{a,j}) \quad \text{for } j = 1 \text{ to } Nx$$

$$\dot{E}_{H2Oe,i} = \dot{N}_{H2Oe,i} \cdot h('H2O', T_i) \quad \text{for } j = 1 \text{ to } Nx$$

Appendix III

Balance-of-Plant EES Models^{*}

- A3.1. Pre-reformer
- A3.2. Jet Pump / Ejector
- A3.3. Hot Water Heater

^{*} Note that the models presented in this Appendix are a partial set. The complete set of BOP models and design data can be found in the attached CD-ROM or via S.A. Klein (klein @engr.wisc.edu).

A3.1 Pre-reformer

The pre-reformer EES code is written in the form of a module which can be called from the main EES program. This module is called into the finite-difference SOFC model.

MODULE PREREFORM (T, P, S\C, x : $\Delta H_{\text{prereform}}$, X_{CH_4} , X_{CO} , X_{CO_2} , X_{H_2} , $X_{\text{H}_2\text{O}}$, K)

$R_u = 8.314$ Gas constant

Reforming Stoichiometry: $\text{CH}_4 + \text{H}_2\text{O} = 3\text{H}_2 + \text{CO}$

General Balance: $m\text{CH}_4 + n\text{H}_2\text{O} = 3x\text{H}_2 + x\text{CO} + (1-x)\text{CH}_4 + S\C(1-x)\text{H}_2\text{O}$

Stoichiometric reaction coefficients:

$$v_{\text{CH}_4} = -1$$

$$v_{\text{H}_2\text{O}} = -1$$

$$v_{\text{H}_2} = 3$$

$$v_{\text{CO}} = 1$$

$$m = 1$$

$$n = S\C \cdot m$$

Fractional conversion of methane in Prereformer

$$N_{\text{CH}_4,i} = m + v_{\text{CH}_4} \cdot x \quad i = \text{intermediate species}$$

$$N_{\text{H}_2\text{O},i} = S\C + v_{\text{H}_2\text{O}} \cdot \frac{x}{m}$$

$$N_{\text{H}_2,i} = v_{\text{H}_2} \cdot \frac{x}{m}$$

$$N_{\text{CO},i} = v_{\text{CO}} \cdot \frac{x}{m}$$

$$N_{\text{CO}_2,i} = 0$$

Water-gas shift equilibrium

$$K = \frac{N_{\text{H}_2} \cdot N_{\text{CO}_2}}{N_{\text{CO}} \cdot N_{\text{H}_2\text{O}}}$$

$$\ln(K) = \frac{-\Delta G_s}{R_u \cdot (T + 273)}$$

$$\Delta G_s = g_{\text{H}_2} + g_{\text{CO}_2} - (g_{\text{CO}} + g_{\text{H}_2\text{O}})$$

$$N_{\text{tot}} = N_{\text{H}_2} + N_{\text{H}_2\text{O}} + N_{\text{CO}} + N_{\text{CO}_2} + N_{\text{CH}_4,i}$$

Shift reaxn mass balances ($\text{CO} + \text{H}_2\text{O} = \text{CO}_2 + \text{H}_2$)

$$N_{\text{CO},i} + N_{\text{CO}_2,i} = N_{\text{CO}} + N_{\text{CO}_2} \quad \text{Carbon balance}$$

$$N_{\text{H}_2,i} + N_{\text{H}_2\text{O},i} = N_{\text{H}_2} + N_{\text{H}_2\text{O}} \quad \text{Hydrogen balance}$$

$$N_{\text{CO},i} + 2 \cdot N_{\text{CO}_2,i} + N_{\text{H}_2\text{O},i} = N_{\text{CO}} + 2 \cdot N_{\text{CO}_2} + N_{\text{H}_2\text{O}} \quad \text{Oxygen balance}$$

Note: $N_{\text{CH}_4,i}$ is not included in the above balances as it cancels by virtue of the fact that it does not participate in the shift

Final Composition

$$X_{\text{H}_2} = \frac{N_{\text{H}_2}}{N_{\text{tot}}}$$

$$X_{\text{H}_2\text{O}} = \frac{N_{\text{H}_2\text{O}}}{N_{\text{tot}}}$$

$$X_{\text{CO}} = \frac{N_{\text{CO}}}{N_{\text{tot}}}$$

$$X_{\text{CO}_2} = \frac{N_{\text{CO}_2}}{N_{\text{tot}}}$$

$$X_{\text{CH}_4} = \frac{N_{\text{CH}_4,i}}{N_{\text{tot}}}$$

Energy Requirements

$$\Delta H_{\text{preref}} = N_{\text{H}_2} \cdot h_{\text{H}_2} + N_{\text{H}_2\text{O}} \cdot h_{\text{H}_2\text{O}} + N_{\text{CO}} \cdot h_{\text{CO}} + N_{\text{CO}_2} \cdot h_{\text{CO}_2} + N_{\text{CH}_4,i} \cdot h_{\text{CH}_4} - (m \cdot h_{\text{CH}_4} + n \cdot h_{\text{H}_2\text{O}})$$

Properties

$$h_{\text{H}_2} = h(\text{'H}_2\text{'}, T=T) \cdot \text{MolarMass}(\text{'H}_2\text{'})$$

$$h_{\text{H}_2\text{O}} = h(\text{'H}_2\text{O'}, T=T) \cdot \text{MolarMass}(\text{'H}_2\text{O'})$$

$$h_{\text{CH}_4} = h(\text{'CH}_4\text{'}, T=T) \cdot \text{MolarMass}(\text{'CH}_4\text{'})$$

$$h_{\text{CO}} = h(\text{'CO'}, T=T) \cdot \text{MolarMass}(\text{'CO'})$$

$$h_{\text{CO}_2} = h(\text{'CO}_2\text{'}, T=T) \cdot \text{MolarMass}(\text{'CO}_2\text{'})$$

$$s_{\text{H}_2} = s(\text{'H}_2\text{'}, T=T, P=P) \cdot \text{MolarMass}(\text{'H}_2\text{'})$$

$$s_{\text{H}_2\text{O}} = s(\text{'H}_2\text{O'}, T=T, P=P) \cdot \text{MolarMass}(\text{'H}_2\text{O'})$$

$$s_{\text{CH}_4} = s(\text{'CH}_4\text{'}, T=T, P=P) \cdot \text{MolarMass}(\text{'CH}_4\text{'})$$

$$s_{\text{CO}} = s(\text{'CO'}, T=T, P=P) \cdot \text{MolarMass}(\text{'CO'})$$

$$s_{\text{CO}_2} = s(\text{'CO}_2\text{'}, T=T, P=P) \cdot \text{MolarMass}(\text{'CO}_2\text{'})$$

$$g_{\text{H}_2} = h_{\text{H}_2} - (T + 273) \cdot s_{\text{H}_2}$$

$$g_{\text{H}_2\text{O}} = h_{\text{H}_2\text{O}} - (T + 273) \cdot s_{\text{H}_2\text{O}}$$

$$g_{\text{CO}} = h_{\text{CO}} - (T + 273) \cdot s_{\text{CO}}$$

$$g_{\text{CO}_2} = h_{\text{CO}_2} - (T + 273) \cdot s_{\text{CO}_2}$$

A3.2 Jet pump/Ejector

The jet pump model employed in the design effort is shown below. The model itself was not utilized for off-design operation. Instead it was assumed that the driving pressure required and the fraction of recycled gases were fixed as operating load was varied.

=====

Simple Jet Pump Model
Equations based on BSL, Ch. 15

R. Braun
12 Aug 2002

=====

Numbering
1 -- fresh air supply
2 -- recycled cathode exhaust gases
3 -- mixed gases supplied to cathode compartment

--- Mass Balance ---

$$\dot{m}_1 + \dot{m}_2 = \dot{m}_3$$

----- Momentum Balance -----

$$\dot{m}_1 \cdot u_1 + p_1 \cdot A_1 \cdot \left[100000 \cdot \frac{Pa}{bar} \right] + \dot{m}_2 \cdot u_2 + p_2 \cdot A_2 \cdot \left[100000 \cdot \frac{Pa}{bar} \right] = \dot{m}_3 \cdot u_3 + p_3 \cdot A_3 \cdot \left[100000 \cdot \frac{Pa}{bar} \right]$$

----- Energy Balance -----

$$\dot{m}_1 \cdot \left[h_1 \cdot \left(1000 \cdot \frac{J}{kJ} \right) + 1 / 2 \cdot u_1^2 \right] + \dot{m}_2 \cdot \left[h_2 \cdot \left(1000 \cdot \frac{J}{kJ} \right) + 1 / 2 \cdot u_2^2 \right] = \dot{m}_3 \cdot \left[h_3 \cdot \left(1000 \cdot \frac{J}{kJ} \right) + 1 / 2 \cdot u_3^2 \right]$$

$$h_1 = h('Air', T=T_1) \quad \text{Enthalpy of gas stream 1}$$

$$h_2 = h('Air', T=T_2)$$

$$h_3 = h('Air', T=T_3)$$

----- Properties -----

$$p_3 \cdot \left[100000 \cdot \frac{Pa}{bar} \right] = p_3 \cdot R_u \cdot \left[\frac{T_3 + 273}{MW_3} \right] \cdot \left[1000 \cdot \frac{J}{kJ} \right]$$

$$\rho_1 = \rho('Air', T=T_1, P=p_1) \quad \text{Density of gas stream 1}$$

$$\rho_2 = \rho('Air', T=T_2, P=p_2)$$

$$\rho_3 = \rho('Air', T=T_3, P=p_3)$$

----- Other Relationships and constants -----

$$\dot{m}_1 = \rho_1 \cdot A_1 \cdot u_1 \quad \text{mass flow of driving fluid (fresh air)}$$

$$\dot{m}_2 = \rho_2 \cdot A_2 \cdot u_2 \quad \text{mass flow of recirculated gases}$$

$$\dot{m}_3 = \rho_3 \cdot A_3 \cdot u_3 \quad \text{mass flow of mixed gases supplied to the cathode inlet}$$

$$A_1 = \pi \cdot \frac{\left[d_1 \cdot \left(0.0254 \cdot \frac{m}{in} \right) \right]^2}{4} \quad \text{cross-sectional flow area in supply tube}$$

$$A_2 = A_3 - A_1 \quad \text{Annular flow area}$$

$$A_3 = \pi \cdot \frac{\left[d_2 \cdot \left(0.0254 \cdot \frac{m}{in} \right) \right]^2}{4} \quad \text{cross-sectional flow area of mixed gases in outlet}$$

$$R_u = (8.31434 \text{ kJ/kmole-K}) \quad \text{universal gas constant}$$

$$\text{CGR} = \frac{\dot{m}_2}{\dot{m}_3} \quad \text{Cathode gas recycle fraction}$$

$$\delta = \frac{d_2}{d_1} \quad \text{Ratio of tube diameters: fresh air-to-recycled exhaust tubes}$$

$$\Delta P = (p_3 - p_2) \cdot \left[1000 \cdot \frac{\text{millibar}}{\text{bar}} \right] \quad \text{pressure drop across cathode compartment}$$

----- Inputs -----

$$d_1 = 0.5 \text{ in, diameter of fresh air supply tube}$$

$$\delta = 2$$

$$\dot{m}_1 = \dot{m}_{\text{air,in}} \cdot \left[0.001 \cdot \frac{\text{kg}}{\text{g}} \right] \quad \text{kg/s}$$

$$\dot{m}_{\text{air,in}} = 3.4$$

$$\dot{m}_2 = 3.1 \cdot \left[0.001 \cdot \frac{\text{kg}}{\text{g}} \right] \quad \text{kg/s}$$

$$T_0 = 25 \text{ }^\circ\text{C, ambient temperature}$$

$$T_1 = 590 \text{ }^\circ\text{C, temperature of fresh air feed}$$

$$T_2 = 785 \text{ temperature of recycled cathode exhaust gas}$$

$$T_3 = 685 \text{ temperature of mixed gases supplied to cathode}$$

$$\Delta P = 20 \text{ mbar}$$

$$\dot{W}_{\text{blower}} = \dot{V} \cdot \frac{\Delta P_{\text{sys}}}{\eta_{\text{fan,s}}} \quad \text{Blower work required}$$

$$\dot{V} = \frac{\dot{m}_1}{\rho(\text{Air}, T=15, P=P_0)} \quad \text{Volumetric flow}$$

$$\eta_{\text{fan,s}} = 0.625 \quad \text{Isentropic blower efficiency}$$

$$P_0 = 1.01325 \text{ Ambient pressure}$$

A3.3 Hot Water Heater Tank

A two-tank (preheat and standby) thermal energy recovery system was used in system simulations. The preheat unit was modeled as a single-node thermal storage unit, and the standby tank was modeled as an instantaneous, i.e., no storage. The preheat tank model is described below.

----- Domestic Hot Water Storage Tank -----

Unsteady Energy Balance

$$\frac{\dot{m}_w}{\text{MW}_{\text{H}_2\text{O}}} \cdot c_{p_w} \cdot dT dt = \varepsilon \cdot C_{f_{cg}} \cdot (T_{f_{cg}} - T_{\text{tank}}) + \frac{\dot{m}_w}{\text{MW}_{\text{H}_2\text{O}}} \cdot c_{p_w} \cdot (T_s - T_{\text{tank}}) - UA_{\text{tank}} \cdot \left[3600 \cdot \frac{\text{kJ/h}}{\text{kW}} \right] \cdot (T_{\text{tank}} - T_o)$$

$$T_{\text{tank}} = T_i + \int (dT dt) d\text{Time} \quad \text{tank temp at any time } t$$

$$T_i = 30 \quad \text{Initial tank temperature}$$

$$\bar{T}_{\text{tank}} = \frac{T_i + \int (T_{\text{tank}}) d\text{Time}}{\frac{8760}{\text{TF}}} \quad \text{average tank temperature}$$

$$m_w = 60 \cdot \left[0.003785 \cdot \frac{\text{m}^3}{\text{gal}} \right] \cdot \rho(\text{'Water', } T=35, P=P_o) \cdot \text{MW}_{\text{H}_2\text{O}} \quad \text{mass of water in } \sim 225 \text{ kg} \dots 60 \text{ gal tank}$$

$$V_{\text{tank}} = \frac{m_w}{\rho(\text{'Water', } T=T_{\text{tank}}, P=P_o)} \cdot \left[264.172 \cdot \frac{\text{gal}}{\text{m}^3} \right] \quad \text{tank volume}$$

$$\dot{Q}_{\text{loss}} = UA_{\text{tank}} \cdot \left[3600 \cdot \frac{\text{kJ/h}}{\text{kW}} \right] \cdot (T_{\text{tank}} - T_o) \quad \text{Tank heat loss}$$

$$UA_{\text{tank}} = 0.005 \quad \text{kW/C} \dots \text{Heat loss UA}$$

$$Q_{\text{gain}} = \frac{\dot{m}_w}{\text{MW}_{\text{H}_2\text{O}}} \cdot c_{p_w} \cdot (T_{\text{tank}} - T_s) \cdot \left[0.000277778 \cdot \frac{\text{kW}}{\text{kJ/h}} \right]$$

$$\varepsilon = \frac{\dot{Q}_{\text{HR}}}{\dot{Q}_{\text{HR,max}}} \quad \text{Heat exchanger effectiveness}$$

$$\dot{Q}_{\text{HR}} = ((C_{f_{cg}} + 0.00001) \cdot (T_{f_{cg}} - T_{f_{cg,o}})) \cdot \left[0.000277778 \cdot \frac{\text{kW}}{\text{kJ/h}} \right]$$

$$UA_{\text{HR}} = UA_{\text{HR,ref}} \cdot \left[\frac{C_{f_{cg}}}{CR_{f_{cg,ref}}} \right]^{0.91}$$

$$\dot{Q}_{\text{HR}} = UA_{\text{HR}} \cdot \Delta T_{\text{LM}}$$

$$\Delta T_{\text{LM}} = \frac{T_{f_{cg}} - T_{\text{tank}} - \text{dtsak}}{\ln(\text{LNNT})}$$

$$\text{dtsak} = \text{Max}(T_{f_{cg,o}} - T_{\text{tank}}, 0.01) + 0.25 \quad \text{Enables convergence for large steps}$$

$$\text{LNNT} = \frac{T_{f_{cg}} - T_{\text{tank}}}{\text{dtsak}}$$

$$\Delta T_{LM2} = \frac{T_{fcg} + T_{fcg,o}}{2} - T_{tank}$$

Q_{MAX} CALCULATION

$$\dot{Q}_{HR,max} = ((C_{min} + 0.0001) \cdot (T_{fcg} - T_s)) \cdot \left[0.000277778 \cdot \frac{kW}{kJ/h} \right]$$

PROPERTY DATA

$$P_{sat} = P('Steam_{NBS}', T=T_s, x=0)$$

$$MW_{H2O} = \mathbf{MolarMass}('H2O')$$

$$cp_w = \mathbf{Cp}('Water', T=T_{tank}, P=10000)$$

$$C_{min} = C_{fcg} \quad \text{minimum thermal capacitance rate}$$

$$C_{max} = \frac{\dot{m}_w}{MW_{H2O}} \cdot cp_w \quad \text{maximum thermal capacitance rate}$$

Appendix IV

EES Economic Cost Model

The following EES code describes the detailed cost modeling of the SOFC cogeneration system as discussed in Chapter 6 of the present study. The cost model includes capital, operating, and life cycle cost (expressed as cost-of-electricity) estimations. Model inputs and assumptions are also presented.

=====
 Cost Analysis
 =====

(All Costs in 2001 U.S. \$...Values converted from 1988 to 2001 via Chemical Engineering Plant Cost Index)

Assumptions:

- (1) SOFC stack manufacturing costs are fixed over the life of the system
(i.e., no product cost reduction improvements included)
- (2) BOP Equipment costs are fixed over the life of the unit
- (3) Voltage degradation over the life of the stack unit is not included
- (4) No Stack performance (ASR) improvements over the system life are considered
- (5) Fuel costs are fixed (no fuel inflation rate)

----- Economic Inputs -----

FC = 7 · Unc_{fuel} Nat. Gas cost in \$/MMBtu

CF = 0.8 Annual Capacity Factor

np = 20 Plant life (yrs)

dr = 0.2 Discount rate = cost of capital (8%) + ROI(5.5% after taxes --> 0.055/(1-0.4))

int = 0.08 Cost of capital (interest rate)

P_{ref} = 5 Reference SOFC Power Rating for Costs

Unc_{fuel} = 1 Uncertainty in fuel cost

Unc_{fc} = 1 Uncertainty in SOFC stack cost

Unc_{bop} = 1 Uncertainty in system BOP cost

Unc_{cap} = 1 Uncertainty in total system cost

F_{th} = 1 2 tank recovery system enables 100% as long as storage tank is sized appropriately

η_{dts} = 0.8 efficiency of displaced thermal source....hot water heater

----- Total System Unit cost -----

C_{sys,eo} = (C_{FC} + C_{BOP} + C_{FAB}) · Unc_{cap} SOFC system capital cost --electric-only

C_{sys,cog} = (C_{FC} + C_{BOP} + C_{FAB} + C_{tank}) · Unc_{cap} SOFC cogen system capital cost

C_{BOP} = (C_{FP} + C_{CC} + C_{AP} + C_{Blowr} + C_{INV} + C_{IC} + C_{Misc}) · Unc_{bop} BOP Capital cost

----- Cost of Electricity -----

$$COE_2 = \frac{C_1}{CF} \cdot AP \cdot C_{sys,cog} + M_C + Fuel_{cost} - Heat_{credit} \quad \text{Fuel cell system}$$

$$M_C = 0.5 \quad \text{Operation and maintenance cost; cents/kWh}$$

$$Fuel_{cost} = C_2 \cdot \frac{FC}{\frac{\eta_{sys}}{100}}$$

$$Heat_{credit} = C_2 \cdot F_{th} \cdot (\eta_{cogen} - \eta_{sys}) \cdot \frac{FC}{\eta_{sys} \cdot \eta_{dts}} \quad \text{As present}$$

$$AP = \frac{dr \cdot (1 + dr)^{np}}{(1 + dr)^{np} - 1} \quad \text{Capital recovery factor}$$

$$C_1 = \frac{1000}{8760 \cdot 10} \quad \text{COE unit conversion constant}$$

$$C_2 = \left[\frac{3412.14 \cdot \frac{Btu}{kWh}}{1000000} \right] \cdot \left[100 \cdot \frac{cents}{\$} \right] \quad \text{COE unit conversion}$$

$$COE_1 = \frac{C_1}{CF} \cdot AP \cdot C_{sys,co} + M_C + Fuel_{cost} \quad \text{Fuel cell system}$$

$$COE_3 = \frac{C_1}{CF} \cdot AP \cdot C_{sys,cog} + M_C + Fuel_{cost2} \quad \text{Includes hot water}$$

$$Fuel_{cost2} = C_2 \cdot \frac{FC}{\frac{\eta_{cogen}}{100}}$$

$$COE_{HW} = COE_1 - COE_3 \quad \text{Alternative estimate of value of heat}$$

Individual Contributions to COE

$$Cap_{OM} = C_1 \cdot \left[\frac{AP \cdot C_{sys,cog} + C_{OM}}{CF} \right] \quad \text{O\&M}$$

$$Cap_{cost} = \frac{C_1}{CF} \cdot AP \cdot C_{sys,cog} \quad \text{Capital}$$

$$FC_{cost} = \frac{C_1}{CF} \cdot AP \cdot C_{FC} \quad \text{Fuel}$$

$$BOP_{cost} = \frac{C_1}{CF} \cdot AP \cdot (C_{sys,cog} - C_{FC}) \quad \text{BOP}$$

$$Tank_{cost} = \frac{C_1}{CF} \cdot AP \cdot C_{tank} \quad \text{Thermal storage}$$

Fractional costs

$$\text{Fuel}_{\text{Cost,R}} = \frac{\text{Fuel}_{\text{cost}}}{\text{COE}_1} \cdot 100$$

$$\text{FC}_{\text{Cost,R}} = \frac{\text{FC}_{\text{cost}}}{\text{COE}_1} \cdot 100$$

$$\text{BOP}_{\text{Cost,R}} = \frac{\text{BOP}_{\text{cost}}}{\text{COE}_1} \cdot 100$$

$$\text{Air}_{\text{Cost,R}} = \frac{\text{Air}_{\text{cost}}}{\text{COE}_1} \cdot 100$$

$$\text{Air}_{\text{BOP,R}} = \frac{\text{Air}_{\text{cost}}}{\text{BOP}_{\text{cost}}} \cdot 100$$

$$\text{Power}_{\text{kW}} = \text{Power}_{\text{net}} \cdot \left[0.001 \cdot \frac{\text{kW}}{\text{W}} \right]$$

===== System Component Capital Costs =====

----- Fuel Cell Stack Costs -----

Entire stack replaced every 5 years with 1/3 salvage value -- Chen et al

$$C_{\text{FC},1} = C_{\text{stk}} \cdot \left[\frac{A_{\text{stk}}}{\text{Power}_{\text{kW}} + 0.001} \right] \quad \$/\text{kWe}$$

$$C_{\text{FC},2} = \frac{2/3 \cdot C_{\text{stk}} \cdot \left[\frac{A_{\text{stk}}}{\text{Power}_{\text{kW}} + 0.001} \right]}{(1 + \text{int})^5}$$

$$C_{\text{FC},3} = \frac{2/3 \cdot C_{\text{stk}} \cdot \left[\frac{A_{\text{stk}}}{\text{Power}_{\text{kW}} + 0.001} \right]}{(1 + \text{int})^{10}}$$

$$C_{\text{FC},4} = \frac{2/3 \cdot C_{\text{stk}} \cdot \left[\frac{A_{\text{stk}}}{\text{Power}_{\text{kW}} + 0.001} \right]}{(1 + \text{int})^{15}}$$

$$C_{\text{FC}} = \sum_{i=1}^4 (C_{\text{FC},i}) \cdot \text{Unc}_{\text{fc}}$$

$$C_{\text{stk}} = 500 \quad \text{SOFC unit cost; } \$/\text{m}^2$$

----- Fuel Compressor, Preheater, & Processor Costs -----

Cost includes desulfurizer, ejector, prereformer/reformer, fuel preheater, fuel compressor ('deprc'), and bed catalyst -- (W.L. Lundberg, GRI report, 1989)

$$C_{FP} = C_{derpc} + C_{cat}$$

$$C_{derpc} = \frac{CC_{derpc}}{\frac{Power_{net}}{1000}}$$

$$CC_{derpc} = 1300 \cdot 1.5 \cdot \left[\frac{\dot{m}_{meth}}{m_{ref}} \right]^{(-0.33 + 1)} \quad \text{50\% cost adder for pre-reformer and ejector}$$

Cost for catalyst replacement every 4 years

$$C_{cat,1} = \frac{20}{(1 + int)^4}$$

$$C_{cat,2} = \frac{20}{(1 + int)^8}$$

$$C_{cat,3} = \frac{20}{(1 + int)^{12}}$$

$$C_{cat,4} = \frac{20}{(1 + int)^{16}}$$

$$C_{cat} = \sum_{i=1}^4 (C_{cat,i})$$

ZnO bed cost based on ADL (2001) report to DOE on 5 kW Aux Power SOFC systems, and increased by 100%

----- Catalytic Combustor -----

$C_{CC} = 20$ \$/kW.....based on ADL (2001) report to DOE on 5 kW Aux Power SOFC systems and increased b

----- Air Preheat Costs -----

Lundberg, GRI Report, 1989....unit costs based on 5 kW numbers extrapolated from 50 kW data

$$C_{AP} = \frac{CC_{AP}}{Power_{kW}}$$

$$CC_{AP} = 5350 \cdot \left[\frac{UA_{AP}}{UA_{star,AP}} \right]^{(-0.1687 + 1)}$$

$UA_{star,AP} = 2000$ value from 50kW run data 0.7V / 85% U_f

----- Air Blower & Filter Costs -----

$$C_{\text{Blower}} = \frac{CC_{\text{blower}}}{\text{Power}_{\text{kW}}}$$

$$CC_{\text{blower}} = 2950 \cdot \left[\frac{\dot{W}_{\text{blower}}}{\dot{W}_{\text{B,ref}}} \right]^{(-0.1687 + 1)}$$

$$\dot{W}_{\text{B,ref}} = \dot{V}_{\text{ref}} \cdot DP_{\text{ref}} \cdot \frac{\left[100000 \cdot \frac{\text{Pa}}{\text{bar}} \right]}{\eta_{\text{fan,s}}}$$

$$\dot{V}_{\text{ref}} = 0.115 \text{ m}^3/\text{s}, \text{ Reference flowrate from 50 kW data from S-W Design....Lundberg (1989)}$$

$$DP_{\text{ref}} = 0.145 \text{ bar}, \text{ Reference pressure drop from 50 kW data from S-W....Lundberg (1989)}$$

Lundberg, GRI Report, 1989....unit costs based on 50 kW S-W data (air filter cost included)

----- Inverter, Misc., and O&M -----

...these unit costs were assumed to be constant within the 1-10 kW size range.....

$$C_{\text{INV}} = 250 \cdot \left[\frac{\text{Power}_{\text{kW}}}{P_{\text{ref}}} \right]^{-0.22} \text{ \$/kWe} \quad \text{Baker, Exceltec, private communication, Aug, 2000.}$$

Inst & Controls Lundberg, 1989: (very favorable estimate...likely should be \$500-1000/kW)

$$CC_{\text{IC}} = 300 \text{ fixed cost....Includes cost of instrumentation, controls, startup boiler, N}_2 \text{ system}$$

$$C_{\text{IC}} = \frac{CC_{\text{IC}}}{\text{Power}_{\text{kW}}}$$

$$CC_{\text{FAB}} = 250 \text{ fixed cost....fabrication \& Assembly (labor) costs from ADL (2001) report to DOE on 5 kW Aux Power}$$

$$C_{\text{FAB}} = \frac{CC_{\text{FAB}}}{\text{Power}_{\text{kW}}}$$

$$C_{\text{Misc}} = 50 \text{ \$/kWe.....piping, valves, wiring, insulation}$$

----- Heat Recovery -----

Hot Water Heater

$$\text{Tank}_{\text{HW}} = 350 \text{ Fixed Cost for supplementary tank and HW Heater Retrofit}$$

$$C_{\text{tank}} = \frac{\text{Tank}_{\text{HW}}}{\text{Power}_{\text{kW}} + 0.0001}$$

